

TECHNISCHE UNIVERSITÄT MÜNCHEN

Lehrstuhl für Technische Chemie II

Photoreforming of oxygenates on noble metal decorated semiconductors

Kai Erik Sanwald

Vollständiger Abdruck der von der Fakultät für Chemie der Technischen Universität
München zur Erlangung des akademischen Grades eines

Doktors der Naturwissenschaften (Dr. rer. nat.)

genehmigten Dissertation.

Vorsitzender: Prof. Dr.-Ing. Kai-Olaf M. Hinrichsen

Prüfer der Dissertation:

1. Prof. Dr. Johannes A. Lercher
2. Prof. Dr. Ulrich K. Heiz
3. Prof. Dr. Rolf J. Behm

Die Dissertation wurde am 14.03.2017 bei der Technischen Universität München
eingereicht und durch die Fakultät für Chemie am 05.07.2017 angenommen.

*For my parents
and Verena*

...industrial colonies without smoke and without smokestacks... will extend over the plains and glass buildings will rise everywhere; inside of these will take place the photochemical processes that hitherto have been the guarded secret of the plants, but that will have been mastered by human industry... and if in a distant future the supply of coal becomes completely exhausted, civilization will continue as long as the sun shines! If our black and nervous civilization, based on coal, shall be followed by a quieter civilization based on the utilization of solar energy, that will not be harmful to progress and to human happiness.

G. Ciamician, The Photochemistry of the Future, *Science* (1912)

Acknowledgements

The accomplishment of this work would not have been possible without support by many persons whom I want to express my deepest gratitude.

I am very grateful to Prof. Dr. Johannes A. Lercher for the guidance, trust and scientific freedom you provided. Our discussions and your advice have been enriching. Your aspiration and persistence made me develop new skills and competences - on a scientific and personal level - and helped me to overcome even seemingly intractable problems.

I am greatly indebted to my supervisor Dr. Oliver Y. Gutiérrez. Your steadily positive and encouraging attitude has been inspiration and motivation for me. I am aware and owe you a great debt of gratitude for the constant availability for discussion, the assertiveness and the efforts you have invested in my issues. It has been a pleasure to work with you and I have enjoyed the pragmatic and productive collaboration that we have established along this journey.

I specifically thank my former colleague and mate Dr. Tobias Berto for the intensive and reliable cooperation. We have complemented each other very well. The precision, endurance, consistency and experience you shared improved my quality of work. I deeply value that we have always dealt with each other in a very open and fair manner even during periods of difficulty.

I express my gratitude to Prof. Dr. Wolfgang Eisenreich and Christine Schwarz for their contributions and support concerning the adaptation of quantitative NMR methodology. These tools have become an essential basis enabling many achievements of this work. Thank you also very much for the generosity applied regarding my claims of measurement times.

I appreciate the excellent technical assistance, experience and consultation by Xaver Hecht and his engagement in fixing spontaneously emerging problems. I acknowledge the help of Martin Neukamm performing AAS and SEM measurements and the technical support by Andreas Marx. Moreover, I am also grateful to the staff of the mechanical workshop for a pleasant and successful cooperation.

I am very grateful to Ulrike Sanwald, Stefanie Seibold and Bettina Federmann for the help and organizational work.

I thank all the colleagues who have been part of the group throughout the last 3.5 years for their support and for creating a pleasant environment during daily work and travels. Specifically, I am grateful to Udishnu Sanyal for his efforts in getting the best micrographs from our TEM equipment. I thank Matthias Steib for his help and discussions about the XAFS activities. I am very grateful and enjoyed the times with Sylvia Albersberger, Ferdinand Vogelgsang, Daniel Melzer, Andreas Ehrmaier, Moritz Schreiber and Rachit Khare in day and night shifts during beamtimes.

I owe the students I have supervised my deepest respect and appreciation. Alexander Boeth, Benjamin Strehle, Cindy Tran, Hazmil bin Jainal, Max Schütz, Nadia Almunawa, Simon Vogt, Tianyi Ma and Tony Gao Shuai, thank you for your interest, motivation to work hard and the contributions.

I want to thank my friends, particularly, Simon Rittmeyer and Stephan Tschigg, for their support and encouragements. Thank you for being very patient with me accepting my ups and downs and whenever I had to prioritize work over other activities.

I am indebted to the loving support by Verena and my family. Thank you for your endless and invaluable patience and encouragements which are clearly the foundation for my achievements.

Kai

Munich, March 9, 2017

Abbreviations

AAS	Atomic absorption spectroscopy
AM 1.5 G	Air mass 1.5 global
AQE	Apparent quantum efficiency
BET	Brunauer-Emmett-Teller
BJH	Barrett-Joyner-Halenda
CB	Conduction band
CC	Cosine corrector
CM	Cold Mirror
CMA-ES	Covariance matrix adaptation evaluation strategy
DESY	Deutsches Elektronen-Synchrotron
DFT	Density functional theory
DHA	Dihydroxyacetone
DR	Diffuse reflectance
EPR	Electron paramagnetic resonance
ESRF	European Synchrotron Radiation Facility
FCI	Fonds der Chemischen Industrie
FID	Flame ionization detector
FWHM	Full width at half maximum
GAD	Glyceraldehyde
GC	Gas chromatography
HA	Hydroxyacetone
HER	Hydrogen evolution reaction
HGF	Helmholtz-Gemeinschaft Deutscher Forschungszentren
HHV	Higher heating value
HOMO	Highest occupied molecular orbital
HOR	Hydrogen oxidation reaction
HPLC	High-performance liquid chromatography
IC	Ion chromatography
ICP	Inductively coupled plasma
IR	Infrared
LED	Light-emitting diode

MAS	Magic-angle spinning
NHE	Normal hydrogen electrode
NMR	Nuclear magnetic resonance
NOESY	Nuclear Overhauser effect spectroscopy
ODE	Ordinary differential equation
OES	Optical emission spectrometry
PIPS	Passivated implanted planar silicon
PROX	Preferential oxidation
PTFE	Polytetrafluoroethylene
PSA	Pressure swing adsorption
PZC	Point of zero charge
RI	Refractive index
SEM	Scanning electron microscopy
SFG	Sum-frequency generation
STH	Solar-to-hydrogen
STO	Strontium titanate (SrTiO_3)
TCD	Thermal conductivity detector
TEM	Transmission electron microscopy
UV	Ultraviolet
VB	Valence band
Vis	Visible
WGS	Water-gas shift
XAFS	X-ray absorption fine structure
XANES	X-ray absorption near-edge structure
XAS	X-ray absorption spectroscopy
XRD	X-ray diffraction

Symbols

<i>Symbol</i>	<i>Description</i>	<i>Unit</i>
A	Illuminated area	[m ²]
c_i	Concentration of component i	[mol m ⁻³]
e^-	Photogenerated electron	[-]
$E'_{F,M}$	Metal Fermi level energy (after contact)	[J]
$E'_{F,S}$	Semiconductor Fermi level energy (after contact)	[J]
ΔE^0	Standard electromotive force	[V]
$E^0_{(Ox./Red.)}$	Standard reduction potential	[V]
E^0_{Anode}	Standard anodic half-cell potential	[V]
$E^0_{Cathode}$	Standard cathodic half-cell potential	[V]
E_{CB}	Conduction band edge potential	[V]
$E_{F,M}$	Metal Fermi level energy	[J]
$E_{F,S}$	Semiconductor Fermi level energy	[J]
E_g	Band gap energy	[J]
E_{pot}	Potential energy	[J]
E_{Vac}	Reference vacuum level energy	[J]
E_{VB}	Valence band edge potential	[V]
$F(R)$	Function of reflectance	[a.u.]
ΔG^0	Change in standard Gibbs free energy	[J mol ⁻¹]
h	Planck's constant	[J s]
h^+	Photogenerated hole	[-]
J	Coupling constant	[Hz]
k^{app}	Intrinsic rate constant	[mol s ⁻¹]
K^{app}	Apparent adsorption constant	[-]
$K^{L,app}_f$	Apparent Langmuir adsorption constant	[L mol ⁻¹]
$N_A(t)$	Time-dependent molar amount of species A	[mol]
$N_{A,0}$	Initial amount of species A	[mol]
P_{total}	Total incident illumination power density	[W m ⁻²]
R	Reflectance	[%]
r_i	Reaction/formation rate of component i	[mol s ⁻¹]
R_S	Reflectance of sample	[%]

R_T	Reflectance of PTFE reference	[%]
$T1$	Longitudinal relaxation time	[s]
V_O	Oxygen vacancy	[-]
X_A	Conversion of species A	[%]
$N(\gamma)$	Incident photon flux	[s ⁻¹]

<i>Greek symbol</i>	<i>Description</i>	<i>Unit</i>
ϕ_B	Schottky barrier height	[J]
ϕ_M	Metal work function	[J]
ϕ_S	Semiconductor work function	[J]
Φ_{AQE}	Apparent quantum efficiency	[%]
Δ	Thermal energy	[J]
θ	Scattering angle	[°]
θ_i^L	Coverage of component i (Langmuir model)	[-]
ν	Frequency	[Hz]
λ	Wavelength	[m]
χ	Stoichiometric coefficient	[mol ⁻¹]

Abstract

Photoreforming allows for coupled H_2 -generation and purification of wastewater by oxidation of polyalcohols to CO_2 . Selectivities between C-C cleavage and oxidation to carbonyl groups in polyols and sugar aldoses depend on molecular structure. Controlling pH for OH^- -induced hydrolysis or adjusting the contribution of overall water splitting to the generation of oxidation equivalents are effective strategies to overcome kinetic constraints and tune selectivities towards efficient mineralization.

Kurzzusammenfassung

Photoreformierung von Polyalkoholen ermöglicht eine gekoppelte H_2 -Erzeugung und Abwasserreinigung durch Oxidation zu CO_2 . Die Selektivitäten zwischen C-C Spaltung und Oxidation zu Carbonylgruppen für Polyole und Aldosen sind abhängig von der Molekularstruktur. pH-Steuerung von OH^- -Hydrolyse oder die Anpassung des Beitrags der Wasserspaltung zur Erzeugung von Oxidationsäquivalenten sind effektive Strategien, um kinetische Hemmnisse der Mineralisierung zu überwinden.

Table of contents

Acknowledgements.....	I
Abbreviations.....	III
Symbols.....	V
Abstract.....	VII
Table of contents.....	VIII
1. General introduction.....	2
1.1 Heterogeneous catalysis and photochemistry for the production of energy carriers.....	2
1.2 Scope of the thesis	4
1.3 Heterogeneous photocatalysis – working principles.....	6
1.4 Hydrogen – chemical intermediate and energy carrier.....	8
1.5 Photocatalytic H ₂ -generation via photoreforming and water splitting	12
1.6 Materials	16
1.7 Role and function of co-catalysts	18
1.7.1 H ₂ -evolution catalysis.....	18
1.7.2 Charge transfer	19
1.7.3 Suppression of water formation	21
1.8 Kinetics and mechanism of oxygenate photoreforming.....	25
1.8.1 Factors governing photoreforming rates.....	25
1.8.2 Oxygenate transformations during photoreforming	28
1.9 References.....	34
1.10 Supporting information	43
2. Catalytic routes and oxidation mechanisms in photoreforming of polyols.....	45
2.1 Abstract	45

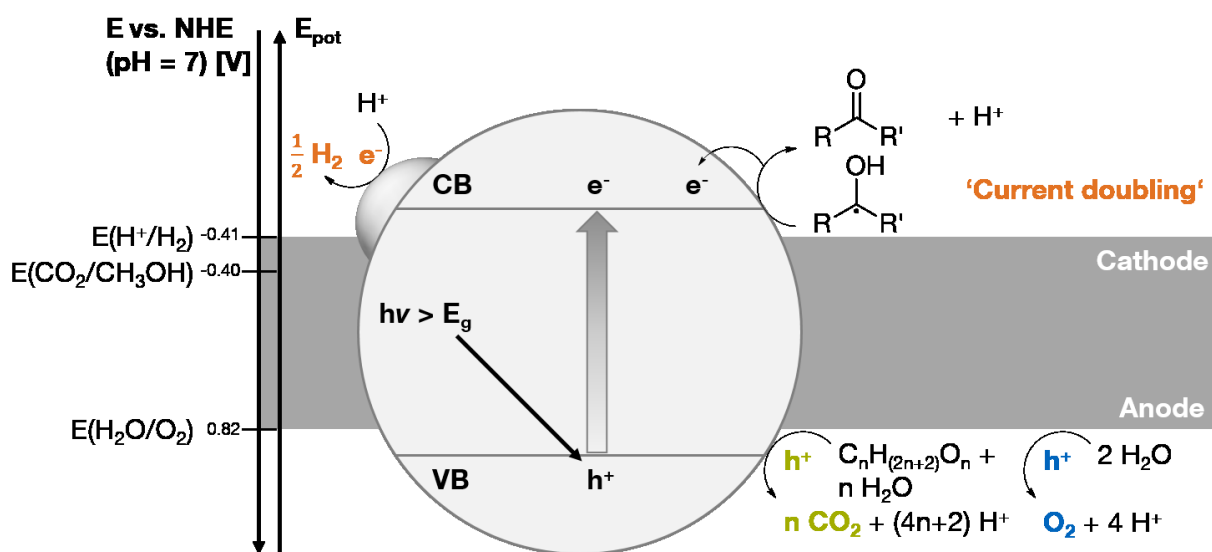
2.2	Introduction.....	46
2.3	Experimental	48
2.3.1	Materials	48
2.3.2	Photocatalyst preparation	48
2.3.3	Photocatalytic test	49
2.3.4	Physicochemical characterization.....	51
2.4	Results and discussion	53
2.4.1	Physicochemical properties of the photocatalyst	53
2.4.2	Kinetics of photoreforming of glycerol and C ₃ -intermediates.....	54
2.4.3	Path 4: Direct oxidative C-C cleavage of glycerol.....	63
2.4.4	Photoreforming of C ₄ -C ₆ polyols	68
2.4.5	Mechanistic aspects of anodic transformations of polyols	72
2.5	Conclusions	75
2.6	Acknowledgements	76
2.7	References.....	77
2.8	Supporting information	81
3.	Identifying and overcoming the rate-limiting reaction during photoreforming of sugar aldehydes for H₂-generation.....	96
3.1	Abstract	96
3.2	Introduction.....	97
3.3	Experimental	99
3.3.1	Materials	99
3.3.2	Photocatalyst preparation	99
3.3.3	Photocatalytic test	100
3.3.4	Physicochemical characterization.....	102
3.4	Results and discussion	104

3.4.1	On the oxidation state of the co-catalysts	104
3.4.2	H ₂ -evolution during sugar photoreforming	107
3.4.3	Anodic reaction pathways.....	108
3.4.4	Mechanistic considerations.....	114
3.4.5	Pathways for formate hydrolysis	115
3.4.6	Photoreforming of sugar aldoses in alkaline media.....	116
3.5	Conclusions	121
3.6	Acknowledgements	122
3.7	References.....	123
3.8	Supporting information	126
4.	Kinetic coupling of water splitting and photoreforming on SrTiO₃-based photocatalysts.....	152
4.1	Abstract	152
4.2	Introduction.....	153
4.3	Experimental	155
4.3.1	Materials	155
4.3.2	Photocatalyst preparation	155
4.3.3	Photocatalytic test	156
4.3.4	Physicochemical characterization.....	157
4.4	Results and discussion	160
4.4.1	Physicochemical properties of the photocatalysts.....	160
4.4.2	H ₂ -generation from coupled H ₂ O-splitting and photoreforming	163
4.4.3	Anodic glycerol conversion on STO-Al photocatalysts	164
4.4.4	Reaction network for glycerol oxidation.....	166
4.4.5	Effect of the nature of the oxygenate and its concentration on H ₂ -evolution rates.....	169

4.4.6	Kinetic isotope effects in H ₂ -evolution rates	171
4.4.7	Effect of the nature of the oxygenate and its concentration on H ₂ O and oxygenate oxidation selectivity	172
4.4.8	Effect of light intensity.....	173
4.4.9	Mechanistic considerations.....	174
4.5	Conclusions	179
4.6	Acknowledgements	180
4.7	References.....	181
4.8	Supporting information	184
5.	Summary and conclusions	203
6.	Zusammenfassung und Schlussfolgerungen	206
	Curriculum vitae	210
	List of publications	212
	Conference contributions	213

Chapter 1

General introduction



1. General introduction

1.1 Heterogeneous catalysis and photochemistry for the production of energy carriers

The development of an environmentally friendly energy economy will involve the introduction of technologies based on the utilization of renewable sources of energy. The solar energy that reaches Earth provides within about one hour the amount of energy covering the power that is demanded by mankind throughout a whole year (15 TW in 2011) [1-4]. Thus, efficient conversion of solar energy into chemical energy carriers is an attractive prospect that has the potential to dwarf power generation based on depleting fossil resources (or on any other renewable resource, e.g. wind or biomass) that our current energy infrastructure relies upon. Following this pathway holds promise for a cleaner and more sustainable energy supply in the carbon constrained future.

Heterogeneous photocatalysis on powdered semiconductor photoabsorbers may provide a technologically simple means for photochemical energy conversion that operates at ambient conditions to directly convert solar energy into a chemical fuel in a one-step process [5, 6]. That way, in comparison to photovoltaic energy capture coupled to downstream conversion technologies (e.g. water electrolysis) the intermediary generation of electrical energy is bypassed. Efficient solar photochemical energy conversion requires that large parts of the solar spectrum are harvested. This calls for visible-light absorbing, narrow band-gap semiconductor photoabsorbers [5, 6]. The energy input upon absorption of a single, visible-light photon is approximately in the range of 1.5 – 3.0 eV (about 150 – 300 kJ mol⁻¹) which enables to drive chemical reactions.

In anaerobic environment and aqueous-phase different pathways exist to generate hydrogen photocatalytically as a simple chemical fuel. Photocatalytic overall water splitting into hydrogen and oxygen is regarded as an important route to produce solar H₂ [5-7]. However, measures to prevent back-reaction and to allow for separation of the highly reactive gas mixture generated have to be taken [6, 8-11]. As an alternative, coupled H₂-evolution and photocatalytic degradation to CO₂ occurs in the presence of organic

substrates, e.g. derived from abundant biomass constituents or contaminants in natural or industrial wastewater [12-14]. Due to the similarities of the gas-phase product distributions to thermocatalytic reforming the latter coupled photocatalytic process has been referred to as ‘photoreforming’ [15]. Oxygenate photoreforming enables H_2 production while benefiting from the generation of added-value through environmental remediation in terms of mineralization of wastewater constituents (i.e. transformation of an organic compound into an inorganic one like CO_2). The process exploits the potential of (sun)light and wastewater as resources while concomitant CO_2 evolved may be recycled to the natural photosynthesis capacity [13]. (Poly)alcohols like glycerol from triglyceride transesterification, e.g. during biodiesel manufacture (about 1.8 Mio. t aqueous, raw glycerol annually), and carbohydrates including cellulose and biomass-derived sugars, are targeted feedstocks [16, 17].

1.2 Scope of the thesis

In this thesis, photocatalytic H₂-generation *via* photoreforming on noble metal decorated TiO₂- and SrTiO₃-based semiconductors has been investigated. The work is focused on the exploration of the reaction pathways, nature of the organic intermediates, selectivities and mechanisms in the photocatalytic and thermal surface transformations which constitute the last step of the photocatalytic cycle. Using C₁-C₆ oxygenates, i.e. (poly)alcohols and sugar aldoses as probe molecules, the implications of molecular structure on the chemistry in the anodic half-reactions, the overall photocatalytic H₂-evolution rates and the mineralization behavior are addressed. Moreover, the impact of a semiconductor photoabsorber capable of oxidizing water to O₂ (a process that does not occur on TiO₂ but proceeds on SrTiO₃-based photocatalysts) for efficient H₂ production was elucidated. Specifically, the contribution of water splitting to the generation of oxidation equivalents and their mechanism of action providing additional reduction equivalents was examined.

Photocatalytic technologies for environmental remediation, i.e. in the removal of (in)organic contaminants from air, water and soil, by oxidation under aerobic conditions mainly on undecorated TiO₂-based semiconductors have been successfully established on a commercial scale in the past three decades [18-21]. Operating under anaerobic conditions (in presence of a suitable co-catalyst) enables photocatalytic H₂-generation. Yet, in absence of O₂ the oxidants available for mineralization can only be formed from photogenerated holes and/or oxidants generated therefrom. To date, in order to improve photocatalytic rates research efforts have been mainly devoted to the development of visible-light responsive semiconductors and strategies towards realization of efficient charge carrier separation mitigating recombination reactions. However, the lack of detailed mechanistic understanding of the photocatalytic reactions involved under these conditions has limited the success in the rational development of suitable photocatalysts and associated processes for photoreforming.

In the introductory chapter the working principle of heterogeneous photocatalysis on powdered semiconductors, the current practice in the production and usage of H₂ as a chemical intermediate and its potential as energy carrier are briefly summarized.

Moreover, a comparison of overall water splitting and photoreforming, description of the function of co-catalysts for H₂-evolution and the state-of-the-art knowledge of the factors influencing the kinetics and mechanisms of oxygenate photoreforming are presented.

In Chapter 2 the catalytic routes and oxidation mechanisms for photoreforming of C₃-C₆ polyols on a benchmark Rh/TiO₂ photocatalyst are reported. On the basis of quantitative detection of liquid- and gas-phase species reaction networks were derived. The anodic transformations, i.e. C-C cleavage, oxidation to carbonyl moieties and dehydration, were rationalized considering the nature of different interfacial hole transfer mechanisms involved. The dependence of the selectivities between these pathways on polyol chain length, i.e. number of anchoring OH-functionalities, was systematically explored. Independent of chemical bond transformation rate equations based on Langmuir adsorption successfully described the photoreforming kinetics revealing the primary correlation of oxygenate coverage and H₂-evolution rates.

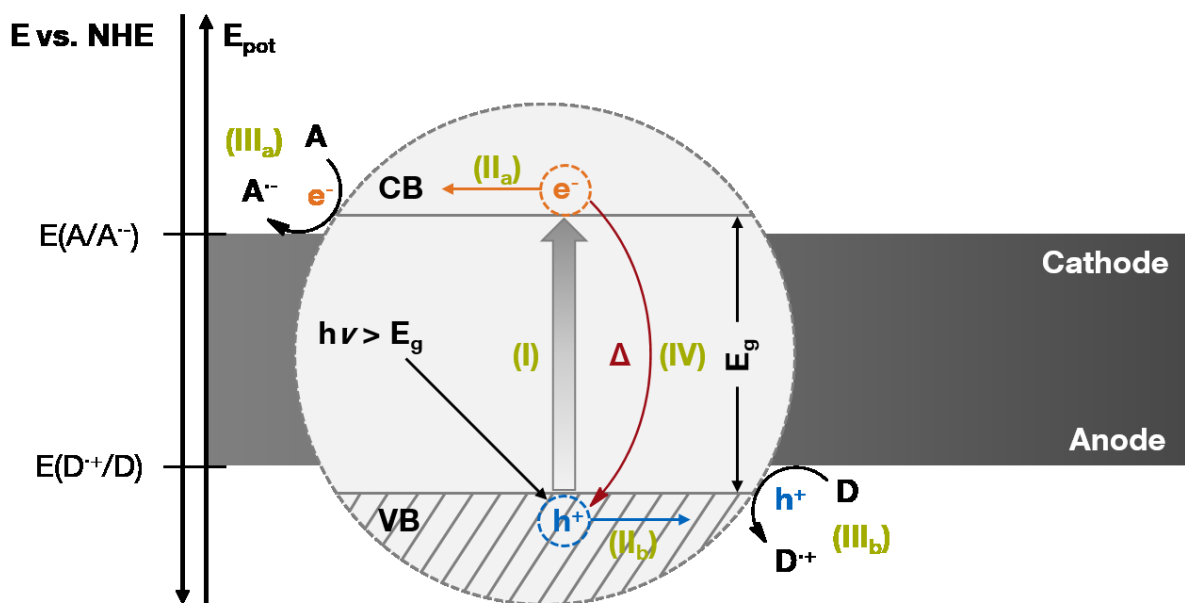
In the third chapter photoreforming of sugar aldoses, particularly glucose, on noble metal (Rh, Pd, Pt) decorated TiO₂ is presented. Unlike polyol photoreforming the reaction proceeded with rapidly declining H₂-evolution rates. We identified the origin of the sluggish kinetics in terms of the rate-limiting reaction step that lead to intermediate accumulation and blocking of anodic sites under pH-neutral and acidic conditions. Maintaining alkaline pH is demonstrated to enable stable H₂-evolution and sugar conversion. OH⁻-induced hydrolytic cleavage of intermediates aids to overcome the kinetic constraints in photocatalytic degradation reactions. Additionally, the oxidation state of the co-catalysts under H₂-evolution conditions was determined by X-ray absorption spectroscopy (XAS).

In Chapter 4 the kinetic and mechanistic consequences of coupling the anodic half-reactions of photoreforming and overall water splitting, i.e. oxygenate and water oxidation, on Rh/SrTiO₃-Al and RhCrO_x/SrTiO₃-Al photocatalysts for photocatalytic H₂-evolution are elucidated. The factors contributing to H₂-evolution and those controlling the selectivities between photoreforming and water splitting were investigated under conditions of suppressed back-reaction. The nature of the active oxidant species tuning the selectivities in oxygenate oxidation towards efficient mineralization is discussed. A strategy for activation of concomitant O₂ from water splitting to participate in anodic oxygenate degradation is presented.

1.3 Heterogeneous photocatalysis – working principles

Heterogeneous photocatalysis refers to a photoelectrochemical reaction initiated by the interaction of electromagnetic radiation with suitable energy and a solid semiconductor photoabsorber to create photogenerated charges, i.e. electron-hole (e^- - h^+) pairs. These charge carriers may subsequently be trapped into chemical entities, e.g. radical species, or engage directly in concerted surface redox half-reactions with adsorbed reactants reconstituting the initial state of the photocatalyst [22-25].

The processes ensuing band gap irradiation of a semiconductor particle are depicted in Scheme 1.1. Upon impingement of a photon with energy equal or larger than the semiconductor band gap absorption and photoexcitation of electrons from a filled valence band (VB) into unoccupied states of a conduction band (CB) may occur (I). A positive hole is left in that VB. After thermal relaxation of electron and hole to CB bottom and VB top edges, respectively, these semiconductor band edge potentials equal the electrochemical potentials of the respective charge carrier [24, 26]. For subsequent surface trapping and interfacial charge transfer to take place (II_{a+b}) it is thermodynamically required that the



Scheme 1.1. Processes occurring upon band gap irradiation of a semiconductor. (I) Photoexcitation of an electron-hole pair. (II) Surface migration/trapping. (III_a) Cathodic surface half-reaction: Electron transfer onto acceptor species A. (III_b) Anodic surface half-reaction: Hole transfer onto donor species D. (IV) Competing electron-hole recombination.

electrochemical potential of photogenerated electron/hole is more negative/positive (or more cathodic/anodic) than the one-electron redox potential of the corresponding adsorbate to be reduced/oxidized. This principle is illustrated by means of acceptor species A and donor species D in Scheme 1.1.

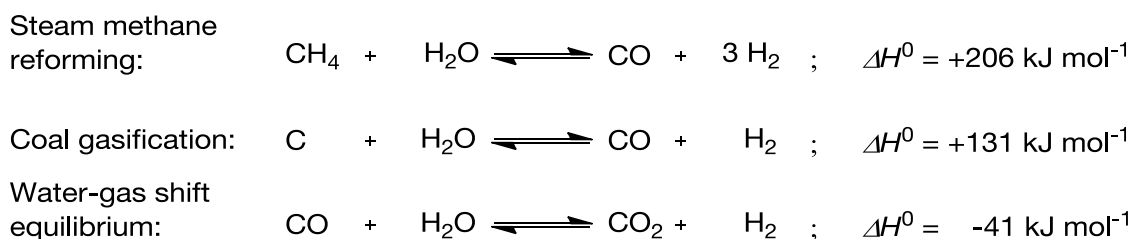
The photocatalytic redox half-reactions (III_{a+b}) give rise to two distinct types of surface reaction sites which may be classified as cathode and anode due to the different nature of electrons and holes. Thus, photocatalytic reactions in dispersed powder systems in aqueous electrolyte, which ensures proton conductivity and, hence, chemical charge equalization, may be viewed as micro-electrochemical cells [27, 28]. Note that unlike in electrochemistry, cathodic and anodic sites are located on the same particle. Moreover, in absence of external bias charge carrier recombination (IV) may compete with photocatalysis at any stage of the catalytic cycle.

As electromagnetic energy is introduced in the first step, both, exergonic and endergonic reactions, may be driven by photocatalysis without external input of thermal energy. In the endergonic case, in conjunction with the production of a chemical fuel, the photocatalyst enables the storage of the energy of light in chemical energy partly realizing the functionality of an 'artificial leaf' [29].

1.4 Hydrogen – chemical intermediate and energy carrier

At present, the global production of H_2 amounts to more than 50 Mio. t (more than 600 GNm³) annually. H_2 derives almost exclusively (about 95 %) from reforming of natural gas, petroleum as well as from coal gasification with the remainder being generated mainly *via* water electrolysis (4 %) and biomass gasification (1 %) [30-33]. Steam reforming as exemplified for methane in Scheme 1.2 and coal gasification are predominantly applied to fossil feedstocks in a first reaction step to generate a gaseous mixture containing H_2 , CO, CO_2 (*via* the water-gas shift (WGS) equilibrium, Scheme 1.2) and steam. The highly endothermic reforming process requires harsh reaction conditions (typically 700 – 900 °C, pressures above 20 bar [34]), imposes drastic requirements upon catalyst stability or regenerability and represents a vast source of CO_2 emissions.

In order to boost H_2 -yields, subsequent WGS stages are performed at lower temperatures (typically about 350 – 550 °C and below 250 °C for high and low-temperature WGS [34]) to overcome thermodynamic limitations for CO consumption due to approach to equilibrium while ensuring rapid kinetics. Eventually, a mixture of mainly H_2 and CO_2 (and steam) is generated. Further processing *via* preferential oxidation (PROX) of CO or selective CO methanation and separation *via* membranes or pressure swing adsorption (PSA) are required to obtain a highly pure H_2 -stream [35]. To date, H_2 is predominantly applied as a chemical intermediate in ammonia synthesis (about 45 %), fed to petroleum refining processes (about 45 %) and methanol synthesis (4 %) [30]. However, large-scale H_2 production using state-of-the-art technology represents a non-sustainable pathway based on fossil resources.



Scheme 1.2. Catalytic routes for H_2 -generation *via* steam reforming of natural gas and coal gasification (exemplified in terms of CH_4 and C, respectively). The water-gas shift equilibrium is used to maximize H_2 outputs. Standard reaction enthalpies were adapted from ref. 34.

Most scalable technologies for H₂ manufacture from abundant, renewable resources such as biomass, (waste)water and (sun)light and options for direct H₂ storage and usage as a chemical energy carrier, e.g. in fuel cells, currently lack economic viability.

Apart from conceptions relying on external input of thermal energy, e.g. thermochemical cycles to cleave water [36], biomass pyrolysis and gasification [37, 38], and biological processes [39], sustainable approaches towards H₂-generation comprise photocatalytic and (photo)electrochemical means. Considering the extent of solar irradiance and the abundance of (waste)water resources photo(electro)catalytic H₂ manufacture *via* cathodic reduction of aqueous protons which enables environmental remediation by anodic degradation reactions holds promise for H₂ production.

The technical target for photocatalytic H₂ production *via* overall water splitting using particulate photocatalysts to become economically viable designates a solar-to-hydrogen (STH) efficiency of larger than 10 % mandatory [40]. The STH efficiency as defined in eq. (1.1) provides a measure of the ‘chemical energy produced’ in terms of the product of H₂-evolution rate r_{H_2} and the change in standard Gibbs free energy (e.g. +237 kJ mol⁻¹ for overall water splitting) per ‘solar energy input’ represented by the product of the total incident illumination power density P_{total} and illuminated area A [41].

$$STH = \left[\frac{r_{H_2} \cdot \Delta G^0}{P_{total} \cdot A} \right]_{AM\ 1.5\ G} \quad (1.1)$$

On the other hand, the apparent quantum efficiency (AQE, eq. (1.2)) for photocatalytic H₂-generation is given by the quotient of r_{H_2} multiplied by a stoichiometric coefficient χ^a and the incident photon flux $N(\gamma)$ under conditions assuming that all irradiated photons are absorbed by the photocatalyst [42].

$$\Phi_{AQE} = \left[\frac{\chi \cdot r_{H_2}}{N(\gamma)} \right]_{\lambda} \quad (1.2)$$

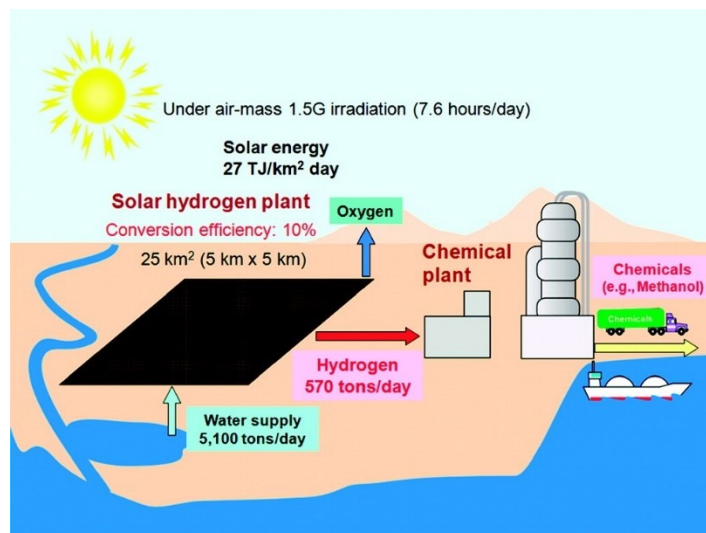
Note that the AQE is uniquely a wavelength dependent quantity, i.e. monochromatic light sources have to be applied. In order to achieve 10 % STH efficiency photocatalyst

^a χ is commonly specified as two accounting for the circumstance that two photogenerated electrons are required to evolve one hydrogen molecule into the gas-phase. Note that in the context of photoreforming this requires the absence of ‘current-doubling’ processes (*vide infra*).

materials have to meet AQEs of about 60 % and 100 % at 600 nm and 500 nm, respectively [6].

To date, the highest STH values reported for photocatalytic H₂-generation from overall water splitting on powdered photocatalyst systems in absence of external bias and sacrificial agents are of the order of 0.1 - 5 % [43-47]. Despite great efforts towards improved STH efficiencies large-scale photocatalytic H₂-generation remains a distant goal. This is due to the lack of reproducible and scalable synthesis protocols, highly active materials not being based on cost-effective, abundant elements and missing demonstration of long-term stability [48].

On the basis of a 10 % STH efficiency and a daily input of Air mass 1.5 global (AM 1.5 G) irradiation for 7.6 h, it was estimated that covering a third of the projected power consumption of humanity in 2050 (equals about 10 TW [3]) by photocatalytic H₂-generation would scale to a single plant harvesting from 250000 km² (1 % of earth's desert area, or equally 10000 plants of 5 km x 5 km dimension). As illustrated in Scheme 1.3, 5.7 Mio. t of H₂ would be generated in total per day [6]. Sealed pools containing photocatalyst suspension, plate or tubular reactors with the photocatalyst being either immobilized and continuously overflowed by reactant solution or configurations where the photocatalyst suspension is circulated are potential reactor concepts [49-52].



Scheme 1.3. Illustration of a large-scale operation of photocatalytic H₂-generation via overall water splitting ('solar hydrogen plant') and downstream H₂ conversion into liquid fuels. *Reprinted with permission from ref. 6. Copyright (2010) American Chemical Society.*

Moreover, the slow uptake of conceptions relying on the direct utilization of H₂ as an energy carrier in mobile or stationary applications results from the necessity of compression or liquefaction to achieve reasonable volumetric energy densities as listed in Table 1.1. As indicated in Scheme 1.3, in future, these circumstances might render consecutive H₂ transformation, e.g. in the production of liquid, hydrocarbon-based fuels with high volumetric energy densities preferable. To this end, photocatalytic options, e.g. transfer hydrogenation of organic compounds [53, 54] or reduction of CO₂ [55, 56] are developed which are beyond the scope of this thesis.

Table 1.1. Comparison of specific and volumetric energy densities of H₂ with conventional fuels. *Adapted from ref. 57, Energy Policy, Copyright 2008, with permission from Elsevier (license number: 4031940993969).*

Energy carrier	Specific energy density	Volumetric energy density
	[kWh kg ⁻¹]	[kWh L ⁻¹]
H ₂ (gas, 200 bar)	33.3	0.5
H ₂ (liquid)	33.3	2.4
Natural gas (200 bar)	13.9	2.3
Natural gas (liquid)	13.9	5.6
Methanol	5.5	4.4
Diesel	12.6	10.6

1.5 Photocatalytic H₂-generation *via* photoreforming and water splitting

The redox half-reactions in overall water splitting and photoreforming generalized for polyols are compiled in Table 1.2. Photocatalytic H₂-generation occurs in both cases through cathodic reduction of H⁺ that originates from water by photogenerated electrons and subsequent desorption of molecular H₂ into the gas-phase. H-atoms in oxygenates are primarily not involved in the cathodic half-reaction [58, 59]. The required reduction equivalents for H₂-evolution are provided in the anodic half-reactions in which water and oxygenates engage as electron donors to oxidize to O₂ and CO₂, respectively. In this process oxygenates act as ‘sacrificial agents’ irreversibly consuming photogenerated holes or oxidants derived therefrom to enable H₂ production.

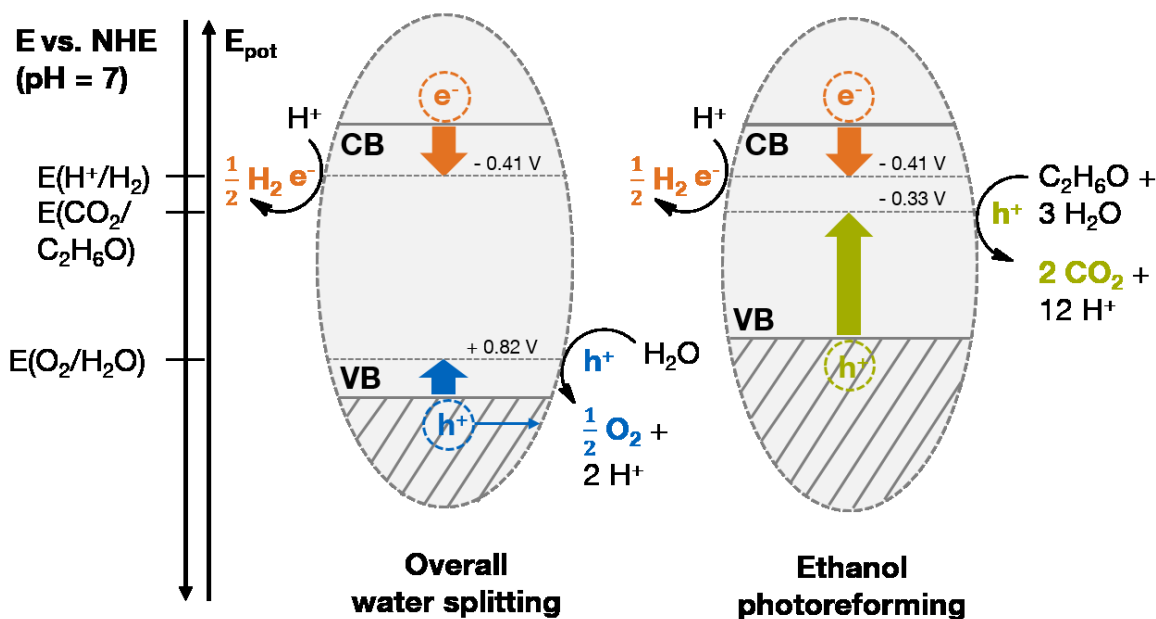
Water oxidation to O₂ or oxygenate oxidation in the anodic half-reactions give rise to diverging energy requirements with respect to semiconductor band edge potentials to be met in order for the overall redox processes to proceed (Scheme 1.4). In case of overall water splitting the energetic separation of H₂- and O₂-evolution reaction ($\Delta E^0 = E^0_{\text{Anode}} - E^0_{\text{Cathode}}$) amounts to $\Delta E^0 = 1.23$ V. Oxygenates typically represent stronger reducing agents compared to water, i.e. oxidation occurs at a more negative potential (Table 1.3). Consequently, the energetic separation of the redox half-reactions is drastically narrowed for photoreforming compared to overall water splitting.

Table 1.2. Anodic, cathodic redox half-reactions and overall reaction equations for H₂-generation *via* overall water splitting and photoreforming of polyols. Note that ‘h⁺’ denotes a hole.

	Overall water splitting	Polyol photoreforming
Cathode	$2 \text{ H}^+ + 2 \text{ e}^- \rightarrow \text{H}_2$	$2 \text{ H}^+ + 2 \text{ e}^- \rightarrow \text{H}_2$
Anode	$2 \text{ H}_2\text{O} + 4 \text{ h}^+ \rightarrow \text{O}_2 + 4 \text{ H}^+$	$\text{C}_n\text{H}_{2n+2}\text{O}_n + n \text{ H}_2\text{O} + (4n+2) \text{ h}^+ \rightarrow$ $n \text{ CO}_2 + (4n+2) \text{ H}^+$
Overall reaction	$2 \text{ H}_2\text{O} \rightarrow 2 \text{ H}_2 + \text{O}_2$	$\text{C}_n\text{H}_{2n+2}\text{O}_n + n \text{ H}_2\text{O} \rightarrow$ $(2n+1) \text{ H}_2 + n \text{ CO}_2$

Exemplified for photoreforming of ethanol, accounting for the redox potentials of the H^+/H_2 and $\text{CO}_2/\text{C}_2\text{H}_6\text{O}$ redox couples (see Scheme 1.4 and Table 1.3) an energetic separation of 0.08 V is derived. However, it should be noted that oxidation of ethanol to CO_2 requires in total the transfer of twelve holes which involves multiple reaction steps. Considering two electron oxidation of ethanol to acetaldehyde (Table 1.3) which is known to constitute the primary intermediate in ethanol photoreforming [60] a potential difference of 0.19 V becomes evident. Thus, determination of the precise energy requirements for oxygenate photoreforming demands knowledge of the oxidation mechanisms, reaction pathways and nature of the organic (stable and radical-like) intermediates generated in any hole transfer step towards oxidation to CO_2 .

Nevertheless, in comparison to overall water splitting appropriate semiconductor band edge potentials are met more easily for photoreforming which renders a larger variety of material classes suitable as photoabsorbers. As a further consequence, larger overpotentials in anodic half-reactions result for oxygenates compared to water oxidation



Scheme 1.4. Relations of redox potentials in overall water splitting and photoreforming (exemplified for ethanol) and semiconductor band edge potentials. Arrows visualize conceptual overpotentials in cathodic and anodic half-reactions. It is highlighted that photoreforming on a semiconductor with even smaller band gap (right, elevated valence band top) results in a higher anodic overpotential compared to overall water splitting.

(Scheme 1.4), which provide an additional driving force accelerating photoreforming rates. Moreover, the alleviated thermodynamic constraints of photoreforming conceptually hold promise for a more facile near-term realization of a visible-light driven process using solar irradiation.

The corresponding changes in standard Gibbs free energy of the photocatalytic transformations enabling H₂-evolution are compiled in Table 1.3. Depending on oxygenate nature photoreforming is a slightly endergonic or even exergonic reaction. In other words, direct storage of photon energy in chemical energy does, if any, takes place only in individual reaction steps which can be endergonic. During photoreforming photon energy is predominantly dissipated in the overpotential losses for the conversion of the chemical energy stored in oxygenates into H₂ (and by-products). Contrarily, overall water splitting is a strongly endergonic reaction where direct storage of photon energy in chemical energy is attained.

Table 1.3. Anodic half-reactions for photoreforming of different oxygenates, corresponding changes in standard oxidation potential and standard Gibbs free energy. ΔG^0 refers to the overall reactions.

Compound	Anodic half-reaction	$E^0_{\text{ox/red}} (\text{pH} = 7)$	ΔG^0
		[V vs. NHE]	[kJ mol ⁻¹]
Methanol	$\text{CH}_4\text{O} + \text{H}_2\text{O} + 6 \text{h}^+ \rightarrow \text{CO}_2 + 6 \text{H}^+$	-0.40 ¹ (-0.38 ^{2,3})	-9 ¹ (-4 ^{2,3})
Ethanol	$\text{C}_2\text{H}_6\text{O} + 3 \text{H}_2\text{O} + 12 \text{h}^+ \rightarrow 2 \text{CO}_2 + 12 \text{H}^+$	-0.33 ¹ (-0.47 ^{2,3})	-97 ¹ (+65 ^{2,3})
Ethanol	$\text{C}_2\text{H}_6\text{O} + 2 \text{h}^+ \rightarrow \text{C}_2\text{H}_4\text{O} + 2 \text{H}^+$	-0.22 ²	-36 ²
Ethylene glycol	$\text{C}_2\text{H}_6\text{O}_2 + 2 \text{H}_2\text{O} + 10 \text{h}^+ \rightarrow 2 \text{CO}_2 + 10 \text{H}^+$	-0.41 ¹	9 ¹
Glycerol	$\text{C}_3\text{H}_8\text{O}_3 + 3 \text{H}_2\text{O} + 14 \text{h}^+ \rightarrow 3 \text{CO}_2 + 14 \text{H}^+$	-0.41 ¹	-5 ¹
Glucose	$\text{C}_6\text{H}_{12}\text{O}_6 + 6 \text{H}_2\text{O} + 24 \text{h}^+ \rightarrow 6 \text{CO}_2 + 24 \text{H}^+$	-0.42 ²	-85 ²
Water	$2 \text{H}_2\text{O} + 4 \text{h}^+ \rightarrow \text{O}_2 + 4 \text{H}^+$	0.82 ²	237 ²

¹: Reference 61. ²: Reference 13. ³: Gas-phase data.

The energy conversion efficiency regarding photocatalytic H₂-generation under the conditions applied in this thesis and subsequent combustion was estimated (see detailed presumptions and calculation in section 1.10). Considering the electrical energy spent to provide band gap irradiation using state-of-the-art UV-LEDs it is assessed that the heat released upon combustion of evolved H₂ in terms of its higher heating value (HHV) accounts for a value in the order of 1 % of the energy spent to operate the light source assuming an AQE of 10 %.

The gaseous mixture of H₂ and CO₂ resulting from photoreforming (e.g. 70 % H₂ and 30 % CO₂ for glycerol photoreforming at full mineralization), which is non-reactive under ambient conditions allows to recourse to established separation technologies for reformer and WGS effluents (see section 1.4). Moreover, amine scrubbing that was promoted in the context of CO₂ capture from concentrated sources can be applied [62, 63]. On the contrary, overall water splitting demands separation of H₂/O₂ mixtures which would have to be developed in parallel [6]. Due to the endergonic nature of water cleavage the back-reaction of H₂ and O₂ to form water is thermodynamically favored. Metal and oxide H₂-evolution co-catalysts deposited onto semiconductors typically catalyze this transformation under ambient conditions [8, 64]. Thus, co-catalyst design to selectively suppress the back-reaction is a prerequisite for efficient H₂-evolution *via* overall water splitting. Simplified co-catalyst concepts are adequate for photoreforming as is treated in further detail in section 1.7.

1.6 Materials

Aeroxide® TiO₂ P 25 and home-prepared Al-doped SrTiO₃ were decorated with a noble metal co-catalyst (Rh, Pd, Pt and (core-shell type) RhCrO_x) and employed as photocatalysts for photoreforming in this thesis. Both semiconductors possess similar electronic structure and band gaps (3.1 – 3.2 eV). The hybrid states at the VB top are mainly composed of filled O 2p (and Sr 4 p) states while the CB bottom predominantly shows contribution of the empty Ti 3d states [65]. Thus, these materials only absorb UV radiation up to about 400 nm which accounts for 3 – 5 % of solar irradiance. However, very high quantum efficiencies can be achieved, i.e. up to 40 % for platinized TiO₂ P 25 during photoreforming of methanol [66] and up to 30 % for Al-doped SrTiO₃ during overall water splitting upon decoration with a RhCrO_x co-catalyst [67], were reported.

Aeroxide® TiO₂ P 25

Aeroxide® TiO₂ P 25 is produced *via* flame hydrolysis (Evonik) and comprises a mixture of rutile and anatase polymorphs with approximately more than 70 % anatase, 15 % rutile and a small amount of amorphous phase [68]. Rutile and anatase phases exhibit slightly different band gaps (3.2 eV and 3.0 eV for rutile and anatase, respectively) and thus band edge potentials [69]. The band edge offsets and formation of interfacial junctions providing charge separation have been suggested for the origin of the high photocatalytic activity of TiO₂ P 25 [69]. Due to its controlled properties TiO₂ P 25 has been frequently employed as a reference material in the field of photocatalysis. Although, co-catalyst decorated TiO₂ P 25 fulfills not only the thermodynamic requirements for oxygenate photoreforming but also for overall water splitting to occur (approximately $E^0 = 2.1$ V and $E^0 = -1.0$ V vs. NHE at pH = 7 for the VB and CB edge, respectively [70]), the material is inactive for photocatalytic O₂-formation in absence of electron acceptors, e.g. Ag⁺. The origin of this behavior is still debated [71-73].

Al-doped SrTiO₃

SrTiO₃ crystallizes in the perovskite (ABO₃) structure. Photocatalysts based on undoped SrTiO₃ show little photocatalytic activity due to rapid electron-hole recombination associated with the presence of Ti³⁺ centers formed upon oxygen removal during SrTiO₃ synthesis at high temperatures [74]. Recrystallization of SrTiO₃ in alkali (earth) metal

chloride flux was shown to result in highly crystalline semiconductors with a reduced density of defect sites [67]. Aliovalent doping with Al^{3+} can be achieved using an alumina crucible which is etched by the flux prior to Al^{3+} incorporation into SrTiO_3 . Compared to undoped SrTiO_3 this treatment results in a 500-fold activity enhancement. This was attributed to follow primarily from the removal of Ti^{3+} sites due to the controlled presence of oxygen vacancies in vicinity of Al^{3+} sites. Unlike TiO_2 , SrTiO_3 -based photocatalysts are active in overall water splitting ($E^0 = 2.0 \text{ V}$ and $E^0 = -1.2 \text{ V}$ vs. NHE at $\text{pH} = 7$ for the VB and CB edge, respectively [70]) when combined with an appropriate co-catalyst [67].

1.7 Role and function of co-catalysts

For cathodic H_2 -evolution to proceed typically semiconductor decoration with a pertinent co-catalyst is mandatory. Diffusion of atomic hydrogen and its combinative desorption on many semiconductors, e.g. on oxides such as TiO_2 , are associated to high activation barriers (in the order of 1 eV) [75-78]. These cannot be overcome at ambient conditions which results in charge carrier recombination. Only few systems capable of evolving H_2 in absence of a co-catalyst were reported including (without any claim to completeness) for instance C_3N_4 [45, 79], SrTiO_3 in very concentrated base [80, 81] or complex mixed metal oxides [82, 83].

1.7.1 H_2 -evolution catalysis

According to the Sabatier principle [84] an ideal catalyst for the hydrogen evolution reaction (HER) must provide an optimal interaction (neither too strong nor too weak), i.e. binding energy, with intermediary adsorbed atomic hydrogen (H_{ad}) in order to maximize HER rates. Combinative desorption of H_2 becomes rate limiting in case of too strong

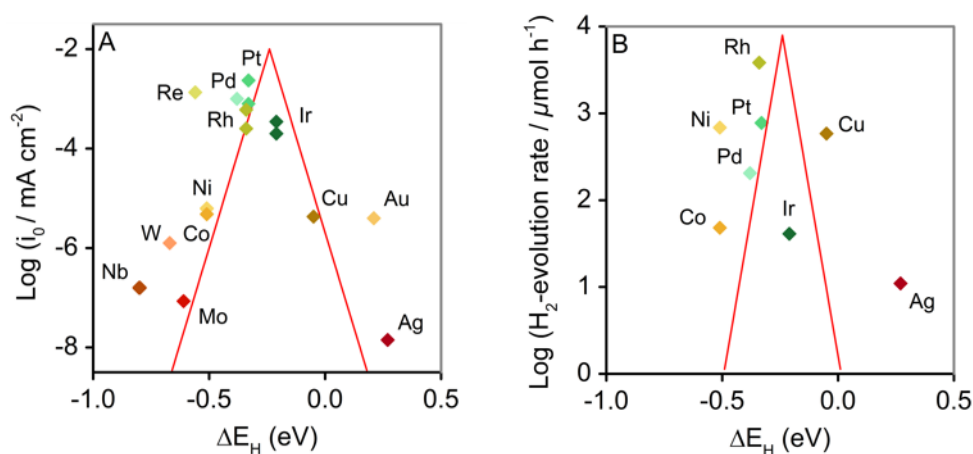


Figure 1.1. (A) Dependence of experimentally determined exchange current densities for H_2 -evolution on different metals in acidic, aqueous electrolyte on computed chemisorption energies. (B) Correlation of photocatalytic H_2 -evolution rates from overall water splitting on co-catalyst decorated GaN:ZnO (co-modified with chromia to suppress back-reaction) and computed chemisorption energies. Volcano-type lines are drawn to guide the eye. *Exchange current densities and chemisorption energies (at a coverage of 0.25) adapted with permission from ref. 85. Copyright 2005, The Electrochemical Society. H_2 -evolution rates adapted from ref. 86, Journal of Catalysis, Copyright 2006, with permission from Elsevier (license number: 4024670635563).*

interactions which leads to a blocking of active sites for the reaction while too weak interactions with H_{ad} result in kinetic limitations imposed by proton reduction [87]. Consequently, a volcano-type dependence of HER rates and catalyst- H_{ad} bond strength has been confirmed in experimental and theoretical works [85, 87]. The dependencies of the exchange current densities in electrocatalytic HER and photocatalytic H_2 -evolution rates from overall water splitting on different metals on the H_{ad} chemisorption energy are shown in Figure 1.1. Generally, noble metals show higher current densities and photocatalytic H_2 -evolution rates compared to base metals. In particular Pt, Pd and Rh, exhibit exceptional HER activities and are thus commonly applied as co-catalysts for photocatalytic H_2 -evolution. Qualitative differences in the sequence of metals are evident when comparing the correlations in Fig. 1.1A and Fig. 1.1B. This is due to the fact that in the photocatalytic case, net H_2 -evolution rates are governed by further parameters beyond HER catalysis (*vide infra*).

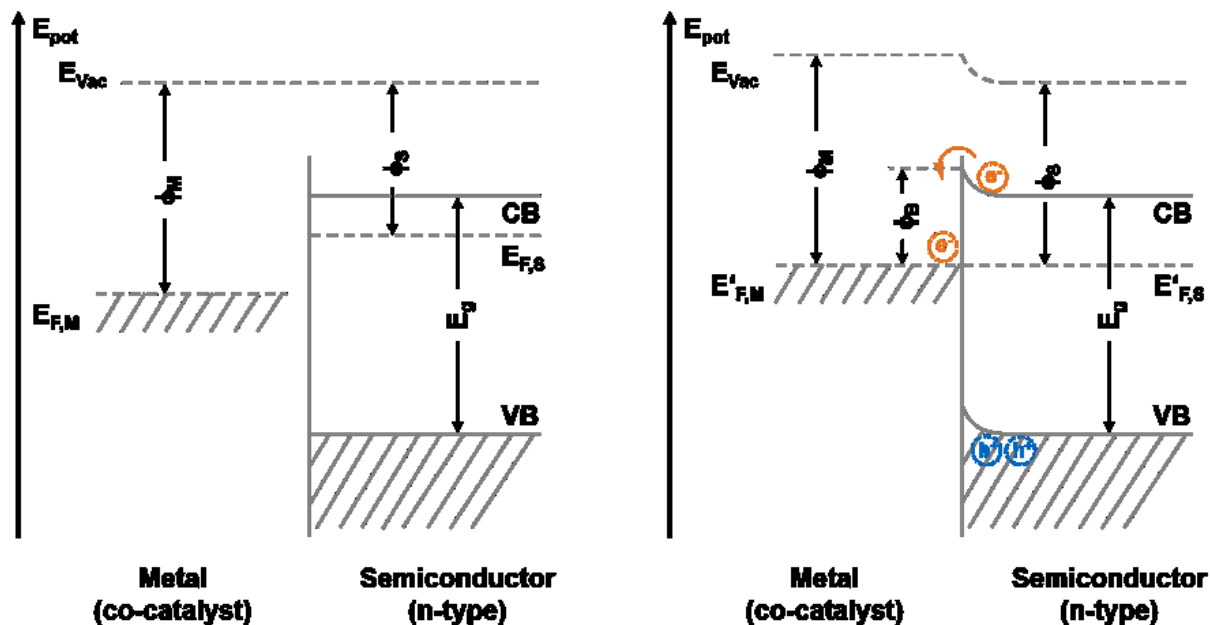
1.7.2 Charge transfer

An efficient transfer of photogenerated electrons across the co-catalyst/semiconductor interface must be established for H_2 -evolution as a further requirement for effective co-catalytic action besides lowering kinetic overpotentials. Briefly, deposited metals and semiconductors exhibit different Fermi level positions. For noble metals on n-type oxide semiconductors (used throughout this thesis) the metal typically depicts the higher work function. For instance, approximately 5.6 eV, 5.2 eV and 5.0 eV for Pt [88, 89], Pd [88, 89] and Rh [89, 90] compared to about 5.0 eV and 4.2 eV for TiO_2^b [91] and $SrTiO_3$ [92], respectively. Thus, in contact, electron migration occurs from the semiconductor to the metal until the Fermi levels are aligned as shown in Scheme 1.5^c. This results in the presence of an excess negative charge at the metal while a net positive charge (depletion layer) remains at the semiconductor surface. The electric field generated at the metal/semiconductor interface prevents further electron transfer in this direction. Specifically, a Schottky barrier ϕ_B forms which is defined as the difference of the interfacial

$$\phi_B = E_{CB} - E'_{F,M} \quad (1.3)$$

^b Work functions of 4.9 eV and 5.1 eV were reported for rutile (100) and anatase (001) surfaces.

^c Charge redistribution due to contact with an aqueous-phase is neglected for simplicity.



Scheme 1.5. Fermi level alignment and Schottky barrier formation between (n-type) semiconductor and (co-catalyst) metal. Energetic situation before contact (left) and equilibrated after contact (right). ϕ_M , ϕ_S and ϕ_B denote metal and semiconductor work function and Schottky barrier height, respectively. E_g is the semiconductor band gap. $E_{F,S}/E'_{F,S}$ and $E_{F,M}/E'_{F,M}$ represent semiconductor and metal Fermi levels before/after contact. E_{vac} is the reference vacuum energy level.

semiconductor CB energy and the aligned metal Fermi level energy (eq. (1.3)). The Schottky barrier constitutes an effective electron trap which provides a means of electron-hole separation. It was shown that trapped electrons exhibit extended lifetimes thereby promoting electron relay towards chemical reduction [93, 94]. Upon band gap irradiation the photogenerated CB electrons may give rise to an upshift of $E'_{F,S}$ to a quasi semiconductor Fermi level. This process enables the transfer of photoexcited electrons across the semiconductor/metal interface which is not available for thermal electrons in the presence of the Schottky barrier [95]. Simultaneously, the photogenerated holes remain at the semiconductor surface.

It is generally believed that the Schottky barrier slows the kinetics of electron injection and should be minimized in order to enable rapid transfer of photogenerated electrons from the semiconductor to the metal [5]. However, a certain barrier height is likely desirable to provide irreversibility of electron transfer (electron trapping) impeding backward transfer from metal into electron trap states of the semiconductor preceding recombination [96].

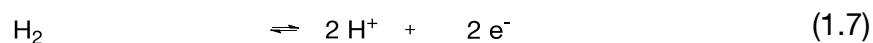
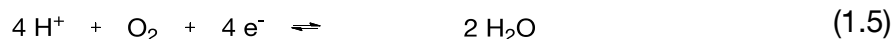
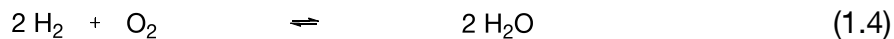
Following the simple Schottky-Mott model the extent of the Schottky barrier height in the absence of interface states is related to the difference of metal work function and semiconductor electron affinity [97]. Correlations between photocatalytic H₂-evolution rates and co-catalyst metal work functions were drawn repeatedly [61, 98, 99]. As a consequence of optimal co-catalyst decoration depending also on the properties of the semiconductor, a universal co-catalyst decoration for photocatalytic H₂-evolution that maximizes photocatalytic rates does not exist. However, noble metals which depict higher work functions than base metals were shown to exhibit in general higher trapping efficiencies, thus offer a good combination of suitable electronic and catalytic properties for photocatalytic H₂-generation with many semiconductors [61, 88-90, 98, 99].

For a very large Schottky barrier, i.e. similar to the extent of the band gap, injection of minority charge carriers, i.e. VB holes in n-type semiconductors, into the co-catalyst is facilitated [100]. Hence, co-catalysts capable of acting as anodic sites exist. In principle, tailoring of the electronic properties of the co-catalyst/semiconductor interface allows for decoration with dual co-catalysts for both redox half-reactions. For instance, activity enhancements were reported by co-decoration of TiO₂ with RuO₂ and SnO_x which acted as anodic and cathodic sites during photoreforming, respectively [101]. Co-deposition of RuO₂, IrO₂ or Mn₃O₄ O₂-evolution co-catalysts onto a RhCrO_x/GaN:ZnO photocatalyst resulted in enhanced gas evolution rates during overall water splitting [102].

1.7.3 Suppression of water formation

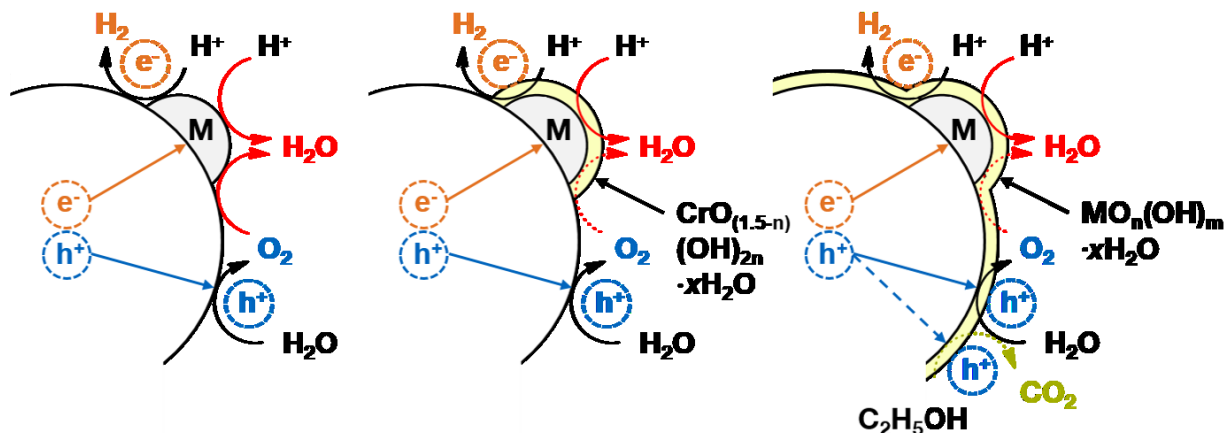
Water splitting experiments on platinized TiO₂ evidenced a high tendency for back-reaction, which causes decreasing gas evolution rates over time towards low steady-state concentrations of H₂ and O₂ [64]. Among noble metal co-catalysts, a 6-fold enhanced activity for water formation was reported for Pt compared to Rh under dark conditions flowing a stoichiometric mixture of H₂ and O₂ at 1 bar [8]. Yet, varying pathways for water formation with different importance may prevail under photocatalytic conditions. The thermal (dark) reaction of H₂ and O₂ to form water is known to occur (eq. (1.4)) [8]. Isotope experiments suggest that photocatalytic reactions of H_{ad} with either reductively activated molecular oxygen (eq. (1.5)), e.g. in form of O₂^{•-}, or reaction with intermediates in water oxidation towards O₂-evolution (eq. (1.6)), at the perimeter of co-catalyst nanoparticles,

may contribute [11, 103]. Furthermore, some reports consider the hydrogen oxidation reaction (HOR, eq. (1.7)) on noble metal co-catalysts constraining H₂-evolution rates under photocatalytic conditions [104].



First successful demonstrations of stable overall water splitting were attained using Ni, Rh and Ru based co-catalysts which exhibit reduced tendency towards water formation [105-107]. Ru-species were shown to be capable of adopting both cathodic and anodic functionalities [108, 109]. In case of Ni, the principle of action appears to be founded in the parallel existence of metallic and oxidic Ni [110-112]. Different models on the structure and functionality of this co-catalyst exist. Domen *et al.* propose Ni-NiO_x core-shell particles with a metallic Ni core at the interface to the semiconductor surrounded by a hydrated NiO_x shell [110, 111]. The co-catalyst is proposed to serve as H₂-evolution site with reduced activity for the back-reaction. Corresponding O₂-evolution occurs on the semiconductor surface [110, 111]. Contrarily, Osterloh *et al.* provide evidence for the separate existence of metallic Ni particles as H₂-evolution sites (electron traps) and NiO_x particles acting as O₂-evolution sites (hole traps) [112]. In the latter model the spatial separation of cathodic and anodic centers and the slow water formation on both co-catalyst components aids stable gas evolution rates. A recent contribution reports on dynamic restructuring of the co-catalyst under reaction conditions [113]. Nevertheless, it is common to all aforementioned co-catalyst concepts that an intrinsic contribution of the back-reaction remains which is difficult to quantify.

Selective poisoning of reaction sites for water formation was achieved by adsorption of I⁻ [114] or CO [11] while retaining H₂-evolution functionality. The preferential adsorption of these species on metal co-catalysts compared to semiconductor surfaces enabled overall water splitting. However, their anodic transformations did occur to some extent resulting in non-stoichiometric evolution of H₂ and O₂, i.e. molar H₂/O₂ ratios in excess of two.



Scheme 1.6. Suppression of water formation during overall water splitting by decoration of metal H_2 -evolution co-catalyst (and semiconductor surface) with an oxyhydroxide shell. Back-reaction proceeds over the bare metal co-catalyst (left) and is inhibited in presence of a chromia shell surrounding the metal core (center). Oxyhydroxides covering the entire photocatalyst surface give rise to suppression of both, back-reaction and oxygenate mineralization (right).

An effective approach towards suppression of the back-reaction is the modification of metal H_2 -evolution co-catalysts with chromia, which significantly promotes gas evolution rates [86]. Different synthetic routes are available to obtain Cr-modified metal co-catalysts such as co-impregnation [86] or Cr(III) photodeposition [9, 115] *via* photoreduction of a Cr(VI) precursor. Photoreduction selectively occurs at deposited metal sites and results in formation of an amorphous, hydrated Cr(III)-oxyhydroxide shell (of the form of $\text{CrO}_{(1.5-n)}(\text{OH})_{2n} \cdot x\text{H}_2\text{O}$) around the metal cores [116]. The shell grows through a self-terminating mechanism up to a thickness of about 2 nm *via* electron tunneling from the metal to solvated or adsorbed Cr(VI) ions [116, 117]. Cyclic voltammetry with Pt and Rh electrodes covered with a nm-sized chromia layer revealed that the presence of chromia did not alter the adsorption of protons and the onset potentials for HER and HOR on the metals. Thus, it was concluded that the chromia layer allows for proton transport to the metal surface and H_2 -desorption therefrom. On the other hand, a corresponding cathodic current resulting from oxygen reduction (eq. (1.5)) on the metals in O_2 -saturated electrolyte was absent upon chromia modification [116]. This indicated that chromia functions as an oxidic membrane which selectively permeates protons and provides a kinetic barrier for the migration of O_2 (and anodic intermediates) to the metal surface where the back-reaction may take place as illustrated in Scheme 1.6. Measurements of water formation from H_2 and O_2 indicate that the degree of suppression of back-reaction is quantitative [8].

Note that chromia by itself does not exhibit any photocatalytic activity for H₂-evolution. Depending on the nature of the semiconductor few cases were reported in which chromia may serve as an O₂-evolution co-catalyst [118, 119].

Decoration with selective oxidic membranes for suppression of the back-reaction is a universal concept applicable independent of the nature of the metal core [86]. Thus, the use of noble metals as efficient H₂-evolution co-catalysts in overall water splitting which by themselves show high activity for water formation is enabled.

Similar functionality and principle of action was proven for amorphous overlayers of Si-, Ti-, Nb- and Ta-oxyhydroxides that were formed by decomposition of the corresponding metal peroxide complexes upon irradiation [10, 120]. That way, the utilization of toxic Cr compounds may be avoided. However, the group IV and V metal oxyhydroxides were found to cover not only the metal particle but the entire photocatalyst surface (Scheme 1.6). It was proposed that decomposition occurred by reduction and oxidation of the peroxo ligands on the co-catalyst metal and semiconductor surface. H₂O₂ represents a stronger oxidant and reductant compared to protons and water, respectively ($E^0(\text{H}_2\text{O}_2/\text{H}_2\text{O}) = 1.36 \text{ V vs. NHE}$, $E^0(\text{O}_2/\text{H}_2\text{O}_2) = -0.27 \text{ V vs. NHE at pH} = 7$) [10]. Hence, decomposition of the metal peroxides on the photocatalyst occurred preferentially over H₂-evolution and water oxidation. However, while the resulting oxyhydroxide layers (about a few nm thickness) allow for overall water splitting to occur, it turned out that these did not permit any permeability to oxygenates, i.e. ethanol [10]. Thus, this co-catalyst concept is incompatible for a coupled application in the context of photoreforming (Scheme 1.6).

1.8 Kinetics and mechanism of oxygenate photoreforming

Photoreforming of oxygenates addresses conversion of renewable energy and pollutant elimination from water in terms of H₂-generation and total oxidation to CO₂ under mild conditions. For successful implementation of photoreforming it is of pivotal importance to advance the understanding of the factors that determine the overall photocatalytic rates. Beyond the parameters affecting the cathodic half-reaction (H₂-evolving function) that have been outlined before (section 1.7), for a given photocatalyst (co-catalyst/semiconductor combination) photocatalytic rates are determined by the kinetics and operating mechanisms in the anodic half-reactions as discussed in the following. Detailed studies have almost exclusively been performed on TiO₂-based photocatalysts. Since complex reaction networks towards full mineralization to CO₂ may prevail in the anodic half-reactions (see section 1.8.2), the H₂-evolution rates have been quantified as a measure of the overall photocatalytic rates.

1.8.1 Factors governing photoreforming rates

Successful photocatalytic H₂-evolution from aqueous solutions of a large number of different oxygenates has been demonstrated in anaerobic atmosphere. On TiO₂-based photocatalysts the H₂-evolution rates during photoreforming of methanol [121], ethylene glycol [103, 122], glycerol [123] and glucose [98] have been determined to obey Langmuir based saturation type kinetics following rate equations of the type depicted in eq. (1.8) (assuming activity coefficients of unity).

$$\frac{dc_i}{dt} = \frac{k_i^{\text{app}} \cdot K_i^{\text{L,app}} \cdot c_i}{1 + \sum_{i=1}^n K_i^{\text{L,app}} \cdot c_i} = k_i^{\text{app}} \cdot \theta_i^{\text{L}} \quad (1.8)$$

Hence, the photocatalytic rates expressed in terms of the temporal change in concentration of component i , $\frac{dc_i}{dt}$ depend on the intrinsic rate constant k_i^{app} and the apparent Langmuir adsorption constant $K_i^{\text{L,app}}$ which are specific to each component involved in the anodic reaction network. Competitive adsorption of the aqueous-phase intermediates generated upon oxygenate oxidation (and competitive adsorption of water) have to be accounted for as expressed in the denominator of eq. (1.8). Figure 1.2 illustrates

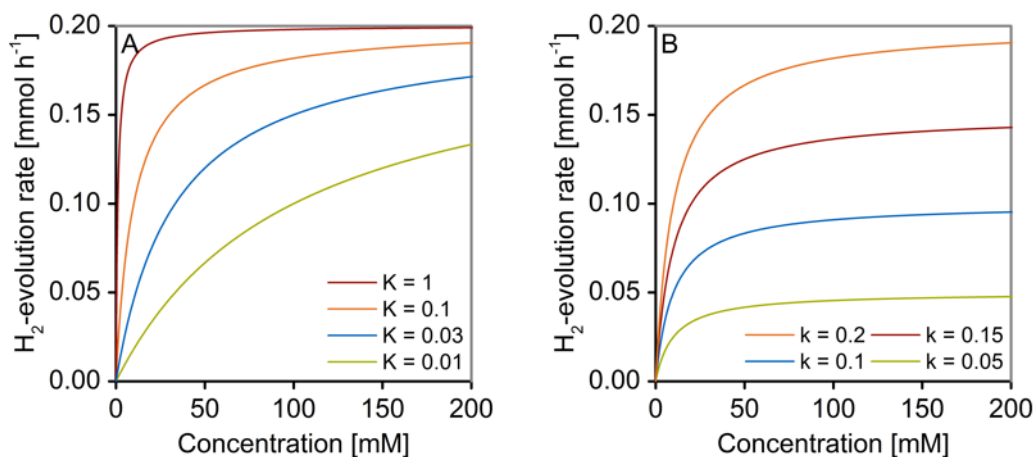


Figure 1.2. Concentration dependence of H₂-evolution rates according to a rate equation based on Langmuir adsorption. (A) Dependence on apparent adsorption constant ($k_i^{\text{app}} = \text{const.} = 0.2 \text{ mM h}^{-1}$). (B) Dependence on intrinsic rate constant ($K_i^{\text{L,app}} = \text{const.} = 0.1 \text{ L mmol}^{-1}$).

the effect of $K_i^{\text{L,app}}$ (at constant k_i^{app} , Fig. 1.2A) and varying k_i^{app} (at constant $K_i^{\text{L,app}}$, Fig. 1.2B) on the rate profiles.

As a consequence of the dependence in eq. (1.8) total oxidation to CO₂ results in decreasing H₂-evolution rates due to low oxygenate concentrations, i.e. at high oxygenate conversions. This is a consequence of decreasing oxygenate coverage θ_i^{L} on the semiconductor surface. Competitive adsorption of intermediates with different k_i^{app} and $K_i^{\text{L,app}}$ might mask or enhance this behavior leading to decreased or increased electron-hole recombination. A linear relation of H₂-evolution rates and oxygenate concentration prevails in the Henry regime at low concentrations ($\sum_{i=1}^n K_i^{\text{L,app}} \cdot c_i \ll 1$). Altogether, to achieve quantitative oxygenate conversion on TiO₂-based photocatalysts involves long reaction times [58, 124, 125].

Photoreforming of (poly)alcohols and carbonyl compounds on noble metal (Pd, Pt, Au) decorated TiO₂ revealed a strong dependence of the H₂-evolution rates on oxygenate nature at constant concentration [16, 61, 126-128]. Generally, for (poly)alcohols H₂-evolution rates were found to follow the order triols > diols > prim. alcohol \cong sec. alcohol > tert. alcohol. An increase in structural complexity, e.g. photoreforming of aldose sugars (cyclic hemiacetals), starch or cellulose commonly resulted in decreasing rates [16, 126, 128]. Albeit, the origin of this behavior has been unknown. Thus, this circumstance is addressed in chapter 3.

Based on the observed relations of H₂-evolution rates and molecular oxygenate structure some empirical rules were derived for qualitative assessments [126]. The negligible rates from tertiary compared to secondary and primary alcohols lead to the conclusion that an α -H-atom is mandatory for effective photoreforming. Concerning the effect of the number of OH-moieties it was argued that the OH-groups provide an effective anchor to the TiO₂ surface promoting the reforming reaction [127]. Distinct intra gap states that act as hole traps to initiate the oxidation process are created upon surface complexation of TiO₂ with oxygenates in many configurations [129-131].

A linear correlation between observed H₂-evolution rates and alcohol polarity was obtained. This descriptor was contended to relate to the degree of an acid-base type interaction of the alcohol with the TiO₂ surface prior to dissociative adsorption. The observed trends in H₂-evolution rates further followed a linear correlation with the exponential of the change in potential upon alcohol oxidation ($e^{-\Delta E^0}$, $\Delta E^0 = E_{\text{VB}(\text{TiO}_2)}^0 - E_{\text{ox}}^0$). The latter quantity is proportional to the rate constant for electron transfer. Thus, a larger energetic separation between the oxidation potential of the alcohol and the TiO₂ VB was concluded to accelerate H₂-evolution [61].

The effect of light intensity on the H₂-evolution rates has been examined for photoreforming of methanol on Pt/TiO₂ [121, 132]. A first-order dependence of H₂-evolution rates on photon flux was obtained at modest and high methanol concentrations (100 mM and 12400 mM) using relatively low irradiances (0.5 – 20 mW cm⁻² provided either by UV LEDs with $\lambda_{\text{max}} = 365$ nm [121] or a 300 W Xe lamp coupled with a diffraction grating (290 nm < λ < 440 nm) [132]). In other words, under these conditions the AQE and the action spectra were unaffected by the rate of genesis of photogenerated charges. Upon progressively increasing light intensities accumulation of charge carriers in the catalyst particles is expected which opens up additional channels for electron-hole recombination following second-order behavior [133, 134]. Thus, transition to a square-root type dependence of photocatalytic rates on photon flux takes place. In addition, a square-root type dependence on photon flux was observed at low methanol concentration (3 mM) and low intensities [121]. Under these conditions, second-order recombination is assumed to arise as a consequence of the low surface coverage. This causes trapped

charge carriers at empty sites to contribute to further electron-hole recombination. At very high intensities mass-transport limitation, i.e. a zero-order behavior, is reached [134].

1.8.2 Oxygenate transformations during photoreforming

General considerations

Stable organic intermediates can be generated from anodic oxygenate conversion in the aqueous-phase. The analysis of reaction pathways and the compilation of reaction networks for photoreforming is based on the notion that each reaction step in the network represents a two electron oxidation towards total oxidation to CO₂.

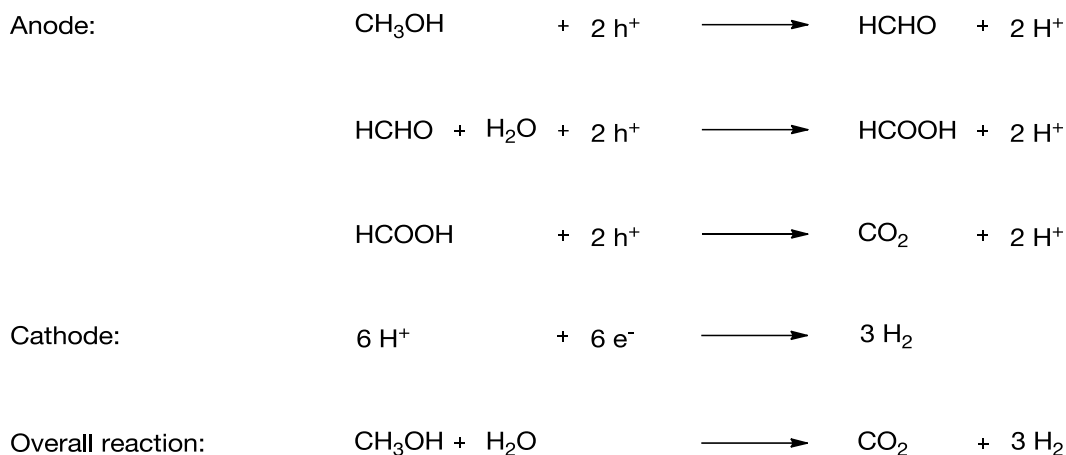
Controversy exists on the nature of the transient, photoinduced radical species involved in the reaction steps on TiO₂, i.e. active in the oxidation of organic substrates under anaerobic conditions. Commonly, the presence of free OH-radicals (\cdot OH) is assumed. These are anticipated to be generated *via* transfer of a photogenerated hole onto a terminal OH-group (under pH-neutral and acidic conditions) followed by desorption into the aqueous-phase or hole transfer onto an adsorbed water molecule [135]. It is well-known that free OH-radicals can be formed under aerobic conditions as a result of the photoreduction of dissolved O₂ [19]. However, experimental studies on well-defined, rutile single crystal surfaces [136, 137] in agreement with computational works [138, 139] suggest that charge transfer from trapped holes at surface lattice oxygen sites to adsorbed water molecules cannot take place. This charge transfer is argued to be inhibited since the highest occupied molecular orbitals (HOMOs) of water are located 1.4 eV below the VB top [139].

Thus, a comprehensive model to describe photocatalytic oxidation mechanisms considers the mechanisms of interfacial hole transfer and the degree of interaction between the organic substrate and the semiconductor [140-142]. Radical species may be formed either *via* direct transfer of photogenerated holes to chemisorbed oxygenates or in an indirect mechanism *via* interaction of the oxygenates with oxidants generated from surface-trapped holes (indirect hole transfer). These mechanisms can be linked to the chemical transformations of oxygenates during photoreforming as is shown in the ensuing chapters of this thesis.

In order to enable the formation of stable organic intermediates consecutive oxidation of the radicals must be accomplished within their lifetime *via* interaction with a second hole/oxidant or a ‘current doubling’ mechanism. Following the first route, besides changing photon flux and quantum efficiency, the availability of a second hole/oxidant on the same photocatalyst particle within the timescale of chemical reactions and radical lifetimes can be tuned by variation of the semiconductor particle size [5]. Assuming an integrated photon flux of UV and visible light up to 600 nm at solar AM 1.5 G the time span between photoexcitation events can be reduced from the ms to the ns range upon increasing the semiconductor particle size from the nm to the μm scale [5]. Regarding the second option for consecutive radical oxidation, it is noted that carbon-centered radicals generated upon H-abstraction represent even stronger reductants compared to their parent oxygenates (e.g. $E^0(\cdot\text{CH}_2\text{OH}/\text{CH}_3\text{OH}) = -1.2 \text{ V vs. NHE}$ and $E^0(\text{CH}_2\text{O}/\cdot\text{CH}_2\text{OH}) = 1.3 \text{ V vs. NHE}$ at pH = 7, respectively [143]). Thus, these radicals are capable of injecting an electron into the semiconductor CB to undergo further oxidation. This process is referred to as current doubling as under photoelectrochemical conditions two electrons per absorbed photon are donated to the external circuit [144]. In the presence of a co-catalyst, the injected electron can be transferred across the co-catalyst/semiconductor interface and contribute to H_2 -evolution. Thus, two reduction equivalents for H_2 -evolution can be available per absorbed photon during photoreforming. This stoichiometry has to be taken into account when calculating STH efficiencies (eq. (1.1)) and AQEs (eq. (1.2)).

Photoreforming of methanol

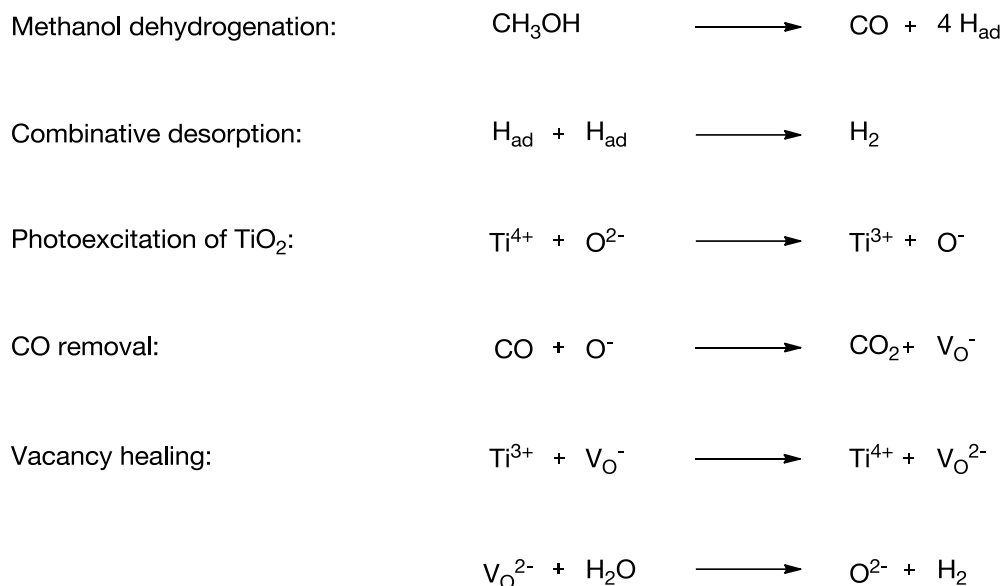
Methanol has been commonly employed as a model compound for photoreforming studies. On M/TiO₂ catalysts (M = RuO₂, Rh, Pd, Ag, Pt, Au) the anodic reaction sequence illustrated in Scheme 1.7 was concluded to comprise two electron oxidation steps *via* formation of formaldehyde which is consecutively oxidized to formic acid, the precursor to CO₂ [121, 145, 146]. Two possible mechanisms have been proposed for the anodic transformation of methanol: (i) Direct hole transfer to adsorbed species or (ii) an indirect mechanism *via* interaction with surface-trapped radical species, e.g. O(H)-radicals [147, 148]. On the basis of the product distributions, both mechanisms are difficult to discern as they result in the formation of the same intermediate. A sum-frequency generation (SFG) study following competitive adsorption of methanol and water suggested that the



Scheme 1.7. Anodic reaction sequence during methanol photoreforming, corresponding cathodic half-reaction and overall reaction equation. Current doubling mechanisms are neglected for simplicity.

type of mechanism prevailing depends on the nature of the adsorbate layer. Direct hole transfer to an adsorbed methoxy (dissociatively adsorbed methanol) which constitutes the photochemically active adsorbate on TiO_2 [149, 150] prevails above a critical coverage (corresponds to a molar water/methanol ratio below about 300). At lower coverages the surface is predominantly covered with water and methanol oxidation is primarily initiated *via* an indirect mechanism. The generated radicals oxidize physisorbed methanol located in a near-surface water layer [151]. Similar conclusions were drawn in a study of methanol photoreforming in the gas-phase [59] highlighting the critical role of the competitive adsorption of methanol and water to the contributions of direct and indirect oxidation mechanisms.

An alternative mechanistic proposal for the photoreforming of methanol has been put forward for Pd/TiO_2 catalysts (Scheme 1.8) [126, 152-155]. In a dark reaction (absence of band gap irradiation) methanol is proposed to fully dehydrogenate on the co-catalyst metal to H_{ad} and CO until blocking of the metal sites with strongly adsorbed CO is reached. Indeed, methanol dehydrogenation on Pd was observed under gas-phase and ultra-high vacuum (UHV) conditions [156, 157]. Subsequently, H_2 -evolution occurs due to combinative H_{ad} desorption from the co-catalyst metal. It is suggested that upon illumination a photogenerated oxidant (of unknown nature) on the TiO_2 surface oxidizes CO to CO_2 at the co-catalyst/semiconductor interface, i.e. the perimeter of the metal particles. Thereby, metal sites are regenerated for methanol dehydrogenation and another

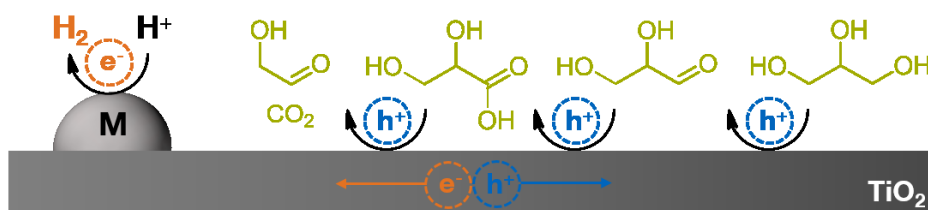
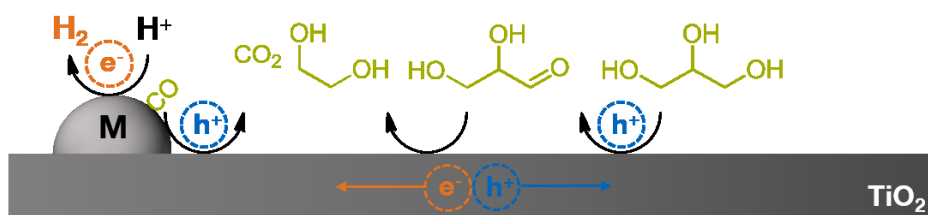
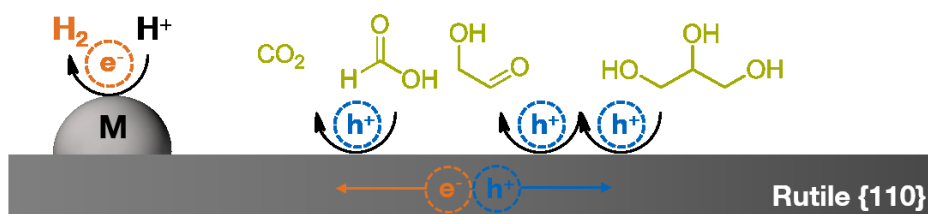


Scheme 1.8. Proposed reaction mechanism for photoreforming of methanol on Pd/TiO_2 [155]. V_{O} denotes a surface oxygen vacancy in TiO_2 .

equivalent of H_2 is generated from water. Oxidative CO removal was proposed to constitute the rate-limiting reaction [126, 152-155].

Photoreforming of higher (poly)alcohols

Photoreforming of higher oxygenates involves the cleavage of C-C bonds prior to total oxidation to CO_2 . Analysis of the gas-phase compositions during photoreforming revealed that polyols carrying an OH-moiety on every carbon atom can be fully mineralized to H_2 and CO_2 [124, 125]. Different mechanisms and reaction sequences for the C-C cleavage steps have been proposed. Taking the example of glycerol the reaction sequences depicted in Scheme 1.9 were suggested. Prior to C-removal glycerol was proposed to oxidize to glyceraldehyde (GAD) and consecutively to glyceric acid, i.e. the corresponding aldehyde and carboxylic acid. Oxidative decarboxylation (Scheme 1.9, sequence (i)) leads to the formation of glycolaldehyde and CO_2 [158, 159]. A direct hole transfer mechanism was concluded for the decarboxylation on the basis of the high adsorption constants determined for carboxylic acids on TiO_2 , e.g. formic acid [141] or oxalic acid [160]. Alternatively, decarbonylation of the intermediate aldehyde (Scheme 1.9, sequence (ii)) was put forward for the C-C scission [124]. The WGS reaction was assumed to rationalize the observation of CO_2 . It should be noted that decarbonylation of a C_n aldehyde to form

(i) Oxidative decarboxylation of carboxylic acids**(ii) Decarbonylation of aldehydes****(iii) Peroxo-radical induced C-C cleavage**

Scheme 1.9. Conceptual illustration of C-C cleavage pathways proposed for glycerol oxidation on co-catalyst decorated TiO_2 photoabsorbers.

the corresponding C_{n-1} (poly)alcohol corresponds to a redox-neutral reaction. A study of glycerol photoreforming on faceted rutile and anatase crystals revealed that the product distribution and the nature of the oxidant were strongly dependent on the exposed TiO_2 facets but independent of the nature of the co-catalyst [161]. Distribution and the nature of the oxidant were strongly dependent on the exposed TiO_2 facets but independent of the nature of the co-catalyst [161]. It was suggested that in the dominant reaction route (formally a four-electron oxidation process) glycolaldehyde and formic acid (which oxidizes to CO_2) represent the outcome of C-C rupture in glycerol (Scheme 1.9, sequence (iii)). On rutile $\{110\}$ facets this pathway proceeds with high selectivity (>90 % at about 20 % glycerol conversion). Evidence for the existence of surface peroxo bridges $[Ti \cdots O \cdots O \cdots Ti]$ constituting the reactive oxygen species (ROS) in an indirect mechanism on

rutile that are formed *via* dimerization of adjacent oxyl radicals $[\text{Ti}\cdot\cdot\text{O}\cdot]$ was provided [161, 162]. The oxyl radicals were suggested to be preferentially produced *via* nucleophilic attack of an adsorbed water molecule to a surface-trapped hole rather than hole trapping at a terminal OH-group [162].

Contrarily, during photoreforming of oxygenates with non-oxygen functionalized carbon(s), i.e. comprising alkyl fragments, the release of alkanes into the gas-phase was observed which causes incomplete mineralization [126, 128]. Photoreforming of primary C_n alcohols lead to the formation of C_{n-1} alkanes [126, 128]. Exemplarily, ethanol photoreforming involves the production of acetaldehyde and acetic acid. Consecutively, two pathways for the C-C cleavage of acetic acid are available. These comprise total oxidation to two equivalents of CO_2 and decarboxylation to CO_2 and CH_4 (Photo-Kolbe reaction) accounting for the observation of CH_4 along with CO_2 and H_2 in the gas-phase [60, 163]. Moreover, decarbonylation of acetaldehyde contributing to CH_4 formation was suggested [159]. Similarly, the formation of methane from isolated methyl groups in 1,2-propylene glycol and 2,3-butylene glycol and ethane from 1-propanol was observed [126, 128]. Methylene groups are completely oxidized to CO_2 . Mechanistically, an OH-radical attack to abstract an α -hydrogen from the alcohol was considered to form a carbon-centered radical ($\text{RC}\cdot\text{HOH}$). The radical further oxidizes to the corresponding aldehyde *via* current doubling on TiO_2 [126, 128]. Accordingly, photoreforming of secondary alcohols ends at the stage of the primary ketone in absence of vicinal oxygen-functionalities, e.g. acetone from isopropanol oxidation, due to the missing α -hydrogen [126].

Note that photoreforming of ethanol on TiO_2 -based photocatalysts proceeds with declining H_2 -evolution rates over time [164]. Photoreforming experiments of the liquid-phase intermediates disclosed lower H_2 -evolution rates compared to the parent alcohol under identical conditions [126]. Thus, ethanol is converted to acetaldehyde and acetic acid (with concomitant H_2 -evolution) with negligible consecutive oxidation to CO_2 , i.e. acetaldehyde and acetic acid accumulate in the liquid-phase [60, 164].

1.9 References

- [1] N.S. Lewis, *Science* 315 (2007) 798-801.
- [2] N.S. Lewis, D.G. Nocera, *Proc. Natl. Acad. Sci.* 103 (2006) 15729-15735.
- [3] R. Van de Krol, M. Grätzel, Part I: Basic Principles: Introduction, in: R. Van de Krol, M. Grätzel (Eds.) *Photoelectrochemical hydrogen production*, Springer, New York, 2012, pp. 3-13.
- [4] K.I. Zamaraev, V.N. Parmon, Development of Molecular Photocatalytic Systems for Solar-Energy Conversion: Catalysts for Oxygen and Hydrogen Evolution from Water, in: M. Grätzel (Ed.) *Energy resources through photochemistry and catalysis*, Elsevier, New York, 2012, pp. 123-129.
- [5] K. Takanabe, K. Domen, *Green* 1 (2011) 313-322.
- [6] K. Maeda, K. Domen, *J. Phys. Chem. Lett.* 1 (2010) 2655-2661.
- [7] M.G. Walter, E.L. Warren, J.R. McKone, S.W. Boettcher, Q. Mi, E.A. Santori, N.S. Lewis, *Chem. Rev.* 110 (2010) 6446-6473.
- [8] F. Dionigi, P.C.K. Vesborg, T. Pedersen, O. Hansen, S. Dahl, A. Xiong, K. Maeda, K. Domen, I. Chorkendorff, *J. Catal.* 292 (2012) 26-31.
- [9] K. Maeda, K. Teramura, D. Lu, N. Saito, Y. Inoue, K. Domen, *Angew. Chem. Int. Edit.* 118 (2006) 7970-7973.
- [10] T. Takata, C. Pan, M. Nakabayashi, N. Shibata, K. Domen, *J. Am. Chem. Soc.* 137 (2015) 9627-9634.
- [11] T.F. Berto, K.E. Sanwald, J.P. Byers, N.D. Browning, O.Y. Gutiérrez, J.A. Lercher, *J. Phys. Chem. Lett.* 7 (2016) 4358-4362.
- [12] Y. Ma, X. Wang, Y. Jia, X. Chen, H. Han, C. Li, *Chem. Rev.* 114 (2014) 9987-10043.
- [13] K. Shimura, H. Yoshida, *Energ. Environ. Sci.* 4 (2011) 2467-2481.
- [14] G.W. Huber, J.A. Dumesic, *Catal. Today* 111 (2006) 119-132.
- [15] A. Patsoura, D.I. Kondarides, X.E. Verykios, *Catal. Today* 124 (2007) 94-102.
- [16] D. Kondarides, V. Daskalaki, A. Patsoura, X. Verykios, *Catal. Lett.* 122 (2008) 26-32.
- [17] M. Kircher, *Biofuels, Bioprod. Biorefin.* 6 (2012) 369-375.
- [18] K. Nakata, A. Fujishima, *J. Photoch. Photobio. C* 13 (2012) 169-189.
- [19] M.R. Hoffmann, S.T. Martin, W. Choi, D.W. Bahnemann, *Chem. Rev.* 95 (1995) 69-96.
- [20] A. Mills, S.-K. Lee, *J. Photochem. Photobiol. A* 152 (2002) 233-247.

- [21] J.-M. Herrmann, *Catal. Today* 53 (1999) 115-129.
- [22] B. Ohtani, *J. Photoch. Photobio. C* 11 (2010) 157-178.
- [23] H. Kisch, *Angew. Chem. Int. Ed.* 52 (2013) 812-847.
- [24] B. Ohtani, *PCCP* 16 (2014) 1788-1797.
- [25] A.L. Linsebigler, G. Lu, J.T. Yates Jr, *Chem. Rev.* 95 (1995) 735-758.
- [26] A. Hakki, J. Schneider, D. Bahnemann, Understanding the Chemistry of Photocatalytic Processes, in: J. Schneider, D. Bahnemann, J. Ye, G. Li Puma, D.D. Dionysiou (Eds.) *Photocatalysis: Fundamentals and Perspectives, Part 1: Fundamental Aspects of Photocatalysis*, Royal Society of Chemistry, Cambridge, 2016, pp. 29-48.
- [27] A.J. Bard, M.A. Fox, *Acc. Chem. Res.* 28 (1995) 141-145.
- [28] A.J. Bard, *J. Photochem.* 10 (1979) 59-75.
- [29] D.G. Nocera, *Acc. Chem. Res.* 45 (2012) 767-776.
- [30] The Department of Energy Hydrogen and Fuel Cells Program Plan, in, Office of Energy Efficiency and Renewable Energy, U.S. Department of Energy, 2011, pp. 1-34.
- [31] The Impact of Increased Use of Hydrogen on Petroleum Consumption and Carbon Dioxide Emissions, in, Energy Information Administration, Office of Integrated Analysis and Forecasting Office of Coal, Nuclear, Electric and Alternate Fuels, U.S. Department of Energy, 2008, pp. 1-25.
- [32] M. Ball, M. Weeda, *Int. J. Hydrogen Energy* 40 (2015) 7903-7919.
- [33] H. Balat, E. Kirtay, *Int. J. Hydrogen Energy* 35 (2010) 7416-7426.
- [34] V. Subramani, P. Sharma, L. Zhang, K. Liu, Catalytic Steam Reforming Technology for the Production of Hydrogen and Syngas, in: *Hydrogen and Syngas Production and Purification Technologies*, John Wiley & Sons, 2009, pp. 14-126.
- [35] M.J. Castaldi, D. Edlund, J.Z. Jin Huang, W.S. Winston Ho, S. Sircar, T.C. Golden, in: K. Liu, C. Song, V. Subramani (Eds.) *Hydrogen and syngas production and purification technologies*, John Wiley & Sons, Hoboken, 2009, pp. 329-450.
- [36] T. Kodama, N. Gokon, *Chem. Rev.* 107 (2007) 4048-4077.
- [37] M. Ni, D.Y.C. Leung, M.K.H. Leung, K. Sumathy, *Fuel Process. Technol.* 87 (2006) 461-472.
- [38] D.B. Levin, R. Chahine, *Int. J. Hydrogen Energy* 35 (2010) 4962-4969.
- [39] P.C. Hallenbeck, J.R. Benemann, *Int. J. Hydrogen Energy* 27 (2002) 1185-1193.

- [40] Fuel Cell Technologies Program Multi-Year Research, Development, and Demonstration Plan, Section 3.1: Hydrogen Production, in, Office of Energy Efficiency and Renewable Energy, U.S. Department of Energy, 2012, pp. 18-19.
- [41] Z. Chen, T.F. Jaramillo, T.G. Deutsch, A. Kleiman-Shwarscstein, A.J. Forman, N. Gaillard, R. Garland, K. Takanabe, C. Heske, M. Sunkara, E.W. McFarland, K. Domen, E.L. Miller, J.A. Turner, H.N. Dinh, *J. Mater. Res.* 25 (2010) 3-16.
- [42] N. Serpone, *J. Photoch. Photobio. A* 104 (1997) 1-12.
- [43] Q. Wang, T. Hisatomi, Q. Jia, H. Tokudome, M. Zhong, C. Wang, Z. Pan, T. Takata, M. Nakabayashi, N. Shibata, Y. Li, I.D. Sharp, A. Kudo, T. Yamada, K. Domen, *Nat. Mater.* 15 (2016) 611-615.
- [44] L. Liao, Q. Zhang, Z. Su, Z. Zhao, Y. Wang, Y. Li, X. Lu, D. Wei, G. Feng, Q. Yu, X. Cai, J. Zhao, Z. Ren, H. Fang, F. Robles-Hernandez, S. Baldelli, J. Bao, *Nat. Nano.* 9 (2014) 69-73.
- [45] J. Liu, Y. Liu, N. Liu, Y. Han, X. Zhang, H. Huang, Y. Lifshitz, S.-T. Lee, J. Zhong, Z. Kang, *Science* 347 (2015) 970-974.
- [46] K. Maeda, K. Teramura, K. Domen, *J. Catal.* 254 (2008) 198-204.
- [47] Q. Wang, T. Hisatomi, Y. Suzuki, Z. Pan, J. Seo, M. Katayama, T. Minegishi, H. Nishiyama, T. Takata, K. Seki, A. Kudo, T. Yamada, K. Domen, *J. Am. Chem. Soc.* 139 (2017) 1675-1683.
- [48] T. Ohno, L. Bai, T. Hisatomi, K. Maeda, K. Domen, *J. Am. Chem. Soc.* 134 (2012) 8254-8259.
- [49] B.D. James, G.N. Baum, J. Perez, K.N. Baum, O.V. Square, Technoeconomic analysis of photoelectrochemical (PEC) hydrogen production, in, Office of Fuel Cell Technologies, Office of Energy Efficiency and Renewable Energy, U.S. Department of Energy, 2009, pp. 24-78.
- [50] A. Xiong, G. Ma, K. Maeda, T. Takata, T. Hisatomi, T. Setoyama, J. Kubota, K. Domen, *Catal. Sci. Technol.* 4 (2014) 325-328.
- [51] D. Jing, L. Guo, L. Zhao, X. Zhang, H. Liu, M. Li, S. Shen, G. Liu, X. Hu, X. Zhang, K. Zhang, L. Ma, P. Guo, *Int. J. Hydrogen Energy* 35 (2010) 7087-7097.
- [52] F.E. Osterloh, B.A. Parkinson, *MRS Bull.* 36 (2011) 17-22.
- [53] S. Kohtani, E. Yoshioka, K. Saito, A. Kudo, H. Miyabe, *J. Phys. Chem. C* 116 (2012) 17705-17713.

- [54] V. Kalousek, P. Wang, T. Minegishi, T. Hisatomi, K. Nakagawa, S. Oshima, Y. Kobori, J. Kubota, K. Domen, *ChemSusChem* 7 (2014) 2690-2694.
- [55] S.N. Habisreutinger, L. Schmidt-Mende, J.K. Stolarczyk, *Angew. Chem. Int. Ed.* 52 (2013) 7372-7408.
- [56] A. Dhakshinamoorthy, S. Navalon, A. Corma, H. Garcia, *Energ. Environ. Sci.* 5 (2012) 9217-9233.
- [57] P.P. Edwards, V.L. Kuznetsov, W.I. David, N.P. Brandon, *Energ. Policy* 36 (2008) 4356-4362.
- [58] T.A. Kandiel, I. Ivanova, D.W. Bahnemann, *Energ. Environ. Sci.* 7 (2014) 1420-1425.
- [59] G.L. Chiarello, D. Ferri, E. Selli, *J. Catal.* 280 (2011) 168-177.
- [60] A.V. Puga, A. Forneli, H. García, A. Corma, *Adv. Funct. Mater.* 24 (2014) 241-248.
- [61] Z.H.N. Al-Azri, W.-T. Chen, A. Chan, V. Jovic, T. Ina, H. Idriss, G.I.N. Waterhouse, *J. Catal.* 329 (2015) 355-367.
- [62] G.T. Rochelle, *Science* 325 (2009) 1652-1654.
- [63] A.B. Rao, E.S. Rubin, *Env. Sci. Technol.* 36 (2002) 4467-4475.
- [64] S. Sato, J.M. White, *Chem. Phys. Lett.* 72 (1980) 83-86.
- [65] S.P. Kowalczyk, F.R. McFeely, L. Ley, V.T. Gritsyna, D.A. Shirley, *Solid State Commun.* 23 (1977) 161-169.
- [66] M.K.I. Senevirathna, P. Pitigala, K. Tennakone, *Sol. Energ. Mat. Sol. Cells* 90 (2006) 2918-2923.
- [67] Y. Ham, T. Hisatomi, Y. Goto, Y. Moriya, Y. Sakata, A. Yamakata, J. Kubota, K. Domen, *J. Mater. Chem. A* 4 (2016) 3027-3033.
- [68] B. Ohtani, O.O. Prieto-Mahaney, D. Li, R. Abe, *J. Photoch. Photobio. A* 216 (2010) 179-182.
- [69] D.O. Scanlon, C.W. Dunnill, J. Buckeridge, S.A. Shevlin, A.J. Logsdail, S.M. Woodley, C.R.A. Catlow, M.J. Powell, R.G. Palgrave, I.P. Parkin, G.W. Watson, T.W. Keal, P. Sherwood, A. Walsh, A.A. Sokol, *Nat. Mater.* 12 (2013) 798-801.
- [70] Y. Xu, M.A. Schoonen, *Am. Mineral.* 85 (2000) 543-556.
- [71] K. Maeda, *Chem. Commun.* 49 (2013) 8404-8406.
- [72] K. Maeda, N. Murakami, T. Ohno, *J. Phys. Chem. C* 118 (2014) 9093-9100.
- [73] J. Schneider, D.W. Bahnemann, *J. Phys. Chem. Lett.* 4 (2013) 3479-3483.
- [74] T. Takata, K. Domen, *J. Phys. Chem. C* 113 (2009) 19386-19388.

- [75] S.-C. Li, Z. Zhang, D. Sheppard, B.D. Kay, J.M. White, Y. Du, I. Lyubinetsky, G. Henkelman, Z. Dohnálek, *J. Am. Chem. Soc.* 130 (2008) 9080-9088.
- [76] M.M. Islam, M. Calatayud, G. Pacchioni, *J. Phys. Chem. C* 115 (2011) 6809-6814.
- [77] Y. Du, N.G. Petrik, N.A. Deskins, Z. Wang, M.A. Henderson, G.A. Kimmel, I. Lyubinetsky, *PCCP* 14 (2012) 3066-3074.
- [78] J. Tao, Q. Cuan, X.-Q. Gong, M. Batzill, *J. Phys. Chem. C* 116 (2012) 20438-20446.
- [79] X. Wang, K. Maeda, A. Thomas, K. Takanabe, G. Xin, J.M. Carlsson, K. Domen, M. Antonietti, *Nat. Mater.* 8 (2009) 76-80.
- [80] F.T. Wagner, G.A. Somorjai, *Nature* 285 (1980) 559-560.
- [81] S. Ouyang, H. Tong, N. Umezawa, J. Cao, P. Li, Y. Bi, Y. Zhang, J. Ye, *J. Am. Chem. Soc.* 134 (2012) 1974-1977.
- [82] A. Mukherji, R. Marschall, A. Tanksale, C. Sun, S.C. Smith, G.Q. Lu, L. Wang, *Adv. Funct. Mater.* 21 (2011) 126-132.
- [83] R. Abe, M. Higashi, K. Sayama, Y. Abe, H. Sugihara, *J. Phys. Chem. B* 110 (2006) 2219-2226.
- [84] P. Sabatier, *Ber. Deutsch. Chem. Ges.* 44 (1911) 1984-2001.
- [85] J.K. Nørskov, T. Bligaard, A. Logadottir, J.R. Kitchin, J.G. Chen, S. Pandelov, U. Stimming, *J. Electrochem. Soc.* 152 (2005) J23-J26.
- [86] K. Maeda, K. Teramura, N. Saito, Y. Inoue, K. Domen, *J. Catal.* 243 (2006) 303-308.
- [87] S. Trasatti, *J. Electroanal. Chem.* 39 (1972) 163-184.
- [88] D.E. Eastman, *Phys. Rev. B* 2 (1970) 1-2.
- [89] H.B. Michaelson, *J. Appl. Phys.* 48 (1977) 4729-4733.
- [90] D.E. Aspnes, A. Heller, *J. Phys. Chem.-US* 87 (1983) 4919-4929.
- [91] G. Xiong, R. Shao, T.C. Droubay, A.G. Joly, K.M. Beck, S.A. Chambers, W.P. Hess, *Adv. Funct. Mater.* 17 (2007) 2133-2138.
- [92] L.F. Zagonel, M. Bäurer, A. Bailly, O. Renault, M. Hoffmann, S. Shih, D. Cockayne, N. Barrett, *J. Phys. Condens. Matter* 21 (2009) 314013.
- [93] A. Yamakata, T.-a. Ishibashi, H. Kato, A. Kudo, H. Onishi, *J. Phys. Chem. B* 107 (2003) 14383-14387.
- [94] A. Yamakata, T.-a. Ishibashi, H. Onishi, *J. Phys. Chem. B* 105 (2001) 7258-7262.
- [95] J. Bisquert, A. Zaban, P. Salvador, *J. Phys. Chem. B* 106 (2002) 8774-8782.

- [96] R. Su, R. Tiruvalam, A.J. Logsdail, Q. He, C.A. Downing, M.T. Jensen, N. Dimitratos, L. Kesavan, P.P. Wells, R. Bechstein, *ACS nano* 8 (2014) 3490-3497.
- [97] F. Cardon, W. Gomes, *J. Phys. D Appl. Phys.* 11 (1978) L63-L67.
- [98] X. Fu, J. Long, X. Wang, D.Y.C. Leung, Z. Ding, L. Wu, Z. Zhang, Z. Li, X. Fu, *Int. J. Hydrogen Energ.* 33 (2008) 6484-6491.
- [99] J.S. Jang, S.M. Ji, S.W. Bae, H.C. Son, J.S. Lee, *J. Photoch. Photobio. A* 188 (2007) 112-119.
- [100] D.L. Scharfetter, *Solid State Electron.* 8 (1965) 299-311.
- [101] Q. Gu, J. Long, L. Fan, L. Chen, L. Zhao, H. Lin, X. Wang, *J. Catal.* 303 (2013) 141-155.
- [102] A. Xiong, T. Yoshinaga, T. Ikeda, M. Takashima, T. Hisatomi, K. Maeda, T. Setoyama, T. Teranishi, K. Domen, *Eur. J. Inorg. Chem.* 2014 (2014) 767-772.
- [103] T.F. Berto, Elucidation of the reaction pathways of the photoreforming and overall water splitting reaction over precious metal decorated semiconductors, in, *Technische Universität München*, 2016, pp. 51-142.
- [104] Y. Hang Li, J. Xing, Z. Jia Chen, Z. Li, F. Tian, L. Rong Zheng, H. Feng Wang, P. Hu, H. Jun Zhao, H. Gui Yang, *Nat. Commun.* 4 (2013) 2500.
- [105] K. Domen, S. Naito, M. Soma, T. Onishi, K. Tamaru, *J. Chem. Soc., Chem. Commun.* (1980) 543-544.
- [106] J.M. Lehn, J.P. Sauvage, R. Zlessel, L. Hilaire, *Isr. J. Chem.* 22 (1982) 168-172.
- [107] Y. Inoue, T. Niiyama, Y. Asai, K. Sato, *J. Chem. Soc., Chem. Commun.* (1992) 579-580.
- [108] T. Sakata, K. Hashimoto, T. Kawai, *J. Phys. Chem.-US* 88 (1984) 5214-5221.
- [109] K. Maeda, R. Abe, K. Domen, *J. Phys. Chem. C* 115 (2011) 3057-3064.
- [110] K. Domen, A. Kudo, T. Onishi, N. Kosugi, H. Kuroda, *J. Phys. Chem.-US* 90 (1986) 292-295.
- [111] K. Domen, S. Naito, T. Onishi, K. Tamaru, M. Soma, *J. Phys. Chem.-US* 86 (1982) 3657-3661.
- [112] T.K. Townsend, N.D. Browning, F.E. Osterloh, *Energ. Environ. Sci.* 5 (2012) 9543-9550.
- [113] K. Han, T. Kreuger, B. Mei, G. Mul, *ACS Catal.* 7 (2017) 1610-1614.
- [114] R. Abe, K. Sayama, H. Arakawa, *Chem. Phys. Lett.* 371 (2003) 360-364.

- [115] K. Maeda, D. Lu, K. Teramura, K. Domen, *Energ. Environ. Sci.* 3 (2010) 470-477.
- [116] M. Yoshida, K. Takanabe, K. Maeda, A. Ishikawa, J. Kubota, Y. Sakata, Y. Ikezawa, K. Domen, *J. Phys. Chem. C* 113 (2009) 10151-10157.
- [117] K. Maeda, K. Teramura, D. Lu, N. Saito, Y. Inoue, K. Domen, *J. Phys. Chem. C* 111 (2007) 7554-7560.
- [118] J. Soldat, G.W. Busser, M. Muhler, M. Wark, *ChemCatChem* 8 (2016) 153-156.
- [119] G.W. Busser, B. Mei, A. Pougin, J. Strunk, R. Gutkowski, W. Schuhmann, M.-G. Willinger, R. Schlögl, M. Muhler, *ChemSusChem* 7 (2014) 1030-1034.
- [120] C. Pan, T. Takata, M. Nakabayashi, T. Matsumoto, N. Shibata, Y. Ikuhara, K. Domen, *Angew. Chem. Int. Ed.* 54 (2015) 2955-2959.
- [121] G.N. Nomikos, P. Panagiotopoulou, D.I. Kondarides, X.E. Verykios, *Appl. Catal. B* 146 (2014) 249-257.
- [122] T.F. Berto, K.E. Sanwald, W. Eisenreich, O.Y. Gutiérrez, J.A. Lercher, *J. Catal.* 338 (2016) 68-81.
- [123] S.-i. Fujita, H. Kawamori, D. Honda, H. Yoshida, M. Arai, *Appl. Catal. B* 181 (2016) 818-824.
- [124] P. Panagiotopoulou, E.E. Karamerou, D.I. Kondarides, *Catal. Today* 209 (2013) 91-98.
- [125] V.M. Daskalaki, D.I. Kondarides, *Catal. Today* 144 (2009) 75-80.
- [126] H. Bahruji, M. Bowker, P.R. Davies, F. Pedrono, *Appl. Catal. B* 107 (2011) 205-209.
- [127] X. Fu, X. Wang, D.Y.C. Leung, Q. Gu, S. Chen, H. Huang, *Appl. Catal. B* 106 (2011) 681-688.
- [128] H. Bahruji, M. Bowker, P.R. Davies, L.S. Al-Mazroai, A. Dickinson, J. Greaves, D. James, L. Millard, F. Pedrono, *J. Photoch. Photobio. A* 216 (2010) 115-118.
- [129] M.-H. Du, J. Feng, S.B. Zhang, *Phys. Rev. Lett.* 98 (2007) 066102.
- [130] G. Kolesov, D. Vinichenko, G.A. Tritsarlis, C.M. Friend, E. Kaxiras, *J. Phys. Chem. Lett.* 6 (2015) 1624-1627.
- [131] G. Balducci, *Chem. Phys. Lett.* 494 (2010) 54-59.
- [132] T. Torimoto, Y. Aburakawa, Y. Kawahara, S. Ikeda, B. Ohtani, *Chem. Phys. Lett.* 392 (2004) 220-224.
- [133] S. Ikeda, N. Sugiyama, B. Pal, G. Marci, L. Palmisano, H. Noguchi, K. Uosaki, B. Ohtani, *PCCP* 3 (2001) 267-273.

- [134] Y. Ohko, A. Fujishima, K. Hashimoto, J. Phys. Chem. B 102 (1998) 1724-1729.
- [135] C.S. Turchi, D.F. Ollis, J. Catal. 122 (1990) 178-192.
- [136] P. Salvador, J. Phys. Chem. C 111 (2007) 17038-17043.
- [137] A. Imanishi, T. Okamura, N. Ohashi, R. Nakamura, Y. Nakato, J. Am. Chem. Soc. 129 (2007) 11569-11578.
- [138] G.A. Tritsarlis, D. Vinichenko, G. Kolesov, C.M. Friend, E. Kaxiras, J. Phys. Chem. C 118 (2014) 27393-27401.
- [139] M. Patel, G. Mallia, L. Liborio, N. Harrison, Phys. Rev. B 86 (2012) 045302.
- [140] J.F. Montoya, J. Peral, P. Salvador, J. Phys. Chem. C 118 (2014) 14266-14275.
- [141] J.F. Montoya, M.F. Atitar, D.W. Bahnemann, J. Peral, P. Salvador, J. Phys. Chem. C 118 (2014) 14276-14290.
- [142] D. Monllor-Satoca, R. Gómez, M. González-Hidalgo, P. Salvador, Catal. Today 129 (2007) 247-255.
- [143] W.H. Koppenol, J.D. Rush, J. Phys. Chem.-US 91 (1987) 4429-4430.
- [144] N. Hykaway, W.M. Sears, H. Morisaki, S.R. Morrison, J. Phys. Chem.-US 90 (1986) 6663-6667.
- [145] T. Kawai, T. Sakata, J. Chem. Soc., Chem. Commun. (1980) 694-695.
- [146] G.L. Chiarello, M.H. Aguirre, E. Selli, J. Catal. 273 (2010) 182-190.
- [147] J. Chen, D.F. Ollis, W.H. Rulkens, H. Bruning, Water Res. 33 (1999) 669-676.
- [148] C.-y. Wang, J. Rabani, D.W. Bahnemann, J.K. Dohrmann, J. Photoch. Photobio. A 148 (2002) 169-176.
- [149] M. Shen, M.A. Henderson, J. Phys. Chem. Lett. 2 (2011) 2707-2710.
- [150] M. Shen, M.A. Henderson, J. Phys. Chem. C 116 (2012) 18788-18795.
- [151] C.-y. Wang, H. Groenzin, M.J. Shultz, J. Am. Chem. Soc. 126 (2004) 8094-8095.
- [152] L.S. Al-Mazroai, M. Bowker, P. Davies, A. Dickinson, J. Greaves, D. James, L. Millard, Catal. Today 122 (2007) 46-50.
- [153] M. Bowker, D. James, P. Stone, R. Bennett, N. Perkins, L. Millard, J. Greaves, A. Dickinson, J. Catal. 217 (2003) 427-433.
- [154] L. Millard, M. Bowker, J. Photoch. Photobio. A 148 (2002) 91-95.
- [155] A. Dickinson, D. James, N. Perkins, T. Cassidy, M. Bowker, J. Mol. Catal. A 146 (1999) 211-221.

- [156] H. Bahruji, M. Bowker, C. Brookes, P.R. Davies, I. Wawata, *Appl. Catal. A* 454 (2013) 66-73.
- [157] M. Morkel, V.V. Kaichev, G. Rupprechter, H.J. Freund, I.P. Prosvirin, V.I. Bukhtiyarov, *J. Phys. Chem. B* 108 (2004) 12955-12961.
- [158] K. Lalitha, G. Sadanandam, V.D. Kumari, M. Subrahmanyam, B. Sreedhar, N.Y. Hebalkar, *J. Phys. Chem. C* 114 (2010) 22181-22189.
- [159] T. Montini, V. Gombac, L. Sordelli, J.J. Delgado, X. Chen, G. Adami, P. Fornasiero, *ChemCatChem* 3 (2011) 574-577.
- [160] C.B. Mendive, T. Bredow, M.A. Blesa, D.W. Bahnemann, *PCCP* 8 (2006) 3232-3247.
- [161] R. Chong, J. Li, X. Zhou, Y. Ma, J. Yang, L. Huang, H. Han, F. Zhang, C. Li, *Chem. Commun.* 50 (2014) 165-167.
- [162] R. Nakamura, Y. Nakato, *J. Am. Chem. Soc.* 126 (2004) 1290-1298.
- [163] B. Kraeutler, A.J. Bard, *J. Am. Chem. Soc.* 100 (1978) 5985-5992.
- [164] T. Sakata, T. Kawai, *Chem. Phys. Lett.* 80 (1981) 341-344.

1.10 Supporting information

Estimation of the energy conversion efficiency considering photocatalytic H₂-generation and combustion

Presumptions:

UV-LEDs ($\lambda = 365 \text{ nm} \pm 5 \text{ nm}$): 12.48 W (31.2 V, 0.40 A)

Photon flux: $9.22 \cdot 10^{18} \text{ photons s}^{-1}$

(in consideration of losses in the top-irradiation photoreactor configuration applied)

AQE (similar to the photocatalysts studied): 10 %

The output energy in terms of the calorific value for H₂ is determined on a higher heating value (HHV) basis.

Calculation:

Photon energy:

$$E = h \cdot \frac{c}{\lambda} = 6.63 \cdot 10^{-34} \text{ Js} \cdot \frac{3.0 \cdot 10^8 \text{ m s}^{-1}}{365 \cdot 10^{-9} \text{ m}} = 5.44 \cdot 10^{-19} \text{ J} = 3.40 \text{ eV}$$

Total irradiated power:

$$P_{\text{tot}} = 5.44 \cdot 10^{-19} \text{ J} \cdot 9.22 \cdot 10^{18} \text{ s}^{-1} = 5.02 \text{ W}$$

Resulting H₂-evolution rate:

$$\frac{3.32 \cdot 10^{22} \text{ h}^{-1}}{10 \cdot 2} \cdot \frac{1}{6.02 \cdot 10^{23} \text{ mol}^{-1}} = 2.76 \cdot 10^{-3} \text{ mol h}^{-1}$$

H₂ mass flow:

$$2.02 \text{ g mol}^{-1} \cdot 2.76 \cdot 10^{-3} \text{ mol h}^{-1} = 5.56 \cdot 10^{-3} \text{ g h}^{-1}$$

Power released upon combustion:

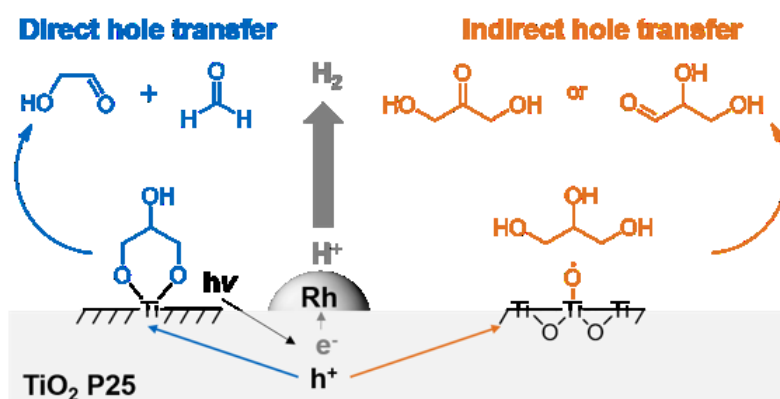
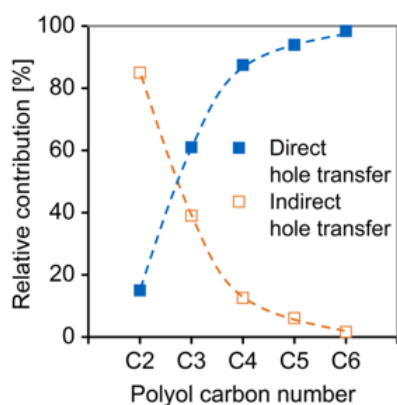
$$5.56 \cdot 10^{-3} \text{ g h}^{-1} \cdot 1.42 \cdot 10^5 \text{ J g}^{-1} = 7.88 \cdot 10^2 \text{ J h}^{-1} = 2.19 \cdot 10^{-1} \text{ W}$$

Energy conversion efficiency:

$$\eta = \frac{2.19 \cdot 10^{-1} \text{ W}}{1.25 \cdot 10^1 \text{ W}} \cdot 100 = 1.75 \%$$

Chapter 2

Catalytic routes and oxidation mechanisms in photoreforming of polyols



2. Catalytic routes and oxidation mechanisms in photoreforming of polyols

This chapter is based on the following article:

K.E. Sanwald, T.F. Berto, W. Eisenreich, O.Y. Gutiérrez, J.A. Lercher, J. Catal. 344 (2016) 806-816.^{a,b}

2.1 Abstract

Photocatalytic reforming of biomass-derived oxygenates leads to H₂-generation and evolution of CO₂ *via* parallel formation of organic intermediates through anodic oxidations on a Rh/TiO₂ photocatalyst. The reaction pathways and kinetics in the photoreforming of C₃-C₆ polyols were explored. Polyols are converted *via* direct and indirect hole transfer pathways resulting in (i) oxidative rupture of C-C bonds, (ii) oxidation to α -oxygen functionalized aldoses and ketoses (carbonyl group formation) and (iii) light-driven dehydration. Direct hole transfer to chemisorbed oxygenates on terminal Ti(IV)-OH groups, generating alkoxy-radicals that undergo β -C-C-cleavage, is proposed for the oxidative C-C rupture. Carbonyl group formation and dehydration are attributed to indirect hole transfer at surface lattice oxygen sites [Ti \cdot -O \cdot -Ti] followed by the generation of carbon-centered radicals. Polyol chain length impacts the contribution of the oxidation mechanisms favoring the C-C bond cleavage (internal preferred over terminal) as the dominant pathway with higher polyol carbon number.

^a Reprinted or adapted from Journal of Catalysis, Copyright (2016), with permission from Elsevier (license number: 4006911133885).

^b K.E.S. planned, designed and conducted the experiments (unless otherwise noted in the acknowledgements section), analyzed and interpreted the data and wrote the manuscript. T.F.B., O.Y.G. and J.A.L. contributed to the discussion of the results and the correction of the manuscript anytime. W.E. programmed the pulse sequences applied in the quantitative NMR measurements and proofread the manuscript.

2.2 Introduction

Photocatalytic H₂-generation from bioderived oxygenates ('photoreforming') is a desired pathway for the production of a chemical energy carrier utilizing solar energy as it lowers the energy requirements compared to water cleavage [1-5]. Aqueous glycerol, an abundant by-product from triglyceride transesterification, and polyol-containing wastewaters, e.g. from industry or catalytic upgrading conceptually, could be suitable feedstocks for photoreforming [1-4, 6]. Thereby valorization and/or purification of those resources are coupled to the production of H₂. Photoreforming benefits from a narrow energetic separation of the two redox half-reactions ($E^0(\text{H}^+/\text{H}_2) = -0.41 \text{ V}$; e.g. for glycerol photoreforming $E^0(\text{CO}_2/\text{C}_3\text{H}_8\text{O}_3) = -0.41(4) \text{ V vs. NHE at pH} = 7$ [7]), which provides a large overpotential at the anode facilitating cathodic H₂-evolution. Moreover, compared to overall water splitting, substitution of the oxygen evolution reaction for anodic oxygenate oxidation to CO₂ eliminates the need of separation and the back-reaction of H₂ and O₂ [8].

While the electron-hole recombination and charge carrier transport to the surface and their relation to physicochemical properties of the photocatalyst have been explored with great depth [9-12], the role of the chemically coupled reactions have been hardly explored mechanistically and kinetically. In such reactions, the co-catalyst decorated semiconductor acts as coupled micro-electrochemical cell [13-15]. Anodic half-reactions are thought to occur on the semiconductor surface as a consequence of interfacial transfer of photogenerated holes through either direct transfer to the oxygenate or *via* an indirect mechanism, e.g. mediated by ·O(H)-radicals [6, 16, 17]. The co-catalyst serves as cathode, electron trap, and, thus, H₂ evolution site and does not participate in the anodic half-reactions [18, 19]. Yet, H₂-evolution and thus oxygenate degradation rates (due to charge balance) are influenced by co-catalyst nature [7], loading and particle size [7, 20] as well as its composition and morphology [21, 22]. The co-catalyst could even aid the suppression of surface back-reactions at the cathode [8, 23]. These factors provide essential means for optimization of the efficiency of electron transfer at the semiconductor/co-catalyst interface.

It is established that H₂-evolution rates on TiO₂-based photocatalysts depend on oxygenate nature and coverage [3, 7, 24-28]. However, there is ambiguity in the anodic

pathways and mechanisms towards full oxidation to CO₂. Initial anodic transformations of polyols over metal/metal oxide loaded TiO₂ were proposed to result in the formation of the corresponding aldehydes, which undergo either decarbonylation followed by water-gas shift [17] or cleavage of formic acid [19]. Oxidation to carboxylic acids that decarboxylate [6, 16] or initial polyol dehydration to compounds with non-functionalized carbon atoms [17] were also suggested prior to C-C-cleavage. On the other hand, photoreforming of linear aldehydes was reported to involve sequential cleavage of formic acid to form the C₁-deficient aldehyde in a single reaction pathway [19, 29].

During aerobic photooxidation of oxygenates, multiple reaction pathways were accounted for by a two-site model for direct and indirect mechanisms [30-32]. Holes trapped at surface lattice oxygen sites [Ti··O··Ti] abstract a H-atom from a C-H bond whereas direct hole transfer yields alkoxy radicals chemisorbed on terminal OH-groups. We hypothesize that under photoreforming conditions (anaerobic environment and H₂ evolving) similar mechanisms operate, which determine the routes towards complete oxidation. We have shown in a preceding contribution that the anodic transformations of ethylene glycol during photoreforming can be rationalized on this basis [18]. We further propose that identical anodic transformations are followed across families of compounds. However, the impact of molecular polyol structure and associated surface adsorption complexes on the contribution of the different reaction pathways to the complete oxidation are largely unknown.

Here, the mechanisms and kinetics of photoreforming of C₃-C₆ polyols on benchmark TiO₂ P 25 with Rh as co-catalyst are explored. On the basis of quantitative analysis of gas- and liquid-phase species general relationships between structural reactant functional groups, anodic reaction pathways and oxidation mechanisms are established. Rationalization of the impact of anodic surface chemistry on the photoreforming kinetics in terms of oxygenate conversion and associated H₂-evolution rates is provided.

2.3 Experimental

2.3.1 Materials

All chemicals were purchased from commercial suppliers and used as provided: Aeroxide® TiO₂ P 25 (Evonik, LOT: 4162092398), rhodium(III) chloride hydrate (Sigma Aldrich, 99.99 % trace metals, 39.0 % Rh), synthetic air (Westfalen), H₂ (Westfalen, 5.0), Ar (Westfalen, 5.0), methanol (Sigma-Aldrich, 99.8%, anhydrous), formaldehyde solution (Fluka, 1000 µg mL⁻¹ in H₂O, IC Standard), formic acid (Merck, 98 – 100 %), ethanol (European Reference Materials, 80 mg 100 mL⁻¹), glycolic acid (Sigma-Aldrich, 99 %), glycerol (Sigma-Aldrich, ≥99.5 %), D-glyceraldehyde (Sigma-Aldrich, > 98 %), dihydroxyacetone (Merck, ≥ 98 %), hydroxyacetone (Alfa Aesar, 95 %), meso-erythritol (Alfa Aesar, 99 %), D-erythrose, L-erythrulose (Omicron Biochemicals, 99 %, aqueous solutions), L-arabitol (Sigma-Aldrich, ≥ 98 %), D-arabinose (Sigma-Aldrich, ≥ 98 %), D-sorbitol (Sigma-Aldrich, 99 %), D-glucose (Sigma-Aldrich, ≥ 99.5 %), D-fructose (Sigma-Aldrich, ≥ 99 %), phloroglucinol (Sigma Aldrich, ≥ 99 %), D₂O (Euriso-Top, 99.85 atom-%), DCl (Acros Organics, 1 M in D₂O, 99.8 atom-%). Aqueous solutions used in photocatalyst synthesis, photoreforming experiments and for derivatization of reactor aliquots for liquid-phase analysis were prepared in ultrapure water (18.2 MΩ cm, Werner Reinstwassersysteme).

2.3.2 Photocatalyst preparation

The 1 wt.% Rh decorated TiO₂ P 25 photocatalyst, hereafter referred to as Rh/TiO₂, was prepared *via* incipient wetness impregnation. TiO₂ P 25 was dried under a static air atmosphere at 473 K for 2 h prior to impregnation. Subsequently, the semiconductor was treated with appropriate amounts of an aqueous solution of RhCl₃·xH₂O in ultrapure water. The resulting precursor was kept in synthetic air at 383 K for 1 h (100 mL min⁻¹, 5 K min⁻¹) and heated to 623 K (100 mL min⁻¹, 5 K min⁻¹) for 1 h. The material was allowed to cool to room temperature before treatment in H₂ at 623 K (100 mL min⁻¹, 5 K min⁻¹) for 1 h. A TiO₂ reference was prepared subjecting as-received TiO₂ P 25 to the same temperature and gas treatments described before.

2.3.3 Photocatalytic test

Photoreforming experiments

Kinetic experiments were performed in a Pyrex top-irradiation photo-reactor connected to a closed gas-circulation system [18]. The setup is equipped with facilities for *online* gas-analysis and liquid-phase sampling. Irradiation is provided by a 300 W Xe lamp with a cold mirror 1 (CM1). A water filter with quartz windows closes the top of the photo-reactor. The photon flux within the reactor at water level is $8.08 \cdot 10^{17} \text{ s}^{-1}$ ($\lambda < 390 \text{ nm}$). Alternatively, high power UV LEDs (Nichia NC4U133A, $365 \text{ nm} \pm 5 \text{ nm}$, $9.22 \cdot 10^{18} \text{ photons s}^{-1}$) were used. Typically, 75 mg of photocatalyst were ultrasonically dispersed in 100 mL of a 20 mM aqueous reactant solution. The system was deaerated by four consecutive evacuations and Ar filling cycles. All reactions were carried out at 288 K and an Ar pressure of 1 bar.

Evolved gases during photocatalytic reactions were analyzed *online via* gas chromatography (Shimadzu, GC 2010 Plus) on a Chromosorb 101 and a Molsieve 5 Å column with a TCD, FID and a methanizer catalyst unit. Ar was used as a carrier gas.

Aliquots of the liquid-phase were manually taken at regular times from the photocatalyst suspension *via* a sample valve. The solid was separated by filtering through $0.2 \mu\text{m}$ nylon filters. Liquid-phase species were quantitatively analyzed by ^1H -NMR spectroscopy. Additionally, high-performance liquid chromatography (HPLC) analysis was performed for photoreforming experiments with C_4 - C_6 oxygenates.

Reactant conversions X_A were calculated according to

$$X_A[\%] = \left(1 - \frac{N_A(t)}{N_{A,0}}\right) \cdot 100. \quad (2.1)$$

Where $N_A(t)$ is the time-dependent molar amount of reactant A and $N_{A,0}$ is the initial molar amount of reactant A, i.e. present at the beginning of the reaction.

^1H -NMR analysis

For quantitative ^1H -NMR measurements reactor aliquots were mixed in a 1:1 volume ratio with an external standard that contained 20 mM 1,3,5-trihydroxybenzene in D_2O adjusted to pH 3 with DCl. ^1H -NMR spectra with water signal suppression were recorded at 305 K using an Avance III HD 500 System (Bruker Biospin, Rheinstetten, Germany) with an

UltraShield 500 MHz magnet (11.75 T) and a BBI 500 S2 probe head (5 mm, inverse $^1\text{H}/\text{X}$ with Z-gradient). The resonance frequency of ^1H was 500.13 MHz. The spectra were acquired using the one-dimensional NOESY sequence from the Bruker library 'noesygppr1d' with presaturation of the residual water signal during the relaxation delay and the mixing time using spoil gradients. Longitudinal relaxation times (T_1) were determined by the inversion recovery pulse method. Relaxation delay and acquisition time were set to 26 s and 4.1 s, respectively. The sum of the latter corresponds to at least three times T_1 of the slowest relaxing ^1H -nucleus (formic acid) and ensures quantitative analysis. Typically, 64 or 128 scans, with 64 k data points were collected. An exponential window function with a line broadening of 0.2 Hz was applied prior to Fourier transformation and the spectra were manually phased, baseline corrected and integrated using Mestre-C 8.1.1 software package. Liquid-phase species were identified according to their chemical shifts (referenced to the internal standard, see SI-Table 2.1) and in comparison to spectra of commercial references recorded under identical conditions. Overlapping signals were deconvoluted using Lorentzian-Gaussian shape type fitting functions. Quantification was done on the basis of the integrated signal intensities which were further calibrated against prepared solutions of known concentration in order to account for signal damping due to the water-suppression in close proximity to the water resonance frequency.

HPLC analysis

Complementary HPLC analysis on an Agilent HP series 100 equipped with a refractive index (RI, 313 K) and a diode array ultraviolet (UV) detector was performed for quantification of erythritol, arabitol and sorbitol. Liquid-phase species were separated on an ion-exclusion column (Rezex ROA, Phenomenex) held at 343 K. 0.005 M H_2SO_4 was used as the mobile phase flowing at 0.5 mL min^{-1} . Reactor aliquots were mixed in a 4:1 volume ratio with an aqueous solution containing 1,3-propylene glycol as internal standard before injection. Integrated signal areas were calibrated against prepared solutions of known concentration.

Combined determination of gas- and liquid-phase concentrations of reaction products and intermediates allowed to quantitatively follow photoreforming kinetics with closed mass-balances.

2.3.4 Physicochemical characterization

N₂-physisorption isotherms were recorded at 77 K on a PMI automated BET sorptometer. Prior to measurements, the sample was outgassed at 523 K for 20 h. Specific surface area and pore size distribution were calculated using the Brunauer-Emmett Teller (BET) method. Cumulative pore volume and pore size distribution were obtained from the Barrett-Joyner-Halenda (BJH) analysis.

Powder X-ray diffraction (XRD) patterns were collected on a Philips X'Pert-1 XRD powder diffractionmeter using Cu-K_α radiation. Average rutile and anatase crystallite sizes were determined from the full width at half maximum (FWHM) of the anatase (101) and rutile (110) reflections at 25.3° 2θ and 27.4° 2θ, respectively, using the Scherrer equation.

The Rh loading was determined by atomic absorption spectroscopy (AAS) on a Thermo Scientific – SOLAAR M Series AA spectrometer. HCN elemental analysis was carried out by the Microanalytical Laboratory at the Technische Universität München.

Mean Rh particle size and dispersion were obtained from H₂-chemisorption at 313 K after activation in H₂ at 573 K for 3 h. Two adsorption isotherms were measured from 1 to 15 kPa, before and after outgassing at 313 K for 1 h, respectively. The second isotherm was subtracted from the first one in order to correct for physisorbed H₂. The amount of chemisorbed H₂ was obtained from extrapolation of the subtracted isotherm to zero pressure. Mean Rh particle size and dispersion were determined assuming hemispherical particle shape and one H-atom chemisorbed on one Rh surface atom.

Diffuse-reflectance UV-Vis spectra were recorded on an Avantes Avaspec 2048 spectrometer equipped with a reflection probe (FCR-7UV200-2-ME) with a home-made sample holder. Reflectance values were transformed into Kubelka-Munk units according to eqs. (2.2) and (2.3).

$$F(R) = \left(\frac{1-R^2}{2 \cdot R} \right) \quad (2.2)$$

$$R = \frac{R_s}{R_T} \quad (2.3)$$

Where R_s is the reflectance of the powdered sample and R_T is the reflectance of PTFE used as a reference.

The photon flux at water level inside the photoreactor was determined using an Avantes Avaspec 2048 spectrometer which was calibrated against a calibrated light source (AvaLight DH-BAL-CAL). Light intensity measurements were conducted using a SMA terminated quartz fiber (FC-UV-200-1-ME-SR) fitted with a cosine corrector (CC-UV/Vis).

TEM micrographs were recorded on a JEOL JEM-2010 transmission electron microscope operating at 120 kV with a magnification of 250 k. The average Rh-particle size was determined from individual measurements of 300 particles. Prior to measurement, the catalyst sample was ground, suspended in ethanol, and ultrasonically dispersed. Droplets of the suspension were transferred to carbon coated Cu grids.

2.4 Results and discussion

2.4.1 Physicochemical properties of the photocatalyst

The textural and structural properties of the photocatalyst are summarized in Table 2.1.

Table 2.1. Physicochemical properties of a TiO₂ reference and the Rh/TiO₂ photocatalyst.

Sample	Rh-loading ^a [wt. %]	Rh particle size [nm]	BET surface area [m ² g ⁻¹]	Cumulative pore volume [cm ³ g ⁻¹]	Band gap ^d [eV]
TiO ₂	-	-	53	0.17	3.1
Rh/TiO ₂	1.0	2.3 ^b	51	0.18	3.1
		1.9 (±0.7) ^c			

a: AAS. b: H₂-chemisorption. c: TEM particle size distribution. d: Tauc plot.

Comparison with the parent TiO₂ sample demonstrates that Rh metal deposition did not modify the physicochemical properties of the TiO₂ photoabsorber support such as bulk phase composition (Fig. 2.1A), anatase (ca. 25 nm) and rutile (ca. 80 nm) particle sizes, optical band gap (3.1 eV, Fig. 2.1B) and rutile content (approximately 13 %). Nominal and determined Rh loading of the Rh/TiO₂ photocatalyst are in very good accordance. TEM analysis (Fig. 2.2) revealed homogeneous distribution of Rh particles over the TiO₂ support with an average particle size of 1.9 ± 0.7 nm which accounts well for the value obtained from H₂-chemisorption (2.3 nm).

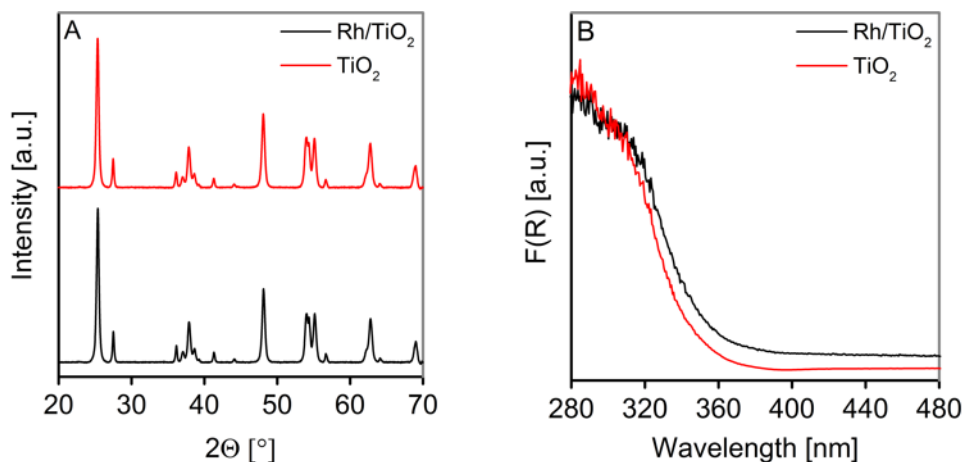


Figure 2.1. (A) X-ray diffractograms and (B) UV-Vis absorption spectra of Rh/TiO₂ and a TiO₂ reference.

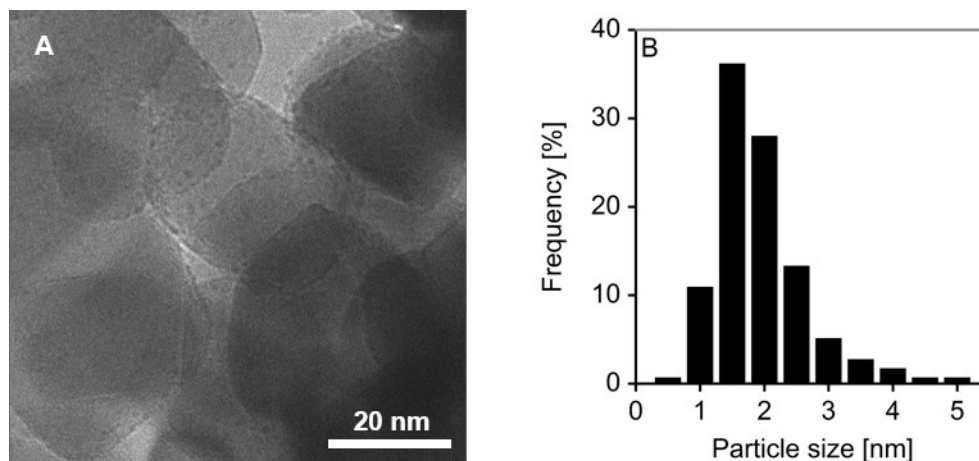


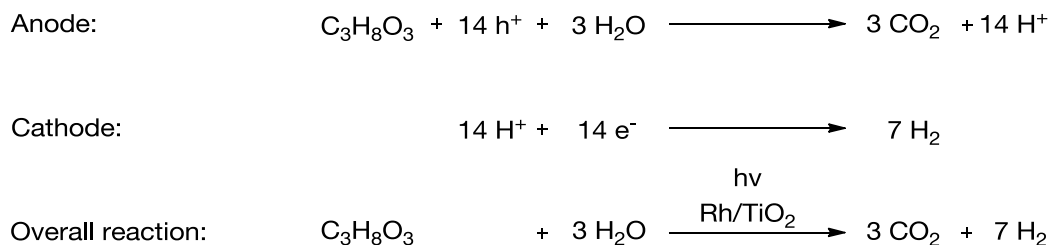
Figure 2.2. (A) TEM micrograph of the 1 wt.% Rh/TiO₂ photocatalyst. (B) Rh particle size distribution.

Absence of XRD reflections of metallic Rh and Rh₂O₃ (Fig. 2.1A) are furthermore indicative of the presence of highly dispersed Rh-species (dispersions of 57 % (TEM) and 47 % (chemisorption)).

2.4.2 Kinetics of photoreforming of glycerol and C₃-intermediates

2.4.2.1 Glycerol photoreforming

Photoreforming of glycerol (Scheme 2.1) proceeded with continuous evolution of H₂ and CO₂ (1405 μmol and 366 μmol, respectively after 12 h reaction time) reaching a conversion of 39 % after 12 h. The H₂-evolution rates declined over time from a maximum value of 143 μmol h⁻¹ to about 95 μmol h⁻¹ after 12 h (Fig. 2.3A). This decline is related to a first-order dependence on concentration (SI-Fig. 2.1, see kinetic model in section 2.4.3). Chemical transformations were not observed in absence of illumination.



Scheme 2.1. Cathodic, anodic half-reactions and overall photoreforming reaction of glycerol.

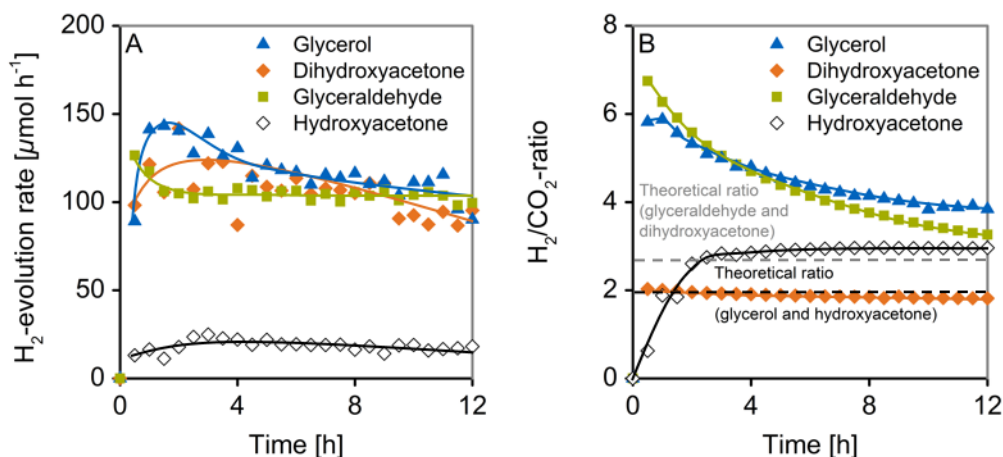


Figure 2.3. (A) Course of H₂-evolution rates during photoreforming of C₃-oxygenates. (B) Course of H₂/CO₂-ratios. Curved lines are drawn as a guide to the eye. Dashed horizontal lines in (B) represent the stoichiometric ratios expected from the overall reaction equations. Reaction conditions: 75 mg photocatalyst, 100 mL aqueous oxygenate solution (20 mM), 288 K, 1 bar Ar, 300 W Xe-lamp (CM1).

H₂/CO₂-ratios (Fig. 2.3B), which decreased throughout the reaction period, were above the theoretical ratio of 2.3 expected from Scheme 2.1 (ratio of 3.8 after 12 h). This observation indicates that full oxidation of glycerol to CO₂ occurs with the formation of organic intermediates in the liquid-phase. A list of molecular structures and overall reaction equations are furthermore given in SI-Table 2.2. An experiment using UV LEDs with high photon flux that allows to follow the reaction up to high glycerol conversion is provided in SI-Fig. 2.2.

Analysis of the aqueous-phase (Fig. 2.4) revealed that formaldehyde (613 μmol after 12 h) was generated as the major species linearly accumulating in solution with reaction time. The oxidation of formaldehyde is slow in the presence of other oxygenates during photoreforming due to its comparatively low apparent adsorption constant on TiO₂ (see section 2.4.3) [18]. Three C₃-species are formed from glycerol in low amounts: glyceraldehyde (GAD, 24 μmol after 12 h) and dihydroxyacetone (DHA, 45 μmol after 12 h) generated *via* two electron oxidation of a primary or secondary carbon atom of glycerol, respectively, as well as hydroxyacetone (HA, 5 μmol after 12 h) formally resulting from a light-driven dehydration. A steady-state concentration of GAD in solution is attained after 4 h indicating consumption of GAD by consecutive reactions. Similarly, the amount of

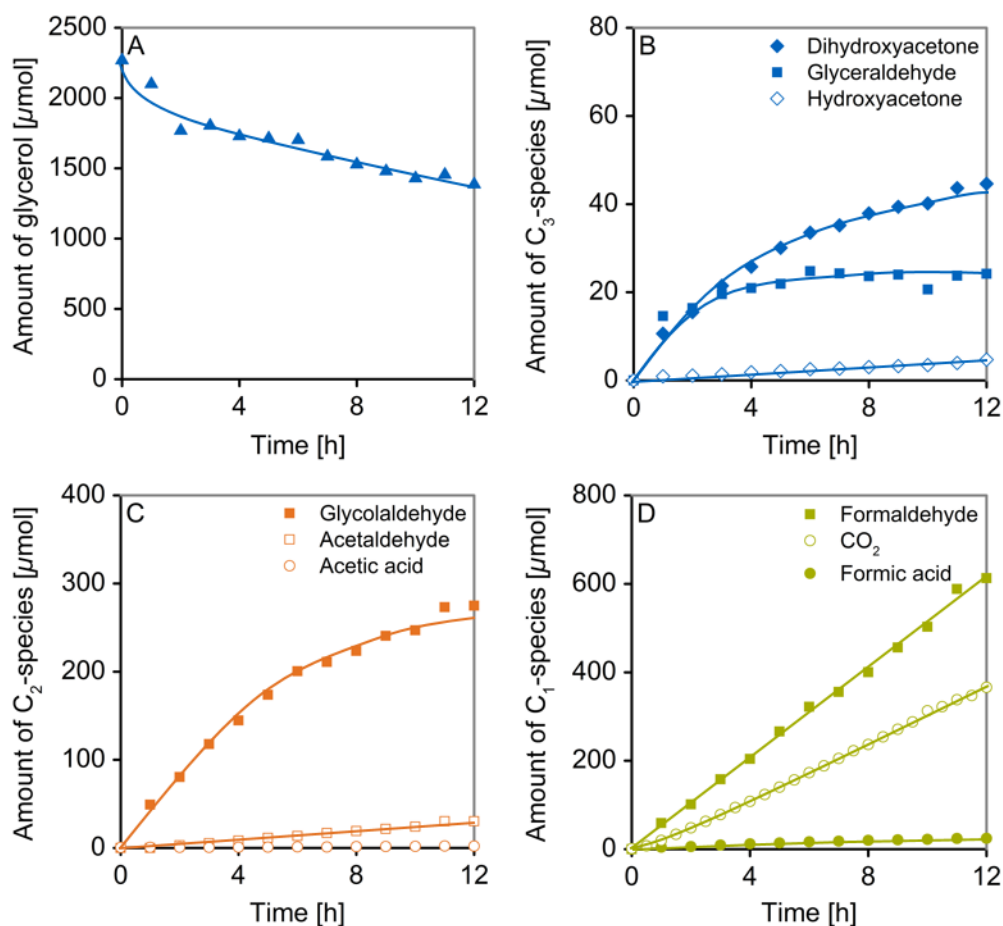
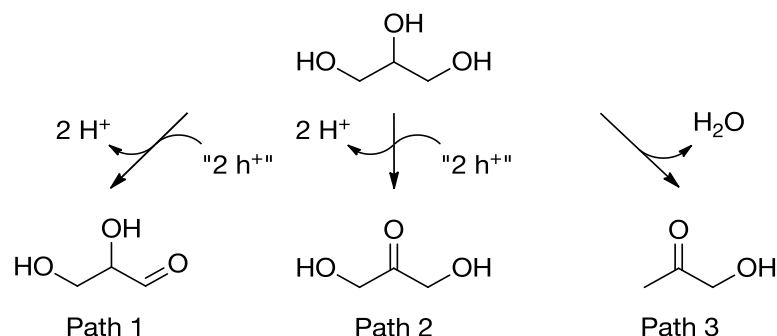


Figure 2.4. Analysis of species generated in anodic half-reactions during glycerol photoreforming. (A) Course of the amount of glycerol. Quantities of different (B) C_3 -, (C) C_2 - and (D) C_1 -species generated. Reaction conditions: 75 mg photocatalyst, 100 mL aqueous glycerol solution (20 mM), 288 K, 1 bar Ar, 300 W Xe-lamp (CM1).

DHA tended to level off with increasing reaction time while the concentration of HA increased gradually with reaction time. In addition to small amounts of formic acid (25 μmol after 12 h), three C_2 species, i.e. glycolaldehyde (275 μmol after 12 h), acetaldehyde (30 μmol after 12 h) whose temporal profile is indicative of a secondary reaction product, and traces of acetic acid (2 μmol after 12 h) were detected.

Interconversion and/or equilibration of GAD and DHA *via* keto-enol tautomerism was not observed under reaction conditions. We concluded that at least three parallel reaction pathways for glycerol oxidation exist, because three non-interconvertible C_3 -products were observed (Scheme 2.2). Further analysis indicated that a fourth pathway exists yielding glycolaldehyde and formaldehyde directly from glycerol (Path 4, *vide infra*).



Scheme 2.2. Initial conceptual reaction pathways for glycerol photoreforming on Rh/TiO₂ on the basis of identification of three C₃-species generated in the liquid-phase.

2.4.2.2 Path 1: Glyceraldehyde (GAD) photoreforming

Photoreforming of GAD yielded H₂ and CO₂ (1264 μmol and 387 μmol, respectively after 12 h) in the gas-phase. In contrast to glycerol photoreforming, H₂-evolution from GAD occurred with constant rate over time (Fig. 2.3A). Analysis of the liquid-phase species (Fig. 2.5) showed glycolaldehyde (614 μmol after 12 h) as the dominant species accompanied by formic acid (421 μmol after 12 h), small amounts of formaldehyde (158 μmol after 12 h) and traces of acetaldehyde and acetic acid (18 μmol and 7 μmol after 12 h, respectively). Oxidation of GAD did not yield glyceric acid as intermediate prior to C-C-scission as proposed in previous studies on photocatalytic conversion of glycerol [6, 16, 33] based on observations from electrocatalytic oxidation of glycerol and GAD [34–38].

The temporal profiles indicate that anodic conversion of GAD involves C-C-cleavage to form glycolaldehyde and a C₁ species. As the amounts of CO₂ and trace CO (4.4 μmol CO after 12 h) produced do not account for the amount of GAD converted (711 μmol after 12 h), the C₁ moiety cleaved from GAD must be contained in formic acid, which forms at equimolar concentrations than glycolaldehyde at low reaction time. Subsequent photoreforming of glycolaldehyde proceeds *via* a selective C-C bond cleavage yielding equimolar amounts of formic acid and formaldehyde [18, 19].

As the apparent adsorption constants of both species differ by two orders of magnitude (see section 2.4.3) consecutive oxidation of formic acid to CO₂ occurs more rapidly than conversion of formaldehyde to formic acid. Indeed, formaldehyde conversion is negligible under reaction conditions while CO₂ is generated from formic acid oxidation [18].

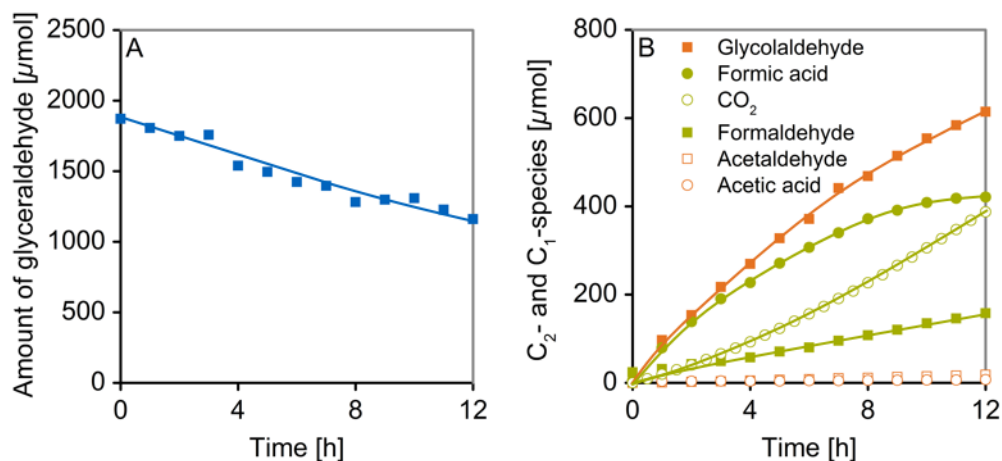
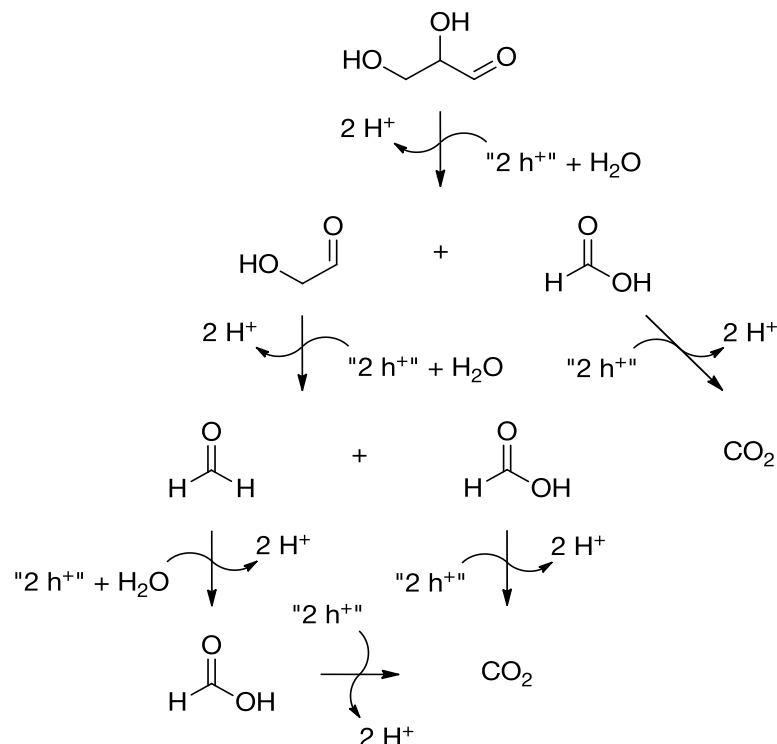


Figure 2.5. Course of anodic reaction products formed during glycerol photoreforming. (A) Course of amount of glyceroldehyde. (B) Temporal profiles of C_2 - and C_1 species generated. Reaction conditions: 75 mg photocatalyst, 100 mL aqueous glycerol solution (20 mM), 288 K, 1 bar Ar, 300 W Xe-lamp (CM1).

This supports our conclusion of the C-C bond cleavage of GAD proceeding *via* formation of formic acid and glycolaldehyde (see section 2.8, see also SI-Fig. 2.3).



Scheme 2.3. Reaction pathway for photocatalytic reforming of glycerol (Path 1): Glycerol is oxidized to glyceroldehyde. Subsequent reaction steps involve sequential cleavage of formic acid through intermediate glycolaldehyde (C_{n-1} aldehyde) and formaldehyde (C_{n-2} aldehyde) towards full oxidation to CO_2 .

The reaction pathway for anodic conversion of glycerol to CO_2 via GAD (Path 1), glycolaldehyde and the respective C_1 species is depicted in Scheme 2.3.

2.4.2.3 Path 2: Dihydroxyacetone (DHA) photoreforming

The ratio of the amounts of H_2 and CO_2 ($1247 \mu\text{mol}$ and $686 \mu\text{mol}$, respectively after 12 h) evolved determined for DHA photoreforming was close to two during the entire reaction (Fig. 2.3B), i.e. the ratio corresponding to the overall reaction equation (SI-Table 2.2). Along with formic acid ($11 \mu\text{mol}$ after 12 h), the liquid-phase contained formaldehyde in quantities, which exceed the amount of DHA converted ($1038 \mu\text{mol}$ and $656 \mu\text{mol}$, respectively after 12 h, Fig. 2.6). This indicates that more than one equivalent of form-

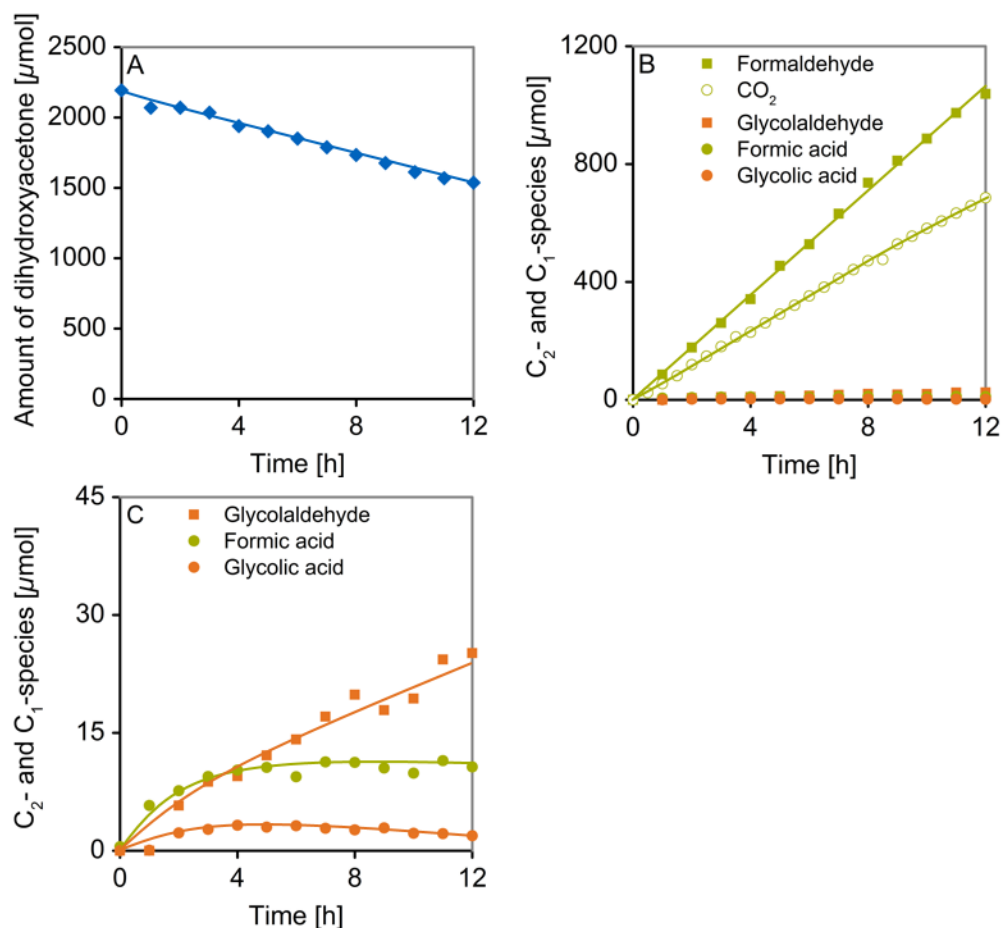


Figure 2.6. Course of anodic reaction products formed during dihydroxyacetone photoreforming. (A) Course of amount of dihydroxyacetone. (B) Temporal profiles of C_2 - and C_1 species generated. (C) Expanded view of (B) to show the reaction products generated in low amounts. Reaction conditions: 75 mg photocatalyst, 100 mL aqueous dihydroxyacetone solution (20 mM), 288 K, 1 bar Ar, 300 W Xe-lamp (CM1).

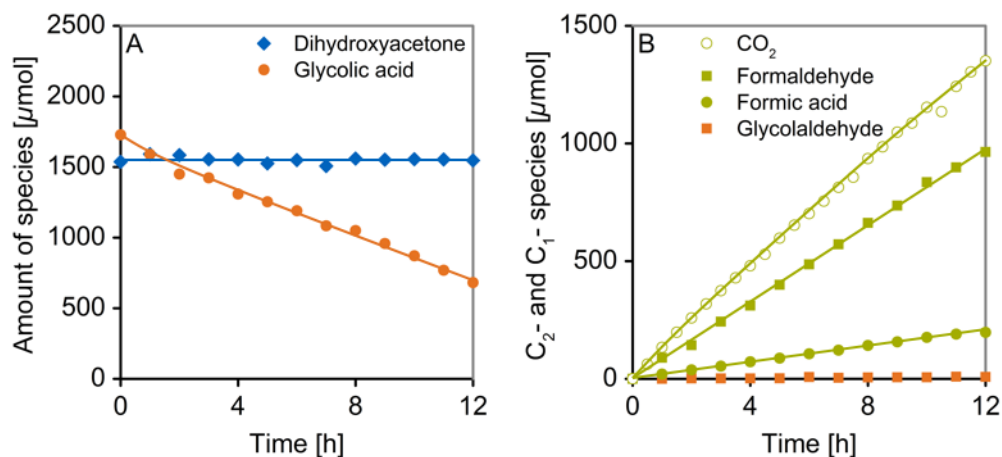
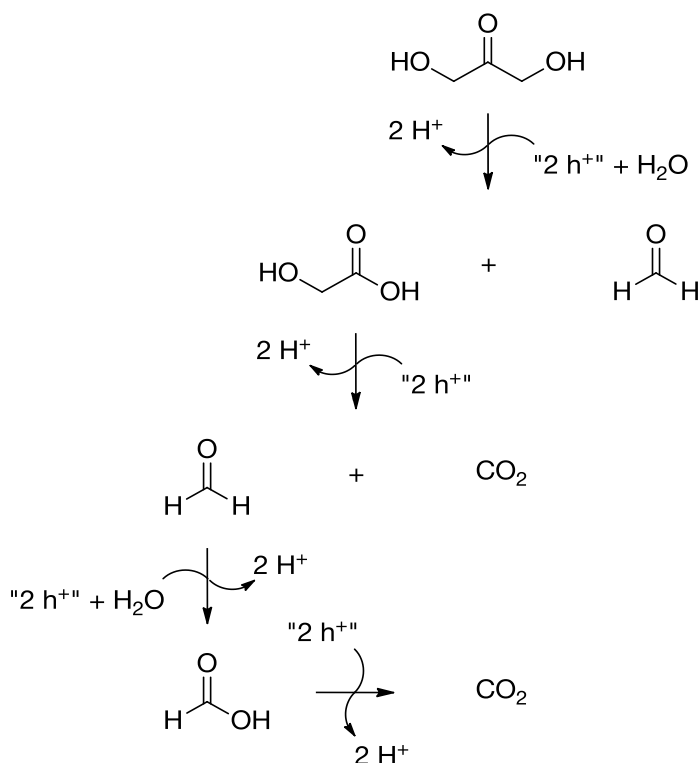


Figure 2.7. Course of amount of reactants and anodic reaction products formed during co-reforming of dihydroxyacetone and glycolic acid. (A) Temporal profiles of dihydroxyacetone and glycolic acid. (B) Courses of C_2 - and C_1 -species generated. Reaction conditions: 75 mg photocatalyst, 100 mL aqueous solution of dihydroxyacetone and glycolic acid (each 15 mM), 288 K, 1 bar Ar, 300 W Xe-lamp (CM1).

aldehyde was formed from DHA and consecutive oxidations. The H_2/CO_2 ratio and quantities of liquid-phase products indicate that DHA photoreforming proceeds *via* formation of two equivalents of formaldehyde and one equivalent of CO_2 . Only small amounts of C_2 -species, i.e. glycolaldehyde and glycolic acid (24 μmol and 2 μmol , respectively after 12 h), were present. During reforming of an equimolar mixture of DHA and glycolic acid, the latter was converted at much higher rates than the former (Fig. 2.7), whereas formaldehyde and CO_2 were observed at concentrations similar to those observed during the reforming of DHA alone. Thus, we conclude that the photoreforming of DHA proceeds *via* glycolic acid as C_2 -intermediate in the first reaction step simultaneously generating one H_2 -equivalent at the cathode (Scheme 2.4). Consecutively, glycolic acid undergoes fast oxidative decarboxylation to form second equivalents of formaldehyde and H_2 (Scheme 2.4.).

Our reaction pathway studies are guided by the principle that stable organic species can be formed after two electron oxidation. In contrast, the formation of glycolaldehyde and formaldehyde from DHA requires the formation of a new C-H bond at the carbonyl carbon atom, which corresponds to a redox-neutral transformation, i.e. one electron oxidation of a primary carbon of DHA to form formaldehyde along with one electron reduction of the



Scheme 2.4. Reaction pathway for photocatalytic reforming of glycerol (Path 2): Two electron oxidation of glycerol to form dihydroxyacetone. Consecutive dihydroxyacetone conversion *via* glycolic acid yields CO_2 and two equivalents of formaldehyde.

secondary carbon. Under photoreforming conditions, a redox-neutral transformation of this kind must be slow because the availability of electrons at the semiconductor surface is expected to be greatly limited in the presence of the co-catalyst acting as an electron trap. An alternative redox-neutral process would involve diffusion of a radical oxidant species to the metal, where the reduction step would occur competing with H_2 -evolution. Thus, generation of glycolaldehyde as relevant C_2 -intermediate in the reforming of DHA is considered a minor side reaction.

During photoreforming of the next higher homologous ketose of DHA (erythrulose, refer to SI-Figs. 2.4 and 2.5), also the characteristic H_2/CO_2 -ratio of two was observed, while the corresponding C_3 -intermediate acid could not be detected. Thus, in the photoreforming of linear ketoses intermediate C_{n-1} acid, if formed, rapidly reacts further yielding a C_{n-2} aldehyde as apparent primary product.

2.4.2.4 Path 3: Hydroxyacetone (HA) photoreforming

The amounts of H_2 and CO_2 (222 μmol and 57 μmol , respectively after 12 h) evolved during photoreforming of HA (Fig. 2.3) are about 80 % lower than those from DHA, GAD, and glycerol. In general, H_2 -evolution rates are lower for compounds carrying non-oxygen-functionalized carbons compared to their counterparts with maximum number of oxygen-functionalities. In particular, α -oxygen functionalization is required for efficient hole transfer [18, 24, 25, 39]. Note that the amounts of H_2 obtained from photoreforming of 20 mM solutions of 1,2- and 1,3-propanediol (997 μmol and 447 μmol after 12 h, respectively) were lower than those from glycerol (1405 μmol after 12 h) under identical reaction conditions.

Liquid-phase analysis (Fig. 2.8) during HA photoreforming disclosed acetic acid as a main primary product and formaldehyde (99 μmol and 56 μmol , respectively, after 12 h). Formic acid is virtually absent (1 μmol after 12 h). Acetaldehyde, which is known to undergo slow consecutive oxidation to acetic acid, and hence to accumulate in liquid-phase [40, 41], was not observed. This suggests that acetic acid was indeed formed as a primary product from HA. Consecutive oxidation of acetic acid may progress either to CO_2 , or to CH_4 and CO_2 (Photo-Kolbe reaction) [18, 42-44] suggested by the detection of CH_4 in the gas-phase (5 μmol CH_4 after 12 h). In line with the concluded decomposition of HA *via* acetic

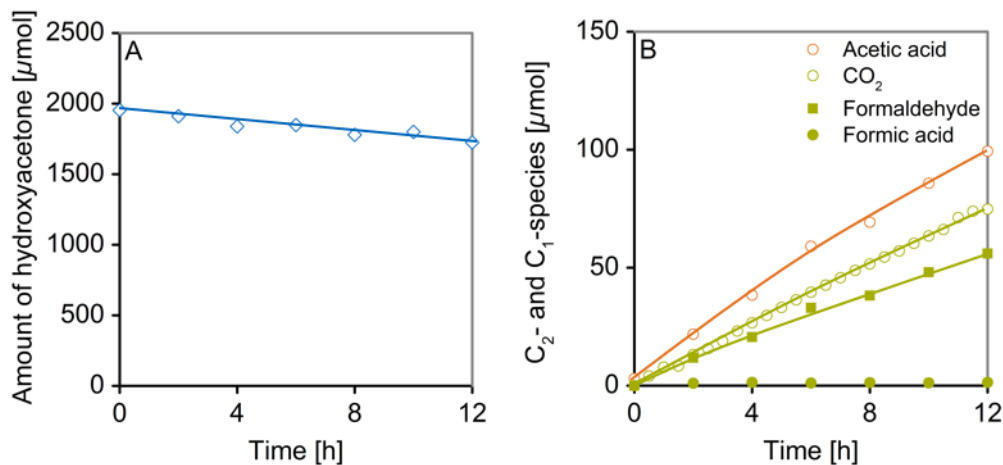
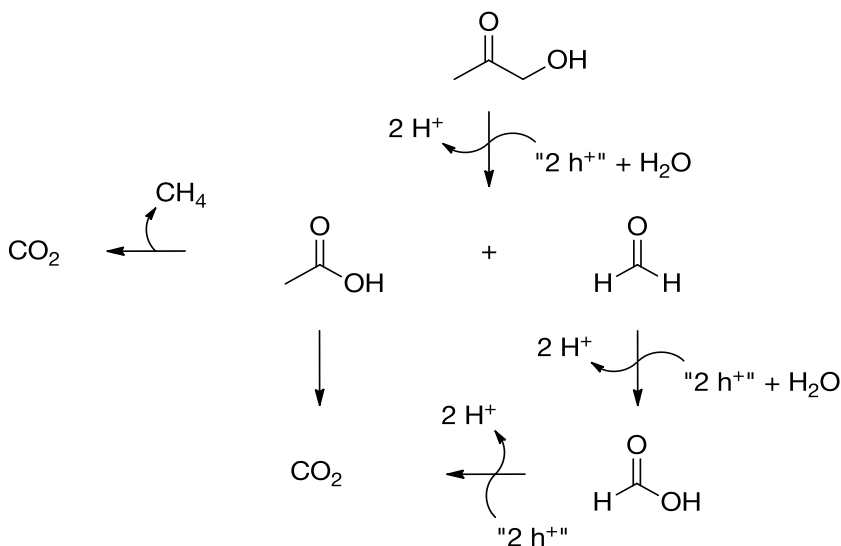


Figure 2.8. Course of anodic reaction products formed during photoreforming of hydroxyacetone. (A) Course of amount of hydroxyacetone. (B) Temporal profiles of C_2 - and C_1 -species generated. Reaction conditions: 75 mg photocatalyst, 100 mL aqueous hydroxyacetone (HA) solution (20 mM), 288 K, 1 bar Ar, 300 W Xe-lamp (CM1).



Scheme 2.5. Reaction pathway for photocatalytic reforming of glycerol (Path 3): Light-driven dehydration of glycerol to form hydroxyacetone. Consecutive oxidation of hydroxyacetone leads to the formation of acetic acid and formaldehyde intermediates towards full oxidation to CO₂.

acid (associated to low H₂-evolution rates), considerably lower H₂-evolution rates from acetic acid/acetate solutions in comparison to C₁-C₃ alcohols and polyols have been obtained over noble metal decorated TiO₂ [25, 44].

In analogy to DHA photoreforming, we conclude that formaldehyde is generated with acetic acid upon C-C scission of HA. The reaction pathway for glycerol photoreforming *via* intermediate formation of HA is represented in Scheme 2.5. HA contents during glycerol photoreforming were the smallest among the C₃-intermediates generated while the consecutive reforming reactions of HA are significantly slower compared to GAD and DHA. Thus, the light induced dehydration of glycerol to HA is a side-reaction.

2.4.3 Path 4: Direct oxidative C-C cleavage of glycerol

Photoreforming of glycerol, DHA, GAD, and HA showed different initial H₂-evolution rates under identical reaction conditions. It was established previously, that under experimental conditions H₂-evolution rates over Rh/TiO₂ for different C₂ and C₁ oxygenates that exclusively exhibit oxygen-functionalized carbons converge towards a maximum value of 200 μmol h⁻¹ which is reached for very reactive species, e.g. formic acid, already at a concentration of 20 mM [18, 45]. Similarly, the concentration dependence of the H₂-evolution rates from aqueous glycerol solution (Fig. 2.9) evidences saturation-type

kinetics and converges against a rate of about $200 \mu\text{mol h}^{-1}$ at high concentrations. The observation of first-order dependence on glycerol concentration during photoreforming of a 20 mM solution (SI-Fig. 2.1) is a consequence of the proportionality of liquid concentration and surface coverage at low concentration (Henry isotherm regime). Thus, photoreforming kinetics were shown to obey a Langmuir adsorption based rate expression (eq. (2.4)).

$$\frac{dc_i}{dt} = \frac{k^{\text{app}} \cdot K_i^{\text{L,app}} \cdot c_i}{1 + \sum_{i=1}^n K_i^{\text{L,app}} \cdot c_i} \quad (2.4)$$

Where dc_i/dt denotes the reaction rate of reactant i [mM min^{-1}], k^{app} is the intrinsic rate constant of component i [mM min^{-1}], $K_i^{\text{L,app}}$ is the apparent Langmuir adsorption constant of component i [L mmol^{-1}] and c_i is the concentration of component i [mmol L^{-1}]. Competition for adsorption sites during progression of photoreforming of species i by n organic intermediates generated in the anodic half reaction is accounted for in the denominator of eq. (2.4). Apparent adsorption constants K_i^{app} (dimensionless) are obtained from $K_i^{\text{L,app}}$ by multiplication with the solvent molar concentration (water, $55508 \text{ mmol L}^{-1}$ [46]).

The Langmuir model is compatible with a disrupted adsorption kinetic model (eq. (2.5)) which considers the dependence of the apparent Langmuir adsorption constants on light intensity [47].

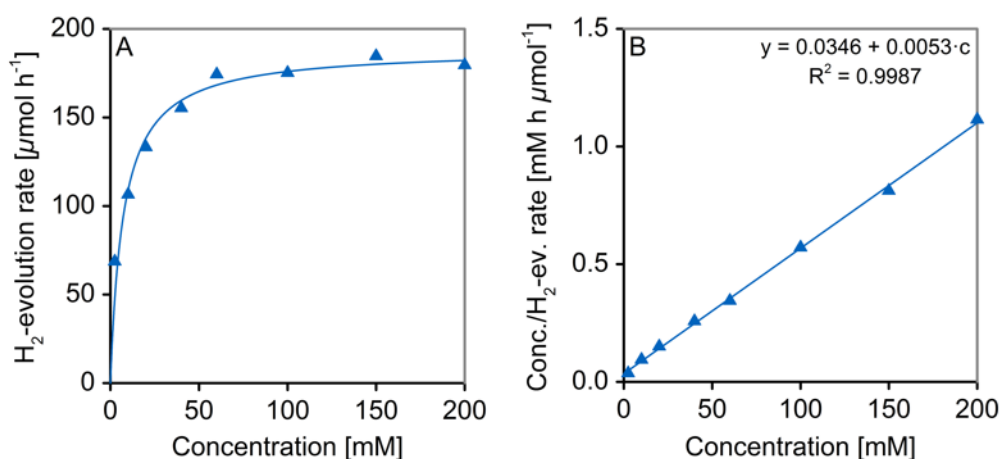


Figure 2.9. (A) Dependence of H₂-evolution rates (averaged over 5 h) on glycerol concentration and fitted rate curve for saturation-type kinetics in terms of the Langmuir adsorption based kinetic model. (B) Linearization of experimental H₂-evolution rate data demonstrating the dependence on substrate coverage and the applicability of the Langmuir model.

$$\frac{dc_i}{dt} = \frac{k^{\text{app}} \cdot K_i^{\text{DA,app}} \cdot c_i}{1 + \sum_{i=1}^n K_i^{\text{DA,app}} \cdot c_i} \quad (2.5)$$

In this equation dc_i/dt denotes the reaction rate of reactant i [$\text{mM} \cdot \text{min}^{-1}$], k^{app} is the intrinsic rate constant of component i [$\text{mM} \cdot \text{min}^{-1}$], $K_i^{\text{DA,app}}$ is the apparent adsorption constant of component i [$\text{L} \cdot \text{mmol}^{-1}$] and c_i is the concentration of component i [$\text{mmol} \cdot \text{L}^{-1}$]. Details of the derivation of the kinetic model may be found in ref. 48.

Here, we extend the outlined approach to the description of the photoreforming kinetics of glycerol and C_3 -intermediates to quantitatively validate the proposed reaction schemes. Assuming the intrinsic rate constants to be substrate independent it follows that photoreforming rates of oxygenates primarily depend on their apparent adsorption constants and associated surface coverages (under constant illumination conditions) irrespective of the nature of the charge carrier transfer mechanism. The contributions of individual reaction channels in glycerol photoreforming were evaluated on the basis of the respective contributions to the intrinsic rate constant for the overall anodic half-reaction (equals the intrinsic rate constant for cathodic H_2 -evolution) which was restrained to a maximum rate of $200 \mu\text{mol h}^{-1}$ during fitting.

Experimental data were fitted using two built-in MATLAB subroutines. Minimization of the objective function was carried out with a CMA-ES algorithm and the numerical integration of the differential equations was carried out using ode45-function.

A comparison of experimental and fitted photoreforming kinetics of glycerol, GAD and DHA is given in Figs. 2.10 – 2.12. Apparent adsorption constants of C_1 - C_3 oxygenates (Table 2.2) attained from different photoreforming experiments are in reasonable agreement among each other and in comparison with preceding work [18] demonstrating the consistency of the approach and its validity for photoreforming of C_3 -oxygenates.

Direct oxidative C-C-cleavage of glycerol to yield glycolaldehyde and formaldehyde, which had been proposed during aerobic conversion of glycerol over non-metallized TiO_2 P 25 [31], had to be included in the model (besides the parallel reaction pathways from glycerol that yield C_3 oxygenates) in order to achieve reasonable agreement with the experimental data. Evidence for this transformation is provided from product distributions obtained for photoreforming of higher polyols and is discussed in section 2.4.4.

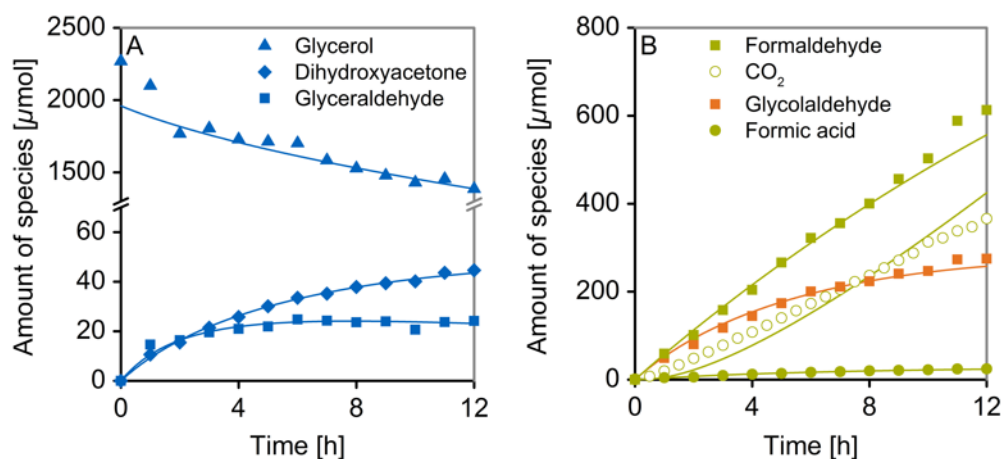


Figure 2.10. Comparison of experimental and fitted temporal profiles for glycerol photoreforming.

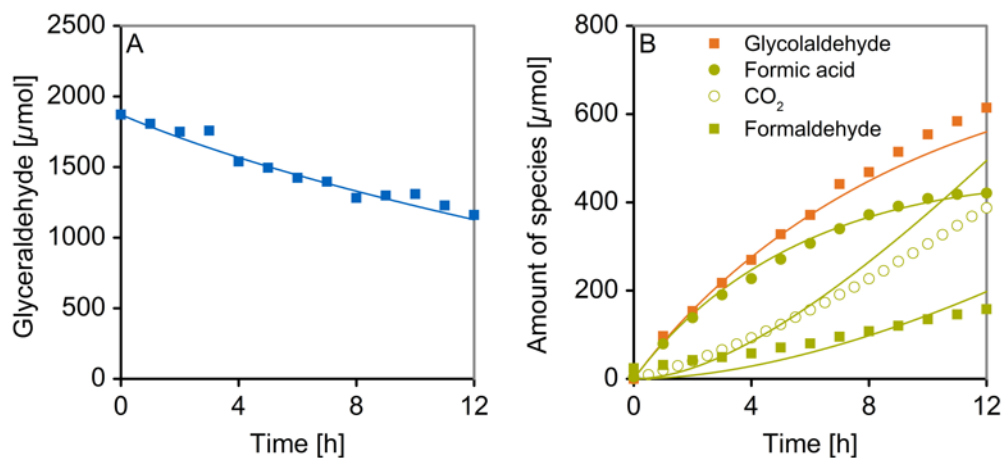


Figure 2.11. Comparison of experimental and fitted temporal profiles for glyceraldehyde photoreforming.

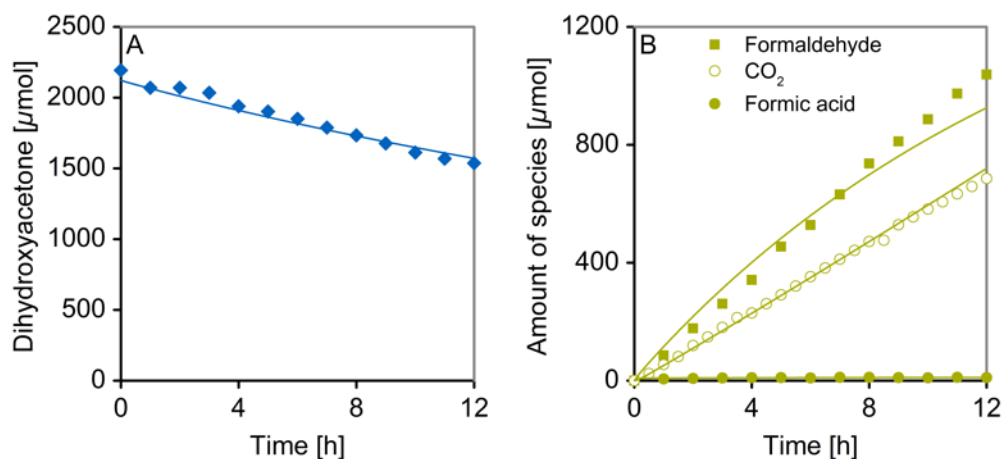
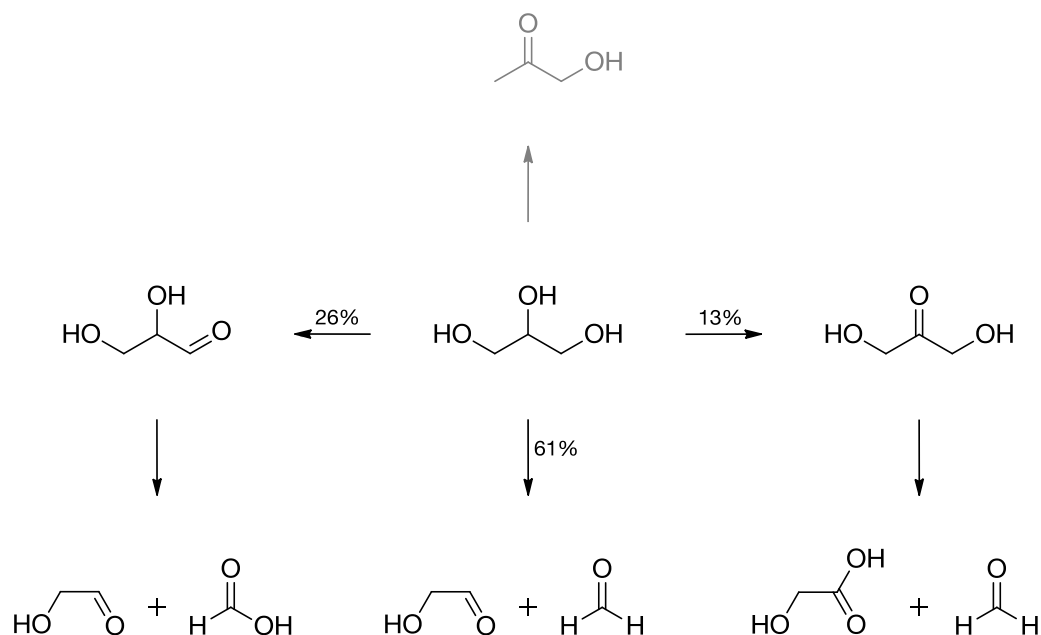


Figure 2.12. Comparison of experimental and fitted temporal profiles for dihydroxyacetone photoreforming.

Table 2.2. Apparent adsorption constants of C₁-C₃ oxygenates from photoreforming reactions of different C₃ compounds at 288 K.

	Probe molecule	Glycerol photoreforming	Glyceraldehyde photoreforming	Dihydroxyacetone photoreforming
Apparent adsorption constant [·10 ⁴]	Glycerol	0.33	-	-
	Glyceraldehyde	4.64	2.69	-
	Dihydroxyacetone	0.85	-	0.18
	Glycolaldehyde	1.09	1.30	-
	Formaldehyde	0.43	0.12	0.21
	Formic acid	28	5	44

**Scheme 2.6.** Reaction network for photocatalytic reforming of glycerol. Initial anodic glycerol transformation involves four reaction pathways. C-C-cleavage to form glycolaldehyde and formaldehyde occurs primarily over formation of carbonyl groups to produce glyceraldehyde or dihydroxyacetone. Light-driven dehydration to hydroxyacetone constitutes a side reaction.

Kinetic modeling confirmed a negligible contribution of HA formation from glycerol and successive oxidations (Path 3).

In conclusion, we propose the reaction network depicted in Scheme 2.6 for glycerol photoreforming from gas-, liquid-phase analysis and kinetic modeling. Anodic glycerol

conversion predominantly involves oxidative C-C-scission (61%) to yield glycolaldehyde and formaldehyde. Oxidation of primary and secondary carbons that lead to the formation of GAD (26%) and DHA (13%) represent minor reaction channels.

2.4.4 Photoreforming of C₄-C₆ polyols

The courses of the H₂-evolution rates during photoreforming of erythritol, arabitol and sorbitol (C₄, C₅, and C₆, polyols, respectively) are presented in Fig. 2.13. The 49 % decline from initial H₂-evolution rates over 12 h of reaction time, particularly steep during the first 4 h for all three polyols, is more pronounced than for glycerol photoreforming (33 %). The course of the evolution of intermediates and reaction products in the anodic half-reactions during sorbitol photoreforming is exemplarily depicted in Fig. 2.14 (corresponding data for erythritol and arabitol are found in SI-Figs. 2.6 and 2.7).

The product distributions in the photoreforming of erythritol, arabitol and sorbitol show common features. All shorter chain (C_{n-1}, C_{n-2}, etc.) aldoses with decreasing carbon number down to C₂ and formaldehyde were encountered during photoreforming of the corresponding C_n polyol. However, higher initial selectivities were obtained to C_{n-2} aldoses (being constant over time) compared to C_{n-1} aldoses and formaldehyde (SI-Figs. 2.8 – 2.10). Furthermore, glycolaldehyde is the major species in each case accumulating over time in liquid-phase, with the highest and almost constant selectivity with increasing reaction time (SI-Figs. 2.8-2.10). Larger amounts of glycolaldehyde were produced at similar amounts

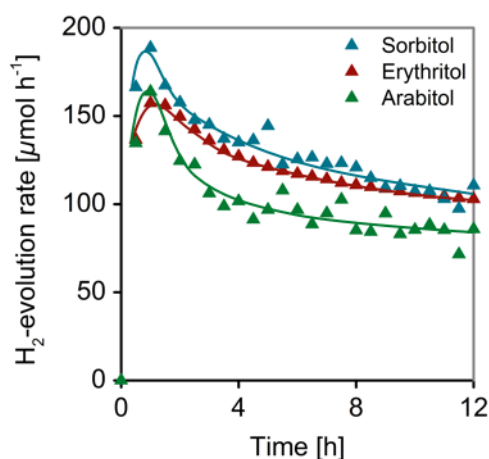


Figure 2.13. Course of H₂-evolution rates during photoreforming of C₄-C₆ polyols. Reaction conditions: 75 mg photocatalyst, 100 mL aqueous oxygenate solution (20 mM), 288 K, 1 bar Ar, 300 W Xe-lamp (CM1).

of H_2 generated with increasing polyol carbon number (Table 2.3). These observations indicate that glycolaldehyde is not formed as a result of a reaction cascade, but as a primary product from the polyols. Thus, initial polyol conversion must predominantly proceed through oxidative cleavage of an internal C-C bond, i.e. the C2-C3 bond in erythritol, arabitol, and sorbitol (Scheme 2.7, and SI-Schemes 2.1 and 2.2).

Constant selectivity profiles for C_{2+} aldoses over time (SI-Figs. 2.8 – 2.10) indicate that every C-C bond may also undergo oxidative cleavage in the first step although the internal cleavage is preferred. Similar distributions of these aldoses were encountered in studies conducted on noble metal decorated TiO_2 [29, 49]. However, we did not find evidence for the generation of gluconic acid as reported earlier [29, 49].

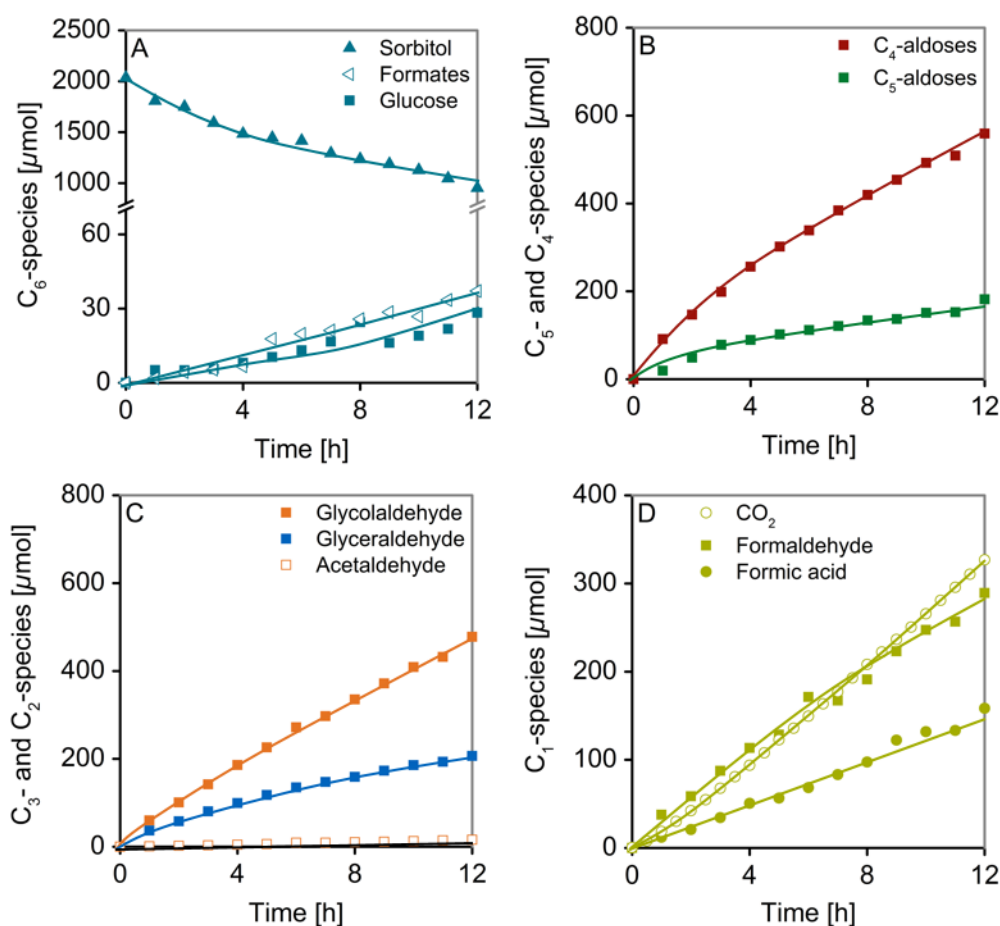


Figure 2.14. Temporal profiles of anodic reaction products formed during sorbitol photoreforming. (A) Course of amount of sorbitol and C_6 -intermediates. Course of (B) C_5/C_4 -, (C) C_3/C_2 - and (D) C_1 -species generated. Reaction conditions: 75 mg photocatalyst, 100 mL aqueous sorbitol solution (20 mM), 288 K, 1 bar Ar, 300 W Xe-lamp (CM1).

C_n aldoses generated from oxidation of a terminal polyol carbon, i.e. erythrose from erythritol, arabinose and lyxose from arabitol, and glucose from sorbitol were present in small quantities (initial selectivities of 1-8 % decreasing with increasing polyol carbon number). C_n ketoses resulting from oxidation of a secondary carbon in 2-position (i.e. formation of erythrulose from erythritol with an initial selectivity of 3 %) were absent in the cases of arabitol and sorbitol photoreforming. These low selectivities to C_n ketoses and C_n aldoses from polyols corroborate the minor contribution of pathways yielding C_n species with primary or secondary sp²-carbon.

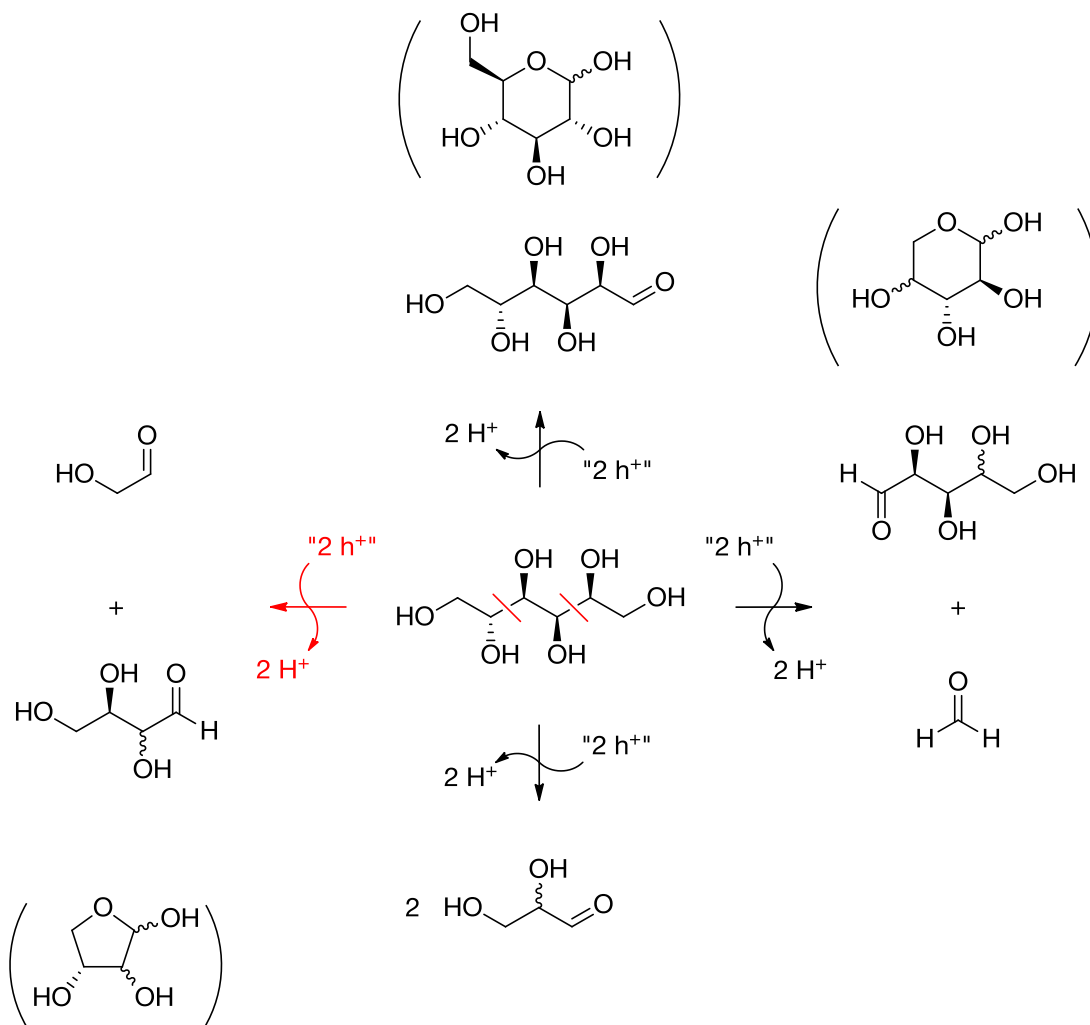
Compounds bearing non-functionalized carbon as a consequence of dehydration reactions were not observed except for small quantities of acetaldehyde (e.g. of 30 μmol after 12 h during photoreforming of erythritol) that were present with all polyols and decreasing with increasing polyol chain length. The origin, properties and impact of multiple formic acid esters (summed to a total amount of ‘formates’) encountered with minor abundance as a consequence of the presence of cyclic hemiacetal intermediates (erythrose, arabinose, xylose, lyxose and glucose) is addressed in detail in chapter 3 of this thesis.

Thus, initial anodic transformations of erythritol, arabitol and sorbitol involve multiple oxidative C-C-scission pathways. The reaction pathways for sorbitol photoreforming are exemplarily displayed in Scheme 2.7 (reaction pathways for erythritol and arabitol conversion can be found in SI-Schemes 2.1 and 2.2). Generally, oxidative cleavage of

Table 2.3. Comparison of amounts of glycolaldehyde and CO₂ generated at comparable H₂ yields during photoreforming of polyols.

Compound	Glycerol	Erythritol	Arabitol	Sorbitol
Amount of H ₂ [μmol]	1200	1235	1218	1246
Reaction time [h]	10	12	12	9
Amount of glycolaldehyde [μmol]	247	696	833	846
Amount of CO ₂ [μmol]	313	392	298	237

each individual C-C bond is feasible in the first step. However, cleavage of the internal C-C bonds, i.e. C2-C3 for erythritol and arabitol and C2-C3 preferred over C3-C4 for sorbitol, constitute the dominant reaction pathways.

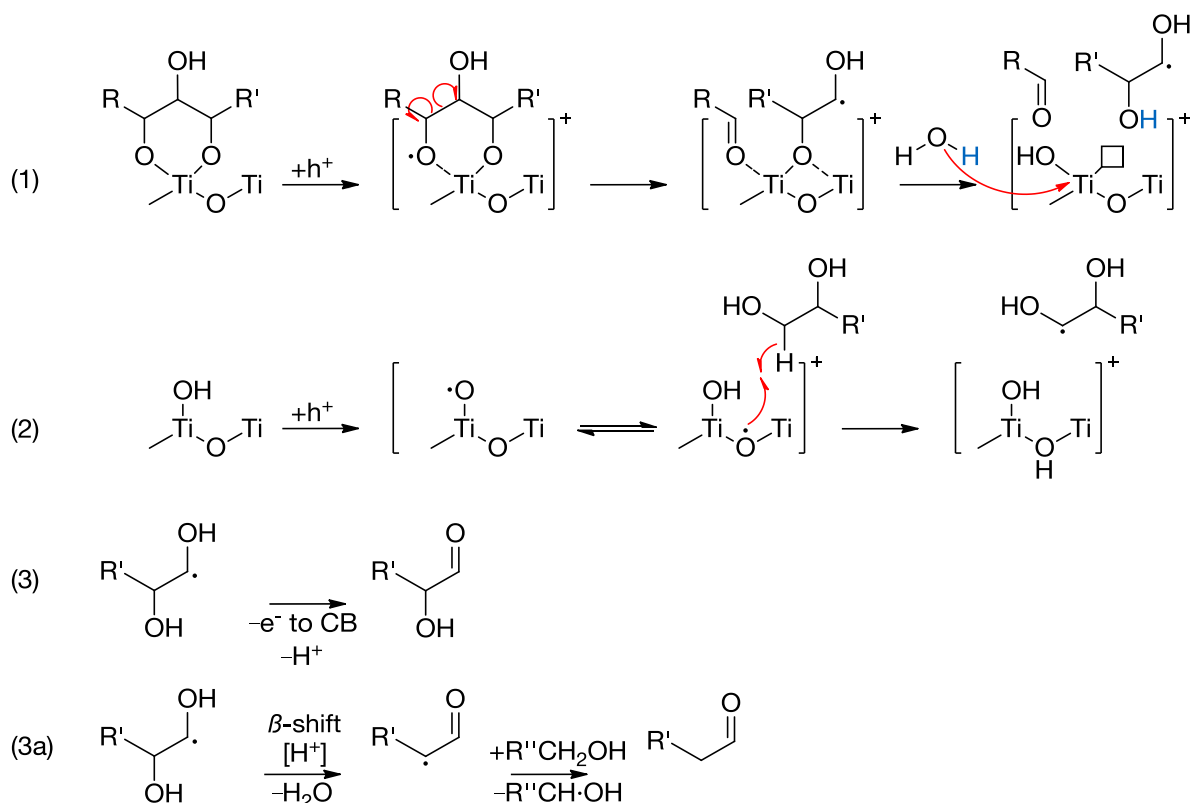


Scheme 2.7. Reaction network for photocatalytic reforming of sorbitol. Initial anodic conversion may proceed through four pathways. C-C-scission (C2-C3) to form glycolaldehyde and erythrose constitutes the dominant reaction pathway (red arrows). Cleavage of all other C-C bonds and formation of glucose represent minor reaction channels.

2.4.5 Mechanistic aspects of anodic transformations of polyols

A unified description involving two different reaction sites is proposed to rationalize the elementary steps in the anodic transformations of polyols, i.e. oxidative C-C cleavage (direct charge carrier transfer), oxidation to the corresponding aldehydes and ketones (indirect charge carrier transfer) and dehydration (side reaction within indirect mechanism).

Oxidative C-C cleavage is initialized by direct hole transfer from 'deep surface hole traps', which are constituted by chemisorbed oxygenates on terminal OH-groups at oxygen coordinatively unsaturated Ti-sites [18, 31, 50] as illustrated in Scheme 2.8, sequence (1).



Scheme 2.8. Illustration of proposed anodic transformations *via* direct and indirect oxidation mechanisms. (1) Direct hole transfer to a chemisorbed oxygenate on a coordinatively unsaturated Ti(IV)-OH site to generate an alkoxy radical followed by β -C-C-scission. Nucleophilic attack of water is proposed for active site recovery and product release. (2) Generation of carbon-centered H-loss radicals *via* interaction with shallowly trapped holes at surface lattice oxygen sites. (3) Formation of stable organic species through either current doubling of carbon-centered radicals or (3a) dehydration *via* acid-catalyzed β -shift of the radicals.

As a consequence of hole transfer to the adsorbate, alkoxy radicals are formed which undergo β -C-C-scission [51] to form one aldehyde equivalent and a carbon-centered radical. Oxidation of the latter radicals to a second aldehyde moiety under anaerobic conditions is hypothesized to proceed preferentially through injection of an electron into the CB of TiO_2 , i.e. a 'current doubling' process. Formally, the reaction products from C-C-cleavage reflect the outcome of a Malaprade periodic acid oxidation chemistry [52].

Beyond that, holes may be trapped at surface lattice oxygen sites $[\text{Ti}\cdot\text{O}\cdot\text{Ti}]$ [18, 31, 50]. These sites act as shallow hole traps that catalyze OH-radical/Fenton's reagent like chemical transformations (Scheme 2.8, sequence (2)), i.e. the formation of the corresponding aldehydes and ketones from polyols [18, 31]. Carbon-centered radicals from H-abstraction may form stable organic species upon current doubling (Scheme 2.8, sequence (3)). In a side reaction during photoreforming, the radicals may undergo an acid-catalyzed β -shift (Scheme 2.8, sequence (3a)) which subsequently results in the associated dehydration products [18, 53-55], e.g. production of HA from glycerol. Acid-catalyzed elimination of water upon β -shift of a carbon-centered radical to form a carbon radical (or intermediate radical cation upon proton association) stabilized by a vicinal carbonyl group (Scheme 2.8) is well-known to occur during free OH-radical mediated oxidations [53-55].

Aerobic photooxidation studies demonstrated that the contributions of direct and indirect oxidation mechanisms critically depend on molecular reactant structure [50, 56-58]. For instance, photocatalytic degradation of phenol over TiO_2 P 25 proceeded predominantly through interaction with 'shallowly trapped holes' with a minor contribution of a direct hole transfer mechanism [57]. Polyols possess a high tendency towards coordination to Ti(IV) cations. Evidence for a bidentate mode of binding was provided from the changes in the pre-edge structure in Ti K-edge XANES [59]. Those were interpreted in terms of an almost quantitative change in coordination environment around Ti(IV) sites from square pyramidal towards octahedral upon adsorption of polyols. In case of glycerol, IR-spectroscopic studies provide evidence that glycerol dissociatively establishes a bridging alkoxy bond *via* a primary OH-functionality to a coordinatively unsaturated Ti(IV) site [60, 61]. An increasing tendency for polyol chemisorption with increasing number of OH-functionalities was shown for competitive adsorption of water and polyols on hydrated Al_2O_3 [60, 62].

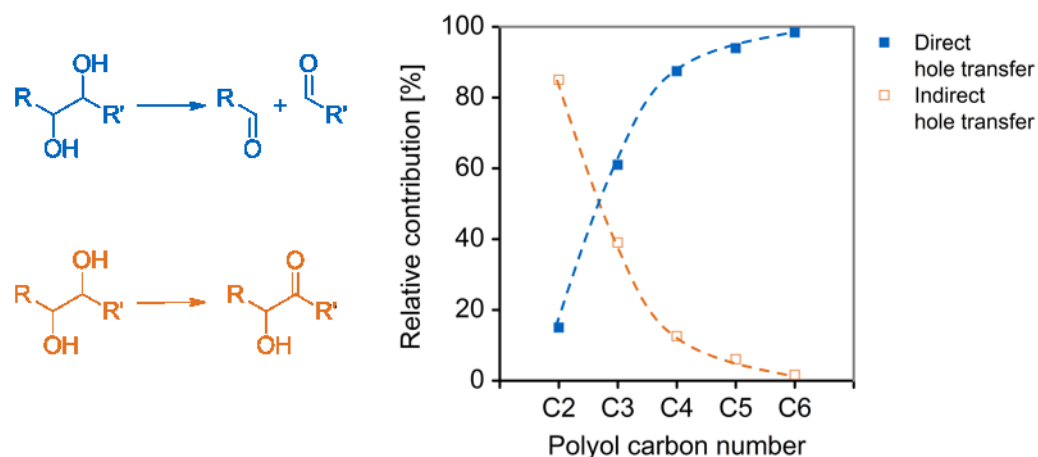


Figure 2.15. Relative contributions of direct (C-C-cleavage) and indirect (oxidation to C_n aldoses and ketoses and dehydration) charge transfer mechanisms to the anodic transformations of C_2 - C_6 polyols during photoreforming on Rh/TiO₂ derived from reaction pathway analysis. Data for C_2 -polyol was taken from ref. 18.

Investigation of the anodic reaction networks of ethylene glycol [18] and C_3 - C_6 polyols shows a change from oxidation of a primary carbon (reaction of ethylene glycol to glycolaldehyde *via* an indirect mechanism) to C-C-cleavage (direct mechanism) for glycerol and higher polyols in the dominant reaction pathway. The relative contributions of direct and indirect mechanisms to the anodic conversion of C_n polyols are presented in Fig. 2.15 (Data for C_2 -polyol was taken from ref. 18.). The contributions were derived from the rate constants from kinetic modeling in case of ethylene glycol and glycerol and the initial selectivities of the primary products for C_4 - C_6 polyol photoreforming. The direct mechanism becomes progressively dominant with increasing polyol chain length, i.e. the relative contribution increases from 15 % for ethylene glycol to 61 % for glycerol and 98 % for sorbitol photoreforming, respectively. This is in line with the complexation of coordinatively unsaturated Ti(IV)-sites expected to be more effective, i.e. a larger polyol fraction in a chemisorbed state at constant concentration, with increasing number of anchoring OH-groups. In parallel, the participation of indirect reaction channels diminishes accordingly. The decreasing selectivity for dehydration with increasing polyol carbon number that leads to the absence of the respective products during photoreforming of C_4 - C_6 polyols corroborates a side-reaction within the indirect mechanism.

2.5 Conclusions

Photocatalytic rates of linear C₁-C₃ oxygenates are primarily dependent on the substrate specific apparent adsorption constants and follow a Langmuir adsorption model. In the anodic half-reactions of photoreforming linear polyols are converted *via* (i) oxidative rupture of C-C bonds, (ii) oxidation to the corresponding aldoses or ketoses or (iii) light-driven dehydration, while evolving H₂ at the cathode. The first pathway is proposed to result from direct hole transfer to the chemisorbed oxygenate on terminal Ti(IV)-OH groups to form alkoxy-radicals which undergo β -C-C-cleavage. The latter pathways are attributed to an indirect mechanism initiated by hole trapping at surface lattice oxygen sites [Ti \cdot -O \cdot -Ti].

Accordingly, the anodic reaction network of glycerol photoreforming follows four reaction pathways. Oxidative C-C-cleavage leads to glycolaldehyde and formaldehyde as the dominant pathway (61 %). Oxidation of the primary or secondary carbon gives rise to glyceraldehyde (26 %) or dihydroxyacetone (13 %), respectively. Light-driven dehydration of glycerol to hydroxyacetone proceeds in a minor side-reaction.

With increasing polyol chain length (number of carbons and OH-groups) the selectivities shift to favor anodic conversion through C-C-cleavage even further with internal C-C bonds preferentially cleaved over terminal ones. This is attributed to the increasing number of anchoring OH-functionalities favoring conversion through a direct hole transfer mechanism.

2.6 Acknowledgements

We would like to thank Clariant for fruitful discussions within the framework of MuniCat and the iC⁴ PhotoCOO project. The authors are grateful to Donald M. Camaioni for critical reading of the manuscript. Additionally, we would like to thank the German Federal Ministry of Education and Research (BMBF) for financial support (project no. 01RC1106A). K.E.S. gratefully acknowledges financial support by the Fonds der Chemischen Industrie (FCI). The authors thank Xaver Hecht for BET and H₂-chemisorption measurements and Martin Neukamm for AAS measurements. Christine Schwarz and Martina Haack are acknowledged for technical assistance concerning NMR and HPLC analysis, respectively.

2.7 References

- [1] K. Shimura, H. Yoshida, *Energ. Environ. Sci.* 4 (2011) 2467-2481.
- [2] R.M. Navarro, M.C. Sanchez-Sanchez, M.C. Alvarez-Galvan, F. del Valle, J.L.G. Fierro, *Energ. Environ. Sci.* 2 (2009) 35-54.
- [3] D. Kondarides, V. Daskalaki, A. Patsoura, X. Verykios, *Catal. Lett.* 122 (2008) 26-32.
- [4] Y. Ma, X. Wang, Y. Jia, X. Chen, H. Han, C. Li, *Chem. Rev.* 114 (2014) 9987-10043.
- [5] X. Chen, S. Shen, L. Guo, S.S. Mao, *Chem. Rev.* 110 (2010) 6503-6570.
- [6] M. Cargnello, A. Gasparotto, V. Gombac, T. Montini, D. Barreca, P. Fornasiero, *Eur. J. Inorg. Chem.* 2011 (2011) 4309-4323.
- [7] Z.H.N. Al-Azri, W.-T. Chen, A. Chan, V. Jovic, T. Ina, H. Idriss, G.I.N. Waterhouse, *J. Catal.* 329 (2015) 355-367.
- [8] F. Dionigi, P.C.K. Vesborg, T. Pedersen, O. Hansen, S. Dahl, A. Xiong, K. Maeda, K. Domen, I. Chorkendorff, *J. Catal.* 292 (2012) 26-31.
- [9] W. Jiao, L. Wang, G. Liu, G.Q. Lu, H.-M. Cheng, *ACS Catal.* 2 (2012) 1854-1859.
- [10] J. Zhang, Q. Xu, Z. Feng, M. Li, C. Li, *Angew. Chem. Int. Ed.* 120 (2008) 1790-1793.
- [11] Y.K. Kho, A. Iwase, W.Y. Teoh, L. Mädler, A. Kudo, R. Amal, *J. Phys. Chem. C* 114 (2010) 2821-2829.
- [12] A. Tanaka, S. Sakaguchi, K. Hashimoto, H. Kominami, *ACS Catal.* 3 (2013) 79-85.
- [13] A.J. Bard, M.A. Fox, *Acc. Chem. Res.* 28 (1995) 141-145.
- [14] A.J. Bard, *J. Photochem.* 10 (1979) 59-75.
- [15] J. Chen, D.F. Ollis, W.H. Rulkens, H. Bruning, *Water Res.* 33 (1999) 1173-1180.
- [16] K. Lalitha, G. Sadanandam, V.D. Kumari, M. Subrahmanyam, B. Sreedhar, N.Y. Hebalkar, *J. Phys. Chem. C* 114 (2010) 22181-22189.
- [17] P. Panagiotopoulou, E.E. Karamerou, D.I. Kondarides, *Catal. Today* 209 (2013) 91-98.
- [18] T.F. Berto, K.E. Sanwald, W. Eisenreich, O.Y. Gutiérrez, J.A. Lercher, *J. Catal.* 338 (2016) 68-81.
- [19] R. Chong, J. Li, X. Zhou, Y. Ma, J. Yang, L. Huang, H. Han, F. Zhang, C. Li, *Chem. Commun.* 50 (2014) 165-167.
- [20] M. Murdoch, G.I.N. Waterhouse, M.A. Nadeem, J.B. Metson, M.A. Keane, R.F. Howe, J. Llorca, H. Idriss, *Nat. Chem.* 3 (2011) 489-492.

- [21] R. Su, R. Tiruvalam, A.J. Logsdail, Q. He, C.A. Downing, M.T. Jensen, N. Dimitratos, L. Kesavan, P.P. Wells, R. Bechstein, *ACS nano* 8 (2014) 3490-3497.
- [22] W. Jones, R. Su, P.P. Wells, Y. Shen, N. Dimitratos, M. Bowker, D. Morgan, B.B. Iversen, A. Chutia, F. Besenbacher, G.J. Hutchings, *PCCP* 16 (2014) 26638-26644.
- [23] Y. Hang Li, J. Xing, Z. Jia Chen, Z. Li, F. Tian, L. Rong Zheng, H. Feng Wang, P. Hu, H. Jun Zhao, H. Gui Yang, *Nat. Commun.* 4 (2013) 2500.
- [24] H. Bahruji, M. Bowker, P.R. Davies, L.S. Al-Mazroai, A. Dickinson, J. Greaves, D. James, L. Millard, F. Pedrono, *J. Photoch. Photobio. A* 216 (2010) 115-118.
- [25] H. Bahruji, M. Bowker, P.R. Davies, F. Pedrono, *Appl. Catal. B* 107 (2011) 205-209.
- [26] G.N. Nomikos, P. Panagiotopoulou, D.I. Kondarides, X.E. Verykios, *Appl. Catal. B* 146 (2014) 249-257.
- [27] X. Fu, J. Long, X. Wang, D.Y.C. Leung, Z. Ding, L. Wu, Z. Zhang, Z. Li, X. Fu, *Int. J. Hydrogen Energ.* 33 (2008) 6484-6491.
- [28] V.M. Daskalaki, D.I. Kondarides, *Catal. Today* 144 (2009) 75-80.
- [29] R. Chong, J. Li, Y. Ma, B. Zhang, H. Han, C. Li, *J. Catal.* 314 (2014) 101-108.
- [30] C. Minero, E. Pelizzetti, P. Pichat, M. Sega, M. Vincenti, *Env. Sci. Technol.* 29 (1995) 2226-2234.
- [31] C. Minero, A. Bedini, V. Maurino, *Appl. Catal. B* 128 (2012) 135-143.
- [32] V. Maurino, A. Bedini, M. Minella, F. Rubertelli, E. Pelizzetti, C. Minero, *J. Adv. Oxid. Technol.* 11 (2008) 184-192.
- [33] T. Montini, V. Gombac, L. Sordelli, J.J. Delgado, X. Chen, G. Adami, P. Fornasiero, *ChemCatChem* 3 (2011) 574-577.
- [34] J. Schnaidt, M. Heinen, D. Denot, Z. Jusys, R.J. Behm, *J. Electroanal. Chem.* 661 (2011) 250-264.
- [35] C.A. Martins, M.J. Giz, G.A. Camara, *Electrochim. Acta* 56 (2011) 4549-4553.
- [36] Y. Kwon, K.J.P. Schouten, M.T.M. Koper, *ChemCatChem* 3 (2011) 1176-1185.
- [37] H.J. Kim, J. Lee, S.K. Green, G.W. Huber, W.B. Kim, *ChemSusChem* 7 (2014) 1051-1056.
- [38] L. Roquet, E.M. Belgsir, J.M. Léger, C. Lamy, *Electrochim. Acta* 39 (1994) 2387-2394.
- [39] X. Fu, X. Wang, D.Y.C. Leung, Q. Gu, S. Chen, H. Huang, *Appl. Catal. B* 106 (2011) 681-688.

- [40] A. Gallo, M. Marelli, R. Psaro, V. Gombac, T. Montini, P. Fornasiero, R. Pievo, V.D. Santo, *Green Chem.* 14 (2012) 330-333.
- [41] T. Sakata, T. Kawai, *Chem. Phys. Lett.* 80 (1981) 341-344.
- [42] T. Sakata, T. Kawai, K. Hashimoto, *J. Phys. Chem.-US* 88 (1984) 2344-2350.
- [43] B. Kraeutler, A.J. Bard, *J. Am. Chem. Soc.* 100 (1978) 5985-5992.
- [44] X.-J. Zheng, L.-F. Wei, Z.-H. Zhang, Q.-J. Jiang, Y.-J. Wei, B. Xie, M.-B. Wei, *Int. J. Hydrogen Energ.* 34 (2009) 9033-9041.
- [45] T.F. Berto, Elucidation of the reaction pathways of the photoreforming and overall water splitting reaction over precious metal decorated semiconductors, in, *Technische Universität München*, 2016, pp. 51-104.
- [46] S.K. Milonjić, *J. Serb. Chem. Soc* 72 (2007) 1363-1367.
- [47] D.F. Ollis, *J. Phys. Chem. B* 109 (2005) 2439-2444.
- [48] A. Mills, C. O'Rourke, K. Moore, *J. Photochem. Photobiol. A* 310 (2015) 66-105.
- [49] M. Bellardita, E.I. García-López, G. Marcì, L. Palmisano, *Int. J. Hydrogen Energ.* 41 (2016) 5934-5947.
- [50] J.F. Montoya, M.F. Atitar, D.W. Bahnemann, J. Peral, P. Salvador, *J. Phys. Chem. C* 118 (2014) 14276-14290.
- [51] A. Boto, D. Hernández, R. Hernández, E. Suárez, *J. Org. Chem.* 68 (2003) 5310-5319.
- [52] G. Dryhurst, *Periodate oxidation of diol and other functional groups: analytical and structural applications*, Pergamom Press, Oxford, 2013, chapter 3.
- [53] A.L. Buley, R.O.C. Norman, R.J. Pritchett, *J. Chem. Soc. B* (1966) 849-852.
- [54] C. Walling, R.A. Johnson, *J. Am. Chem. Soc.* 97 (1975) 2405-2407.
- [55] D. Jiang, S. Barata-Vallejo, B.T. Golding, C. Ferreri, C. Chatgililoglu, *Org. Biomol. Chem.* 10 (2012) 1102-1107.
- [56] C. Minero, G. Mariella, V. Maurino, E. Pelizzetti, *Langmuir* 16 (2000) 2632-2641.
- [57] C. Minero, G. Mariella, V. Maurino, D. Vione, E. Pelizzetti, *Langmuir* 16 (2000) 8964-8972.
- [58] J.M. Kesselman, O. Weres, N.S. Lewis, M.R. Hoffmann, *J. Phys. Chem. B* 101 (1997) 2637-2643.
- [59] I.A. Shkrob, M.C. Sauer, D. Gosztola, *J. Phys. Chem. B* 108 (2004) 12512-12517.
- [60] J.R. Copeland, X.-R. Shi, D.S. Sholl, C. Sievers, *Langmuir* 29 (2013) 581-593.

[61] J.R. Copeland, I.A. Santillan, S.M. Schimming, J.L. Ewbank, C. Sievers, J. Phys. Chem. C 117 (2013) 21413-21425.

[62] W. van Bronswijk, H.R. Watling, Z. Yu, Colloid. Surface A 157 (1999) 85-94.

2.8 Supporting information

SI-Table 2.1. List of ^1H -NMR signals of C_1 - C_6 oxygenates used for quantification. Chemical shifts are referenced to the internal standard 1,3,5-trihydroxybenzene.

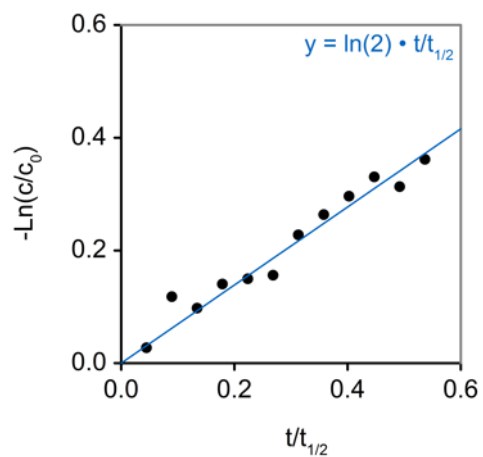
	Compound	Chemical shift [ppm]	Multiplet	J [Hz]	#H
C_1	Methanol	3.29	s	-	3
	Formaldehyde (hydrate)	4.77	s	-	2
	Formic acid	8.19	s	-	1
C_2	Ethylene glycol	3.60	s	-	4
	Glyoxal (hydrate)	4.75	s	-	2
	Glycolaldehyde	3.45	d	5.1	2
		4.38	s	-	2
		4.99	t	5.1	1
		9.56	s	-	1
	Glycolic acid	4.14	s	-	2
	Glyoxylic acid	5.28	s	-	1
	Acetaldehyde (dimer)	1.25	d	5.2	6
	(hydrate)	1.33	d	7.0	3
	(formyl)	2.18	d	3.0	3
	(dimer)	5.18	q	5.2	2
	(formyl)	9.62	q	3.0	1
	Acetic acid	2.02	s	-	3
C_3	Glycerol	3.50	m	-	2
		3.59	m	-	2
		3.72	m	-	1
	Glyceraldehyde (hydrate)	4.89	d	5.2	1
		9.62	s	-	1

SI-Table 2.1 continued

C ₃	Dihydroxyacetone (hydrate)	3.52	s	-	4
	(ketone)	4.36	s	-	4
	Hydroxyacetone	2.09	s	-	3
		4.30	s	-	2
	Glyceric acid	3.80	m	-	2
		4.29	t	4.1	1
C ₄	Erythritol	3.59	m	-	4
		3.72	m	-	2
	Erythrose	5.05	d	4.0	1
		5.20	d	3.4	1
		5.22	d	4.7	1
		9.69	s	-	1
	Threose	5.35	d	4.2	1
	Erythrulose	3.80	m	-	2
		4.39	t	4.1	1
C ₅	Arabinose	4.45	d	7.8	1
		5.17	d	3.6	1
		5.18	d	2.7	1
		5.24	d	4.5	1
	Xylose	4.51	d	7.9	1
		5.13	d	3.7	1
	Lyxose	5.36	d	4.3	1
		4.95	d	4.5	1
C ₆	Glucose	5.17	d	3.8	1
	Gluconic acid	4.36	d	4.0	1

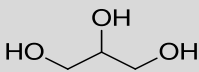
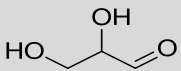
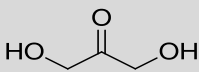
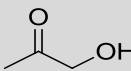
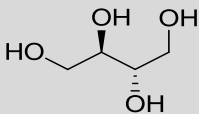
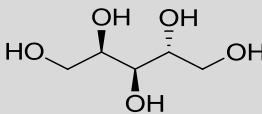
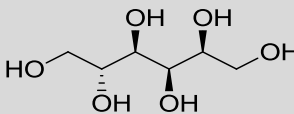
SI-Table 2.1 continued

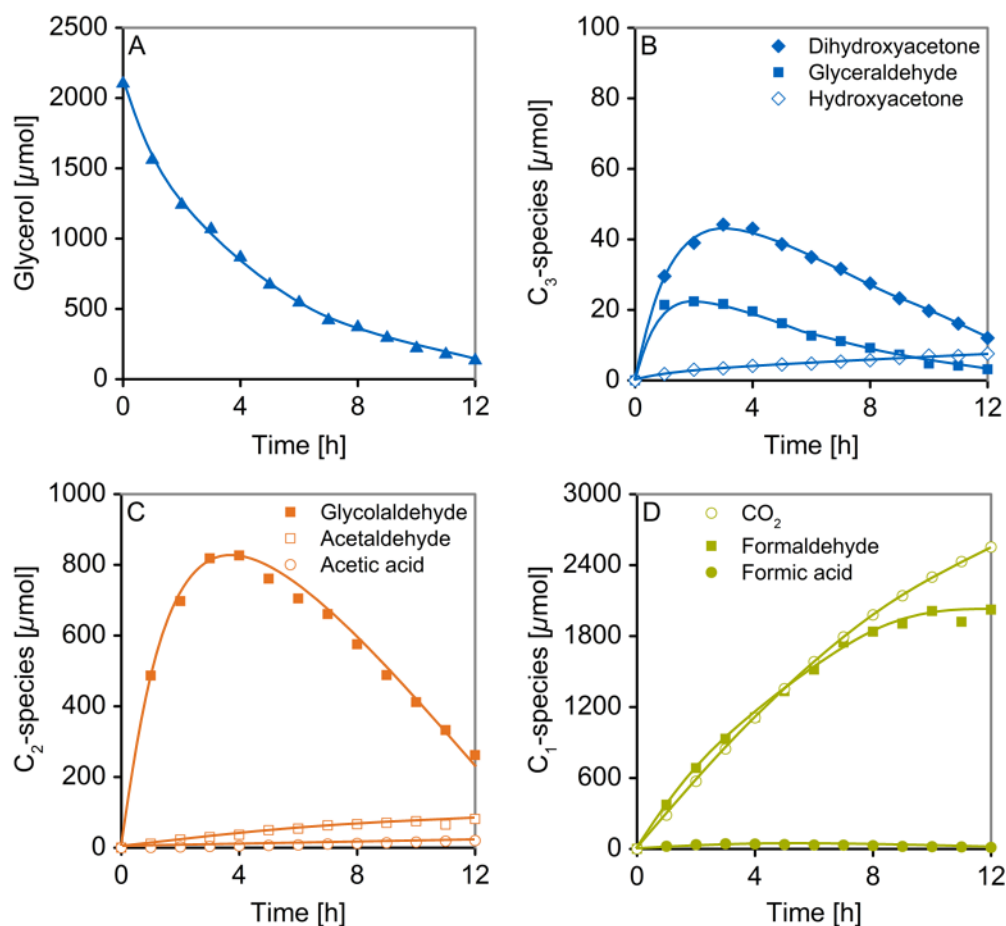
	1,3,5-Trihydroxybenzene	5.94	s	-	3
--	-------------------------	------	---	---	---



SI-Figure 2.1. Projection of glycerol concentration profile during photoreforming onto first-order rate law (trend line) for determination of reaction order.

SI-Table 2.2. Reaction equations and H₂/CO₂-ratios for photoreforming reactions of C₃-C₆ oxygenates.

	Compound	Overall reaction equation	Stoichiometric H ₂ /CO ₂ -ratio
C ₃	Glycerol	 $+ 3 \text{ H}_2\text{O} \xrightarrow{h\nu} 3 \text{ CO}_2 + 7 \text{ H}_2$	2.3
	Glycer-aldehyde	 $+ 3 \text{ H}_2\text{O} \xrightarrow{h\nu} 3 \text{ CO}_2 + 6 \text{ H}_2$	2.0
	Dihydroxy-acetone	 $+ 3 \text{ H}_2\text{O} \xrightarrow{h\nu} 3 \text{ CO}_2 + 6 \text{ H}_2$	2.0
	Hydroxy-acetone	 $+ 4 \text{ H}_2\text{O} \xrightarrow{h\nu} 3 \text{ CO}_2 + 7 \text{ H}_2$	2.3
C ₄	Erythritol	 $+ 4 \text{ H}_2\text{O} \xrightarrow{h\nu} 4 \text{ CO}_2 + 9 \text{ H}_2$	2.3
C ₅	Arabitol	 $+ 5 \text{ H}_2\text{O} \xrightarrow{h\nu} 5 \text{ CO}_2 + 11 \text{ H}_2$	2.2
C ₆	Sorbitol	 $+ 6 \text{ H}_2\text{O} \xrightarrow{h\nu} 6 \text{ CO}_2 + 13 \text{ H}_2$	2.2



SI-Figure 2.2. Analysis of species generated in anodic half-reactions during glycerol photoreforming. (A) Course of the amount of glycerol. Quantities of different (B) C_3 -, (C) C_2 - and (D) C_1 -species generated. Reaction conditions: 75 mg photocatalyst, 100 mL aqueous glycerol solution (20 mM), 288 K, 1 bar Ar, UV LEDs (365 nm \pm 5 nm), $9.22 \cdot 10^{18}$ photons s^{-1} .

Glyceraldehyde (GAD) photoreforming

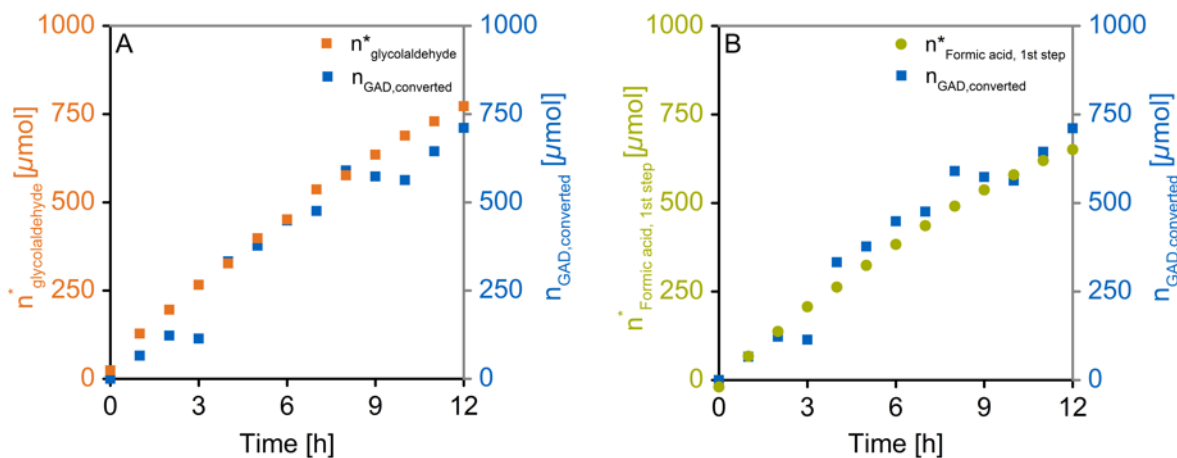
Based on the reaction sequence for GAD photoreforming proposed in Scheme 2.3 and assuming negligible consecutive oxidation of formaldehyde under reaction conditions (i.e. CO₂ solely stems from formic acid oxidation), the total amount of glycolaldehyde $n_{\text{glycolaldehyde}}^*$ generated during reaction must equal the amount of GAD converted following the relation expressed in eq. (2.6).

$$n_{\text{glycolaldehyde}}^* \cong n_{\text{glycolaldehyde}} + n_{\text{formaldehyde}} \cong n_{\text{GAD,converted}} \quad (2.6)$$

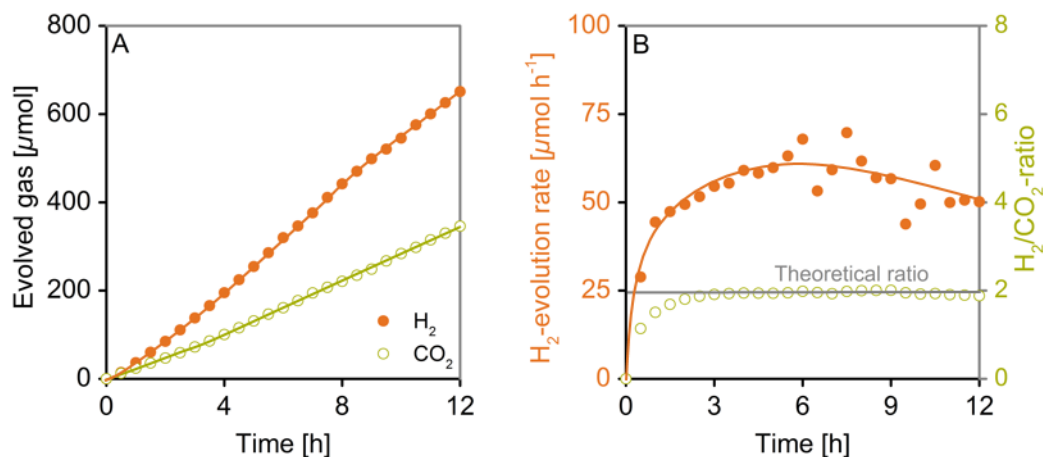
Correlation of the corresponding experimental data in SI- Fig. 2.3A demonstrates that glycolaldehyde is selectively formed in the first step from GAD. The amount of formic acid released from initial C-C cleavage of GAD is obtained from the determined amount of formic acid by accounting for consecutive reaction to CO₂ and formic acid generation *via* glycolaldehyde oxidation according to eq. (2.7).

$$n_{\text{formic acid,1st step}}^* \cong n_{\text{formic acid}} + n_{\text{CO}_2} - n_{\text{formaldehyde}} \cong n_{\text{GAD,converted}} \quad (2.7)$$

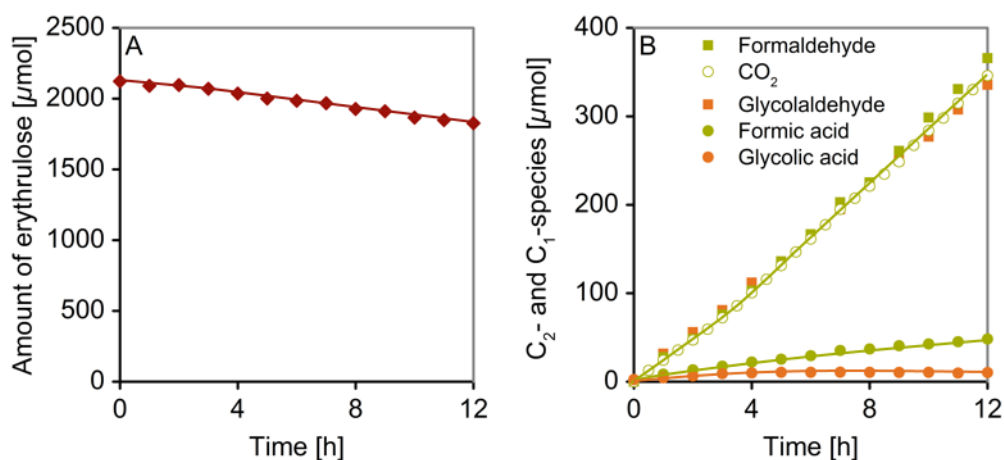
The calculated amount of formic acid $n_{\text{formic acid,1st step}}^*$ aligns well with the amount of GAD converted (SI-Fig. 2.3B) corroborating that formic acid is concomitantly generated from initial GAD oxidation.



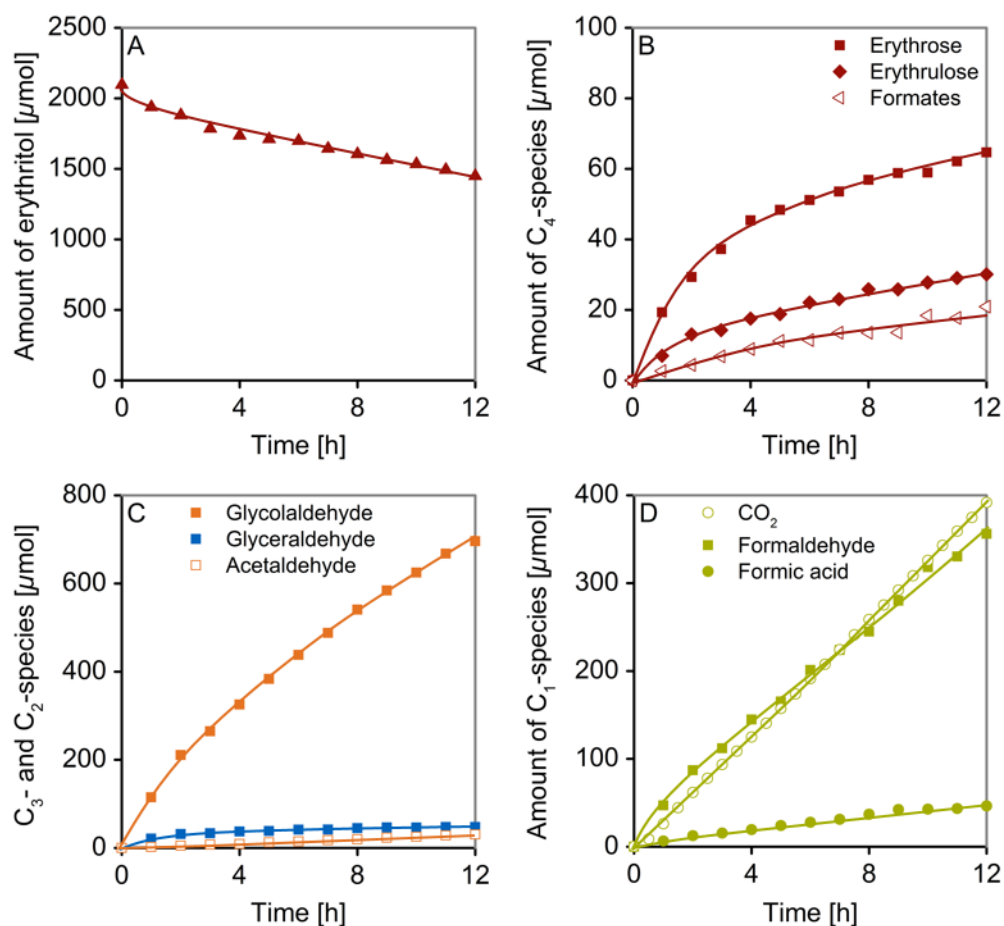
SI-Figure 2.3. Correlation of (A) total amount of glycolaldehyde formed (eq. (2.6)) and (B) amount of formic acid released in the first step of glyceraldehyde photoreforming (eq. (2.7)) with the converted amounts of glyceraldehyde, respectively.



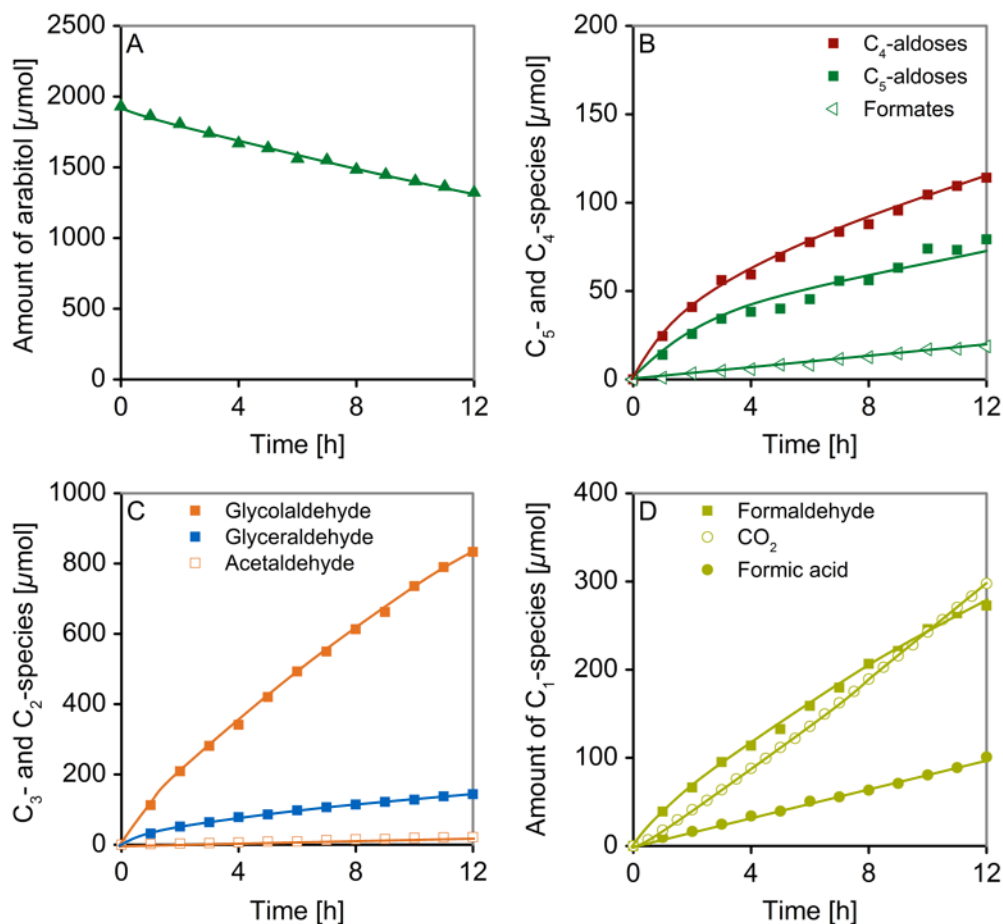
SI-Figure 2.4. (A) Course of amounts of H₂ and CO₂ evolved during photoreforming of erythrose. (B) H₂-evolution rates and H₂/CO₂-ratios in comparison with stoichiometric ratio. Reaction conditions: 75 mg photocatalyst, 100 mL aqueous erythrose solution (20 mM), 288 K, 1 bar Ar, 300 W Xe-lamp (CM1).



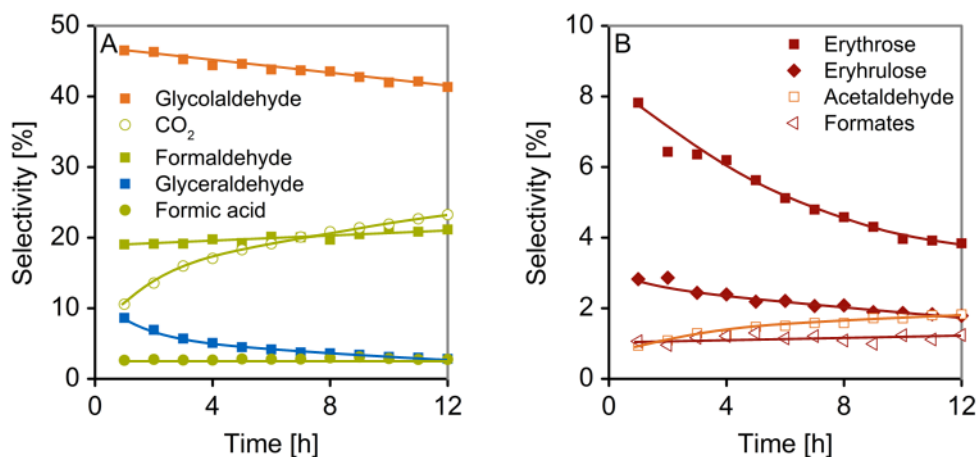
SI-Figure 2.5. Course of anodic reaction products formed during erythrose photoreforming. (A) Course of amount of erythrose. (B) Temporal profiles of C₂- and C₁-species generated. Reaction conditions: 75 mg photocatalyst, 100 mL aqueous erythrose solution (20 mM), 288 K, 1 bar Ar, 300 W Xe-lamp (CM1).



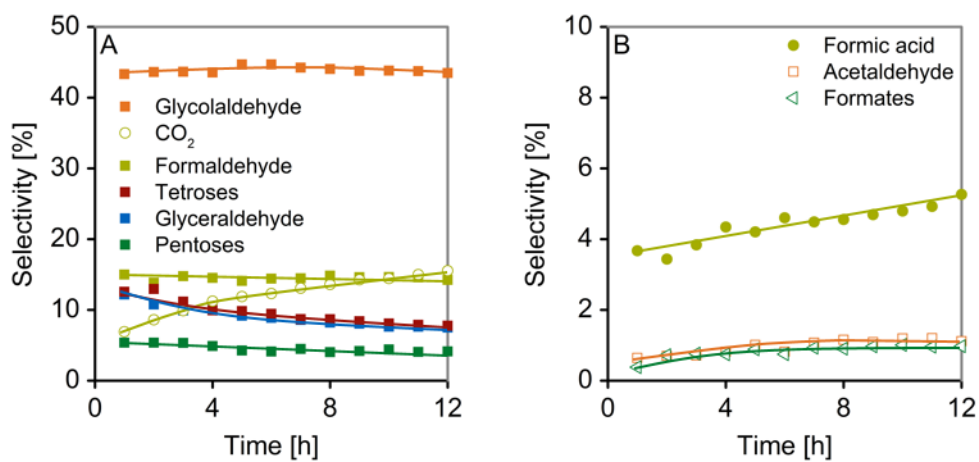
SI-Figure 2.6. Temporal profiles of anodic reaction products formed during erythritol photoreforming. (A) Course of amount of erythritol. Course of C_4 - (B), C_3 -/ C_2 - (C) and C_1 -species (A) generated. Reaction conditions: 75 mg photocatalyst, 100 mL aqueous erythritol solution (20 mM), 288 K, 1 bar Ar, 300 W Xe-lamp (CM1).



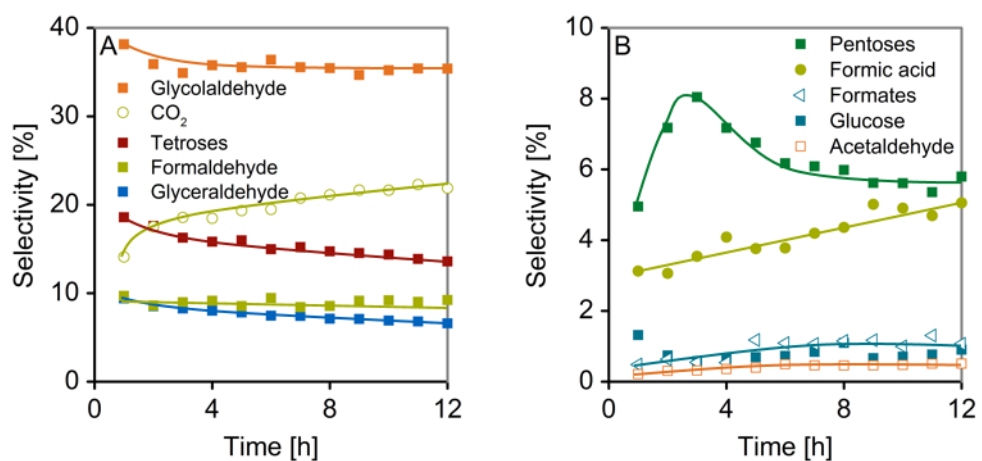
SI-Figure 2.7. Temporal profiles of anodic reaction products formed during arabitol photoreforming. (A) Course of amount of arabitol. Course of C_5/C_4 - (B), C_3/C_2 - (C) and C_1 -species (A) generated. Arabinose and lyxose, and erythrose and threose have been summed up to total amounts of pentoses and tetroses, respectively. Reaction conditions: 75 mg photocatalyst, 100 mL aqueous arabitol solution (20 mM), 288 K, 1 bar Ar, 300 W Xe-lamp (CM1).



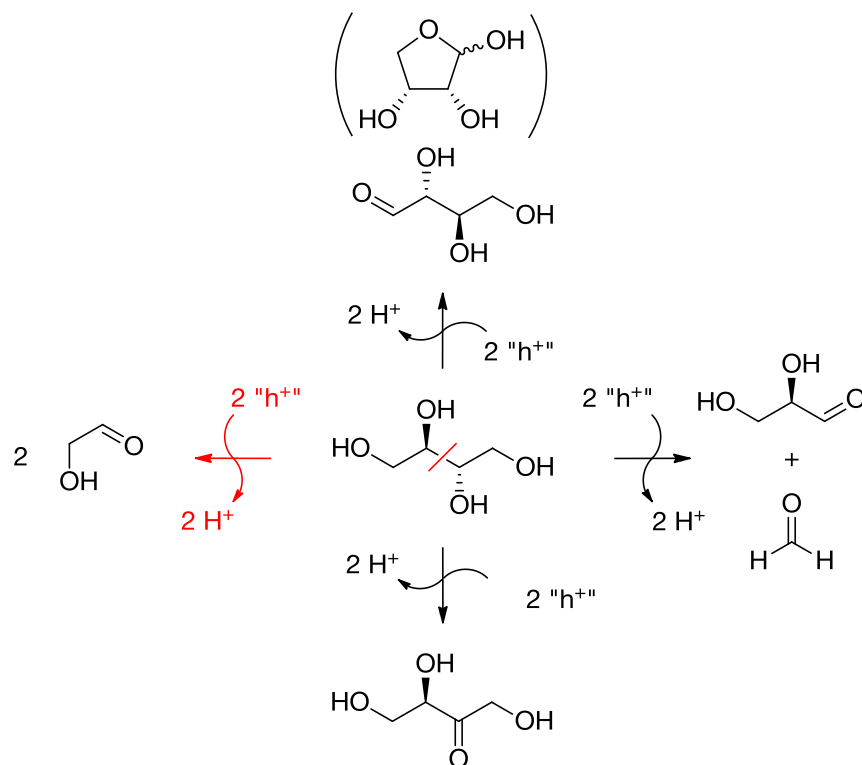
SI-Figure 2.8. Course of selectivities of anodic reaction products generated during photoreforming of erythritol. For clarity, the species have been divided into two separate graphs. Reaction conditions: 75 mg photocatalyst, 100 mL aqueous erythritol solution (20 mM), 288 K, 1 bar Ar, 300 W Xe-lamp (CM1).



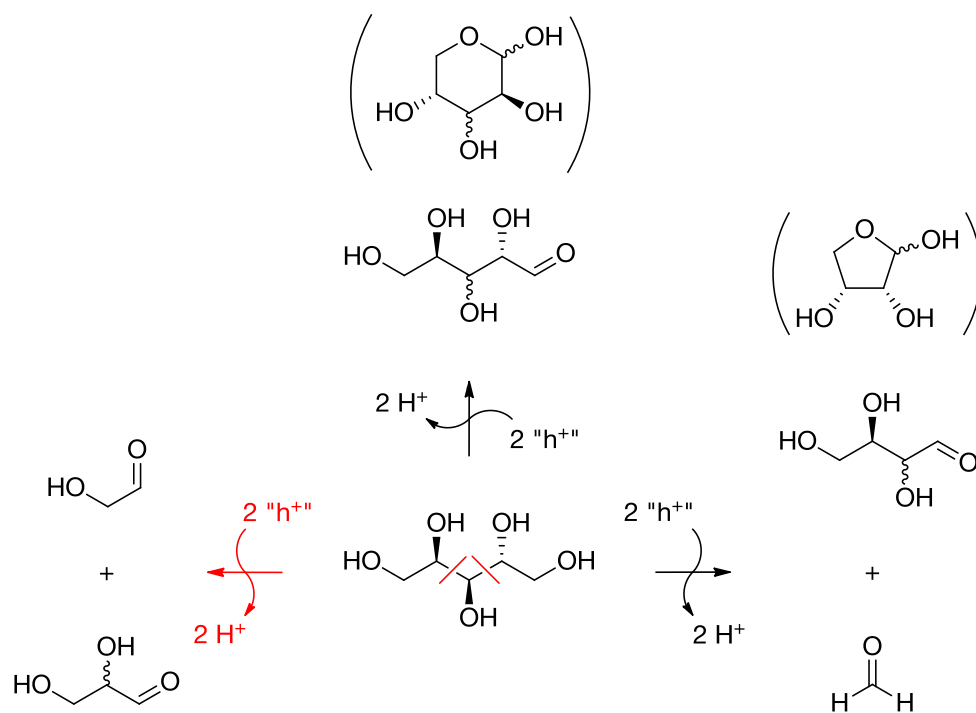
SI-Figure 2.9. Course of selectivities of anodic reaction products generated during photoreforming of arabitol. For clarity, the species have been divided into two separate graphs. Reaction conditions: 75 mg photocatalyst, 100 mL aqueous arabitol solution (20 mM), 288 K, 1 bar Ar, 300 W Xe-lamp (CM1).



SI-Figure 2.10. Course of selectivities of anodic reaction products generated during photoreforming of sorbitol. For clarity, the species have been divided into two separate graphs. Reaction conditions: 75 mg photocatalyst, 100 mL aqueous sorbitol solution (20 mM), 288 K, 1 bar Ar, 300 W Xe-lamp (CM1).



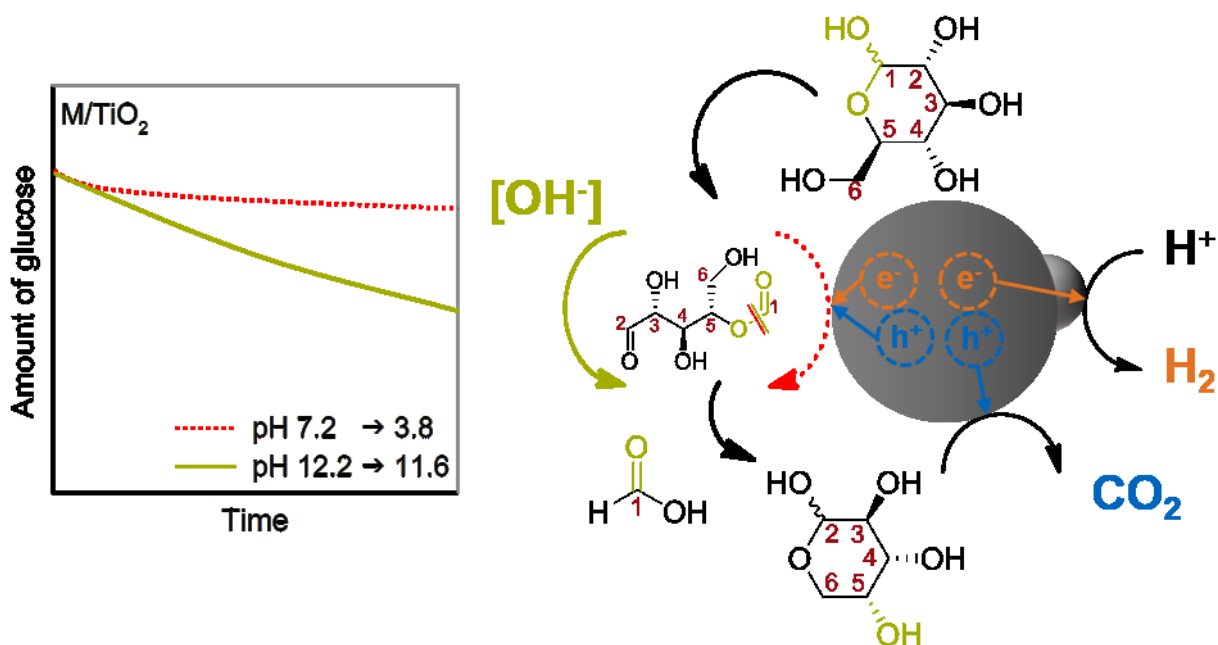
SI-Scheme 2.1. Reaction network for erythritol photoreforming. Initial anodic conversion may proceed through four pathways. Oxidative scission of the internal C-C bond (C2–C3) to form two equivalents of glycolaldehyde occurs preferentially (red arrow). Terminal C-C-scission and oxidation of terminal carbons and carbons in 2-position occur in minor reaction channels.



SI-Scheme 2.2. Reaction network for photoreforming of arabinol. Three reaction pathways are evident. Predominantly, oxidative C-C-cleavage occurs in between C2–C3 (red arrows). Scission of terminal C-C bonds with concomitant formaldehyde release as well as oxidation of terminal carbons occur subordinately.

Chapter 3

Identifying and overcoming the rate-limiting reaction during photoreforming of sugar aldehydes for H_2 -generation



3. Identifying and overcoming the rate-limiting reaction during photoreforming of sugar aldoses for H₂-generation

This chapter is based on a manuscript submitted for publication:

K.E. Sanwald, T.F. Berto, W. Eisenreich, O.Y. Gutiérrez, A. Jentys, J.A. Lercher, Overcoming the rate-limiting reaction during photoreforming of sugar aldoses for H₂-generation, *submitted*.^a

3.1 Abstract

Photoreforming of sugars on metal-loaded semiconductors is an attractive process for H₂-generation. However, the reaction proceeds only with rapidly decreasing rates. We identified that this decrease is due to kinetic constraints rather than to catalyst deactivation. Thus, the nature of the rate-limiting reaction was elucidated by investigation of the reaction pathways and oxidation mechanisms during photoreforming of sugar aldoses on TiO₂ decorated with Rh, Pd or Pt. Using selective isotope labelling it is shown that ring opening of aldoses *via* direct hole transfer to the chemisorbed oxygenates yields primary formate esters. Under pH-neutral and acidic conditions, formates convert to the consecutive aldose intermediate through light-driven, redox-neutral hydrolysis. The slow kinetics of this step, which requires interaction with negative and positive photogenerated charges, leads to blocking of active sites at the photoanode and enhanced electron-hole recombination. Stable H₂-evolution and sugar conversion over time is achieved through alkalization of the aqueous-phase due to fast OH⁻-induced hydrolytic cleavage of formate intermediates.

^a K.E.S. planned, designed and conducted the experiments (unless otherwise noted in the acknowledgements section), analyzed and interpreted the data and wrote the manuscript. T.F.B., O.Y.G., A.J. and J.A.L. contributed to the discussion of the results and the correction of the manuscript anytime. W.E. programmed the pulse sequences applied in the quantitative NMR measurements and proofread the manuscript.

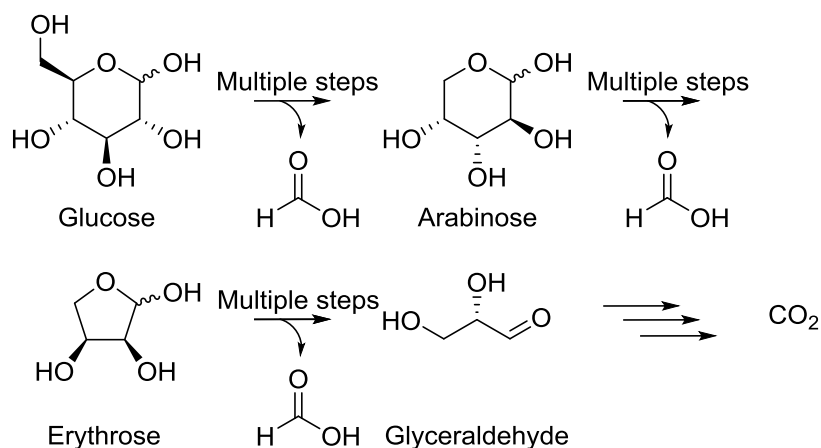
3.2 Introduction

Photoreforming of biomass-derived oxygenates is an attractive concept for photocatalytic H₂-generation. While evolving H₂ at the cathode, the process would allow in parallel the purification of diluted wastewater streams, if total oxidation to CO₂ is achieved in the anodic half-reactions [1-4]. Oxidative conversion of sugar aldoses such as glucose by photoreforming is particularly attractive, as these intermediates from biomass processing constitute cheap and abundant feedstocks [5]. Previous studies of glucose oxidation on TiO₂-based photocatalysts showed that the main reaction pathway proceeds *via* sequential removal of formic acid to form the consecutive C₁-deficient C_{n-1} aldose (Scheme 3.1) [6, 7]. However, neither full oxidation to CO₂ nor quantitative transformation of glucose to organic intermediates could be achieved thus far. This is associated to strongly decreasing H₂-evolution rates over time, independent of the nature of the H₂-evolution co-catalyst applied [8-10]. Such behavior is not observed for other classes of oxygenates, e.g. C₁-C₃ polyols and corresponding linear aldoses and ketoses [11, 12]. Thus, particular anodic transformations in the oxidation chemistry of glucose and sugar aldoses (cyclic hemiacetals) negatively affect overall photocatalytic rates.

Oxidation of oxygenated hydrocarbons during photoreforming proceeds *via* direct hole transfer to the chemisorbed oxygenate or *via* an indirect mechanism mediated by oxygen-centered radicals (generated on hole trapping at surface oxygen lattice sites). These mechanisms give rise to different reaction pathways, i.e. C-C bond cleavage and formation of carbonyl moieties from OH-groups [11, 12]. The selectivity to each pathway depends on the adsorption of the oxygenate [11-14].

In order to achieve maximum quantum efficiencies and H₂-evolution rates it is thus of primary importance to unravel the origin of the slow kinetics *via* a molecular level description of the reaction pathways and oxidation mechanisms during sugar aldose photoreforming. This understanding is also critical for photoreforming of other biomass surrogates, e.g. C₄₍₊₎ polyols, where sugar aldoses are formed as intermediates [12].

Therefore, we have studied photoreforming of glucose and its corresponding pentose and tetrose intermediates on a TiO₂ P 25 semiconductor decorated with a noble metal co-



Scheme 3.1. Anodic reaction sequence during photoreforming of glucose. Oxidation of glyceraldehyde to CO_2 is abbreviated and proceeds in an analogous manner *via* consecutive formation of glycolaldehyde, formaldehyde and formic acid as discussed in depth in chapter 2.

catalyst (Rh, Pd, Pt), focusing on a 1 wt.% Rh/ TiO_2 photocatalyst that was described and characterized in detail in chapter 2. We elucidate the general network for the photoreforming of cyclic hemiacetals and identify that selective oxidative ring opening through α -scission yields open-chain formic acid esters, i.e. formate species. Consecutively, formates must undergo a redox-neutral hydrolysis, which is identified as a light-driven reaction, to generate a further aldose intermediate. We pinpoint that formate hydrolysis is the step that constrains photocatalytic rates. Examination of photoreforming kinetics at different solution pH shows that rapid formate hydrolysis occurs in alkaline media enabling stable H_2 -evolution and aldose conversion over time whilst OH^- is available.

3.3 Experimental

3.3.1 Materials

All chemicals were purchased from commercial suppliers and used as provided: Aeroxide® TiO₂ P 25 (Evonik, LOT: 4162092398), rhodium(III) chloride hydrate (Sigma Aldrich, 99.99 % trace metals, 39.0 % Rh), H₂PtCl₆ solution (Alfa Aesar, 20 wt.% Pt), PdCl₂ (Sigma Aldrich, 5 wt.% solution in 10 wt.% HCl), synthetic air (Westfalen), H₂ (Westfalen, 5.0), Ar (Westfalen, 5.0), sulfuric acid (Merck, TitriPur, 0.5 M), sodium hydroxide (Sigma-Aldrich, ≥ 98 %, anhydrous), borate buffer solution (VWR, TITRINORM, pH 9), methanol (Sigma-Aldrich, 99.8%, anhydrous), methyl formate (Sigma Aldrich, anhydrous, 99 %), formaldehyde solution (Fluka, 1000 µg mL⁻¹ in H₂O, IC Standard), ethanol (European Reference Materials, 80 mg 100 ml⁻¹), ethylene glycol diformate (BOC Sciences), glycolic acid (Sigma-Aldrich, 99 %), glycerol (Sigma-Aldrich, ≥99.5 %), D-glyceraldehyde (Sigma-Aldrich, > 98 %), dihydroxyacetone (Merck, ≥ 98 %), meso-erythritol (Alfa Aesar, 99 %), D-erythrose (Omicron Biochemicals, 99 %, aqueous solution), L-arabitol (Sigma-Aldrich, ≥ 98 %), D-arabinose (Sigma-Aldrich, ≥ 98 %), D-sorbitol (Sigma-Aldrich, 99 %), D-glucose (Sigma-Aldrich, ≥ 99.5 %), D-fructose (Sigma-Aldrich, ≥ 99 %), D-[1-²H]erythrose, D-[1-²H]arabinose, D-[1-²H]glucose (Omicron Biochemicals, 99 %, 98 atom-% ²H), D-[1-¹³C]glucose (Sigma Aldrich, 99 atom-% ¹³C), glyoxal trimer dihydrate (Fluka, ≥ 95 %), phloroglucinol (Sigma Aldrich, ≥ 99 %), D₂O (Euriso-Top, 99.85 atom-%), DCl (Acros Organics, 1 M in D₂O, 99.8 atom-%). Aqueous solutions used in photocatalyst synthesis, photoreforming experiments and for derivatization of reactor aliquots for liquid-phase analysis were prepared in ultrapure water (18.2 MΩ cm, Werner Reinstwassersysteme).

3.3.2 Photocatalyst preparation

AEROXIDE® TiO₂ P 25 hereafter referred to as TiO₂ was loaded with 1 wt.% of either Rh, Pd or Pt by incipient wetness impregnation with aqueous solutions containing appropriate amounts of either RhCl₃·xH₂O, PdCl₂ (adjusted to pH 1 with HCl) or H₂PtCl₆. TiO₂ was dried at 473 K for 2 h prior to impregnation. The impregnated materials were exposed to flowing synthetic air (383 K, 1 h, 100 mL min⁻¹, 5 K min⁻¹) and subsequently heated to 623 K

(100 mL min⁻¹, 5 K min⁻¹) for 1 h. After naturally cooling to room temperature heat treatment in H₂ at 623 K (100 mL min⁻¹, 5 K min⁻¹) was applied for 1 h.

3.3.3 Photocatalytic test

Photoreforming experiments

All photoreforming experiments were conducted in a top-irradiation photo-reactor made of Pyrex with *online* gas- and liquid-phase sampling that was connected to a closed gas-circulation system [12]. Irradiation was provided by a 300 W Xe lamp with a cold mirror 1 (CM1) and a water filter enclosed within quartz windows. The photon flux inside the reactor at water level using this configuration is $8.08 \cdot 10^{17} \text{ s}^{-1}$ ($\lambda < 390 \text{ nm}$). Alternatively, high power UV LEDs (Nichia NC4U133A, 365 nm \pm 5 nm) that were tuned in intensity from $1.16 \cdot 10^{18} \text{ photons s}^{-1}$ to $3.46 \cdot 10^{18} \text{ photons s}^{-1}$ were applied.

Typically, 75 mg of photocatalyst were ultrasonically dispersed in 100 mL of a 20 mM aqueous reactant solution. Four consecutive evacuation and Ar filling cycles were conducted in order to deaerate the system. All reactions were carried out at 288 K and an Ar pressure of 1 bar.

Online analysis of gaseous species evolving *via* gas chromatography (Shimadzu, GC 2010 Plus) on a Chromosorb 101 and a Molsieve 5 Å column with a TCD, FID and a methanizer catalyst unit was applied using Ar as a carrier gas.

Aliquots from the photocatalyst suspension were collected regularly using a sample valve. Photocatalyst separation was done by filtering through 0.2 μm nylon filters. Aqueous-phase species were analyzed by quantitative ¹H-NMR spectroscopy.

¹H-NMR analysis

For quantitative ¹H-NMR measurements reactor aliquots were mixed with an equal volume of a 20 mM 1,3,5-trihydroxybenzene solution in D₂O adjusted to pH 3 with DCI that served as an internal standard. For experiments with initial pH values of the reaction media adjusted to pH 12, pH 12.2 and pH 12.5, respectively, standard solutions with pH 2 or pH 1.5 in the latter two cases were applied and added immediately after sampling from the reactor to preserve sample composition. An Avance III HD 500 System (Bruker Biospin,

Rheinstetten, Germany) with an UltraShield 500 MHz magnet (11.75 T) and a BBI 500 S2 probe head (5 mm, inverse $^1\text{H}/\text{X}$ with Z-gradient) at 305 K was used to record ^1H -NMR spectra with water signal suppression. The resonance frequency of ^1H was 500.13 MHz. The one-dimensional NOESY sequence from the Bruker library 'noesygppr1d' with presaturation of the residual water signal during the relaxation delay and the mixing time using spoil gradients was used for spectra acquisition. The inversion recovery pulse method was applied for determination of longitudinal relaxation times (T_1). Acquisition time and relaxation delay (4.1 s and 26 s, respectively) were chosen such that the sum of the latter is at least equal or greater than three times T_1 of the slowest relaxing ^1H -nucleus (formic acid) in order to satisfy requirements for quantification. 64 or 128 scans, with 64 k data points were collected. Chemical shifts were referenced to the internal standard (SI-Table 3.1). Spectra of commercial references recorded under identical conditions were used for identification of liquid-phase species. Integrated signal intensities that were used for quantification were further calibrated against home-prepared standard solutions in order to account for signal damping due to the water-suppression in close proximity to the water resonance frequency. Further details regarding data processing and analysis procedures were described in detail in refs. 11 and 12 before.

^{13}C -NMR analysis

^{13}C -NMR measurements were conducted at 300 K on an Avance III 500 System (Bruker Biospin, Rheinstetten, Germany) with an UltraShield 500 MHz magnet (11.75 T) and a Cryo-QNP probe head (5 mm, direct $^{13}\text{C}/^{31}\text{P}/^{29}\text{Si}/^{19}\text{F}$ with Z-gradient). Reactor samples were derivatized with equal volumes of D_2O adjusted to pH 3 with DCl. The resonance frequency of ^{13}C was 125.07 MHz. The spectra were acquired using the one-dimensional 'zgpg' sequence from the Bruker library using waltz16 ^1H -decoupling and a 30° ^{13}C -pulse. Relaxation delay and acquisition time were set to 4 s and 1.2 s, respectively. 1024 scans with 64 k data points were collected. Spectra were manually phased and background corrected after application of an exponential window function with a line broadening of 1 Hz prior to Fourier transformation. For signal assignment on the basis of the chemical shifts spectra of commercial references were recorded under identical conditions.

NMR titration experiments

Rate constants for homogeneous acid-catalyzed hydrolysis of formate species were estimated following their concentration by continuous acquisition of quantitative ^1H -NMR spectra at 288 K using the procedures described above. Reactor aliquots taken after 12 h of reaction during photoreforming of different oxygenates were acidified with appropriate amounts of DCl in D_2O and adjusted to pH 1, 1.25, 1.5 and 2. In a separate set of experiments reactor aliquots were added to borate buffer solution (pH 9). The concentration of D_2O was set to 10 Vol.% in all samples.

3.3.4 Physicochemical characterization

N_2 -physisorption isotherms for determination of specific surface areas according to the Brunauer-Emmett Teller (BET) method were recorded at 77 K on a PMI automated BET sorptometer. Prior to measurements, the sample was outgassed at 523 K for 20 h.

Powder X-ray diffraction (XRD) patterns were collected on a Philips X'Pert-1 XRD powder diffractionmeter using Cu-K_α radiation.

Atomic absorption spectroscopy (AAS) on a Thermo Scientific – SOLAAR M Series AA spectrometer was used to determine co-catalyst loadings.

H_2 -chemisorption measurements were conducted at 313 K after activation in H_2 at 573 K for 3 h for determination of mean metal particle sizes. Adsorption isotherms were measured from 1 to 15 kPa, before and after outgassing at 313 K for 1 h, respectively. Physisorbed H_2 was accounted for by subtracting the second isotherm from the first one. The subtracted isotherm was extrapolated to zero pressure in order to determine the amount of chemisorbed H_2 . Mean metal particle sizes were determined assuming hemispherical particle shape and one H-atom chemisorbed per metal surface atom. Note that formation of Pd-hydride species can be excluded under these conditions [15, 16].

Optical band gaps were determined *via* diffuse-reflectance UV-Vis spectroscopy on an Avantes Avaspec 2048 spectrometer equipped with a reflection probe (FCR-7UV200-2-ME) and a home-made sample holder.

In situ X-ray absorption near-edge structure (XANES) measurements at the Rh K-edge, Pd

K-edge and Pt L₃-edge were carried out at ESRF beamline ID26 and DESY beamline P65 (both storage rings were operated at 6 GeV, with ring currents about 90 mA in top-up mode) using a Si(311) double crystal monochromator detuned to about 60 % of the maximum intensity in order to suppress the reflections at higher order. Spectra were obtained in fluorescence mode at room temperature using a silicon drift detector (ID26) or a passivated implanted planar silicon (PIPS) detector (P65). After an energy calibration using the edge position of the corresponding metal foils the scattering background was removed and the data were normalized to an edge step height of one absorption unit. Data analysis was carried out with Athena software from the IFEFFIT package.

The photocatalysts were studied in the as-prepared state in flowing Ar and after thermal reduction in flowing H₂ (5 Vol.% in He, 5 mL min⁻¹, 250 °C, 5 K min⁻¹, 1 h). The reference compounds were diluted 1:10 (by mass) with boron nitride. For all samples about 2 mg of powder were packed into quartz capillary reactors (2 mm diameter, 0.02 mm wall thickness, Hilgenberg), fixed with quartz wool plugs and connected to gas in- and outlets as described in detail in ref. 17. Heating was provided from below by a hot air gas blower (FMB Oxford).

Liquid-phase measurements were conducted by immersing 2 mg of photocatalyst powder in 0.5 mL of liquid (either pure H₂O or 20 mM aqueous glucose solution) in a quartz NMR tube (5 mm diameter, 0.04 mm wall thickness, Norell) closed with a J Young valve. The cell was deaerated by consecutive evacuation and Ar filling cycles using a Schlenk line. After examination of the samples under dark conditions (absence of irradiation) illumination was provided for 20 min by a 200 W Hg(Xe)-lamp equipped with a water filter kept at 303 K. Due to the limited penetration depth of UV irradiation into TiO₂ (approximately up to a few μm [18-20]) the powders were dispersed in the aqueous-phase during illumination by vigorous shaking of the tubes in order to assure that all particles were absorbing UV radiation. Before the X-ray spectra were collected the powder samples were re-settled in the quartz tubes.

3.4 Results and discussion

3.4.1 On the oxidation state of the co-catalysts

The physicochemical characterization of the photocatalysts is compiled in section 3.8 (SI-Table 3.2). We have examined the electronic state of the noble metal (Rh, Pd, Pt) co-catalyst decorating TiO_2 *in situ* aiming at the characterization of the active state of the metal under H_2 -evolution conditions. Spectra at the Rh K-edge recorded under dry (as-prepared and after reduction in H_2) and liquid-phase conditions and associated reference spectra are depicted in Fig. 3.1. The corresponding data for the Pd/ TiO_2 and Pt/ TiO_2 photocatalyst are shown in Figs. 3.2 and 3.3.

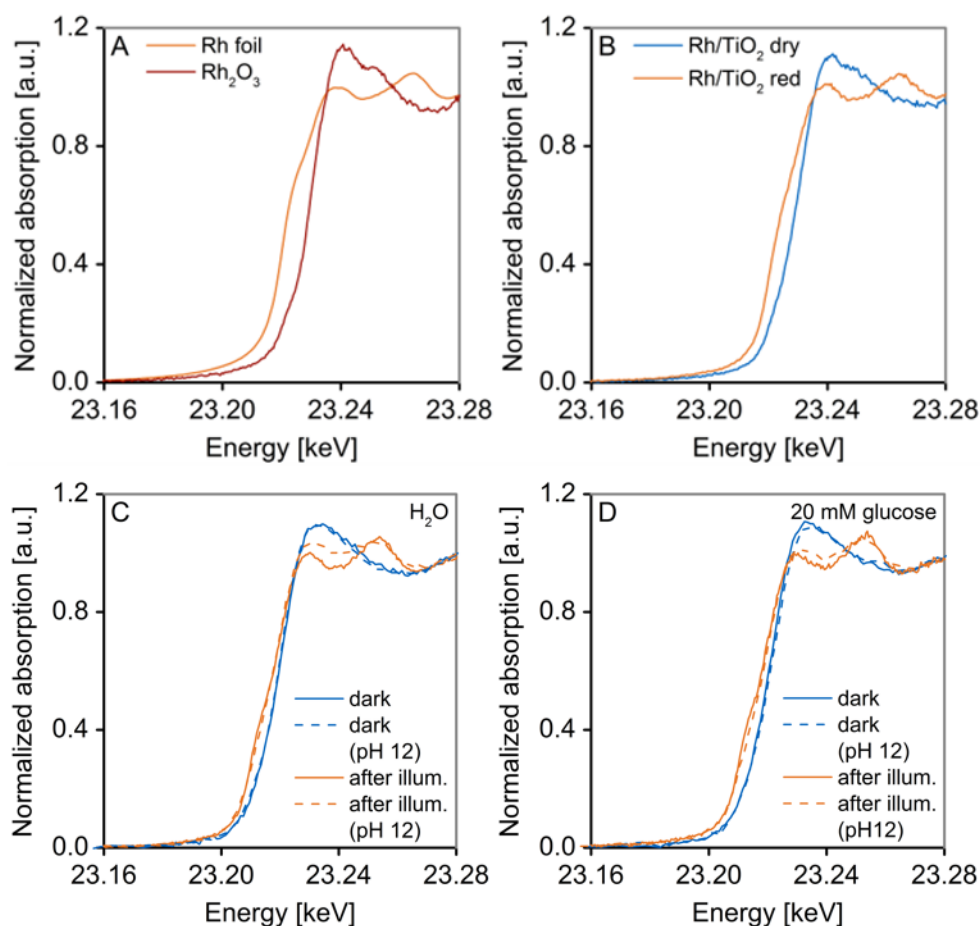


Figure 3.1. Rh K-edge XANES of a Rh/ TiO_2 photocatalyst. (A) Reference spectra. (B) As-prepared, dry state and reduced sample after heat treatment in H_2 . (C) Catalyst immersed in liquid H_2O or aqueous NaOH (pH 12) before and after UV-Vis illumination. (D) Catalyst immersed in aqueous glucose (pH unadjusted or pH 12 with NaOH) before and after UV-Vis illumination.

Rh was present in its oxidic form in the dry catalyst, as deduced from the similarity to the spectrum of Rh_2O_3 , likely due to re-oxidation upon exposure to air after preparation. Complete reduction to the metal was achieved upon heat treatment in H_2 (Fig. 3.1B).

The as-prepared Rh/TiO_2 photocatalyst retained its oxidic state upon immersion in H_2O under anaerobic conditions. However, after irradiation with UV-Vis quantitative transformation to metallic Rh was observed (Fig. 3.1C). As the H_2 -evolution activities of TiO_2 -based photocatalysts in H_2O (in the absence of oxygenated hydrocarbons) are very poor, the reduction of Rh oxide species upon band gap irradiation indicates that co-catalyst reduction originates directly from photogenerated electrons rather than from photogenerated H_2 .

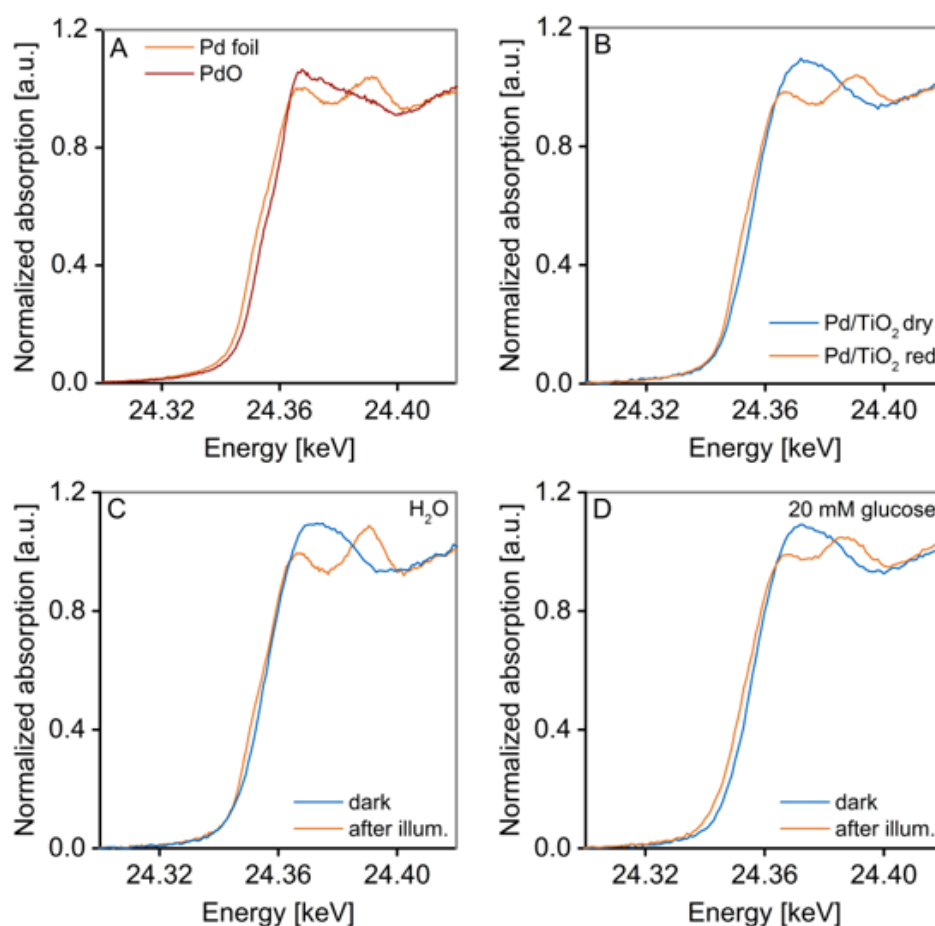


Figure 3.2. Pd K-edge XANES of a Pd/TiO_2 photocatalyst. (A) Reference spectra. (B) As-prepared, dry state and reduced sample after heat treatment in H_2 . (C) Catalyst immersed in liquid H_2O before and after UV-Vis illumination. (D) Catalyst immersed in aqueous glucose before and after UV-Vis illumination.

Similar findings were obtained upon changing the pH to 12 by NaOH, while the differences in the spectra obtained after illumination indicate the presence of a minor fraction of oxidic Rh species. Linear combination fitting using fully reduced Rh/TiO₂ and Rh₂O₃ as standards suggests the presence of a small fraction of Rh₂O₃ in the order of a few percent remaining in alkaline milieu. In the presence of glucose, reduction of RhO_x was solely encountered after illumination (Fig. 3.1D), which provides evidence that the oxygenate is not capable of acting as a reducing agent under these conditions.

This observation is in line with absence of chemical reactivity and corresponding glucose oxidation products under dark conditions in kinetic photoreforming experiments (*vide infra*). In addition, XANES of Pd/TiO₂ and Pt/TiO₂ (Figs. 3.2 and 3.3) displayed quantitative transformation to the metallic species upon illumination in H₂O and aqueous glucose.

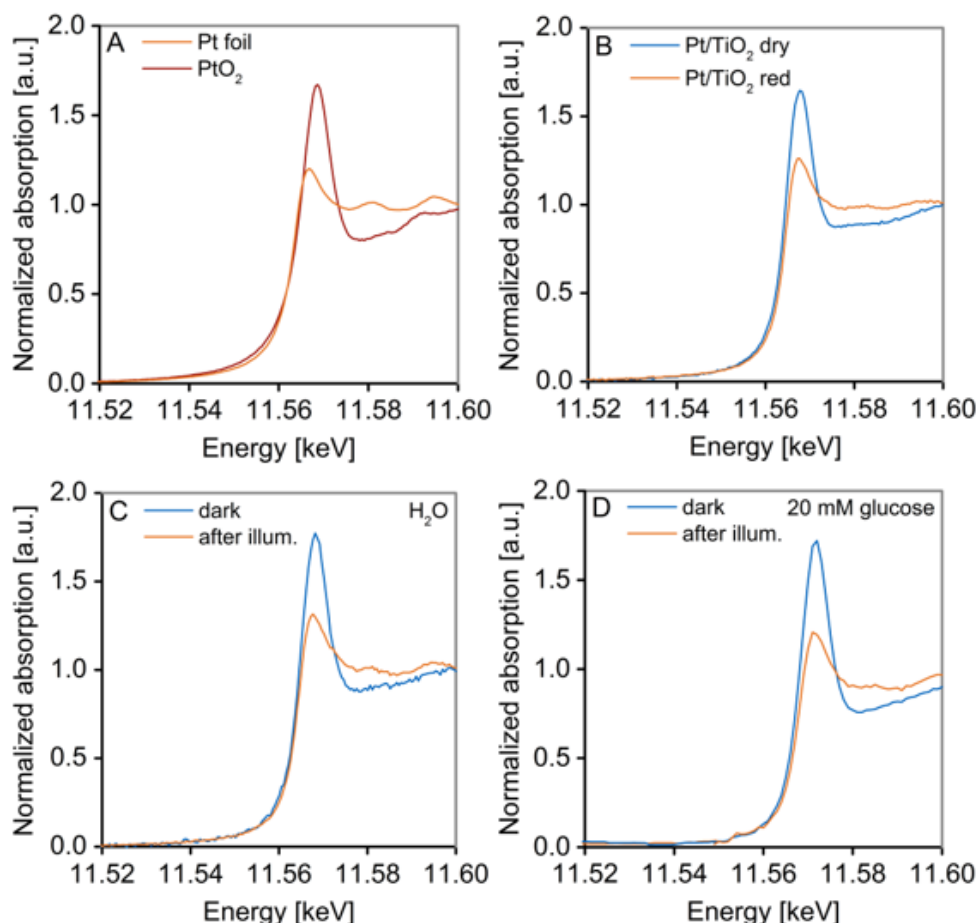


Figure 3.3. Pt L₃-edge XANES of a Pt/TiO₂ photocatalyst. (A) Reference spectra. (B) As-prepared, dry state and reduced sample after heat treatment in H₂. (C) Catalyst immersed in liquid H₂O before and after UV-Vis illumination. (D) Catalyst immersed in aqueous glucose before and after UV-Vis illumination.

Previously, partial photoreduction was reported to take place on a fluorinated Pt/TiO₂ catalyst during gas-phase photoreforming of methanol, which remained incomplete possibly due to the limited penetration depth of the UV light into the fixed bed configuration applied [21]. Our results clearly evidence that in aqueous-phase the co-catalyst is present in its reduced (metallic) form, which is the (photo)catalytically active state of the co-catalysts under H₂-evolution conditions.

3.4.2 H₂-evolution during sugar photoreforming

The courses of the H₂-evolution rates obtained during photoreforming of erythrose (C₄), arabinose (C₅) and glucose (C₆) as well as glycerol (for comparison) on Rh/TiO₂ are depicted in Fig. 3.4. The H₂-evolution profile for glycerol may be rationalized on the basis of a first-order dependence on concentration [12]. On the other hand, the decrease in rates of aldoses over time became more severe with increasing aldose carbon number. After 12 h, the normalized decreases, compared to initial rates, were 56 % for erythrose, 77 % for arabinose, and 84 % for glucose. At this point, the H₂-evolution rates from erythrose, arabinose, and glucose photoreforming (63 $\mu\text{mol h}^{-1}$, 31 $\mu\text{mol h}^{-1}$, and 23 $\mu\text{mol h}^{-1}$, respectively) were similar or lower than rates featured by photoreforming of compounds weakly interacting with TiO₂ such as formaldehyde or methanol (100 $\mu\text{mol h}^{-1}$, and 40 $\mu\text{mol h}^{-1}$, respectively). Qualitatively similar findings were obtained for photo-

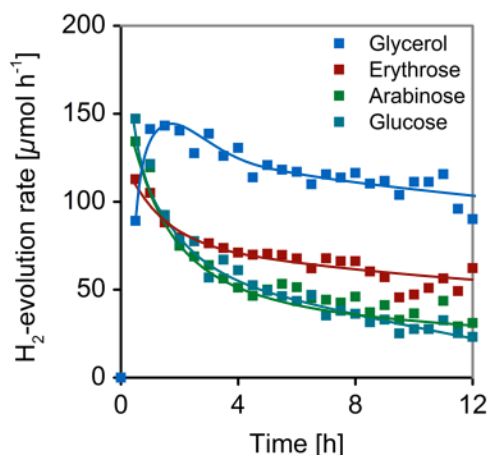


Figure 3.4. Course of H₂-evolution rates during photoreforming of C₄-C₆ sugar aldoles on Rh/TiO₂. The profile for glycerol photoreforming was adopted from ref. 12 and is given for comparison. The pH values of the reaction media after 12 h were 3.9, 3.3, 3.5 and 3.8 in case of glycerol, erythrose, arabinose and glucose, respectively. Reaction conditions: 75 mg photocatalyst, 100 mL aqueous oxygenate solution (20 mM), 288 K, 1 bar Ar, 300 W Xe-lamp (CM1).

reforming of glucose on Pt/TiO₂ and Pd/TiO₂ (SI-Fig. 3.1). Thus, the temporal H₂-evolution declines, independent of the noble metal co-catalyst applied.

The dependence of the initial H₂-evolution rates on photon flux (at 365 nm ± 5 nm) during glucose photoreforming on Rh/TiO₂ (SI-Fig. 3.2) was nearly first-order, which is expected from quasi first-order recombination kinetics, as reported for photoreforming of methanol [22, 23]. In contrast, the H₂-evolution rates after the initial strong decrease (first 9 h) have a dependence on photon flux of approximately square-root. This indicates accelerated electron-hole recombination that is attributed to adsorbed surface species present during sugar photoreforming as described in the following.

In order to assess the origin of the decrease in H₂-evolution rates, we performed glucose photoreforming on Rh/TiO₂ for 5 h; then injected an aqueous solution containing glyoxal (a reagent that strongly interacts with TiO₂) into the reaction medium to establish a glyoxal concentration of 15 mM. On glyoxal injection, the H₂-evolution rates increased from 48 μmol h⁻¹ to 105 μmol h⁻¹ and remained constant for at least 5 h thereafter (SI-Fig. 3.3A). However, the latter rate was still lower than that observed during the photoreforming of glyoxal alone (about 140 μmol h⁻¹). The difference is attributed to competitive adsorption of glucose and its reaction intermediates. An analogous experiment injecting an aqueous solution of RhCl₃·xH₂O resulted in Rh photodeposition on TiO₂ (Rh loading of 1.3 wt.% of spent photocatalyst), which did not cause a noticeable change in the rate of H₂-evolution (SI-Fig. 3.3B).

These observations led to the conclusion that the cathodic half-reaction does not limit the overall photocatalytic rates under these conditions, i.e. the H₂-evolution functionality is fully retained during photoreforming of C₄-C₆ aldoses. The constraints in photocatalytic rates are, therefore, concluded to be associated to strongly adsorbed species (that are partially displaced by glyoxal), which undergo slow consecutive oxidation on TiO₂, resulting in enhanced electron-hole recombination.

3.4.3 Anodic reaction pathways

Analysis of the species generated from the anodic half-reactions during glucose photoreforming on Rh/TiO₂ is presented in Fig. 3.5 (see SI-Figs. 3.4 and 3.5 for erythrose and arabinose and SI-Figs. 3.6 and 3.7 for glucose photoreforming on Pt/TiO₂ and

Pd/TiO₂, respectively). The reaction products comprised of a homologous series of lower aldehydes, i.e. arabinose (C₅), erythrose (C₄), glyceraldehyde (GAD, C₃), glycolaldehyde (C₂), and formaldehyde (C₁), in decreasing amounts with decreasing carbon number, along with formic acid and major quantities of CO₂. Photoreforming reactions with arabinose (C₅) and erythrose (C₄) yielded erythrose (C₄) and GAD (C₃) as primary products, respectively, accompanied by species from their consecutive oxidations. Consequently, we conclude that a common reaction pathway is shared by these reactants. Oxidation of aldoses to carboxylic acids prior to C-removal or phototautomerism is not observed under these conditions. The quantities of the products indicate that a C_{n-1} aldose/aldehyde is generated from its C_n parent compound in a sequential manner to finally yield

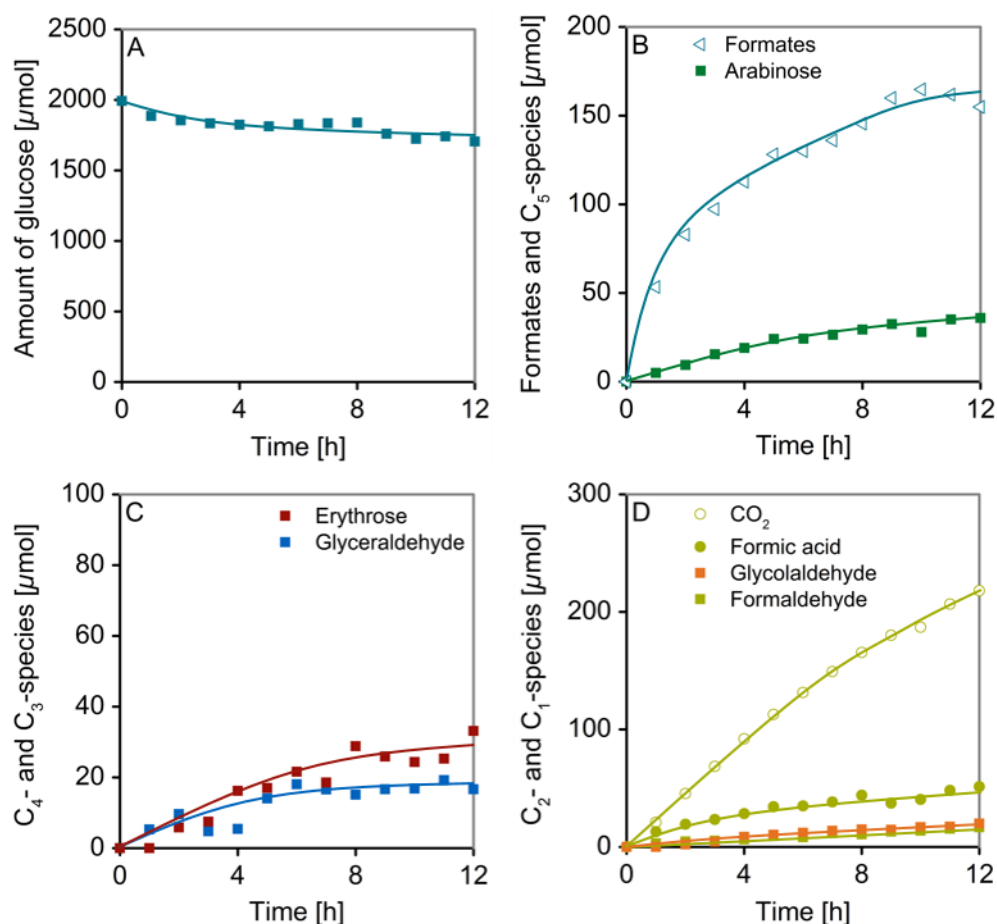


Figure 3.5. Temporal profiles of anodic reaction products formed during photoreforming of glucose on Rh/TiO₂. (A) Course of amount of glucose. Course of formates and C₅- (B), C₄-/C₃- (C) and C₂-/C₁-species (D) generated. The reaction medium exhibited a pH of 3.8 after 12 h reaction time. Reaction conditions: 75 mg photocatalyst, 100 mL aqueous glucose solution (20 mM), 288 K, 1 bar Ar, 300 W Xe-lamp (CM1).

formaldehyde. From the amounts of CO₂ and formic acid formed we deduce that, as in the case of linear C_n aldoses [11, 12], formic acid is the C₁ moiety cleaved in each step as shown in Scheme 3.1.

C₄-C₆ aldoses primarily exist as cyclic hemiacetals (equilibrium compositions of aqueous aldose solutions are given in SI-Table 3.3). While glucose and arabinose are exclusively present as cyclic hemiacetals in aqueous-phase (glucose existing in two anomeric pyranose forms), arabinose (4 % furanose) and erythrose (12 % linear open-chain form) show contributions of further diastereomers consistent with the analysis of the NMR data. Due to their cyclic structure, C₄-C₆ aldoses (unlike linear C₁-C₃ aldoses) react in multiple steps (*vide infra*) during their anodic conversion to the next C_{n-1} aldose (Scheme 3.1).

Besides aldoses/aldehydes, photoreforming of C₄-C₆ aldoses on Rh/TiO₂ produced compounds with multiple ¹H-NMR singlet signals with chemical shifts similar to formic acid (¹H: 8.19 ppm) at 8.12 - 8.25 ppm as shown in Fig. 3.6 (see SI-Fig. 3.8 for spectra obtained after glucose photoreforming on Pt/TiO₂ and Pd/TiO₂). Corresponding ¹³C-NMR signatures with chemical shifts of 162.5 - 163.1 ppm (formic acid ¹³C: 166.3 ppm) were observed during photoreforming of [1-¹³C]glucose on Rh/TiO₂ (SI-Fig. 3.9). These observations agree well with the formation of formic acid ester (formate) species (Scheme 3.2, see also ¹H and ¹³C chemical shifts of methyl formate and ethylene glycol diformate in SI-Table 3.1). Formates were identified during photoreforming of cyclic hemiacetals (Fig. 3.6A-C) and in the reactions of the corresponding C₄-C₆ polyols (Fig. 3.6D), wherein cyclic hemiacetals form as intermediates [12]. Thus, the generation of formates is directly related to the presence of cyclic hemiacetal structures. These analogous ¹H- and ¹³C-NMR signatures are absent during photoreforming of linear C₃ oxygenates (e.g. glycerol, Fig. 3.6D). If formed, multiple formate species are identified, i.e. three from erythrose, at least eight from arabinose and glucose photoreforming in quantities larger than 0.5 μmol (approximate detection limit). Their ¹H-NMR chemical shifts are listed in SI-Table 3.4. Deconvolution of the formate peaks into the contributions of the individual signals are compiled in SI-Fig. 3.10. ¹H-NMR signals after photoreforming on Rh/TiO₂ for erythrose-derived formates (total amount of 82 μmol after 12 h) appeared among the formates generated during arabinose (37 μmol in total after 12 h) and glucose photoreforming (total amount of 155 μmol after 12 h), which is attributed to the participation of formates in the

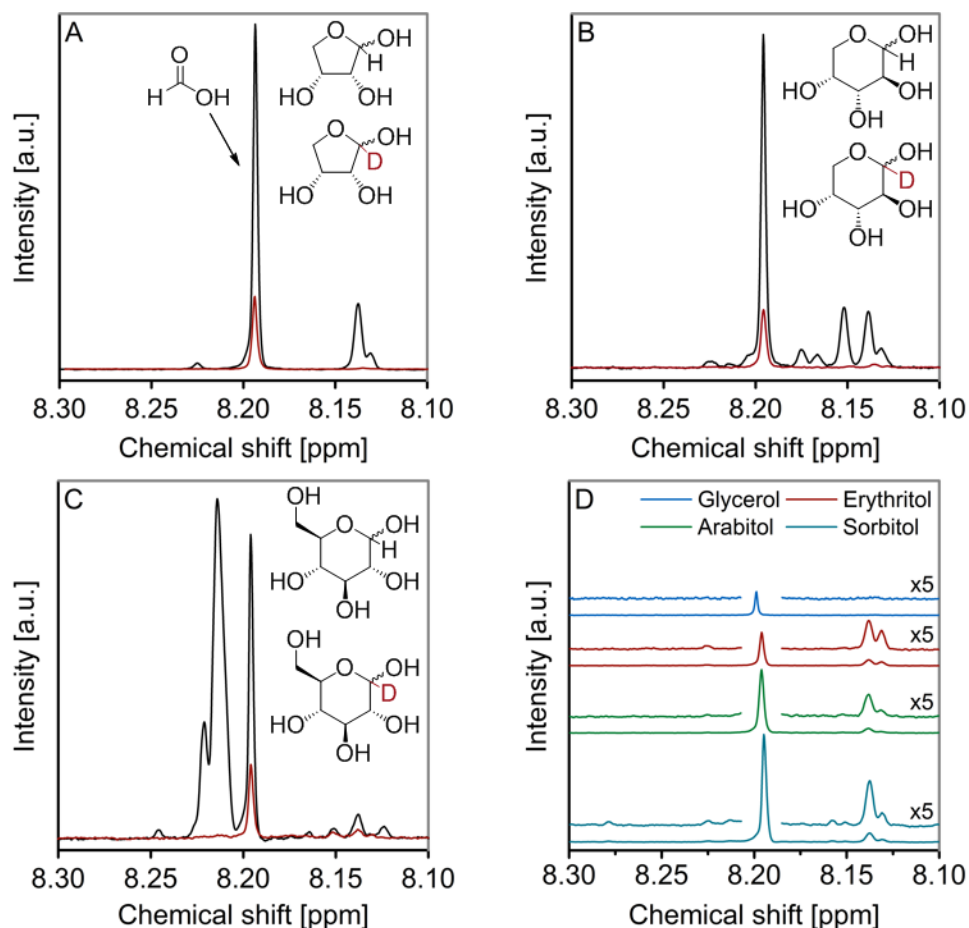
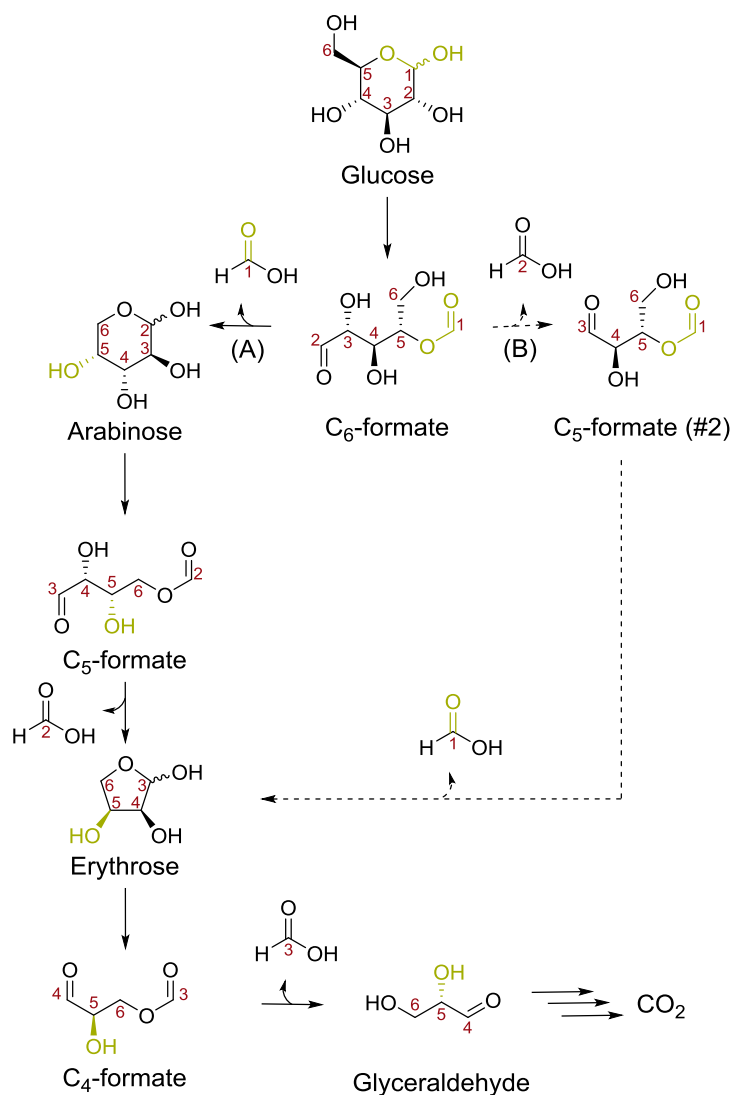


Figure 3.6. Comparison of partial ^1H -NMR spectra of liquid-phase reactor aliquots collected after 12 h for different photoreforming reactions on Rh/TiO_2 . (A) Erythrose (black) and $[1\text{-}^2\text{H}]$ erythrose (red). (B) Arabinose (black) and $[1\text{-}^2\text{H}]$ arabinose (red). (C) Glucose (black) and $[1\text{-}^2\text{H}]$ glucose (red). (D) $\text{C}_3\text{-C}_6$ polyols.

common reaction pathway interconverting these intermediates. For glucose photoreforming on all catalysts, the total amount of formates (derived from the ^1H -NMR signals at 8.21 ppm and 8.22 ppm) clearly exceeded the amounts of all other intermediates in the liquid-phase (Fig. 3.5, SI-Figs. 3.6 and 3.7). These formate species were only observed during glucose and arabinose photoreforming. Thus, the highest accumulation of formate species in liquid-phase (Fig. 3.5, SI-Figs. 3.4-3.7) during glucose photoreforming coincided with the most pronounced decline in H_2 -evolution rates.

Photoreforming experiments with isotope labelled compounds deuterated at the anomeric carbon atom, i.e. D - $[1\text{-}^2\text{H}]$ -erythrose, D - $[1\text{-}^2\text{H}]$ arabinose and D - $[1\text{-}^2\text{H}]$ glucose, were performed on Rh/TiO_2 . Comparison of the ^1H -NMR spectra obtained after 12 h of reaction



Scheme 3.2. Proposed anodic reaction pathways for photoreforming of C₄-C₆ cyclic hemiacetals. Initially, α -scission of the cyclic hemiacetal leads to the formation of formate species. Consecutive formate conversion is proposed to proceed through hydrolysis to the corresponding C_{n-1} aldose (A) or oxidative C-C-cleavage to generate another formate (B). Starting from arabinose- and erythrose-derived formates further pathways *via* oxidative C-C-cleavage analogous to oxidation of C₆-formate *via* Path (B) appear conceivable. The latter transformations have been omitted for simplicity.

time (Fig. 3.6) with labeled and unlabeled reactants showed almost complete disappearance of all formate related signals upon deuteration. We conclude, therefore, that anodic transformations of cyclic hemiacetals proceed through α -scission, i.e. a selective ring-opening by oxidative cleavage of the C1-C2 bond following the numbering sequence in glucose of Scheme 3.2. The presence of the vicinal ring oxygen atom leads

to the generation of an open-chain formate species upon α -scission with the ^2H -label at the ester carbonyl carbon in case of a [$1\text{-}^2\text{H}$] labelled aldose (e.g. C1 in C_6 -formate, C2 in C_5 -formate and C3 in C_4 -formate in Scheme 3.2). The detection of formate signatures in ^{13}C -NMR spectra during photoreforming of [$1\text{-}^{13}\text{C}$]glucose (SI-Fig. 3.9) further confirms this reaction pathway.

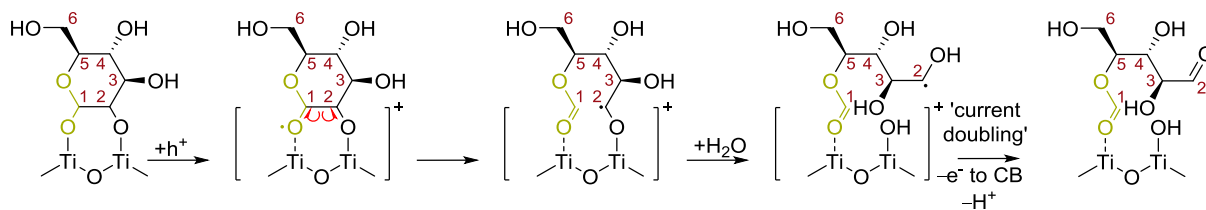
The ^1H -NMR spectra recorded after reaction of the deuterated compounds showed a contribution of the NMR-silent deuterated formic acid, evident in the reduction in intensity of the formic acid signals at 8.19 ppm (Fig. 3.6). The amounts of all other intermediates remained unaffected upon deuteration. The presence of deuterated formic acid suggests that anodic transformation of formates involves the cleavage of the ester formyl moiety to release formic acid (Scheme 3.2, e.g. reactions of C_6 -formate to arabinose or C_5 -formate to erythrose).

Generation of a C_{n-1} cyclic hemiacetal *via* oxidative ring-opening of a C1 deuterated C_n cyclic hemiacetal followed by removal of the ester formyl group (e.g. formation of arabinose and erythrose from glucose and arabinose, respectively) would result in the disappearance of the ^1H -NMR formate signals only in the primary formate (e.g. C_6 -formate from glucose, Scheme 3.2, Fig. 3.6). Signals of formate species derived from C_{n-1} and C_{n-2} cyclic hemiacetal intermediates would remain visible. In the experiments reported here, formate signatures disappeared almost completely (Fig. 3.6). Thus, pathways for C_n formate conversion to additional formates are concluded to exist, competing with ester formyl group removal, where the [^2H] labeled C1 remains in the formate molecule. The oxidative C-C-scission from the formate chain (i.e. the cleavage of C2 from the C_6 -formate, Scheme 3.2, Path (B)) is a likely pathway and consistent with transformations of linear aldoses during photoreforming [6, 11, 12, 24]. The low concentration of non-deuterated formate species in the isotope experiments suggests that Path (B) occurs faster than hydrolysis and these C-C scission routes may account for the presence of several formate species formed in low quantities (Scheme 3.2, SI-Fig. 3.10). However, the importance of the latter formates for the overall glucose photoreforming process is considered to be minor (*vide infra*). Note that hydrolysis and oxidative C-C-cleavage (Scheme 3.2) are consistent with the stereochemical configurations in the sequence glucose, arabinose, erythrose and do not require involvement of further aldose diastereomers.

3.4.4 Mechanistic considerations

Density functional theory (DFT) studies of the structure of adsorption complexes of glucose on anhydrous anatase (101) showed that a bidentate mode of adsorption *via* vicinal OH-groups to generate bridging $[\text{Ti}\cdots\text{O}\cdots\text{C}]$ is most stable [25, 26]. A configuration involving the OH-groups at C1 and C2 is favored by about 0.2-0.3 eV over configurations involving C2 and C3 or C3 and C4 [25]. This is in agreement with our experimental evidence for selective ring-opening through α -scission. Such surface complexation results in the creation of intra gap states, thus, satisfying thermodynamic conditions for trapping of photogenerated holes with the highest occupied electronic states of the adsorption complexes being mainly localized on the adsorbate [25]. Electron paramagnetic resonance (EPR) spectroscopy studies demonstrated that glucose oxidation on photoexcited TiO_2 leads to radical formation at C1, which was attributed to an H-atom loss [27]. Subsequently, a rearrangement was proposed, which leads to the elimination of a formyl moiety from C1 in agreement with our results from selective isotope labelling. Similarly, formate esters were encountered in Malaprade reactions that lead to oxidative C-C scission of vicinal diol units. Periodic acid treatment of glucose resulted in formation of β -formylglyceraldehyde (1-hydroxy-3-oxopropan-2-yl formate), and further formate ester moieties formed from terminal glucose units were identified with polysaccharides [28]. Both cases provide evidence that oxidative rupture of the C1-C2 bond did occur [28].

In summary, we conclude that during photoreforming cyclic hemiacetals are selectively activated, by direct hole transfer to the chemisorbed oxygenate, to undergo α -scission to



Scheme 3.3. Mechanism proposed for anodic ring-opening of glucose to produce a formate species. Direct hole transfer to adsorbed glucose (*via* C1 and C2) leads to an oxygen-centered radical species followed by C-C bond cleavage in β -position to the radical (α -scission of glucose). The resulting carbon-centered radical of the open-chain formate species is hypothesized to undergo a 'current doubling' process, i.e. injection of an electron into the TiO_2 conduction band, to form a C_6 -formate as stable intermediate.

produce the associate formate species as illustrated in Scheme 3.3. An indirect/OH-radical driven pathway, which would yield carbonyl moieties (e.g. oxidation of cyclic hemiacetals to the corresponding lactones) was not observed.

3.4.5 Pathways for formate hydrolysis

The cleavage of formic acid from formate species to generate a C₁-deficient aldose (Scheme 3.2, Path (A)) corresponds to an ester hydrolysis, i.e. the formal addition of water, a redox-neutral step. C-O hydrolysis may be accomplished *via* three pathways under these conditions: (i) homogeneous, acid-catalyzed hydrolysis, (ii) C-O bond hydrolysis catalyzed by TiO₂ and/or the co-catalyst metal, (iii) a light-driven hydrolysis reaction.

We addressed the possible occurrence of the first pathway by calculating the rate constants for acid-catalyzed hydrolysis of the most abundant formate species in the respective photoreforming reactions *via* NMR titration experiments with aliquots collected after 12 h reaction time as described in section 3.3.3. Formate hydrolysis follows a rate-equation with first-order dependence on the formate and on the acid concentration. The resulting first-order rate constants normalized to the acid concentration are compiled in SI-Table 3.5. The values are of similar order as typical rate constants for acid-catalyzed hydrolysis of aliphatic and aromatic acid esters in water near room-temperature ($10^{-4} \text{ L mol}^{-1} \text{ s}^{-1}$) [29]. Extrapolations to the pH-values of the reaction media (3.3, 3.5, and 3.8 for erythrose, arabinose and glucose photoreforming, respectively, after 12 h) and formate concentrations, indicate that maximum formate hydrolysis rates under photoreforming conditions are about $0.1 \mu\text{mol h}^{-1}$. These extrapolated rates are two orders of magnitude too low to account for the amounts of reaction products detected. In consequence, the contribution of homogeneous acid-catalyzed hydrolysis to formate C-O cleavage is insignificant under reaction conditions. Acidification of the solution to pH 1.5 with H₂SO₄ prior reaction to achieve hydrolysis rates of the order of formate formation rates resulted in strongly reduced H₂-evolution (Fig. 3.7). This is attributed to the detrimental effect of competing SO₄²⁻ adsorption [30].

The hydrolysis pathway (ii) was evaluated performing glucose photoreforming with alternating illumination and dark periods on Rh/TiO₂ (SI-Fig. 3.11). If TiO₂- and/or Rh-catalyzed formate hydrolysis would be a dominating pathway, reduction in the formate

amount would be expected during dark periods. Neither a change in the amount of formates nor in the H_2 -evolution rate recovery was observed after dark periods (SI-Fig. 3.11), indicating that hydrolysis did not occur under these conditions. Consequently, we attribute the formate hydrolysis under photoreforming conditions to pathway (iii), a light-driven reaction.

Photocatalytically enhanced hydrolysis on TiO_2 P 25 has been reported for halogenated compounds under anaerobic conditions [31, 32]. Mechanistically, the hydrolysis was attributed to the sequential interaction of the reactant with photogenerated electron and proton, and a photogenerated oxidant (e.g. an OH-radical), i.e. the redox-neutral water association through a redox mechanism. However, in the presence of an electron-accepting co-catalyst, the availability of electrons at the semiconductor surface is expected to be greatly reduced. Thus, reactant interaction with both kinds of photogenerated charges would require either diffusion between cathodic and anodic reaction sites or close proximity of these sites. In either case, the accumulation of formate species, which bear the anomeric carbon atom of the parent aldose points to a slow consecutive hydrolysis, while further formate species are generated through C-C-cleavage of the formate. Thus, we conclude that formates are responsible for blocking of anodic sites, which results in the decline of oxygenate conversion and corresponding H_2 -evolution rates.

3.4.6 Photoreforming of sugar aldoses in alkaline media

To reactively remove formates the rate of hydrolysis needs to be enhanced. It is known that rate constants for alkaline ester hydrolysis can be up to four orders of magnitude larger than for acid hydrolysis [29]. Thus, we hypothesize that photoreforming in alkaline media may overcome the kinetic constraints imposed by the hydrolysis of formate species. In order to test this hypothesis, we conducted glucose photoreforming on Rh/ TiO_2 , adjusting the reaction media to different pH values by addition of NaOH prior reaction. The corresponding courses of H_2 -evolution rates obtained are shown in Fig. 3.7. When starting from pH 11, lower H_2 -evolution rates than without pH adjustment (initial pH of 7.2) were encountered which, however, converged to similar values at long reaction time. This shows a detrimental effect to the H_2 -evolution rates in presence of Na^+ , although

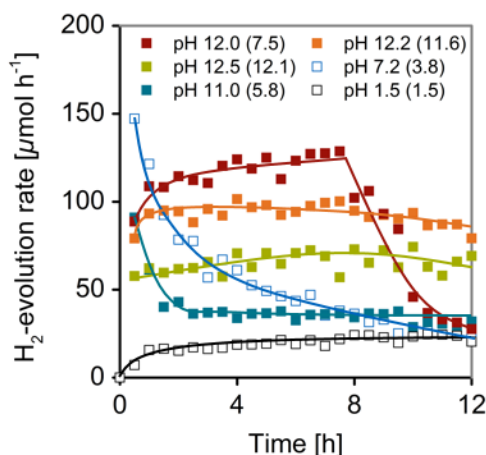


Figure 3.7. Course of H₂-evolution rates during photoreforming of glucose on Rh/TiO₂. Reaction media were adjusted to different initial pH values by addition of H₂SO₄ or NaOH. Blue open squares represent measurement without external alteration of pH. Values in brackets indicate measured pH values after 12 h reaction time. Reaction conditions: 75 mg photocatalyst, 100 mL aqueous oxygenate solution (20 mM), 288 K, 1 bar Ar, 300 W Xe-lamp (CM1).

the concentrations of arabinose and formic acid, which increased in one step at the beginning of the reaction, indicated that hydrolysis of the primary formate from glucose occurred in the early stages of the reaction (SI-Fig. 3.12). The decrease in rates was related to dropping pH, associated with the continuous generation of formic acid, and the concomitant build-up of formates in solution over time (SI-Fig. 3.12).

Adjustment of the reaction medium to initial pH 12 resulted in high and relatively stable H₂-evolution for 8 h with a maximum H₂-evolution rate of 129 μmol h⁻¹ (Fig. 3.7). After this maximum, the rates rapidly declined, which occurred simultaneous to the onset of the concentration of formates in solution (Fig. 3.8). This appearance of formates (absent in the first 9 h of reaction) paralleled the onset of CO₂ in the gas-phase, which was likely dissolved as (bi)carbonate in the alkaline medium. These observations confirm that the presence of formates in solution originates from a drop in pH towards neutral at 8-9 h slowing formate hydrolysis.

Thus, we conclude that in alkaline medium rapid formate hydrolysis occurs, e.g. to form arabinose and formic acid from the C₆-formate (Path (A), Scheme 3.2), thereby irreversibly consuming one equivalent of OH⁻ per hydrolyzed formate in the deprotonation of released formic acid. Formic acid production and OH⁻ consumption gradually lower pH over time.

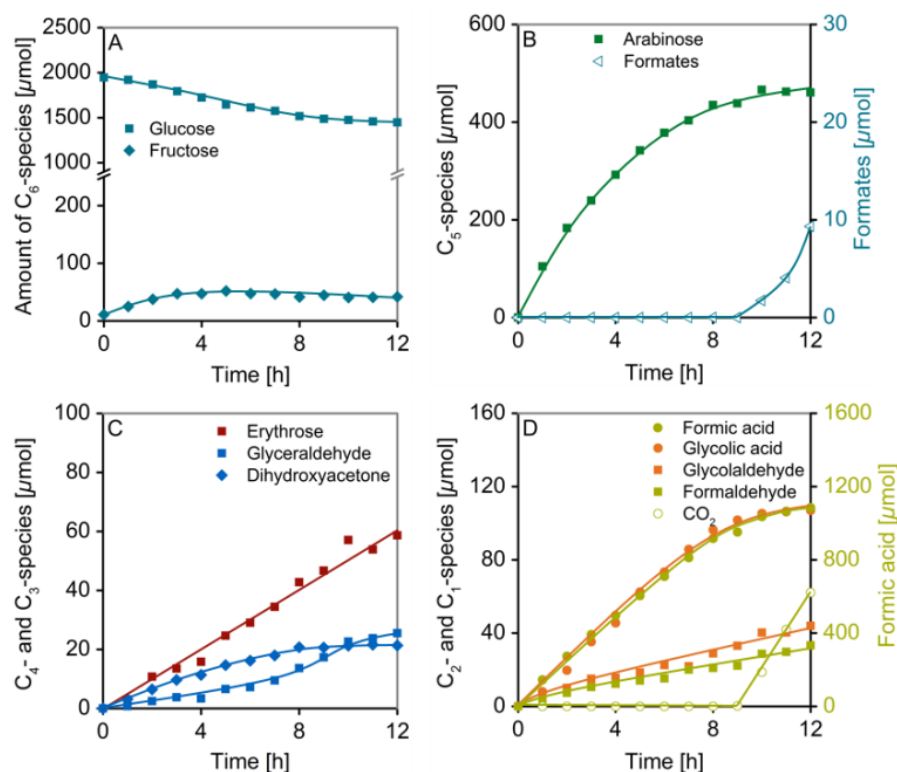


Figure 3.8. Course of anodic reaction products formed during photoreforming of glucose on Rh/TiO₂ with adjustment to pH 12 with NaOH prior reaction (pH 7.5 after 12 h). Course of amount of glucose and fructose (A). Course of formates and C₅- (B), C₄-/C₃- (C) and C₂-/C₁-species (D) generated. Reaction conditions: 75 mg photocatalyst, 100 mL aqueous glucose solution (20 mM), 288 K, 1 bar Ar, 300 W Xe-lamp (CM1).

Establishing initial pH values above 12 enabled stable H₂-evolution over at least 12 h (Fig. 3.7) with continuous conversion of glucose over time independent of the nature of the co-catalyst (SI-Figs. 3.13-3.17), while formate species were absent in solution. However, adjusting such alkaline pH values implied gradually increasing the NaOH concentration, which decreased the rates for H₂-evolution (Fig. 3.7). It follows that controlling the pH during the reaction is mandatory for stable H₂ evolution. This was confirmed by performing the photoreforming of glucose on Rh/TiO₂ in borate buffer at pH 9. Although formate-free conditions and stable H₂-evolution were maintained, the photocatalytic activity was significantly decreased (SI-Fig. 3.18). This is attributed to the intolerance of the photocatalyst towards inorganic salts [30].

Alkalinization may influence the adsorption and charge carrier trapping and increase the density of hydroxyl groups at TiO₂ surfaces during photoreforming [33-37]. Higher

H₂-evolution rates were reported in very concentrated base (5 - 6 M NaOH) compared to pH-neutral/acidic conditions during photoreforming of oxygenates on TiO₂-based photocatalysts [38, 39]. However, we show here that the stabilization of H₂-evolution in alkaline media is predominantly of chemical origin, i.e. occurs through rapid hydrolytic decomposition of formates thereby circumventing the blocking of anodic sites.

In alkaline media, base-catalyzed aldose/ketose tautomerism (Lobry de Bruyn-van Ekenstein rearrangement) was observed in addition to the homologous series of aldoses/aldehydes and formates converting in the main reaction pathways for glucose oxidation (Scheme 3.2). Hence, glucose can be converted through isomerization to fructose (the corresponding ketose) *via* deprotonation of C2 [40]. Accordingly, growing concentrations of fructose were observed with increasing initial solution pH (Fig. 3.8, SI-Figs. 3.12-3.14, maximum of 194 μ mol after 12 h at initial pH 12.5, i.e. 10 % of the initial amount of glucose). Furthermore, similar amounts of fructose were detected after 12 h of glucose conversion in presence and in absence of illumination (194 and 197 μ mol, respectively, SI-Fig. 3.19) at initial pH 12.5. Thus, alkaline induced isomerization is a homogenous reaction step.

Other features of the reaction pathways in alkaline conditions, beyond glucose isomerization, to be highlighted are: (i) the tautomeric transformation of GAD to dihydroxyacetone (DHA, C₃ ketose) [41] and; (ii) the presence of glycolic acid as intermediate, which resulted from C-C cleavage of DHA. Glycolic acid may undergo further oxidation to formaldehyde and CO₂ [12].

In other control experiments, photoreforming of fructose on Rh/TiO₂ proceeded with declining H₂-evolution rates, whereas stabilization of H₂-evolution was observed under basic conditions (SI-Fig. 3.20). Thus, we conclude that increased rates of homogenous reactions involving OH⁻ stabilized the photoreforming of glucose rather than alternative reaction pathways involving fructose as key intermediate.

The main products formed during glucose photoreforming in alkaline milieu are arabinose and formic acid, i.e. the products from hydrolysis of the primary formate. It is, thus, concluded that glucose predominantly converts according to the reaction pathway outlined before (Scheme 3.2, Path (A)) while the addition of OH⁻ did not induce a parallel

OH-radical mediated oxidation pathway. Formic acid and glycolic acid, present as the corresponding carboxylate anions, accumulate in the liquid-phase due to electrostatic repulsion with the negatively charged surface of TiO_2 ($\text{pzc}(\text{TiO}_2 \text{ P } 25) = 6.2$) [42]. The selectivity towards CO_2 (quantitatively present as dissolved (bi)carbonate at $\text{pH} > 9$), which is the product of the oxidation of the acids, occurs therefore only in low amounts. Partial ionization and repulsion of glucose from the TiO_2 surface (pK_a 12.3 [43]), in particular at $\text{pH} > \text{pK}_a$, may additionally contribute to the observed decrease in H_2 -evolution rates with increasing pH .

3.5 Conclusions

During photoreforming, cyclic hemiacetals selectively undergo ring-opening (C-C α -scission) to generate a formate species as primary product *via* direct hole transfer to the associated adsorption complexes. Consecutive light-driven formate hydrolysis to the next lower homologous, i.e. C₁-deficient, aldose/aldehyde is a slow step, as negative and positive charge carriers have to be involved. This leaves C-C cleavage of the intermediate formates to shorter formates as the dominant conversion pathway under pH-neutral and acidic conditions. The slow hydrolysis causes formate accumulation and blocking of anodic reaction sites, leading to enhanced electron-hole recombination. The cathodic half-reaction does not limit the overall photocatalytic rates under these conditions.

Stable H₂-evolution can be achieved, if the OH⁻ concentration in the reaction medium is increased, because rapid hydrolytic cleavage of formates under alkaline conditions prevents their accumulation. In this way, full mineralization of polyols and sugars can be achieved, requiring, however, control of the pH. Beyond this strategy, photocatalysts that allow for alternative activation pathways for cyclic hemiacetals circumventing formate formation, e.g. *via* an indirect oxidation mechanism, and/or means of accelerating light-driven hydrolysis could further enhance efficient photoreforming of sugar aldoses.

3.6 Acknowledgements

K.E.S. gratefully acknowledges financial support by the Fonds der Chemischen Industrie (FCI). The XAFS experiments were performed on beamline ID26 at the European Synchrotron Radiation Facility (ESRF), Grenoble, France and at the light source PETRA III on beamline P65 at DESY, a member of the Helmholtz Association (HGF). We would like to thank Lucia Amidani (ESRF, ID26) and Edmund Welter (DESY, P65) for assistance during the experiments. We are grateful to Xaver Hecht for BET and H₂-chemisorption measurements and Martin Neukamm for AAS measurements. Technical assistance concerning NMR experiments by Christine Schwarz is acknowledged.

3.7 References

- [1] M. Murdoch, G.I.N. Waterhouse, M.A. Nadeem, J.B. Metson, M.A. Keane, R.F. Howe, J. Llorca, H. Idriss, *Nat. Chem.* 3 (2011) 489-492.
- [2] J. Kim, D. Monllor-Satoca, W. Choi, *Energ. Environ. Sci.* 5 (2012) 7647-7656.
- [3] B. You, X. Liu, N. Jiang, Y. Sun, *J. Am. Chem. Soc.* 138 (2016) 13639-13646.
- [4] F. Wang, Y. Jiang, A. Gautam, Y. Li, R. Amal, *ACS Catal.* 4 (2014) 1451-1457.
- [5] L. Zhang, J. Shi, M. Liu, D. Jing, L. Guo, *Chem. Commun.* 50 (2014) 192-194.
- [6] R. Chong, J. Li, Y. Ma, B. Zhang, H. Han, C. Li, *J. Catal.* 314 (2014) 101-108.
- [7] M. Bellardita, E.I. García-López, G. Marci, L. Palmisano, *Int. J. Hydrogen Energ.* 41 (2016) 5934-5947.
- [8] M.R. St. John, A.J. Furgala, A.F. Sammells, *J. Phys. Chem.-US* 87 (1983) 801-805.
- [9] X. Fu, J. Long, X. Wang, D.Y.C. Leung, Z. Ding, L. Wu, Z. Zhang, Z. Li, X. Fu, *Int. J. Hydrogen Energ.* 33 (2008) 6484-6491.
- [10] T. Kawai, T. Sakata, *Nature* 286 (1980) 474-476.
- [11] T.F. Berto, K.E. Sanwald, W. Eisenreich, O.Y. Gutiérrez, J.A. Lercher, *J. Catal.* 338 (2016) 68-81.
- [12] K.E. Sanwald, T.F. Berto, W. Eisenreich, O.Y. Gutiérrez, J.A. Lercher, *J. Catal.* 344 (2016) 806-816.
- [13] J.F. Montoya, M.F. Atitar, D.W. Bahnemann, J. Peral, P. Salvador, *J. Phys. Chem. C* 118 (2014) 14276-14290.
- [14] C. Minero, A. Bedini, V. Maurino, *Appl. Catal. B* 128 (2012) 135-143.
- [15] P.C. Aben, *J. Catal.* 10 (1968) 224-229.
- [16] M. Boudart, H.S. Hwang, *J. Catal.* 39 (1975) 44-52.
- [17] M. Steib, A. Jentys, J.A. Lercher, *J. Phys. Conf. Ser.* 712 (2016) 012049.
- [18] A. Wahl, J. Augustynski, *J. Phys. Chem. B* 102 (1998) 7820-7828.
- [19] M.L. Hitchman, F. Tian, *J. Electroanal. Chem.* 538-539 (2002) 165-172.
- [20] J. Zhang, J. Wang, Z. Zhao, T. Yu, J. Feng, Y. Yuan, Z. Tang, Y. Liu, Z. Li, Z. Zou, *PCCP* 14 (2012) 4763-4769.
- [21] G.L. Chiarello, M.V. Dozzi, M. Scavini, J.-D. Grunwaldt, E. Selli, *Appl. Catal. B* 160-161 (2014) 144-151.

- [22] G.N. Nomikos, P. Panagiotopoulou, D.I. Kondarides, X.E. Verykios, *Appl. Catal. B* 146 (2014) 249-257.
- [23] T. Torimoto, Y. Aburakawa, Y. Kawahara, S. Ikeda, B. Ohtani, *Chem. Phys. Lett.* 392 (2004) 220-224.
- [24] R. Chong, J. Li, X. Zhou, Y. Ma, J. Yang, L. Huang, H. Han, F. Zhang, C. Li, *Chem. Commun.* 50 (2014) 165-167.
- [25] G. Balducci, *Chem. Phys. Lett.* 494 (2010) 54-59.
- [26] M.-H. Du, J. Feng, S.B. Zhang, *Phys. Rev. Lett.* 98 (2007) 066102.
- [27] I.A. Shkrob, T.W. Marin, S.D. Chemerisov, M.D. Sevilla, *J. Phys. Chem. C* 115 (2011) 4642-4648.
- [28] B. Sklarz, *Q. Rev. Chem. Soc.* 21 (1967) 3-28.
- [29] W. Mabey, T. Mill, *J. Phys. Chem. Ref. Data* 7 (1978) 383-415.
- [30] C. Guillard, E. Puzenat, H. Lachheb, A. Houas, J.-M. Herrmann, *Int. J. Photoenergy* 7 (2005) 1-9.
- [31] P. Calza, C. Minero, E. Pelizzetti, *Env. Sci. Technol.* 31 (1997) 2198-2203.
- [32] W. Choi, M.R. Hoffmann, *Env. Sci. Technol.* 31 (1997) 89-95.
- [33] B. Ohtani, Y. Okugawa, S. Nishimoto, T. Kagiya, *J. Phys. Chem.-US* 91 (1987) 3550-3555.
- [34] P. Salvador, *J. Electrochem. Soc.* 128 (1981) 1895-1900.
- [35] A. Piscopo, D. Robert, J.V. Weber, *Appl. Catal. B* 35 (2001) 117-124.
- [36] R. Vargas, O. Núñez, *J. Mol. Catal. A* 300 (2009) 65-71.
- [37] S. Okazaki, T. Kanto, *Nippon Kagaku Kaishi* (1976) 404-409.
- [38] S.-i. Nishimoto, B. Ohtani, T. Kagiya, *J. Chem. Soc. Farad. Trans.* 81 (1985) 2467-2474.
- [39] T. Kawai, T. Sakata, *Chem. Lett.* 10 (1981) 81-84.
- [40] C. Kooyman, K. Vellenga, H.G.J. De Wilt, *Carbohydr. Res.* 54 (1977) 33-44.
- [41] R. Nagorski, J.P. Richard, *J. Am. Chem. Soc.* 123 (2001) 794-802.
- [42] T. Preocanin, N. Kallay, *Croat. Chem. Acta* 79 (2006) 95-106.
- [43] C.A. Bunton, G. Savelli, L. Sepulveda, *J. Org. Chem.* 43 (1978) 1925-1929.
- [44] J.R. Snyder, A.S. Serianni, *Carbohydr. Res.* 210 (1991) 21-38.
- [45] S. Angyal, R. Wheen, *Aust. J. Chem.* 33 (1980) 1001-1011.
- [46] S. Angyal, V. Pickles, *Aust. J. Chem.* 25 (1972) 1695-1710.

[47] K.N. Drew, J. Zajicek, G. Bondo, B. Bose, A.S. Serianni, Carbohydr. Res. 307 (1998) 199-209.

3.8 Supporting information

SI-Table 3.1. List of ^1H -NMR signals of C_1 - C_6 oxygenates used for quantification. Chemical shifts are referenced to the internal standard 1,3,5-trihydroxybenzene.

	Compound	Chemical shift [ppm]	Multiplet	J [Hz]	#H
C_1	Methanol	3.29	s	-	3
	Formaldehyde (hydrate)	4.77	s	-	2
	Formic acid	8.19	s	-	1
	Methyl formate	3.71 (^{13}C : 51.1)	s	-	3
		8.08 (^{13}C : 164.1)	s	-	1
C_2	Ethylene glycol	3.60	s	-	4
	Glyoxal (hydrate)	4.75	s	-	2
	Glycolaldehyde	3.45	d	5.1	2
		4.38	s	-	2
		4.99	t	5.1	1
		9.56	s	-	1
	Glycolic acid	4.14	s	-	2
	Glyoxylic acid	5.28	s	-	1
	Acetaldehyde (dimer) (hydrate) (formyl) (dimer) (formyl)	1.25	d	5.2	6
		1.33	d	7.0	3
		2.18	d	3.0	3
		5.18	q	5.2	2
		9.62	q	3.0	1
	Acetic acid	2.02	s	-	3
C_3	Glycerol	3.50	m	-	2
		3.59	m	-	2
		3.72	m	-	1

SI-Table 3.1 continued

C ₃	Glyceraldehyde (hydrate)	4.89	d	5.2	1
	(formyl)	9.62	s	-	1
	Dihydroxyacetone (hydrate)	3.52	s	-	4
	(ketone)	4.36	s	-	4
	Hydroxyacetone	2.09	s	-	3
		4.30	s	-	2
	Glyceric acid	3.80	m	-	2
		4.29	t	4.1	1
C ₄	Erythritol	3.59	m	-	4
		3.72	m	-	2
	Erythrose	5.05	d	4.0	1
		5.20	d	3.4	1
		5.22	d	4.7	1
		9.69	s	-	1
	Threose	5.35	d	4.2	1
	Erythrulose	3.80	m	-	2
		4.39	t	4.1	1
	Ethylene glycol diformate	4.38	s	-	4
		(¹³ C: 62.0)			
		8.08	s	-	2
C ₅	Arabinose	4.45	d	7.8	1
		5.17	d	3.6	1
		5.18	d	2.7	1
		5.24	d	4.5	1
C ₆	Glucose	5.17	d	3.8	1
	Fructose	4.05	d	3.8	1

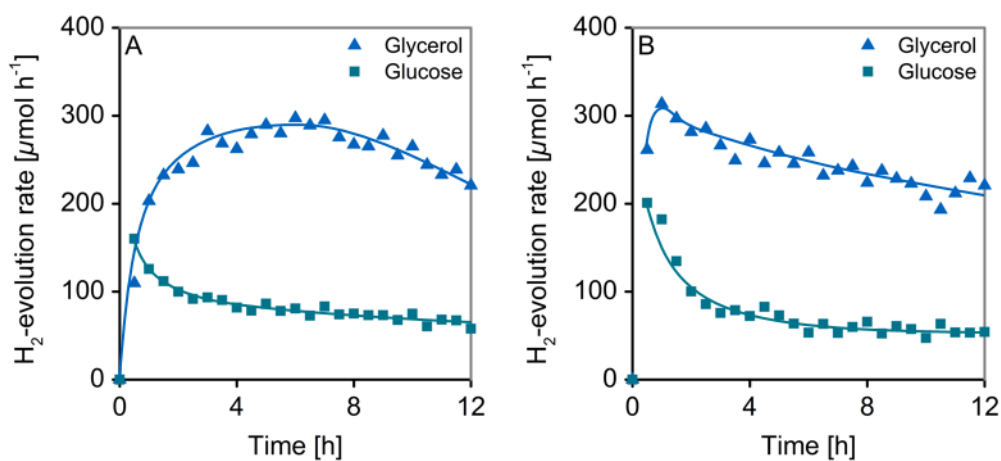
SI-Table 3.1 continued

	1,3,5-Trihydroxybenzene	5.94	s	-	3
--	-------------------------	------	---	---	---

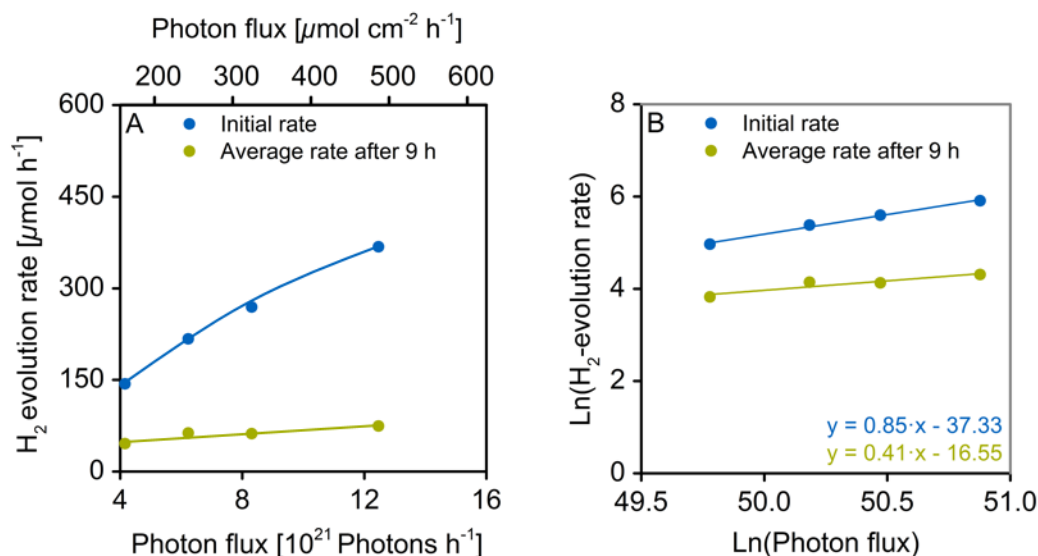
SI-Table 3.2. Summary of physicochemical properties of photocatalysts. Data for TiO₂ reference and Rh/TiO₂ catalyst taken from ref. 12.

Sample	Metal loading ^a	Metal particle size ^b	BET surface area	Band gap ^c
	[wt. %]	[nm]	[m ² g ⁻¹]	[eV]
TiO ₂	-	-	53	3.1
Rh/TiO ₂	1.0	2.3	51	3.1
Pd/TiO ₂	1.0	1.3	47	3.1
Pt/TiO ₂	1.0	2.0	52	3.1

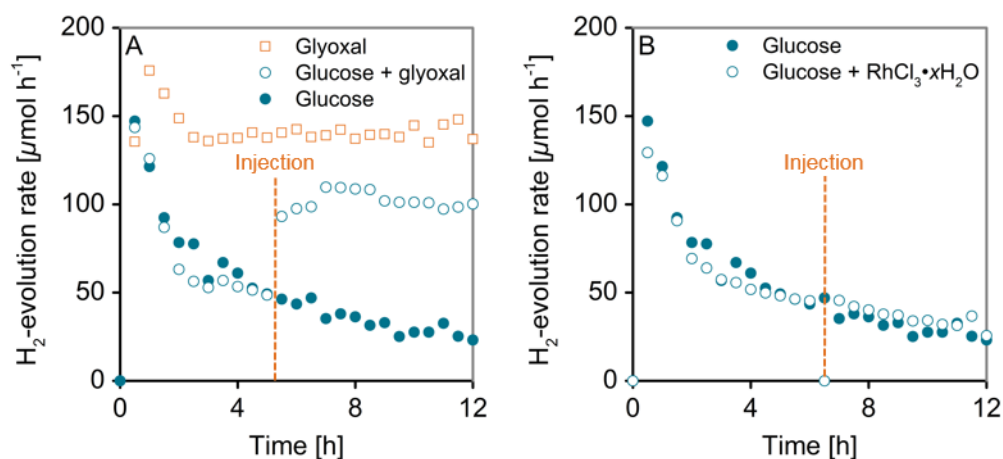
a: AAS. b: H₂-chemisorption. c: Tauc plot.



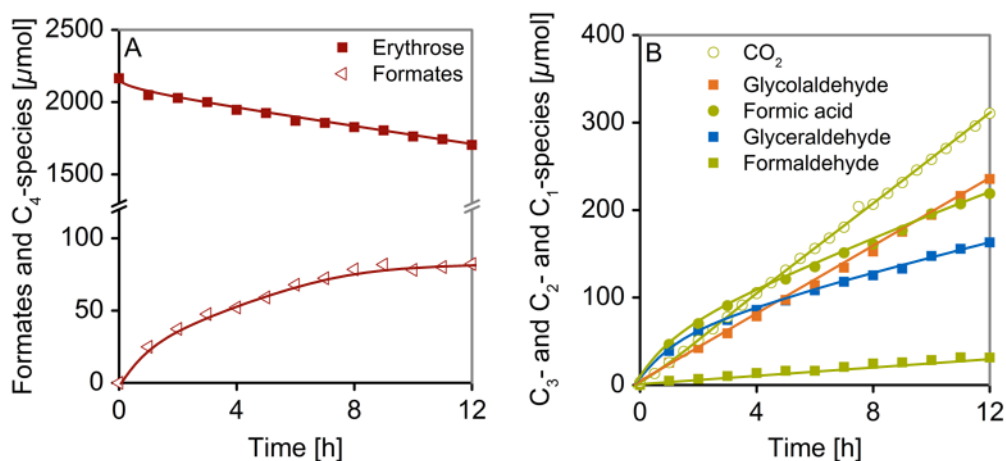
SI-Figure 3.1. Comparison of courses of H₂-evolution rates during photoreforming of glycerol and glucose on Pt/TiO₂ (A) and Pd/TiO₂ (B). Reaction conditions: 75 mg photocatalyst, 100 mL aqueous oxygenate solution (20 mM), 288 K, 1 bar Ar, 300 W Xe-lamp (CM1).



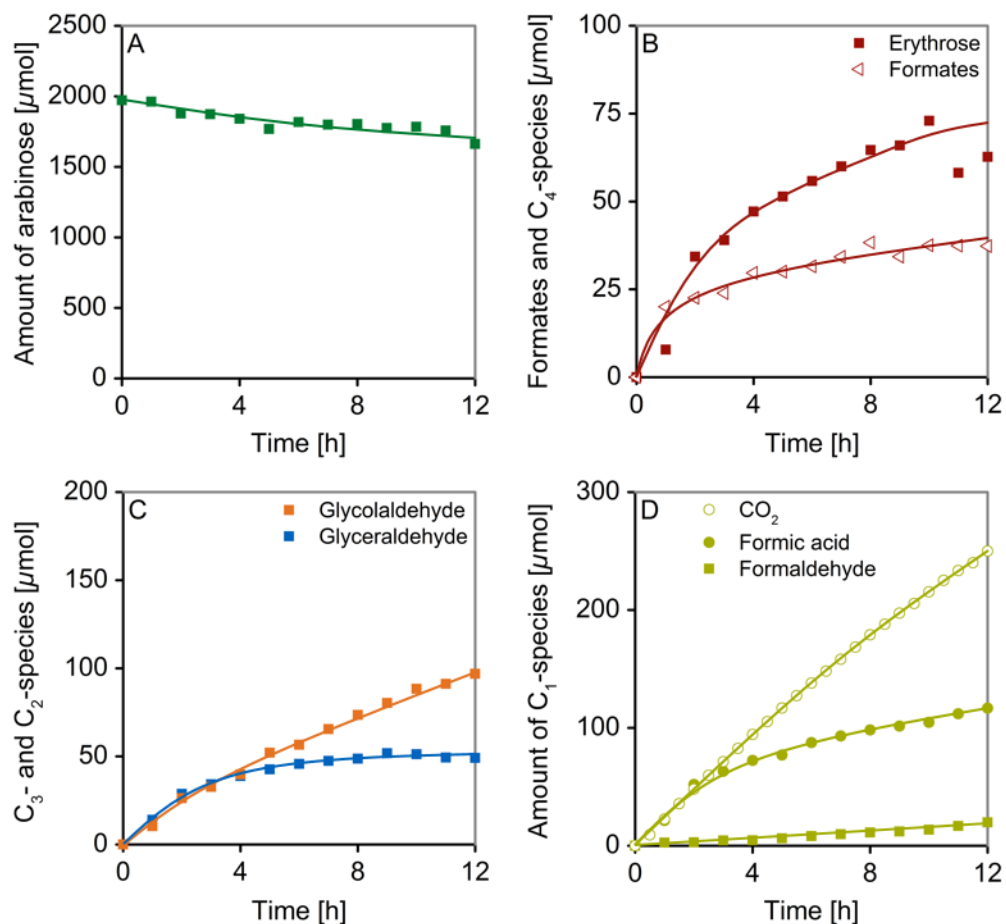
SI-Figure 3.2. Dependence of initial and average H₂-evolution rates (after stabilization during the first 9 h of reaction) during glucose photoreforming on Rh/TiO₂ on photon flux (A). Double logarithmic plot for determination of reaction orders with respect to photon flux (B). Initial rates increased almost linearly with light intensity (reaction order of 0.85) following quasi first-order recombination kinetics. On the other hand, H₂-evolution rates after stabilization during the first 9 h of reaction increased with photon flux according to a square-root correlation (reaction order of 0.41) indicating that additional electron-hole recombination in agreement with second-order kinetics prevails which constrains H₂-evolution. Reaction conditions: 75 mg photocatalyst, 100 mL aqueous glucose solution (20 mM), 288 K, 1 bar Ar, UV LEDs (365 nm \pm 5 nm).



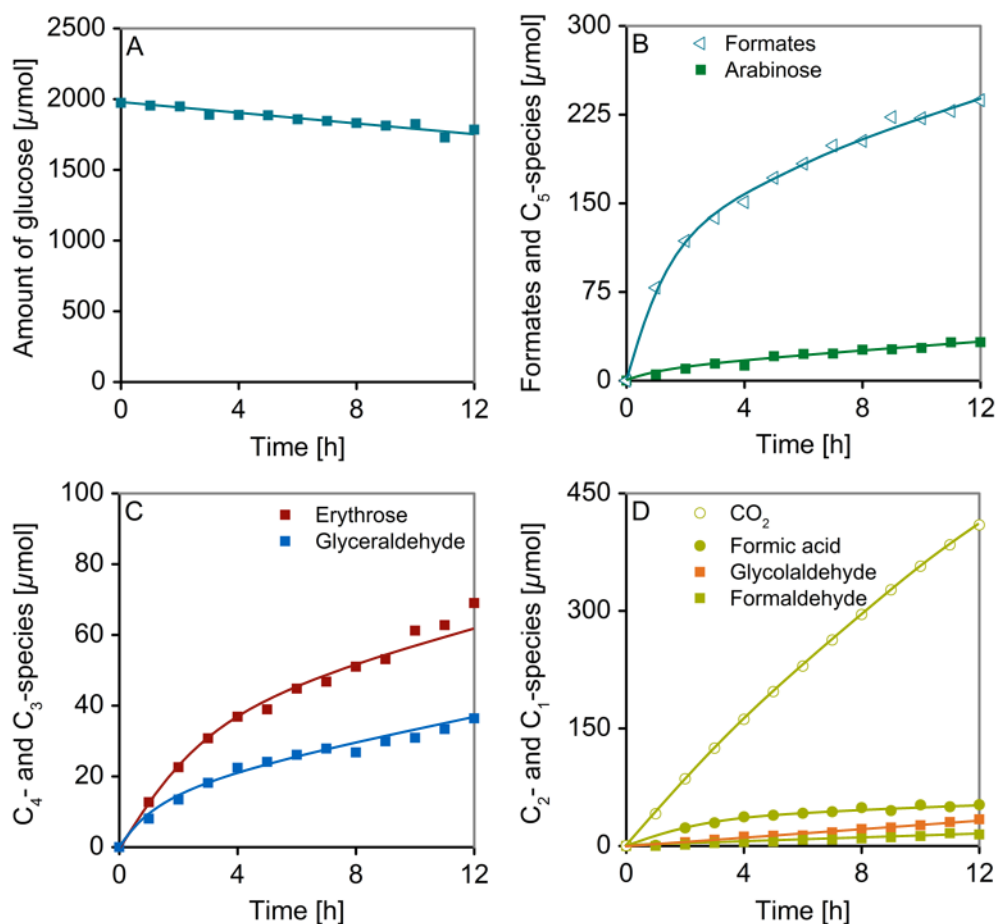
SI-Figure 3.3. Course of H₂-evolution rates during photoreforming of glucose (20 mM), glyoxal (15 mM) and injection of glyoxal (15 mM) after 5 h of glucose photoreforming (A). H₂-evolution rates during glucose photoreforming (20 mM) with and without injection of $\text{RhCl}_3 \cdot x\text{H}_2\text{O}$ after 6 h reaction time (B). Reaction conditions: 75 mg photocatalyst, 100 mL aqueous oxygenate solution, 288 K, 1 bar Ar, 300 W Xe-lamp (CM1).



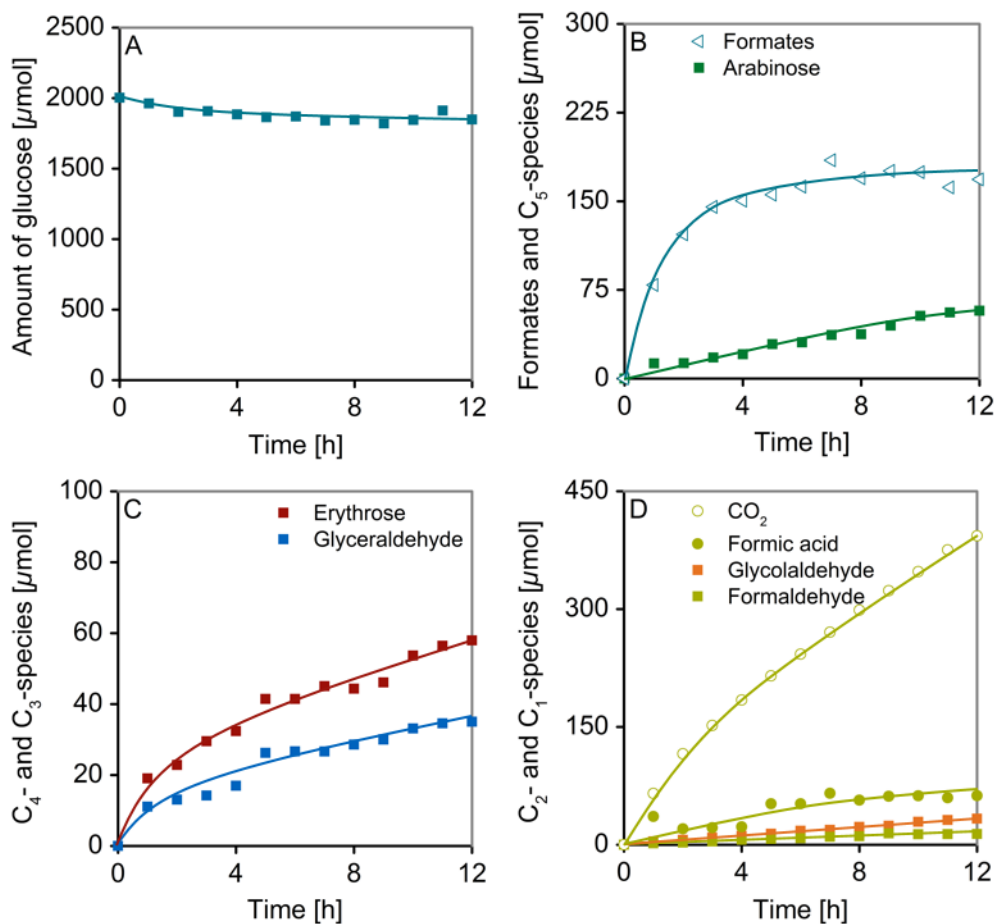
SI-Figure 3.4. Temporal profiles of anodic reaction products formed during photoreforming of erythrose on Rh/TiO₂. Course of amount of erythrose and formates (A). Course of C₃-C₂- and C₁-species generated (B). Reaction conditions: 75 mg photocatalyst, 100 mL aqueous erythrose solution (20 mM), 288 K, 1 bar Ar, 300 W Xe-lamp (CM1).



SI-Figure 3.5. Temporal profiles of anodic reaction products formed during photoreforming of arabinose on Rh/TiO₂. Course of amount of arabinose (A). Course of formates and C₄- (B), C₃-C₂- (C) and C₁-species (D) generated. Reaction conditions: 75 mg photocatalyst, 100 mL aqueous arabinose solution (20 mM), 288 K, 1 bar Ar, 300 W Xe-lamp (CM1).



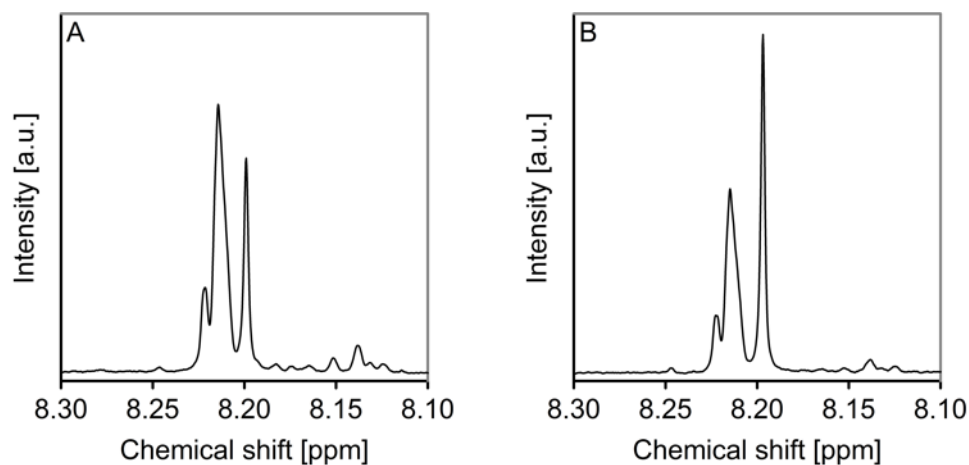
SI-Figure 3.6. Temporal profiles of anodic reaction products formed during photoreforming of glucose on Pt/TiO₂. Course of amount of glucose (A). Course of formates and C₅- (B), C₄-/C₃- (C) and C₂-/C₁-species (D) generated. Reaction conditions: 75 mg photocatalyst, 100 mL aqueous glucose solution (20 mM), 288 K, 1 bar Ar, 300 W Xe-lamp (CM1).



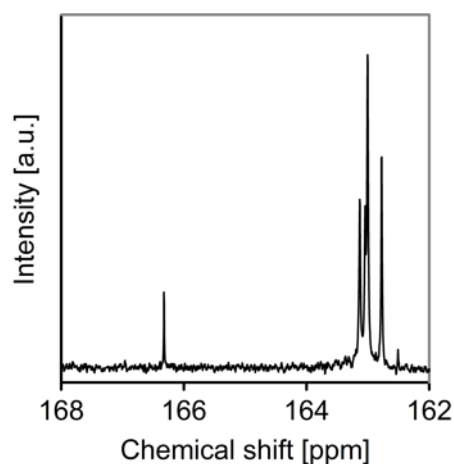
SI-Figure 3.7. Temporal profiles of anodic reaction products formed during photoreforming of glucose on Pd/TiO₂. Course of amount of glucose (A). Course of formates and C₅- (B), C₄-/C₃- (C) and C₂-/C₁-species (D) generated. Reaction conditions: 75 mg photocatalyst, 100 mL aqueous glucose solution (20 mM), 288 K, 1 bar Ar, 300 W Xe-lamp (CM1).

SI-Table 3.3. Summary of equilibrium compositions of aqueous aldose solutions from literature reports.

Compound	T [K]	Furanose α (β) [%]	Pyranose α (β) [%]	Aldehydo [%]	Hydrate [%]	Conditions	Ref.
D-Erythrose	303/ 309	88 (0.4)	–	2	10	$^1\text{H}/^{13}\text{C}$ -NMR, 0.1 M in D_2O	[44],[45]
D-Arabinose	304	4 (3)	95 (1.7)	–	–	^{13}C -NMR, 1.0 M	[46]
D-Glucose	303	0.39 (0.4)	99.6 (0.6)	< 0.01	< 0.01	^{13}C -NMR	[47]



SI-Figure 3.8. Comparison of partial ¹H-NMR spectra of liquid-phase reactor aliquots collected after 12 h of reaction time for photoreforming of glucose on Pt/TiO₂ (A) and Pd/TiO₂ (B). Reaction conditions: 75 mg photocatalyst, 100 mL aqueous glucose solution (20 mM), 288 K, 1 bar Ar, 300 W Xe-lamp (CM1).

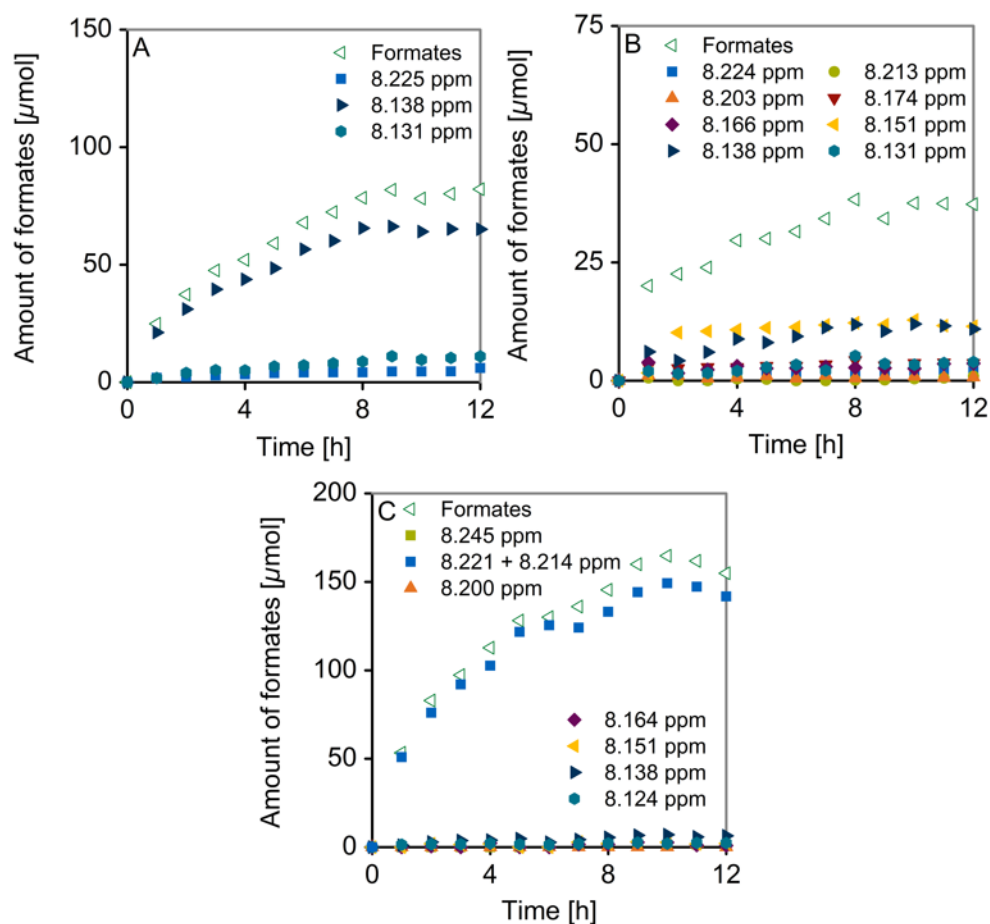


SI- Figure 3.9. Partial ¹³C-NMR spectrum of reactor aliquot collected after 12 h of reaction time for photoreforming of [1-¹³C]glucose. Together with the signal of formic acid at 166.3 ppm, multiple signals from 162.5 ppm to 163.1 ppm attributed to formate species are evident. Reaction conditions: 75 mg photocatalyst, 100 mL aqueous [1-¹³C]glucose solution (20 mM), 288 K, 1 bar Ar, 300 W Xe-lamp (CM1).

SI-Table 3.4. List of ^1H -NMR formate signal positions encountered during photoreforming of C_4 - C_6 oxygenates.

	Photoreforming reaction	^1H -NMR formate signals [ppm]
C_4	Erythritol	8.131, 8.138, 8.225
	Erythrose	8.131, 8.138, 8.225
C_5	Arabitol	8.131, 8.138
	Arabinose	8.131, 8.138, 8.151, 8.166, 8.174, 8.203, 8.213, 8.224
C_6	Sorbitol	8.131, 8.138, 8.151, 8.158, 8.213, 8.225, 8.279
	Glucose	8.124, 8.131, 8.138, 8.151, 8.164, 8.214*, 8.221*, 8.245

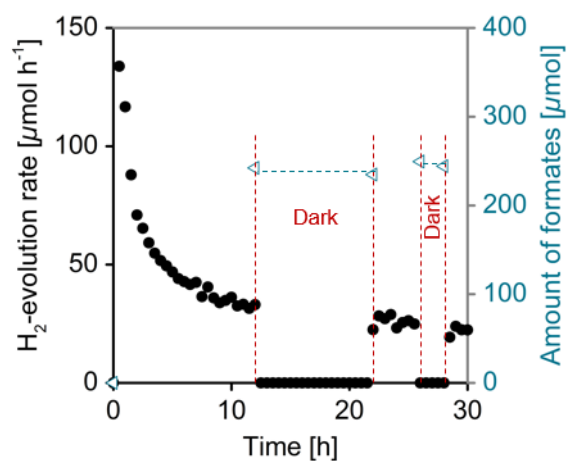
*NMR signals likely contain contributions of multiple species.



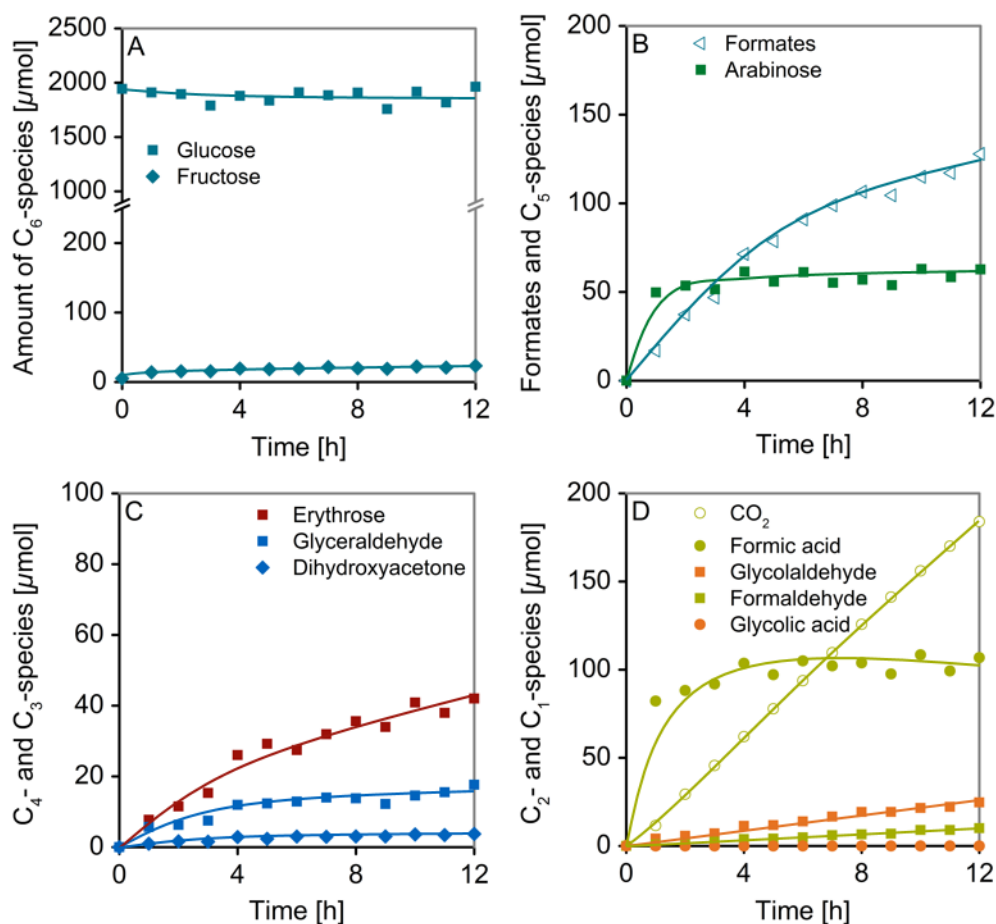
SI-Figure 3.10. Deconvolution of respective contributions of formate species with different ^1H -NMR chemical shift to course of total amount of formates formed during photoreforming of erythrose (A), arabinose (B), and glucose (C) on Rh/TiO_2 .

SI-Table 3.5 Determined rate constants for homogeneous acid-catalyzed formate hydrolysis normalized to the concentration of acid from ^1H -NMR titration experiments.

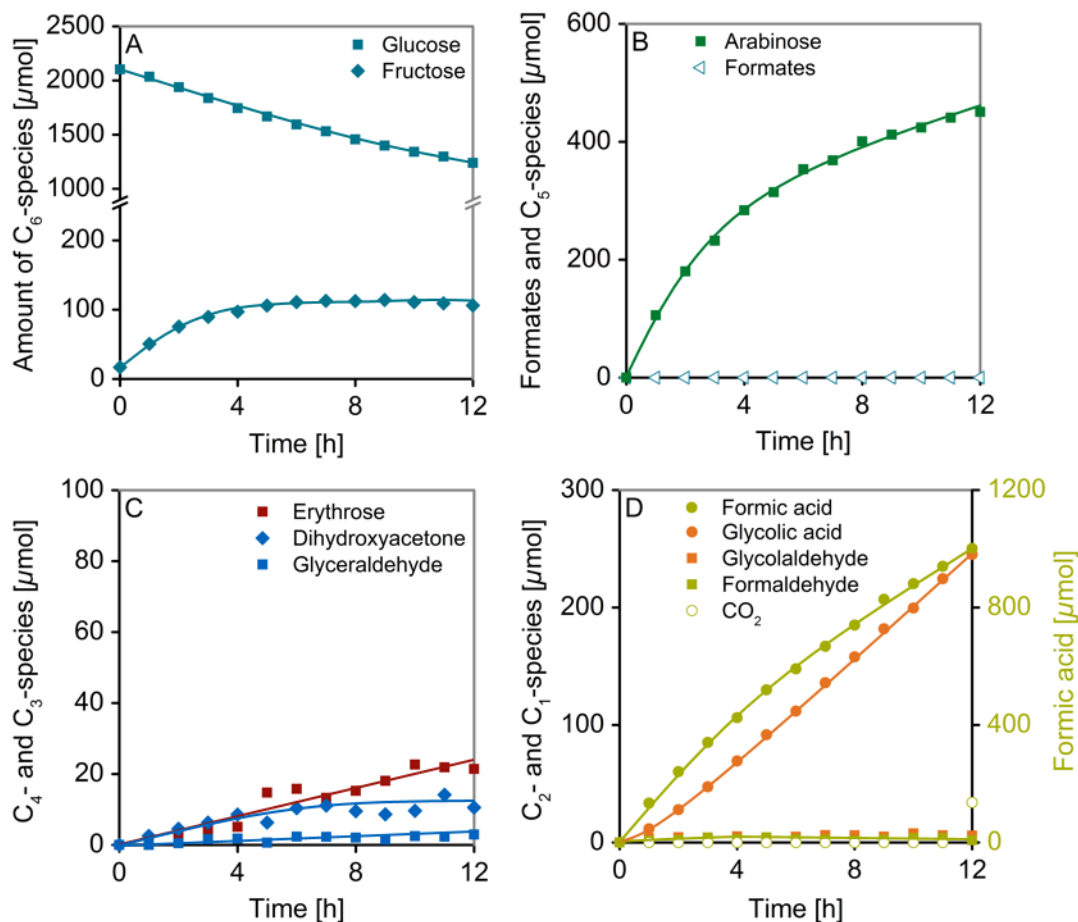
Reactant-derived formates	Chemical shift	1 st order rate constant	pH
	[ppm]	[L mol ⁻¹ s ⁻¹]	[-]
Erythrose	8.12	$6 \cdot 10^{-4}$	1.5
	8.13	$1 \cdot 10^{-3}$	1.5
Arabinose	8.14	$1 \cdot 10^{-3}$	1.5
Glucose	8.21	$7 \cdot 10^{-4}$	1.0
	8.22	$5 \cdot 10^{-4}$	1.0
	8.21	$6 \cdot 10^{-4}$	1.25
	8.22	$4 \cdot 10^{-4}$	1.25
	8.21	$5 \cdot 10^{-4}$	1.5
	8.22	$8 \cdot 10^{-4}$	1.5
	8.21	$6 \cdot 10^{-4}$	2.0
	8.22	$5 \cdot 10^{-4}$	2.0



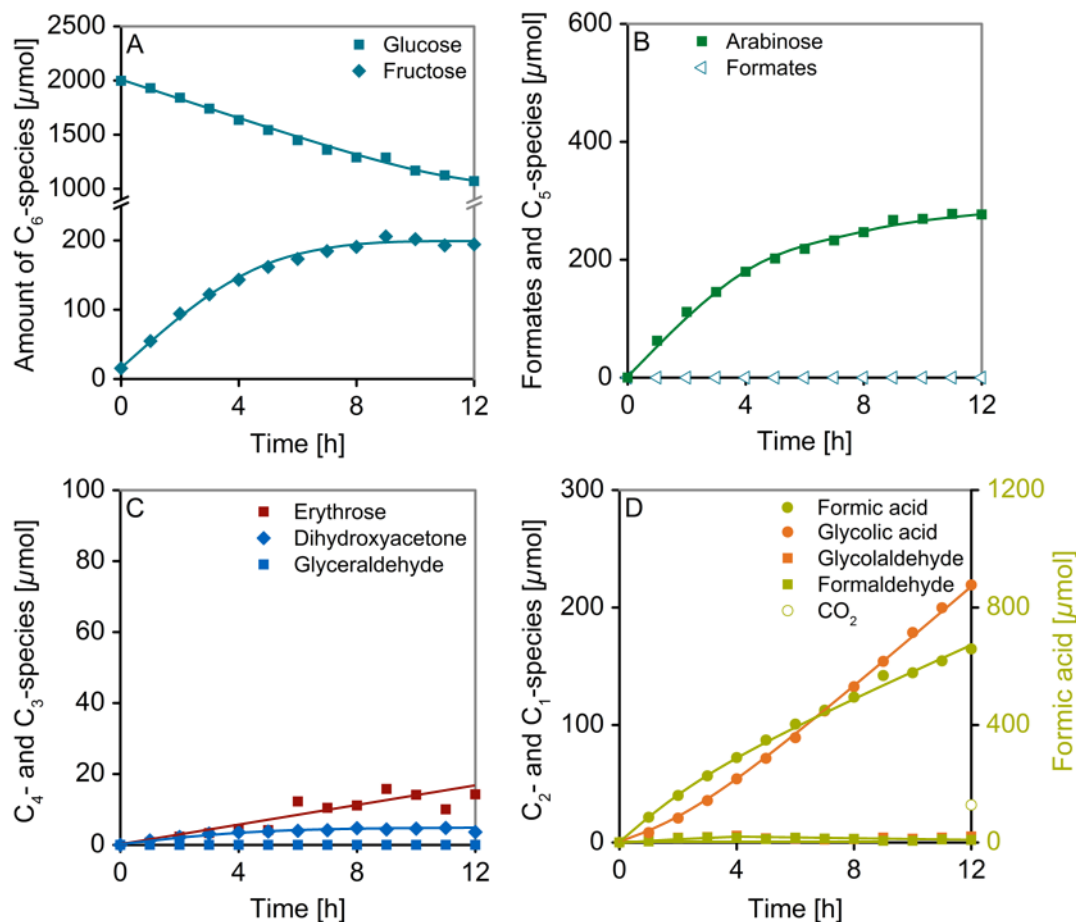
SI-Figure 3.11. Course of H₂-evolution rate and total amount of formates present in liquid-phase during glucose photoreforming conducted with alternating illumination and dark periods. Reaction conditions: 75 mg photocatalyst, 100 mL aqueous glucose solution (20 mM), 288 K, 1 bar Ar, 300 W Xe-lamp (CM1).



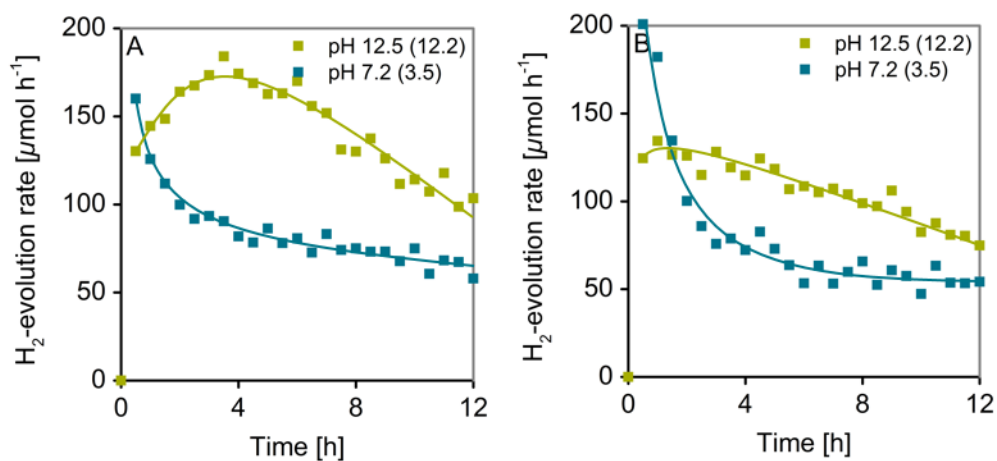
SI-Figure 3.12. Course of anodic reaction products formed during photoreforming of glucose on Rh/TiO₂. The initial pH was adjusted to 11 with NaOH (pH of 5.8 after 12 h reaction time). Course of amount of glucose and fructose (A). Course of formates and C₅- (B), C₄-/C₃- (C) and C₂-/C₁-species (D) generated. Reaction conditions: 75 mg photocatalyst, 100 mL aqueous glucose solution (20 mM), 288 K, 1 bar Ar, 300 W Xe-lamp (CM1).



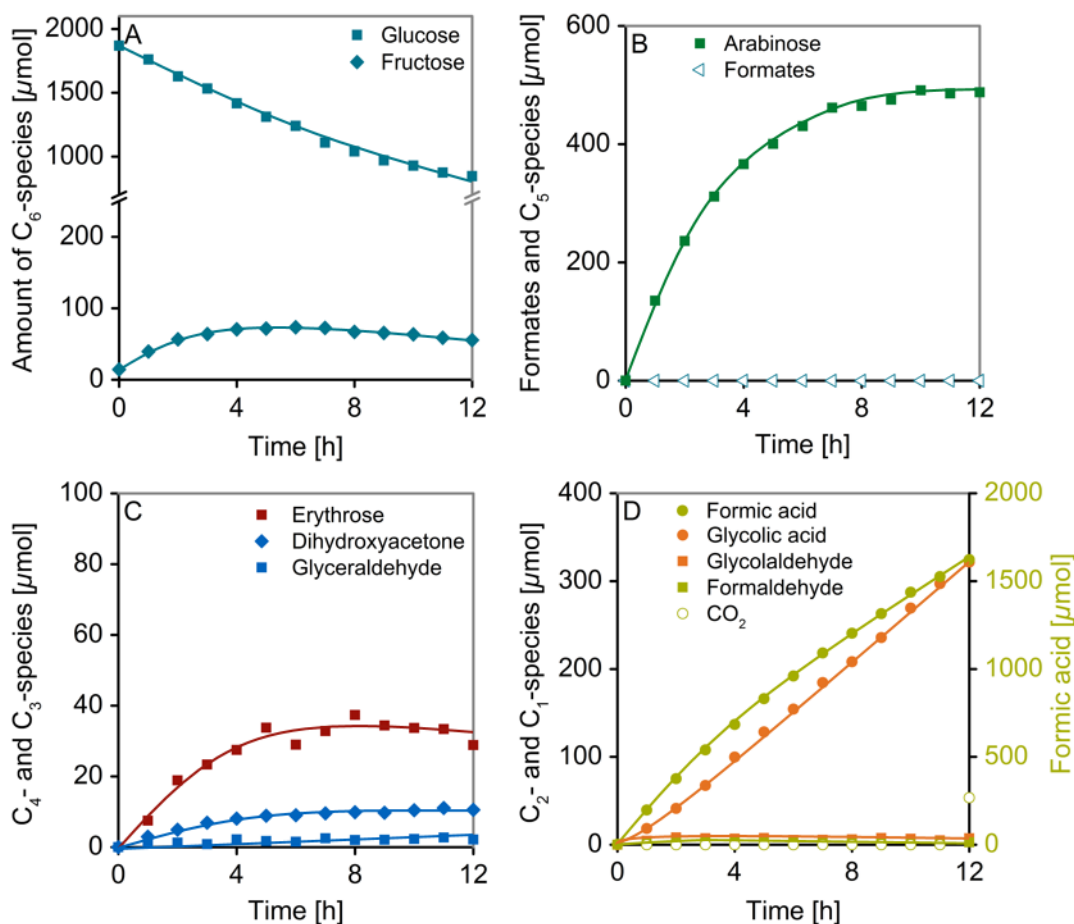
SI-Figure 3.13. Course of anodic reaction products formed during photoreforming of glucose on Rh/TiO₂. The initial pH was adjusted to 12.2 with NaOH (pH of 11.6 after 12 h reaction time). Course of amount of glucose and fructose (A). Course of formates and C₅- (B), C₄-/C₃- (C) and C₂-/C₁-species (D) generated. The total amount of CO₂ generated after 12 h reaction was determined by acidification of the reaction medium with H₂SO₄ to decompose dissolved (bi)carbonate. Reaction conditions: 75 mg photocatalyst, 100 mL aqueous glucose solution (20 mM), 288 K, 1 bar Ar, 300 W Xe-lamp (CM1).



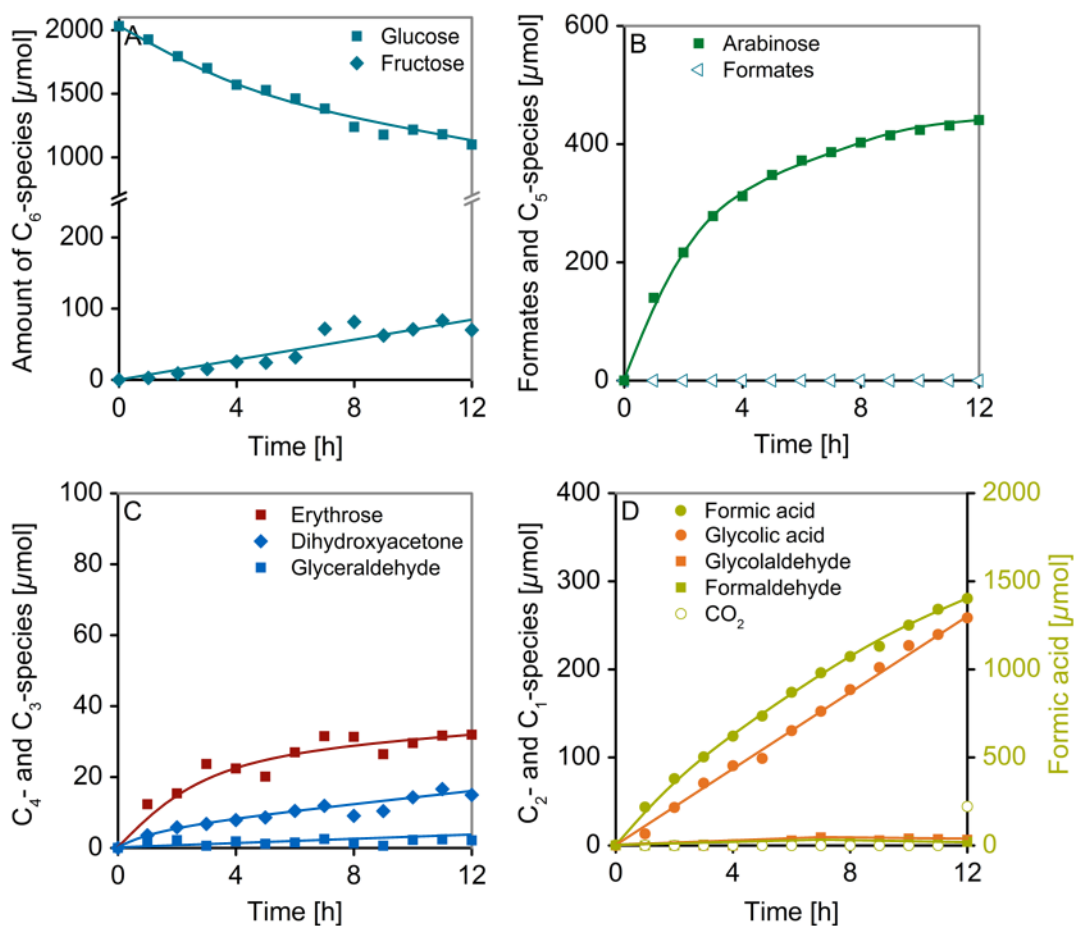
SI-Figure 3.14. Course of anodic reaction products formed during photoreforming of glucose on Rh/TiO₂. The initial pH was adjusted to 12.5 with NaOH (pH of 12.1 after 12 h reaction time). Course of amount of glucose and fructose (A). Course of formates and C₅- (B), C₄-/C₃- (C) and C₂-/C₁-species (D) generated. The total amount of CO₂ generated after 12 h reaction was determined by acidification of the reaction medium with H₂SO₄ to decompose dissolved (bi)carbonate. Reaction conditions: 75 mg photocatalyst, 100 mL aqueous glucose solution (20 mM), 288 K, 1 bar Ar, 300 W Xe-lamp (CM1).



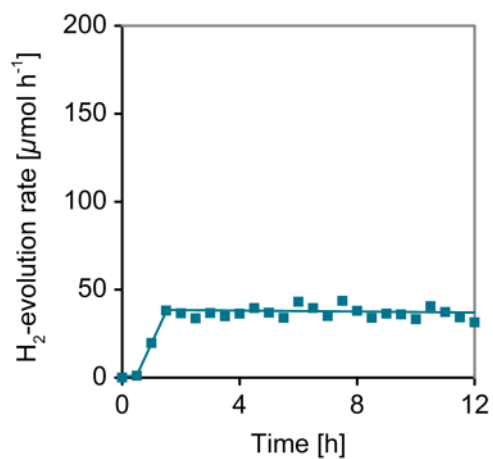
SI-Figure 3.15. Comparison of courses of H₂-evolution rates during photoreforming experiments on (A) Pt/TiO₂ and (B) Pd/TiO₂ in aqueous glucose solution under pH unadjusted conditions and initial pH 12.5 by addition of NaOH. Reaction conditions: 75 mg photocatalyst, 100 mL aqueous glucose solution (20 mM), 288 K, 1 bar Ar, 300 W Xe-lamp (CM1).



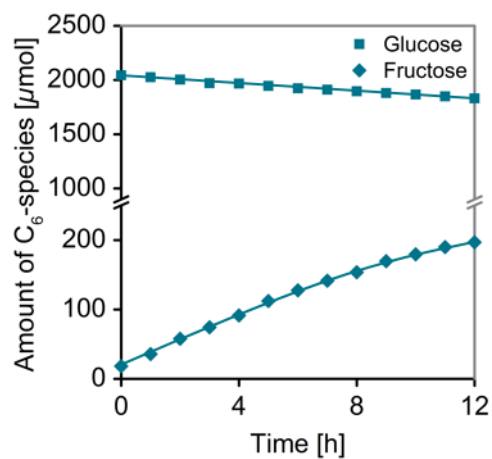
SI-Figure 3.16. Course of anodic reaction products formed during photoreforming of glucose on Pt/TiO₂. The initial pH was adjusted to 12.5 with NaOH (pH of 12.2 after 12 h reaction time). Course of amount of glucose and fructose (A). Course of formates and C₅- (B), C₄-/C₃- (C) and C₂-/C₁-species (D) generated. The total amount of CO₂ generated after 12 h reaction was determined by acidification of the reaction medium with H₂SO₄ to decompose dissolved (bi)carbonate. Reaction conditions: 75 mg photocatalyst, 100 mL aqueous glucose solution (20 mM), 288 K, 1 bar Ar, 300 W Xe-lamp (CM1).



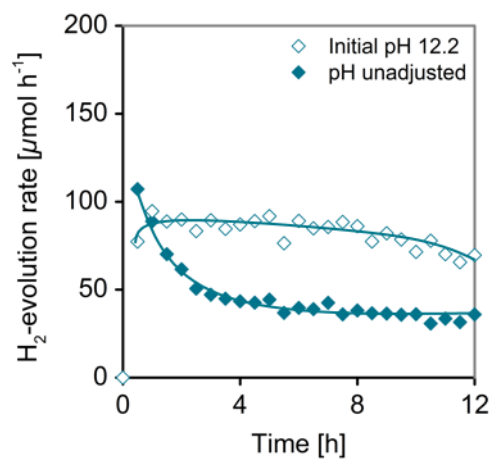
SI-Figure 3.17. Course of anodic reaction products formed during photoreforming of glucose on Pd/TiO₂. The initial pH was adjusted to 12.5 with NaOH (pH of 12.2 after 12 h reaction time). Course of amount of glucose and fructose (A). Course of formates and C₅- (B), C₄-/C₃- (C) and C₂-/C₁-species (D) generated. The total amount of CO₂ generated after 12 h reaction was determined by acidification of the reaction medium with H₂SO₄ to decompose dissolved (bi)carbonate. Reaction conditions: 75 mg photocatalyst, 100 mL aqueous glucose solution (20 mM), 288 K, 1 bar Ar, 300 W Xe-lamp (CM1).



SI-Figure 3.18. Course of H₂-evolution rates during glucose photoreforming on Rh/TiO₂ in borate buffer at pH 9. Reaction conditions: 75 mg photocatalyst, 100 mL aqueous glucose solution (20 mM), 288 K, 1 bar Ar, 300 W Xe-lamp (CM1).



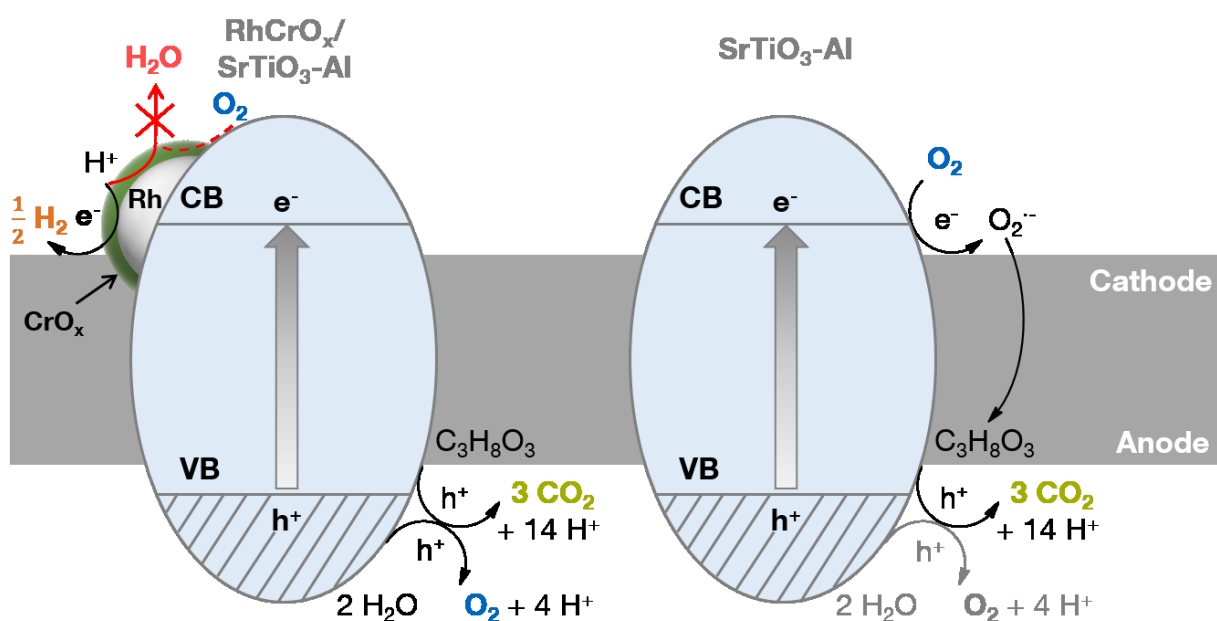
SI-Figure 3.19. Course of glucose and fructose during a control experiment in absence of UV-Vis illumination (dark conditions) on Rh/TiO₂. The initial pH was adjusted to 12.5 with NaOH. Formation of further reaction products in liquid- and/or gas-phase was not observed. Reaction conditions: 75 mg photocatalyst, 100 mL aqueous glucose solution (20 mM), 288 K, 1 bar Ar.



SI-Figure 3.20. Course of H₂-evolution rates during photoreforming experiments on Rh/TiO₂ in aqueous fructose solution with either unadjusted pH or initial pH 12.2 by addition of NaOH. Reaction conditions: 75 mg photocatalyst, 100 mL aqueous fructose solution (20 mM), 288 K, 1 bar Ar, 300 W Xe-lamp (CM1).

Chapter 4

Kinetic coupling of water splitting and photo-reforming on SrTiO₃-based photocatalysts



4. Kinetic coupling of water splitting and photoreforming on SrTiO₃-based photocatalysts

This chapter is used to draft a manuscript for publication:

K.E. Sanwald, T.F. Berto, O.Y. Gutiérrez, A. Jentys, J.A. Lercher, Kinetic coupling of water splitting and photoreforming on SrTiO₃-based photocatalysts, *in preparation*.^a

4.1 Abstract

Coupling the anodic half-reactions of overall water splitting and oxygenate photoreforming (i.e. water and oxygenate oxidations) on Al-doped SrTiO₃ decorated with a co-catalyst enables efficient photocatalytic H₂-generation along with oxygenate conversion without accumulation of undesired intermediates, i.e. glycerol was converted to CO₂ with low formaldehyde selectivity. The net H₂-evolution rates result from the interplay among water oxidation, oxygenate oxidation, and the back-reaction of H₂ and O₂ to water. When the latter is quantitatively suppressed (e.g. on RhCrO_x co-catalyst or in excess of oxygenated hydrocarbons), the initial H₂-evolution rates are independent of oxygenate nature and concentration. This is a consequence of the reduction equivalents for H₂-evolution provided by water oxidation compensating changes in the rates of oxygenate conversion. Thus, under conditions of suppressed back-reaction, water and oxygenate oxidations have equal quantum efficiencies. Contrarily, the selectivities to water and oxygenate oxidation depend on oxygenate nature and concentration. Transformations mediated by indirect hole transfer dominate as a result of the water oxidation activity at the anode and the associated intermediates generated in O₂-evolution catalysis (e.g. ·OH, ·O and ·OOH). On the undecorated semiconductor, the O₂ produced during overall water splitting is reductively activated to participate in glycerol oxidation without consuming evolved H₂.

^a K.E.S. planned, designed and conducted the experiments (unless otherwise noted in the acknowledgements section), analyzed and interpreted the data and wrote the manuscript. T.F.B., O.Y.G., A.J. and J.A.L. contributed to the discussion of the results and the correction of the manuscript anytime.

4.2 Introduction

Photocatalytic H₂-generation may represent a key technology for efficient storage of renewable energy in chemical fuels. Overall water splitting (into H₂ and O₂) using particulate semiconductor photocatalysts is widely pursued for photocatalytic solar hydrogen production [1-3]. However, the reactive H₂/O₂ mixture readily undergoes the thermodynamically favored back-reaction to water, which leads to zero net H₂-evolution rates [4-6].

As an alternative concept for photocatalytic H₂-generation, photoreforming of waste biomass, e.g. polyols and sugars, has evolved in recent years [7-9]. In photoreforming, oxygenates act as electron donors consuming oxidants in anodic reactions while simultaneously providing the reduction equivalents for H₂-evolution under anaerobic conditions. Following this route, an unreactive, more easily separable mixture of H₂ and CO₂ is produced at ambient conditions, while waste substances or contaminants are eliminated. However, fundamental studies of oxygenate photoreforming performed on TiO₂-based catalysts have revealed important challenges to overcome for further technological development. For instance, oxidative rupture of C-C bonds in polyols, the outcome of direct hole transfer to adsorbed oxygenates leads to the formation of formaldehyde, which accumulates due to its weak adsorption on TiO₂ [10, 11]. In addition, quantitative oxygenate oxidation to CO₂ implies low H₂-evolution rates at high conversions due to the Langmuir-type dependence on oxygenate concentration and coverage [12-14].

On photocatalysts with overall water splitting activity, the presence of adsorbates other than water has a strong effect on the H₂ evolution rates [10], whereas photocatalytic organic degradation has been achieved under simultaneous evolution of H₂ and O₂ [15]. Thus, we hypothesized that the kinetic coupling of overall water splitting and photoreforming of oxygenated hydrocarbons will allow to control the operating reaction mechanisms overcoming the drawbacks of both processes.

A photoabsorber active in total oxidation of water in the absence of sacrificial electron acceptors is required in order to establish simultaneous water and oxygenate photooxidation at the anode. The activity for water oxidation is expected to provide reduction equivalents for H₂-evolution at the cathode in addition to those generated by

oxygenate conversion. Furthermore, photogenerated oxidants formed during water oxidation at the anode act as oxidants to the organics. Previously, we provided first evidence that this impacts the anodic reaction pathways for ethylene glycol conversion on a GaN:ZnO photocatalyst [10]. On the other hand, Al-doping of SrTiO₃ has been demonstrated to result in one of the most active UV-photocatalysts for overall water splitting when decorated with a RhCrO_x co-catalyst [16, 17]. Thus, we have studied the kinetic coupling of photocatalytic overall water splitting and photoreforming on an Al-doped SrTiO₃ photoabsorber decorated with either a Rh or RhCrO_x (core-shell) co-catalyst. The fundamental, molecular-level kinetic explorations of the coupled process were achieved using glycerol and the intermediates in the anodic pathways as probe molecules. The factors governing overall H₂-evolution rates and selectivities of O₂-evolution and oxygenate oxidation are evaluated. Using this approach we show that glycerol may be converted with low formaldehyde selectivity simultaneously evolving H₂ at initial rates, which are independent of oxygenate nature, concentration or coverage. We propose that the anodic reaction pathways and the selectivities observed arise from interactions of oxygenates with intermediates in the O₂-evolution catalytic cycle.

4.3 Experimental

4.3.1 Materials

All chemicals were purchased from commercial suppliers and used as provided: alumina crucible (Coors, 99.7 %), K_2CrO_4 (Aldrich, ≥ 99.5 %), CrO_3 (Aldrich, 99.9 %), Cr_2O_3 (Alfa Aesar, 99 %), $RhCl_3 \cdot xH_2O$ (Aldrich, ≥ 99.9 %), $SrCl_2 \cdot 6 H_2O$ (Aldrich, ≥ 99.9 %), $SrTiO_3$ (WAKO, 99.9 %), CO (Westfalen, 3.7), Ar (Westfalen, 5.0), Al AAS standard (Fluka, 1 g L⁻¹), Sr AAS standard (Fluka, 1 g L⁻¹), Ti AAS standard (Fluka, 1 g L⁻¹), Rh AAS standard (Fluka, 1 g L⁻¹), Cr ICP standard (Fluka, 1 g L⁻¹), DL-tartaric acid (Aldrich, ≥ 99.9995 %), boric acid (Aldrich, 99.999 %), sodium carbonate (Aldrich, 99.999 %, anhydrous), hydrogen peroxide solution (Fluka, ≥ 30 %), hydrochloric acid (Fluka, ≥ 30 %), silver nitrate (Alfa Aesar, 99.9995 %), $Al(NO_3)_3 \cdot 9 H_2O$ (Aldrich, 99.997 %), methanol (Aldrich, 99.8%, anhydrous), formaldehyde solution (Fluka, 1 g L⁻¹ in H₂O, IC standard), formic acid (Merck, 98 – 100 %), ethanol (European Reference Materials, 80 mg 100 ml⁻¹), glycolaldehyde dimer (Aldrich), glyoxal trimer dihydrate (Fluka, ≥ 95 %), glycolic acid (Aldrich, 99 %), glyoxylic acid monohydrate (Aldrich, 98%), oxalic acid (Aldrich, > 99 %, anhydrous), glycerol (Aldrich, ≥ 99.5 %), glycerol-d₈ (Aldrich, 98 %, 98 atom-% D), D-glyceraldehyde (Aldrich, > 98 %), dihydroxyacetone (Merck, ≥ 98 %), glyceric acid solution (abcr, 20 % in H₂O), β -hydroxypyruvic acid (Aldrich, ≥ 95 %%), hydroxyacetone (Alfa Aesar, 95 %), phloroglucinol (Aldrich, ≥ 99 %), D₂O (Euriso-Top, 99.85 atom-%), DCI (Acros Organics, 1 M in D₂O, 99.8 atom-%). Aqueous solutions used in photocatalyst synthesis, kinetic experiments and for derivatization of reactor aliquots for liquid-phase analysis were prepared in ultrapure water (18.2 M Ω cm, Werner Reinstwassersysteme).

4.3.2 Photocatalyst preparation

Semiconductor synthesis

$SrTiO_3$ was treated in $SrCl_2$ flux and was doped with aluminum (STO-Al) [16, 18]. A mixture of 0.75 g $SrTiO_3$ (WAKO, 99.9%) and 10.99 g $SrCl_2 \cdot 6 H_2O$ (molar ratio of $SrCl_2 \cdot 6 H_2O / SrTiO_3 = 10$) was thoroughly ground in an agate mortar and transferred into an alumina crucible (Coors, 99.7 %). The mixture was heated to 1323 K (5 K min⁻¹) in static air and was kept for 10 h at this temperature, subsequently cooled to 1073 K at 3 K min⁻¹

and afterwards allowed to cool naturally to room temperature. The residual solid was repeatedly washed with bidistilled water to remove SrCl_2 until no AgCl precipitated upon addition of AgNO_3 to an aliquot of the washing water.

Co-catalyst deposition

STO-Al was decorated with RhO_x by a wet impregnation procedure. 0.25 g of STO-Al were dispersed in 2 mL of an aqueous solution containing appropriate amounts of $\text{RhCl}_3 \cdot x\text{H}_2\text{O}$. The suspension was evaporated to dryness in a ceramic dish over a water bath while stirring with a glass rod. The powder was placed in an alumina boat and treated in static air at 623 K (5 K min^{-1}) for 1 h. A nominal Rh-loading of 0.1 wt.% was applied, which was determined to maximize photocatalytic activity (SI-Fig. 4.1).

Photodeposition of CrO_x -shell

135 mg of $\text{RhO}_x/\text{STO-Al}$ were dispersed in 100 mL of an aqueous solution containing K_2CrO_4 (0.8 mM). The suspension was deaerated and irradiated with a 300 W Xe-lamp (CM1) at 288 K for 3.5 h. This results in photoreduction of Cr(VI) and formation of a hydrated CrO_x shell around the co-catalyst particles [4, 19-21]. The core-shell co-catalyst decorated semiconductor was afterwards recovered by filtration through a nylon filter ($0.2 \mu\text{m}$), thoroughly washed with bidistilled water and dried in static air overnight at 323 K.

4.3.3 Photocatalytic test

Kinetic experiments

Kinetic experiments were conducted in a top-irradiation Pyrex photo-reactor covered by a quartz window. The reactor is connected to a closed gas-circulation system. Irradiation was provided either by a 300 W Xe lamp ($8.08 \cdot 10^{17} \text{ photons s}^{-1}$ within the reactor at water level with $\lambda < 390 \text{ nm}$) with a cold mirror 1 (CM1) and a water filter kept at 303 K or by high power UV LEDs (Nichia NC4U133A, $365 \text{ nm} \pm 5 \text{ nm}$) that were tuned in intensity in the range of $1.16 \cdot 10^{18} \text{ photons s}^{-1}$ to $4.64 \cdot 10^{18} \text{ photons s}^{-1}$. Light intensities were determined as published previously [10, 11]. In a typical kinetic experiment 125 mg of photocatalyst were ultrasonically dispersed in 100 mL H_2O or 20 mM aqueous oxygenate solutions. The system was deaerated by four consecutive evacuations and Ar filling cycles. All reactions were carried out at 288 K and an Ar pressure of 1 bar. Evolved gases were analyzed by

online gas chromatography (Shimadzu, GC 2010 Plus equipped with TCD, FID and a methanizer unit) using Ar as carrier gas. Dissolved gases were accounted for by application of Henry's law. Aliquots of the liquid-phase were manually taken at regular times from the photocatalyst suspension *via* a sample valve and analyzed *via* quantitative ^1H -NMR spectroscopy. The selectivities for reduction equivalents for H_2 -evolution provided from O_2 -evolution (S_{O_2}) or oxygenate oxidation (S_{Organic}) were calculated according to eqs. (4.1) and (4.2).

$$S_{\text{O}_2} [\%] = \left(\frac{2 \cdot n_{\text{O}_2}}{n_{\text{H}_2}} \right) \cdot 100 \quad (4.1)$$

$$S_{\text{Organic}} [\%] = 100 - S_{\text{O}_2} \quad (4.2)$$

Where n_{H_2} and n_{O_2} denote the initial amounts of H_2 and O_2 evolved (after 1 h) [μmol].

^1H -NMR analysis

The procedures applied for quantitative ^1H -NMR analysis of liquid-phase samples and ^1H -NMR signal assignments were described in detail in refs. 10 and 11. Additional NMR signals encountered in the context of this study are compiled in SI-Table 4.1.

4.3.4 Physicochemical characterization

N_2 -physisorption isotherms were recorded at 77 K on a PMI automated BET sorptometer to determine specific surface areas applying the BET model. Samples were outgassed at 523 K for 20 h prior to measurements.

Crystal structures were characterized by X-ray diffraction (XRD) patterns collected on a STOE STADI-P diffractometer ($\text{Cu-K}_{\alpha 1}$ radiation, $\lambda = 1.54051 \text{ \AA}$, Ge-monochromator) with a Dectris Mythen 1 K detector.

Atomic absorption spectroscopy (AAS) on a Thermo Scientific – SOLAAR M Series AA spectrometer was used to determine Sr, Ti, Al and Rh concentrations. Dissolution of STO and STO-Al for analysis of Sr, Ti and Al was performed adopting the procedures described in refs. 16 and 18. Cr concentrations were determined using inductively coupled plasma optical emission spectroscopy (ICP-OES) on an Agilent 700 spectrometer. The absorption of chromium at 267.7 nm and 283.6 nm was determined and quantified against aqueous

reference solutions containing defined concentrations of Cr(VI). No further pre-treatment was applied to samples and standard references.

Scanning electron microscopy (SEM) in secondary electron imaging (SEI) detection was performed on a JEOL JSM 7500F microscope equipped with a cold-cathode type field emission electron gun that was operated at 5.0 kV to determine textural properties of the materials. Transmission electron microscopy (TEM) micrographs were collected on a JEOL JEM-2010 transmission electron microscope. Acceleration voltages of 120 kV and 200 kV were used for particle size distribution and high resolution imaging of core-shell co-catalyst particle structures, respectively. Average Rh particle sizes were determined from measurement of at least 400 individual particles. Catalyst samples were suspended in ethanol and drop casted onto holey carbon coated Cu grids.

Diffuse reflectance UV-Vis spectra were recorded on an Avantes Avaspec 2048 spectrometer equipped with a reflection probe (FCR-7UV200-2-ME) with a home-made sample holder. Reflectance values were transformed into Kubelka-Munk units. PTFE was used as a reference.

Solid state ^{27}Al magic-angle spinning (MAS) NMR spectra were acquired on a Bruker Avance AMX-500 spectrometer. Samples were packed into ZrO_2 rotors and spun at 10 kHz. 24000 scans were collected using an excitation pulse power of 8 dB and a pulse length of $1.16\ \mu\text{s}$. Relaxation delay and acquisition time were set to 2 s and 0.02 s, respectively. Chemical shifts are referenced to an $\text{Al}(\text{NO}_3)_3 \cdot 9\ \text{H}_2\text{O}$ reference. Spectra were manually phased and background corrected using Mestre-C 8.1.1 software package.

X-ray absorption near-edge structure (XANES) measurements at the Cr K-edge were conducted at ESRF beamline ID26 (storage ring operated at 6 GeV, ring current 90 mA, top-up mode) using a Si(311) monochromator. Spectra were obtained in fluorescence mode at room temperature using a silicon drift detector and normalized to an edge step height of one absorption unit. Energy calibration was done setting the edge position of Cr(III) in a Cr_2O_3 reference to 6007 eV [22]. The $\text{RhCrO}_x/\text{STO-Al}$ photocatalyst was examined under varying conditions. In each case, about 2 mg were packed into J Young valve quartz NMR tubes (5 mm diameter, 0.04 mm wall thickness, Norell). Liquid-phase measurements were conducted immersing the powder in 0.5 mL of liquid (either pure H_2O

or 20 mM glycerol solution), which was deaerated by consecutive evacuation and Ar filling cycles using a Schlenk line. UV-Vis illumination of the samples was provided by a 200 W Hg(Xe)-lamp equipped with a water filter.

4.4 Results and discussion

4.4.1 Physicochemical properties of the photocatalysts

Semiconductor photoabsorber

XRD patterns of pristine SrTiO_3 (STO) and Al-doped SrTiO_3 (STO-Al) showed in both cases a pure cubic perovskite SrTiO_3 phase (Fig. 4.1). After flux treatment of STO, sharpened reflections with increased intensities indicated improved crystallinity and growth of particle size, respectively, in agreement with literature [16-18]. The reflections of STO-Al (exemplarily shown for the (110) plane in Fig. 4.1B) appeared at slightly higher diffraction angles 2θ compared to STO and showed a shoulder at the high angle side. This reflects reduction in lattice parameter and local distortion upon high temperature treatment of STO, which were previously attributed to substitution of OH^- for O^{2-} moieties (along with the formation of Sr^{2+} defects [23]) rather than incorporation of aliovalent dopants in agreement with ^{27}Al MAS NMR, see below.

STO exhibited aggregates of irregularly shaped particles of a fraction of a μm in size (SEM imaging, Fig. 4.2). Dissolution and recrystallization from SrCl_2 flux resulted in formation of truncated cubic crystals exposing well-defined surface facets [16-18] resembling the equilibrium crystal shape of SrTiO_3 [24]. The primary particles of the crystal aggregates grew in size up to a few μm . Accordingly, the BET surface area decreased from $5.1 \text{ m}^2 \text{ g}^{-1}$ to $2.7 \text{ m}^2 \text{ g}^{-1}$ (Table 4.1) upon flux treatment.

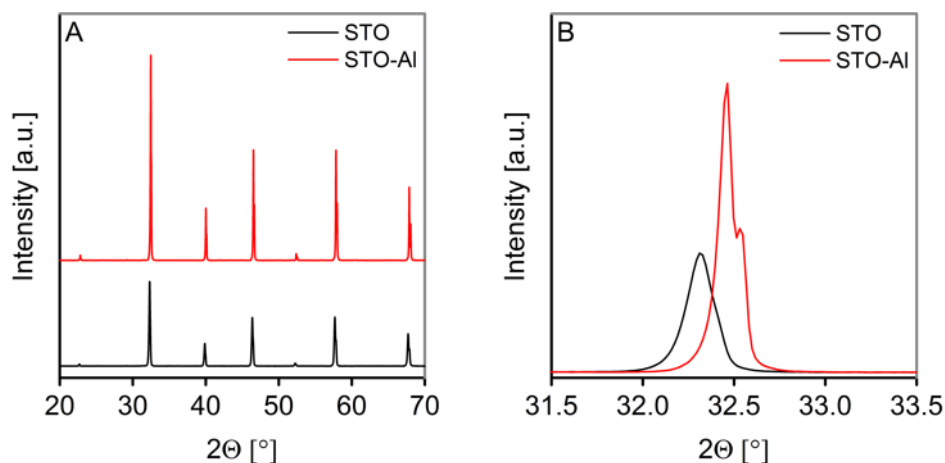


Figure 4.1. (A) Powder XRD patterns of pristine SrTiO_3 (STO) and Al-doped SrTiO_3 (STO-Al). (B) Magnification of the corresponding reflections of the (110) planes. Adapted with permission from ref. 25.

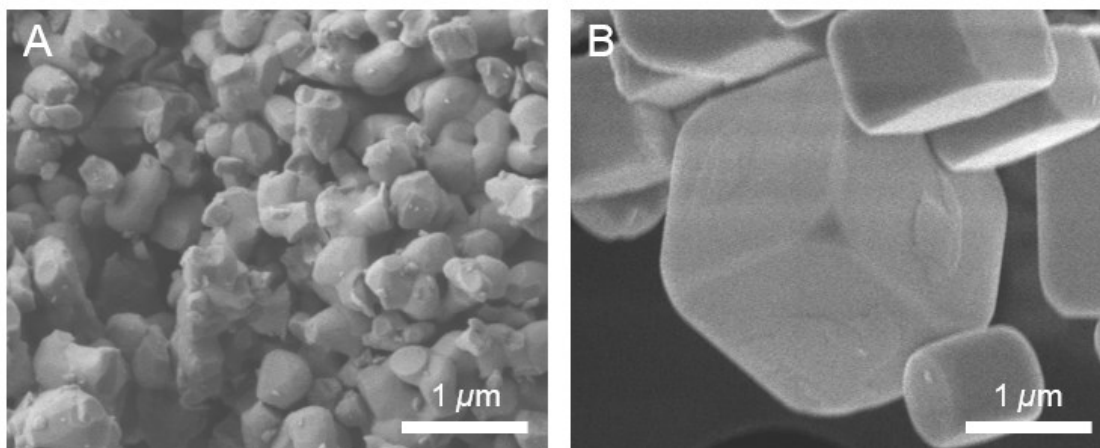


Figure 4.2. SEM micrographs of semiconductor photoabsorbers. (A) SrTiO₃. (B) Al-doped SrTiO₃.

Analysis of the elemental composition of the semiconductor treated in the alumina crucible confirmed doping with Al (Table 4.1). The resulting Al content (0.07 wt.%) corresponds to an incorporation of one Al³⁺ cation per about 220 Ti⁴⁺ sites assuming exclusive substitution of Ti⁴⁺ lattice sites by Al³⁺ (*vide infra*). Note that Al could not be determined in STO beyond the detection limits. Flux-mediated Al-doping did not alter the absorption onset in the DR UV-Vis spectra (SI-Fig. 4.2) and thus band gap (390 nm and 3.2 eV, respectively) in agreement with previous reports [17, 18]. However, the absorption spectrum of STO-Al depicted a steeper absorption edge compared to STO in line with its higher crystallinity and reduced defect density.

In the ²⁷Al MAS NMR spectra of STO-Al (Fig. 4.3), the prominent, narrow, isotropic signal with a chemical shift of 8 ppm was assigned to octahedrally coordinated Al³⁺ in agreement with the environment of Al³⁺ in substituted perovskites [26-30]. Note that ²⁷Al MAS NMR signals were not visible for STO. It is concluded that during SrCl₂ flux treatment Al³⁺ substitutes for Ti⁴⁺ in corner-sharing TiO₆-sites of SrTiO₃. Comparison of the ionic radii of Ti⁴⁺ and Sr²⁺ (0.0605 nm and 0.1180 nm in 6-fold and 12-fold coordination, respectively [31]) with the values for Al³⁺ (0.0535 nm in a 6-fold coordination [31]) corroborates a large

Table 4.1. Physicochemical properties of the semiconductor photoabsorbers.

Sample	BET surface area	Sr/Ti ratio	Al content	Ti/Al ratio	Band gap
	[m ² g ⁻¹]	[-]	[wt.%]	[-]	[eV]
STO	5.1	1.01	< 0.005	> 3050	3.2
STO-Al	2.7	0.98	0.07	220	3.2

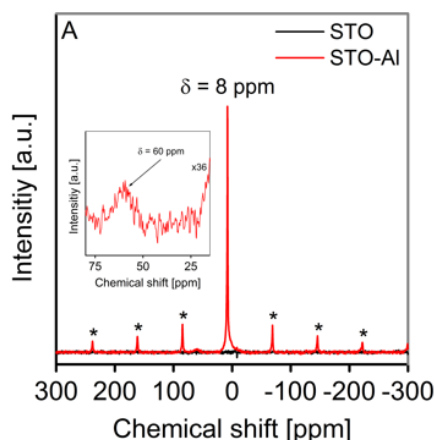


Figure 4.3. ^{27}Al MAS NMR spectra of pristine SrTiO_3 (STO) and Al-doped SrTiO_3 (STO-Al). The inset shows a magnified partial spectrum of STO-Al. Asterisks mark spinning side bands.

mismatch for substitution of Al^{3+} into 12-fold coordinated Sr^{2+} sites which would result in an unfavorable lattice strain. Nevertheless, a minor fraction of Al^{3+} in tetrahedral coordination in STO-Al was identified from a small signal at 60 ppm (inset of Fig. 4.3). Formation of coordinatively unsaturated (four- and five-fold coordinated) Al species through aliovalent doping of perovskites has been attributed to charge compensation and generation of oxygen vacancies/oxygen removal [27].

Co-catalysts

Nominal and experimental Rh loadings were in excellent agreement. Decoration of STO-Al with 0.1 wt.% Rh resulted in formation of $2.3 \text{ nm} \pm 0.9 \text{ nm}$ sized particles (see SI-Fig. 4.3 for TEM particle size distribution). ICP-OES analysis before/after chromia photo-deposition showed a Cr content of 0.1 wt.%, which corresponded to an atomic Cr/Rh ratio close to two. Photoreduction of Cr(VI)O_4^{2-} lead to formation of a Cr(III) shell around the Rh particles (see TEM images in SI-Fig. 4.4) through a self-inhibited growth mechanism [4, 19-21]. The missing pre-edge feature in Cr K-edge XANES (SI-Fig. 4.5) corroborated the absence of Cr(VI) in the prepared core-shell co-catalyst. Differences observed comparing the XANES recorded in aqueous-phase with the spectrum of a dry Cr_2O_3 reference (SI-Fig. 4.5) are attributed to the formation of a hydrated Cr(III)-oxyhydroxide in agreement with previous studies [19]. Beyond that, significant changes in the XANES recorded in different reaction media as well as before/after UV-Vis illumination were not observed.

4.4.2 H₂-generation from coupled H₂O-splitting and photoreforming

In order to elucidate the kinetics of coupled anodic water and oxygenate oxidation for simultaneous H₂-evolution we separately probed photocatalytic activities for overall H₂O-splitting (pure H₂O, in the absence of glycerol) on RhCrO_x/STO-Al and Rh/STO-Al (Fig. 4.4A). On RhCrO_x/STO-Al, H₂ and O₂ evolved stoichiometrically (H₂/O₂ ratio of 1.9 after 12 h) with an initial H₂-evolution rate of 411 $\mu\text{mol h}^{-1}$. Contrarily, on the bare Rh co-catalyst (inset in Fig. 4.4A) a maximum amount of only 35 μmol of H₂ was achieved, which declined (as well as the evolved O₂) over time. The difference in presence of chromia is in agreement with the conclusion that it forms a layer surrounding Rh, which suppresses the back-reaction by selectively inhibiting access of O₂ to the Rh surface while retaining the H⁺-reduction and H₂-evolution functionality [4, 19-21]. In contrast, over bare noble metals back-reaction to H₂O resulted in very low steady-state concentrations of H₂ and O₂ [6].

In aqueous glycerol solution (Fig. 4.4B), lower amounts of H₂ were produced than in pure H₂O (3035 μmol and 4025 μmol , respectively, after 12 h) on RhCrO_x/STO-Al. The initial H₂-evolution rates, however, were similar in the presence of glycerol (385 $\mu\text{mol h}^{-1}$) and in pure water. The amount of O₂ formed decreased substantially in the presence of the

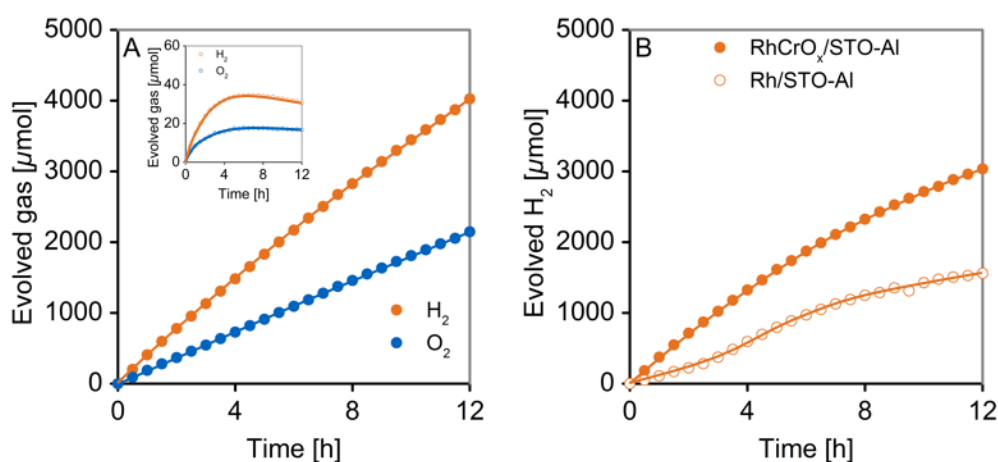


Figure 4.4. (A) Course of H₂- and O₂-evolution from pure H₂O on RhCrO_x/STO-Al. The inset shows H₂O-splitting on Rh/STO-Al. (B) H₂-evolution profiles in 20 mM aqueous glycerol on RhCrO_x/STO-Al and Rh/STO-Al. Lines represent a guide to the eye. Reaction conditions: 125 mg photocatalyst, 100 mL liquid (pure H₂O, pH unadjusted or 20 mM glycerol), 288 K, 1 bar Ar, 300 W Xe-lamp (CM1).

oxygenate (from 2147 μmol in pure H_2O to 1171 μmol after 12 h), which suggests that photogenerated oxidants were consumed to some extent in the oxidation of the organics. This was further confirmed by the detection of oxidation products from glycerol (*vide infra*).

On Rh/STO-Al, an induction period for H_2 -evolution was observed (Fig. 4.4B). We consider that this induction period results from higher initial rates of the back-reaction in agreement with the O_2 -evolution profile (Fig. 4.6). The rates of this back reaction decreased over time due to increasing concentrations of strongly adsorbing intermediates from glycerol oxidation (this is reflected in decreasing H_2/O_2 ratios from 6.8 to 4.0 after 12 h). After 8 h of reaction, the O_2 -partial pressure clearly leveled off (Fig. 4.6C), which indicates consumption of O_2 in the back-reaction in turn decreasing H_2 -evolution.

4.4.3 Anodic glycerol conversion on STO-Al photocatalysts

Equal glycerol conversion of $\sim 20\%$, and equal amounts of CO_2 and organic intermediates were attained on $\text{RhCrO}_x/\text{STO-Al}$ and on Rh/STO-Al after 12 h reaction (Figs. 4.5 and 4.6), despite the significantly lower amount of H_2 evolved on the latter. This observation, and the decreased amounts of O_2 evolved from Rh/STO-Al, allow to conclude that photogenerated oxidation equivalents participate in the back-reaction with H_2 in the absence of chromia, while intrinsic rates and selectivities to water and oxygenate oxidation at the anode are independent of the co-catalyst employed.

Thus, glycerol oxidation yielded similar selectivity profiles for $\text{RhCrO}_x/\text{STO-Al}$ and Rh/STO-Al (compare SI-Figs. 4.6 and 4.7). The only exception thereof, i.e. the increased selectivity to CO in the presence of chromia (maximum selectivities of 1.2 % and 4.4 % for Rh/STO-Al and $\text{RhCrO}_x/\text{STO-Al}$, respectively), is explained by faster oxidative removal of CO on Rh/STO-Al than on $\text{RhCrO}_x/\text{STO-Al}$ as shown by the control experiments described in SI-Fig. 4.8. We relate this difference in CO oxidation rates to the chromia shell hindering the adsorption of CO on the Rh surface [25]. Note, however, that the oxidative conversion of CO to CO_2 was more than an order of magnitude slower (maximum rate of about $2\ \mu\text{mol h}^{-1}$ on Rh/STO-Al) compared to CO_2 formation during glycerol oxidation. Thus, CO formation during glycerol photoreforming is concluded to be a side-

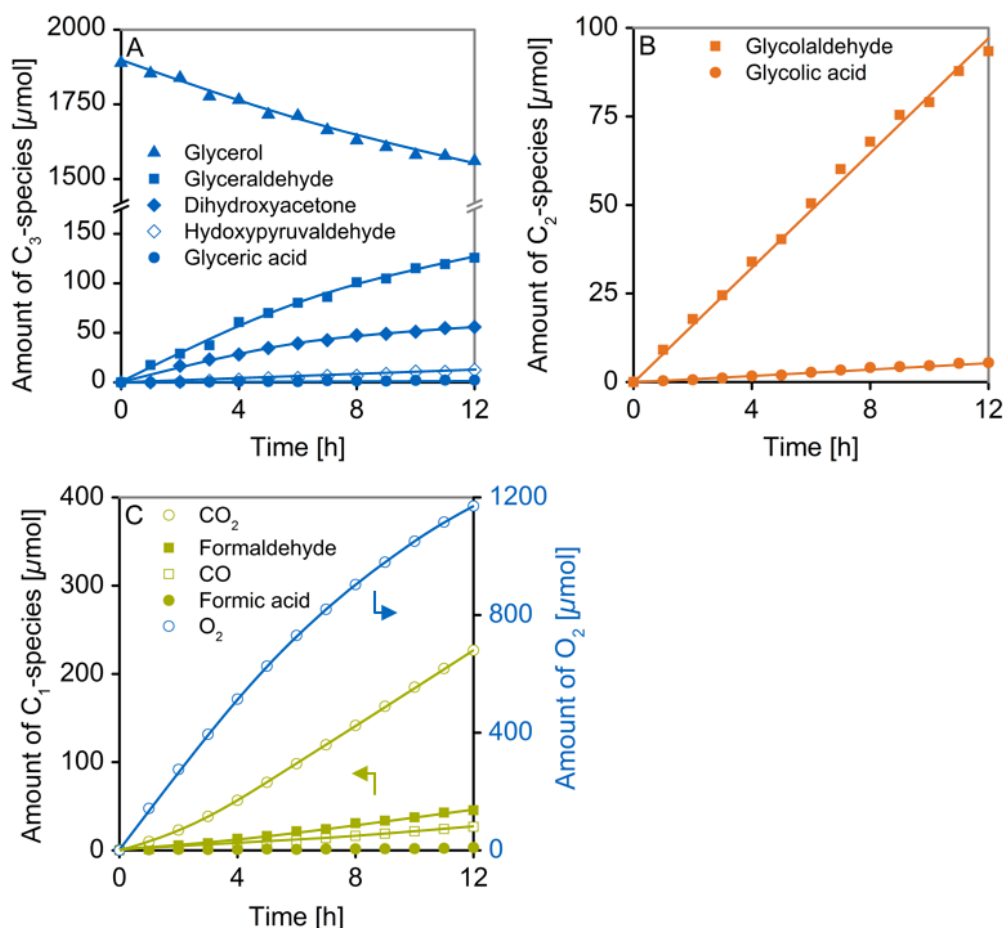


Figure 4.5. Course of glycerol and anodic reaction products during H₂-generation on RhCrO_x/STO-Al. (A) Course of amount of glycerol and C₃-intermediates. (B) Course of C₂-intermediates. (C) Course of C₁-species and O₂. Lines represent a guide to the eye. Reaction conditions: 125 mg photocatalyst, 100 mL aq. glycerol (20 mM), 288 K, 1 bar Ar, 300 W Xe-lamp (CM1).

reaction, instead of a main route masked by the oxidative CO transformation. These CO concentrations (< 2000 ppm) are too small to affect the degree of back-reaction on bare Rh [25]. Altogether, chromia on the co-catalyst prevents the oxidation of H₂ (back reaction to H₂O) and CO, whereas it does not significantly participate in the anodic surface chemistry and/or acts as hole-trapping site itself.

The courses of the anodic reaction products formed from 20 mM glycerol solution on RhCrO_x/STO-Al are presented in Fig. 4.5 (the data obtained on Rh/STO-Al is given in Fig. 4.6). Major products from glycerol oxidation on RhCrO_x/STO-Al in the liquid-phase were glyceraldehyde (GAD), glycolaldehyde and dihydroxyacetone (DHA) (126 μmol, 93 μmol and 56 μmol after 12 h, respectively, for molecular structures see SI-Table 4.2 and Scheme 4.1) along with the major reaction product CO₂ (227 μmol after 12 h) in the gas-

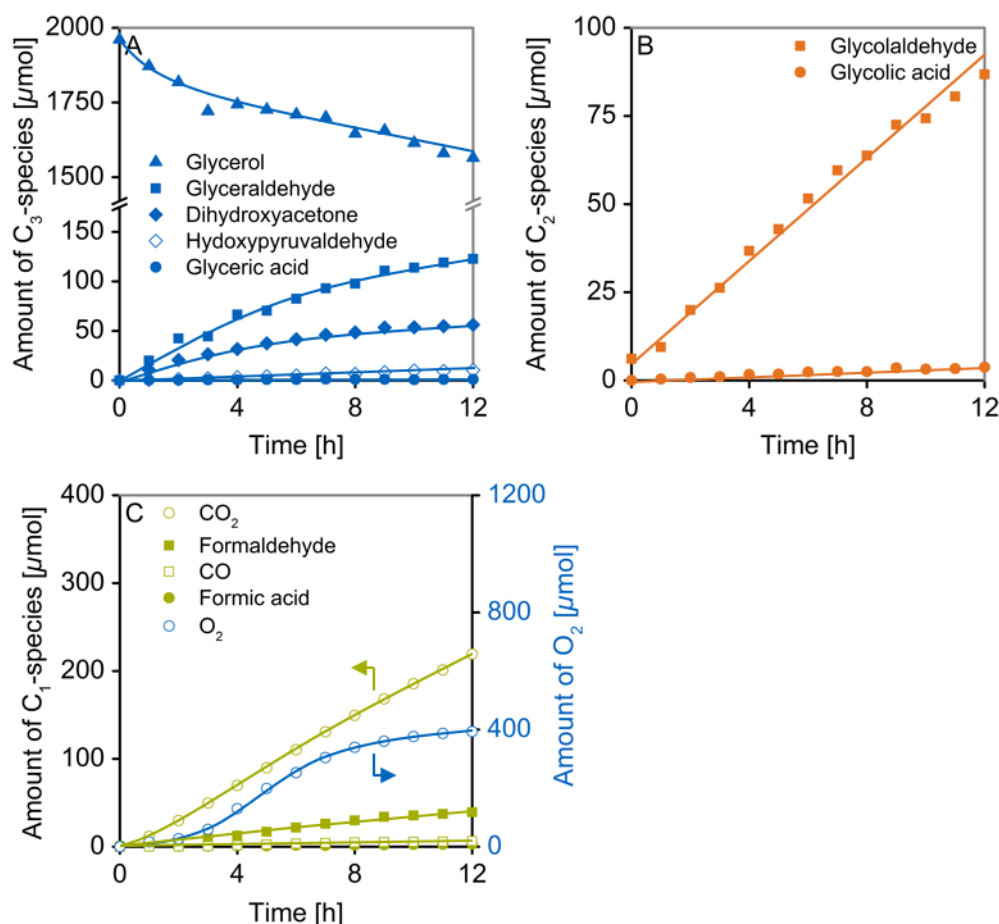
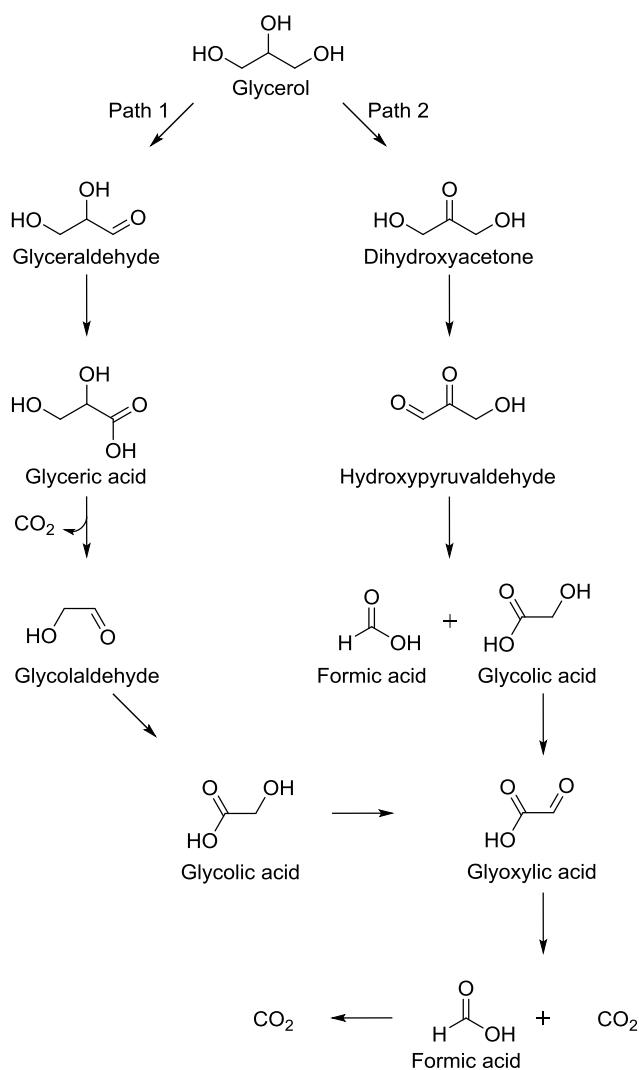


Figure 4.6. Course of glycerol and anodic reaction products during H₂-generation on Rh/STO-Al. (A) Course of amount of glycerol and C₃-intermediates. (B) Course of C₂-intermediates. (C) Course of C₁-species and O₂. Reaction conditions: 125 mg photocatalyst, 100 mL aq. glycerol (20 mM), 288 K, 1 bar Ar, 300 W Xe-lamp (CM1).

phase. The amounts of O₂ produced through water oxidation (1171 μmol after 12 h) exceeded the amounts of oxygenate oxidation products under these conditions. This selectivity, however, depends on oxygenate concentration and nature (*vide infra*).

4.4.4 Reaction network for glycerol oxidation

GAD, DHA, glycolaldehyde, and formaldehyde are primary products of anodic glycerol conversion. The C₃-products result from oxidation of a primary or secondary carbon atom, whereas glycolaldehyde and formaldehyde are formed *via* oxidative rupture of a C-C bond in glycerol in the first reaction step [11, 32]. Glycolaldehyde and formaldehyde may also form in consecutive transformations of GAD and DHA [11]. During glycerol photoreforming



Scheme 4.1. Proposed main reaction pathways for anodic glycerol conversion on photocatalysts based on Al-doped SrTiO_3 . In the first step, glycerol oxidation mainly proceeds *via* oxidation to glyceraldehyde or dihydroxyacetone. C-C cleavage occurs preferentially through removal of CO_2 or formic acid.

on $\text{RhCrO}_x/\text{STO-Al}$ the amounts of glycolaldehyde and formaldehyde present ($93 \mu\text{mol}$ and $45 \mu\text{mol}$, respectively after 12 h) were smaller than the summed amounts of GAD and DHA ($126 \mu\text{mol}$ and $56 \mu\text{mol}$, respectively after 12 h). Also, considering that highest initial selectivities were obtained for GAD and DHA (SI-Fig. 4.6) it becomes evident that glycerol oxidation must predominantly proceed *via* two parallel reaction pathways involving formation of either GAD or DHA in the first step (Scheme 4.1, Path 1 and 2). In other words, the oxidative C-C bond cleavage of glycerol to glycolaldehyde and formaldehyde is concluded to occur to a small extent. In addition to the C_3 aldehyde and ketone, anodic

glycerol conversion on RhCrO_x/STO-Al yielded low amounts of higher C₃-oxygenates as secondary products, i.e. glyceric acid (2 μmol after 12 h) and hydroxypyruvaldehyde (HPA) (12 μmol after 12 h), as well as glycolic acid (5 μmol after 12 h). CO (27 μmol after 12 h) and formic acid (3 μmol after 12 h) were furthermore identified as C₁-species.

In order to elucidate the reaction pathways in the consecutive oxidations of the primary products from glycerol, we examined the anodic transformations of C₃- and C₂-intermediates on RhCrO_x/STO-Al individually. The results are compiled in section 4.8, SI-Figs. 4.9-4.13. In the first pathway (Path I, Scheme 4.1), photocatalytic conversion of GAD (SI-Fig. 4.9) resulted in glycolaldehyde as the main product (175 μmol after 12 h) and a low steady-state amount of glyceric acid (5 μmol after 12 h). This is interpreted as the latter undergoing consecutive oxidation as a consequence of the high adsorption constants expected for carboxylic acids. Similar behavior was observed for glycolic acid (7 μmol after 12 h) and formic acid (10 μmol after 12 h). Indeed, the product distribution obtained from the photoreforming of glyceric acid indicated oxidative decarboxylation to glycolaldehyde (see SI-Fig. 4.10). Thus, in this reaction route, glycerol transforms to GAD, which further oxidizes to glyceric acid, which is consecutively decarboxylated to glycolaldehyde as depicted in Scheme 4.1.

Following the second path for glycerol oxidation (Scheme 4.1), the conversion of DHA (SI-Fig. 4.11) yielded major quantities of hydroxypyruvaldehyde (HPA, 410 μmol after 12 h) with glycolic acid (64 μmol after 12 h) as the only C₂-species. Therefore, DHA (687 μmol converted after 12 h) is primarily oxidized to HPA prior to C-C cleavage. Thus, traces of HPA (4 μmol after 12 h) present during GAD conversion (in the first path) indicate a minor side-reaction. β-Hydroxypyruvic acid, as a possible intermediate, could not be detected. Further oxidation of HPA is proposed to result in formation of glycolic acid and formic acid with the latter being rapidly transformed to CO₂.

Glycolic acid is formed as a primary product during oxidation of glycolaldehyde (SI-Fig. 4.12), whereas the conversion of glycolic acid (SI-Fig. 4.13) discloses further oxidation to glyoxylic acid, a compound not encountered during photoreforming of glycerol. Glyoxylic acid may decarboxylate to formic acid. Further oxidation of glyoxylic acid to oxalic acid (which cannot be detected by ¹H-NMR techniques), whose oxidation would lead exclusively to CO₂, cannot be ruled out.

In summary, primary oxidation of glycerol to its corresponding aldose and ketose is followed by oxidation to higher C₃ oxygenates. These undergo oxidative decarboxylation or cleavage of formic acid, respectively. The oxidation of intermediate glycolaldehyde to higher oxygenates prior to C-C bond rupture was also previously encountered on a Rh decorated GaN:ZnO solid solution semiconductor [10]. The generation of these higher oxygenates, which does not occur on TiO₂ [10, 11], is ascribed to the ability for water oxidation of GaN:ZnO and SrTiO₃ resulting in additional pathways *via* interaction with photogenerated oxidants formed during water oxidation (*vide infra*). We show in this report that starting from GAD, DHA, glycolaldehyde or glycolic acid as C₃/C₂-intermediates similar pathways prevail until full oxidation to CO₂ on SrTiO₃ is achieved.

The production of formaldehyde (selectivities of 5.8 - 7.6 % from glycerol photoreforming on RhCrO_x/STO-Al, SI-Fig. 4.6), which is not represented in the main reaction routes shown in Scheme 4.1, may occur by cleavage of terminal C-C bonds in polyols, aldoses and ketoses, namely (i) glycerol, (ii) DHA; (iii) glycolaldehyde or (iv) glycolic acid as illustrated in SI-Scheme 4.1. Mechanistically, these transformations are attributed to direct hole transfer to the chemisorbed oxygenates [10, 11, 32]. The subordinate role of this type of transformation for compounds without carboxylic groups on STO-Al was consistently observed in the photoreforming experiments with the individual reaction intermediates (SI-Figs. 4.9-4.13). This, and the formation of higher oxygenates from aldoses and ketoses through predominantly indirect mechanisms allow for removal of CO₂ or formic acid as C₁-moieties (Scheme 4.1). Thus, low formaldehyde selectivities compared to glycerol photoreforming on Rh decorated TiO₂ P 25 (selectivity of 36 – 41 % at comparable glycerol conversions [11]) are attained.

4.4.5 Effect of the nature of the oxygenate and its concentration on H₂-evolution rates

We investigated the factors governing H₂-evolution rates and selectivities to water and oxygenate oxidation at the anode by examination of their dependence on glycerol concentration, oxygenate nature at constant concentration (20 mM), on H/D kinetic isotope effects, and on photon-flux. On RhCrO_x/STO-Al, initial H₂-evolution rates during

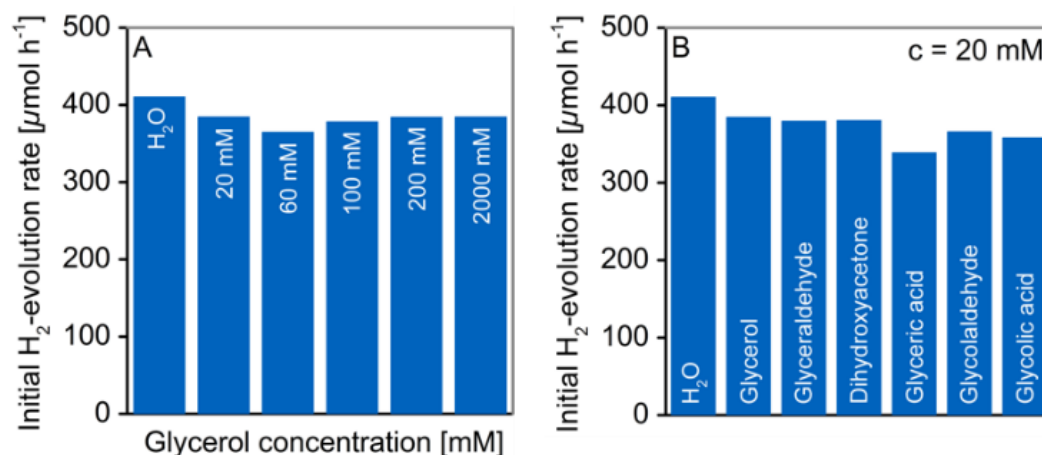


Figure 4.7. Initial H₂-evolution rates during coupled water splitting and oxygenate photoreforming on RhCrO_x/STO-Al. (A) Dependence of H₂-evolution rates on glycerol concentration. (B) Dependence of rates on oxygenate nature at constant concentration (20 mM). Reaction conditions: 125 mg RhCrO_x/STO-Al, 100 mL aq. oxygenate, 288 K, 1 bar Ar, 300 W Xe-lamp (CM1).

photoreforming were similar to the rate during overall water splitting and independent of the glycerol concentration across a wide range (Fig. 4.7A). Initial H₂-evolution rates from aqueous solutions of different C₃- and C₂-oxygenates at constant concentration (20 mM) disclosed a similar behavior (Fig. 4.7B). Hence, overall photocatalytic rates were not affected whether photogenerated oxidation equivalents participated in O₂-evolution or in oxygenate oxidation in the anodic half-reactions. In short, the surface chemical transformations at the anode did not limit the overall photocatalytic rates irrespective of their nature under these conditions. Thus, coupled photocatalytic water splitting and photoreforming on RhCrO_x/STO-Al (under conditions of suppressed back-reaction) allows to maintain high H₂-evolution rates even at low oxygenate concentrations and coverages since water-covered sites catalyze oxidation to O₂ at the same quantum efficiency in the absence of oxygenates. Contrarily, for semiconductors not able to catalyze anodic formation of O₂ from water in the absence of sacrificial agents, e.g. TiO₂, photocatalytic rates depend on oxygenate concentration in terms of surface coverage according to Langmuir-type kinetics [12-14]. As a consequence, full oxidation of oxygenates to CO₂ on the latter systems inevitably involves low H₂-evolution rates at high conversions. Note that under conditions of low oxygenate coverage, holes trapped at sites without interaction with oxygenates (solely surrounded by water) enhance the rates of electron-hole recombination.

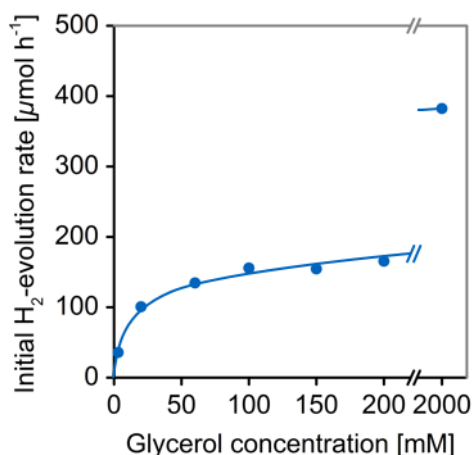


Figure 4.8. Dependence of initial H₂-evolution rates on glycerol concentration on Rh/STO-Al. Reaction conditions: 125 mg Rh/STO-Al, 100 mL aq. glycerol, 288 K, 1 bar Ar, 300 W Xe-lamp (CM1).

On Rh/STO-Al, the initial H₂-evolution rates increased with glycerol concentration following a Langmuir-type behavior at least up to 200 mM glycerol (Fig. 4.8). At that concentration or below, initial H₂-evolution rates on Rh/STO-Al were lower than on RhCrO_x/STO-Al (166 μmol h⁻¹ compared to 384 μmol h⁻¹, respectively). However, at very high glycerol concentrations, e.g. 2000 mM, equivalent rates were achieved on Rh/STO-Al and RhCrO_x/STO-Al (382 μmol h⁻¹ and 385 μmol h⁻¹, respectively). This observation is attributed to an increasing share of photogenerated oxidation equivalents that participated in glycerol oxidation instead of O₂-evolution thereby suppressing O₂-formation and, in turn, the back-reaction on Rh. Therefore, low H₂-evolution rates on Rh/STO-Al at low oxygenate concentrations are due to relatively fast back-reaction.

4.4.6 Kinetic isotope effects in H₂-evolution rates

Whereas H₂-evolution rates on RhCrO_x/STO-Al are not influenced by the anodic half-reactions, we investigated a possible rate-limiting participation of surface reactions at the cathode by examination of kinetic isotope effects for H₂- or D₂-evolution, i.e. the ratio of the corresponding gas evolution rates, in H₂O/D₂O and in glycerol/glycerol-d⁸ solutions in H₂O/D₂O (Fig. 4.9). Kinetic isotope effects of 1.1 in pure H₂O and D₂O or 20 mM glycerol or glycerol-d⁸ in H₂O or D₂O were observed. These are in good agreement with the low H₂O/D₂O isotope effects previously reported for overall water splitting on RhCrO_x decorated semiconductors [33, 34]. Kinetic isotope effects close to unity indicate that, at the optimum co-catalyst loading and irradiation conditions, the factor constraining the rate

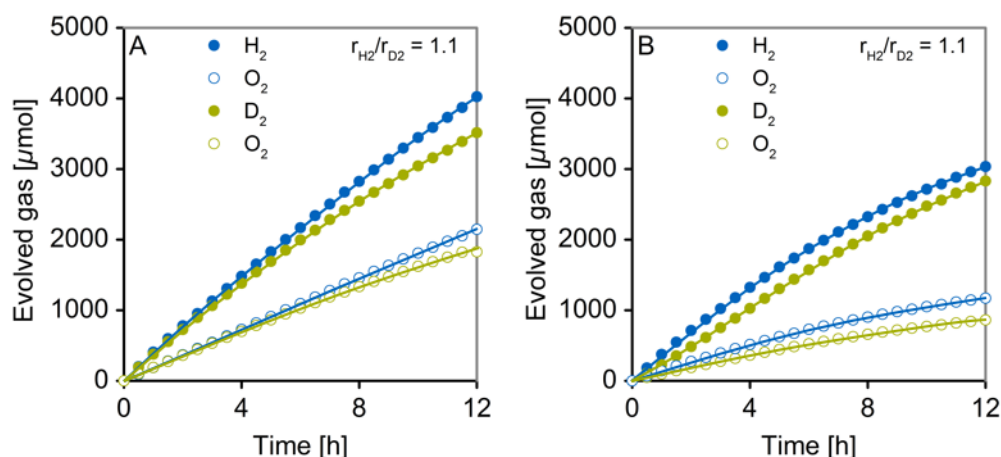


Figure 4.9. Comparison of the courses of H_2 , D_2 and O_2 on $\text{RhCrO}_x/\text{STO-Al}$ during (A) $\text{H}_2\text{O}/\text{D}_2\text{O}$ -splitting and (B) photocatalytic H_2 -evolution from 20mM glycerol/glycerol- d^8 in $\text{H}_2\text{O}/\text{D}_2\text{O}$ for determination of kinetic isotope effects for H_2/D_2 -evolution. Reaction conditions: 125 mg $\text{RhCrO}_x/\text{STO-Al}$, 100 mL liquid, 288 K, 1 bar Ar, 300 W Xe-lamp (CM1).

of surface redox reactions is the availability of photogenerated charge carriers.

4.4.7 Effect of the nature of the oxygenate and its concentration on H_2O and oxygenate oxidation selectivity

Although overall H_2 -evolution rates were independent of glycerol concentration on $\text{RhCrO}_x/\text{STO-Al}$, anodic selectivities gradually favored glycerol photoreforming over O_2 -evolution with increasing glycerol concentration as shown in Fig. 4.10A. At 20 mM, oxidation equivalents generated from 25 % of the trapped holes participated in the oxidation of glycerol, while at 200 mM about 50 % of the holes eventually lead to O_2 -formation. The substantial glycerol concentration of 2000 mM was required in order to nearly prevent anodic O_2 -evolution. Under these conditions, 90 % of the holes participated in glycerol oxidation. This agrees well with the H_2 -evolution rates obtained on $\text{Rh}/\text{STO-Al}$ (Fig. 4.8), which show that O_2 -formation and thus back-reaction is nearly suppressed at 2000 mM glycerol resulting in equal rates compared to $\text{RhCrO}_x/\text{STO-Al}$.

Anodic selectivities obtained from different oxygenates at constant concentration (Fig. 4.10B) show a dependency on molecular nature. The highest selectivities for photoreforming were observed in the presence of carboxylic acids (glyceric acid and

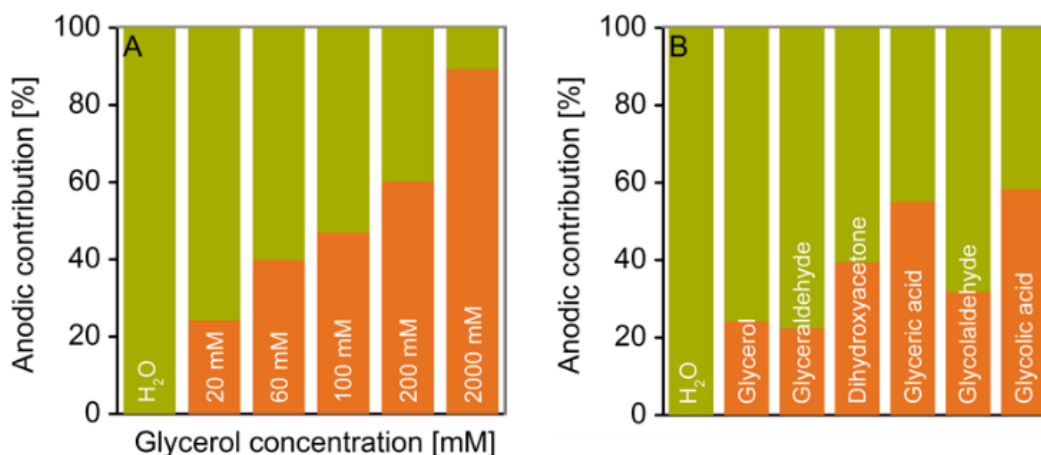


Figure 4.10. Selectivities for O₂-evolution (green) and glycerol oxidation (orange) in the anodic half-reactions on RhCrO_x/STO-Al. (A) Dependence of anodic selectivities on glycerol concentration. (B) Relative anodic contributions in dependence of oxygenate nature at 20 mM. Reaction conditions: 125 mg RhCrO_x/STO-Al, 100 mL aq. oxygenate, 288 K, 1 bar Ar, 300 W Xe-lamp (CM1).

glycolic acid) with up to 58 % of the holes participating in photoreforming in the case of glycolic acid at 20 mM.

This is ascribed to high adsorption constants of acids on coordinatively unsaturated Ti⁴⁺ sites with terminal OH-groups [10, 11, 35] in line with the low steady-state concentrations encountered for these species when formed as intermediates during photoreforming experiments (e.g. see Figs. 4.5 and 4.6). Correspondingly, lower photoreforming selectivities were obtained for ketones, aldehydes and polyols for which weaker adsorption on STO-Al is anticipated.

4.4.8 Effect of light intensity

Initial H₂-, O₂- and CO₂-formation rates increased linearly with increasing photon flux at 200 mM glycerol (Fig. 4.11A). The H₂-evolution rates correspond to an apparent quantum efficiency of about 17 % for the RhCrO_x/STO-Al photocatalyst employed in this study. Previous investigations reported quantum efficiencies of about 30 % at 350 nm and 360 nm for this kind of photocatalyst, albeit, at different reaction conditions [16, 17]. The double logarithmic graph in Fig. 4.11B indicates that H₂-evolution rates followed a first-order dependence on photon flux. This is typically encountered under conditions, where accumulation of photogenerated charge carriers is negligible [12, 36, 37]. Otherwise, charge accumulation opens up additional routes for recombination, which is identified

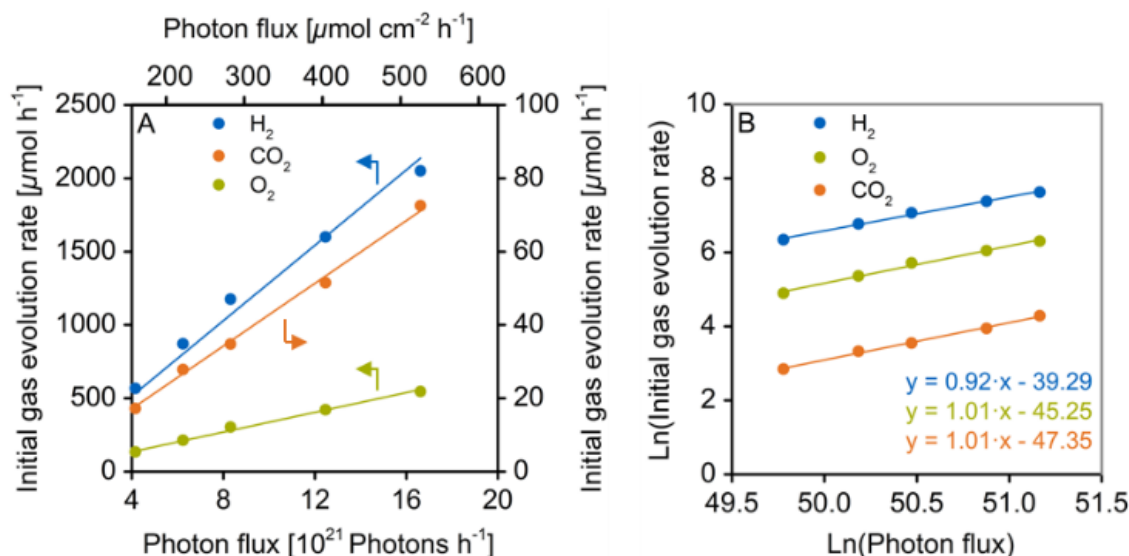


Figure 4.11. Light-intensity dependence of initial photocatalytic rates for H_2 -, O_2 - and CO_2 -evolution on $\text{RhCrO}_x/\text{STO-Al}$. (A) Dependence of initial rates on photon flux. (B) Determination of reaction order with respect to photon flux. Reaction conditions: 125 mg $\text{RhCrO}_x/\text{STO-Al}$, 100 mL aq. glycerol (200 mM), 288 K, 1 bar Ar, UV LEDs ($365 \text{ nm} \pm 5 \text{ nm}$).

with a square-root type dependence on photon flux [12, 36, 37]. In conclusion, overall photocatalytic rates in coupled water splitting and photoreforming on $\text{RhCrO}_x/\text{STO-Al}$ are determined by charge carrier generation (absorption) and separation, i.e. the number of charge carriers available for surface redox reactions. The first-order dependencies for O_2 and CO_2 formation rates imply that the selectivities to water and oxygenate oxidation at the anode were not influenced by photon flux within the range explored.

4.4.9 Mechanistic considerations

Using C_3/C_2 -oxygenates as probe molecules allows for discrimination of direct and indirect pathways as these yield different chemical intermediates. In case of glycerol [10, 11, 32], direct hole transfer generates an alkoxy-radical, which undergoes β -C-C bond cleavage to form glycolaldehyde and formaldehyde. In the indirect mechanism, carbon-centered radicals are formed *via* abstraction of a $\text{H}\cdot$ through interaction with ‘shallowly trapped holes’. These carbon-centered radicals may further oxidize to GAD or DHA [10, 11, 32]. From the reaction network for glycerol oxidation on STO-Al based photocatalysts (Scheme 4.1), it is evident that the two main reaction pathways in the first step of glycerol oxidation formally correspond to an indirect mechanism. As an exception therefrom, oxidative decarboxylation of glyceric acid and glyoxylic acid and C-C bond cleavage of

HPA in the consecutive reactions have to proceed *via* direct hole transfer to the chemisorbed species. Evidence for a direct hole transfer mechanism dominating the oxidative decarboxylation during photooxidation of organic acids was provided for, e.g. terephthalic acid [38], acetic acid [39, 40], oxalic acid [40, 41] and formic acid [35, 42].

For two electron oxidation reactions on TiO_2 *via* sequential transfer of charge carriers, i.e. involving a one-electron oxidized radical species, commonly a ‘current doubling’ process (electron injection of the radical into the semiconductor’s CB) is put forward for the second charge transfer to complete oxidation [43, 44]. This is because the time interval for the availability of the second hole usually exceeds the lifetime of the radicals [45]. However, on the catalysts studied in this work, approximately 10^8 photons s^{-1} impinge per catalyst particle (deduced in detail in section 4.8), which is in the order of the radical lifetimes (ns range). Observation of initial H_2 -evolution rates being unaffected by the selectivity of water and oxygenate oxidation (Figs. 4.7 and 4.10) further indicate a minor contribution of current doubling. This is because with current doubling one photogenerated charge carrier is consumed at the anode but two reduction equivalents are available at the cathode boosting H_2 -evolution. Thus, if a current doubling process would prevail, increasing H_2 -evolution rates are expected to be associated with increasing selectivities for photoreforming over water oxidation. Hence, our experimental observations point to a large contribution of sequential interaction with two photogenerated oxidants to the mechanism of oxygenate oxidation.

Concerning the nature of the oxidant, on a semiconductor active in water oxidation to evolve O_2 at the anode, any intermediate oxygen-centered radical species (assumed as $\cdot\text{OH}$, $\cdot\text{O}$ and $\cdot\text{OOH}$ in the simplified mechanism in SI-Scheme 4.2 [46]) is expected to enable transformations corresponding to an indirect mechanism (as observed in the main pathways for glycerol oxidation) by abstracting a H-atom from a C-H bond. Spectroscopic evidence has been recently provided for the generation of the oxyl radical $[\text{Ti}\cdot\text{O}\cdot]$ during water oxidation upon band gap irradiation of a $\text{SrTiO}_3/\text{water}$ interface [47, 48]. These reports, in combination with our findings that water and oxygenate oxidation proceed with equal quantum efficiencies independent of oxygenate nature or coverage (Fig. 4.7), allow proposing that the intermediates generated in O_2 -evolution catalysis at the anode

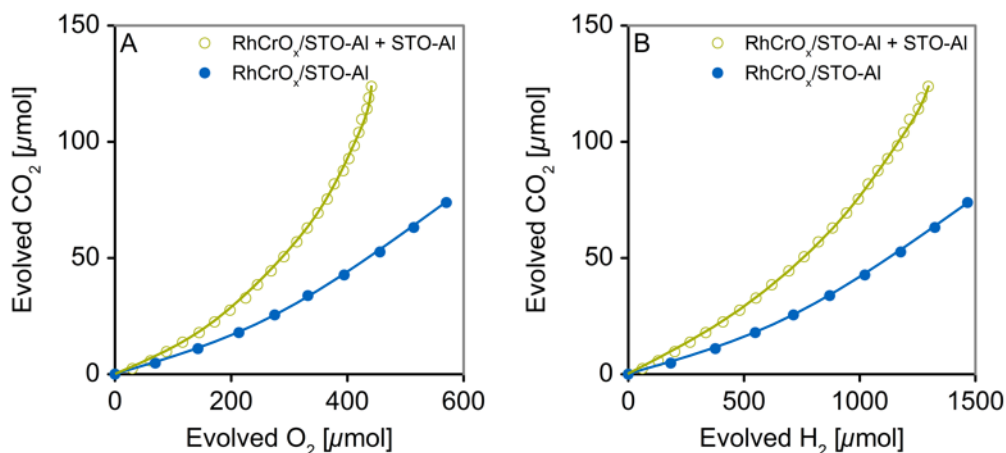
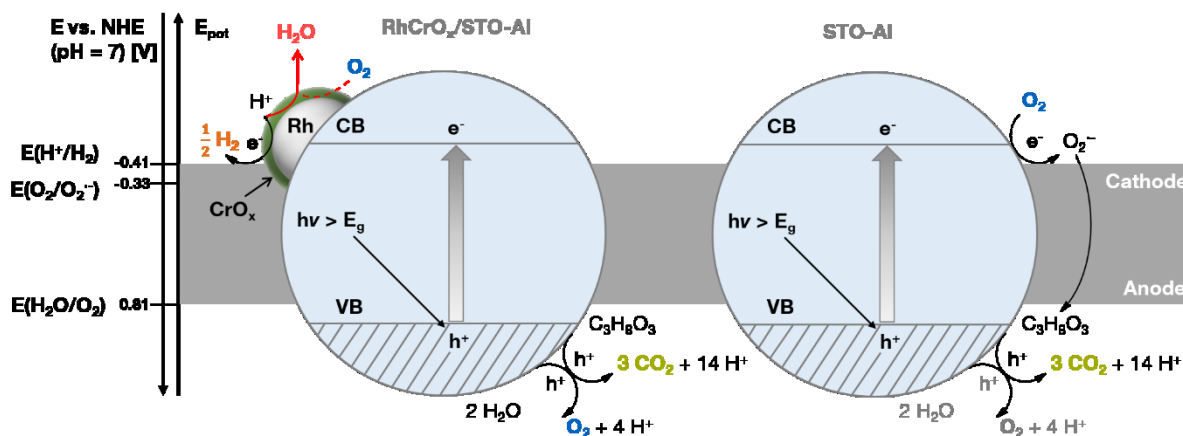


Figure 4.12. Comparison of amounts of evolved CO₂ on RhCrO_x/STO-Al and a physical mixture of RhCrO_x/STO-Al and undecorated STO-Al at (A) given amount of evolved O₂ (B) given amount of evolved H₂. Reaction conditions: 62.5 mg RhCrO_x/STO-Al and 62.5 mg STO-Al (green traces), 125 mg RhCrO_x/STO-Al (blue traces), 100 mL aq. glycerol (20 mM), 288 K, 1 bar Ar, 300 W Xe-lamp (CM1).

constitute the major photogenerated oxidant in this system. This hypothesis is further substantiated in the following.

Molecular O₂ does not act as oxidant for the organics because (i) no chemical transformations were observed in the dark in the presence of O₂, (ii) reductive activation at the cathode under illumination, e.g. to form O₂^{•-}, is suppressed by the chromia shell [4, 19-21], (iii) similar glycerol conversions, product formation rates and selectivities were obtained over Rh and RhCrO_x decorated semiconductors despite different O₂ partial pressures present. Moreover, in the presence of a co-catalyst acting as an electron trap the availability of electrons for O₂ reduction at the semiconductor surface is greatly diminished in contrast to aerobic photooxidation, where O₂ is reductively activated ($E^0(\text{O}_2/\text{O}_2^{\bullet-}) = -0.33 \text{ V vs. NHE at pH} = 7$ [49]) on undecorated STO-Al (CB edge potential $E^0 = -1.2 \text{ V vs. NHE at pH} = 7$ [50]). We provided evidence of this effect of the co-catalyst by testing a physical mixture of RhCrO_x/STO-Al and undecorated STO-Al in glycerol photoreforming (Fig. 4.12 and SI-Fig. 4.14). In this experiment, we observed enhanced CO₂ formation coupled with O₂ consumption compared to RhCrO_x/STO-Al alone. This confirms that O₂ formed in the anodic half-reaction on RhCrO_x/STO-Al was reductively activated on undecorated STO-Al and subsequently consumed in glycerol photooxidation



Scheme 4.2. Illustration of cathodic and anodic half-reactions occurring in a physical mixture of RhCrO_x/STO-Al and undecorated STO-Al upon band gap irradiation in aqueous glycerol. Formation of consecutive oxidants from O₂⁻ in the cathodic half-reaction on undecorated STO-Al and interaction with glycerol was abbreviated for simplicity.

according to the pathways depicted in Scheme 4.2. That way, O₂ could be removed from the gaseous mixture generated by coupling water splitting and photoreforming. No significant changes in selectivities compared to RhCrO_x/STO-Al alone were encountered within the glycerol conversion range explored (SI-Figs. 4.6 and 4.15).

H₂O₂ was previously detected during glycerol photoreforming on Pt/TiO₂ [51] and proposed as an intermediate (or radical species derived therefrom) during water oxidation on oxides [52-54]. Furthermore, UV photolysis of aqueous H₂O₂ (absorbs up to about 400 nm) was reported to yield OH-radicals [55, 56], which oxidize methanol [55]. Thus, we explored the effect of H₂O₂ addition on the product distributions on Rh/STO-Al and RhCrO_x/STO-Al (SI-Fig. 4.16 and Fig. 4.13). Slow formation of O₂ (and likely water) was observed over both catalysts during an initial dark period which is assigned to decomposition of H₂O₂. Upon irradiation, a large amount of O₂ was suddenly released ($E^0(\text{O}_2/\text{H}_2\text{O}_2) = 0.27 \text{ V vs. NHE at pH} = 7$ [57], VB top of STO $E^0 = 2.0 \text{ V vs. NHE at pH} = 7$ [50]), which was not accompanied by any increased formation of organic oxidation products. Selectivities for reaction products on Rh/STO-Al and RhCrO_x/STO-Al remained notably unaffected compared to H₂O₂-free conditions in the subsequent irradiation period (compare SI-Figs. 4.6 and 4.7 with SI-Figs. 4.17 and 4.18). Thus, H₂O₂ exclusively underwent decomposition to O₂ and water under these conditions without itself or species generated therefrom oxidizing glycerol.

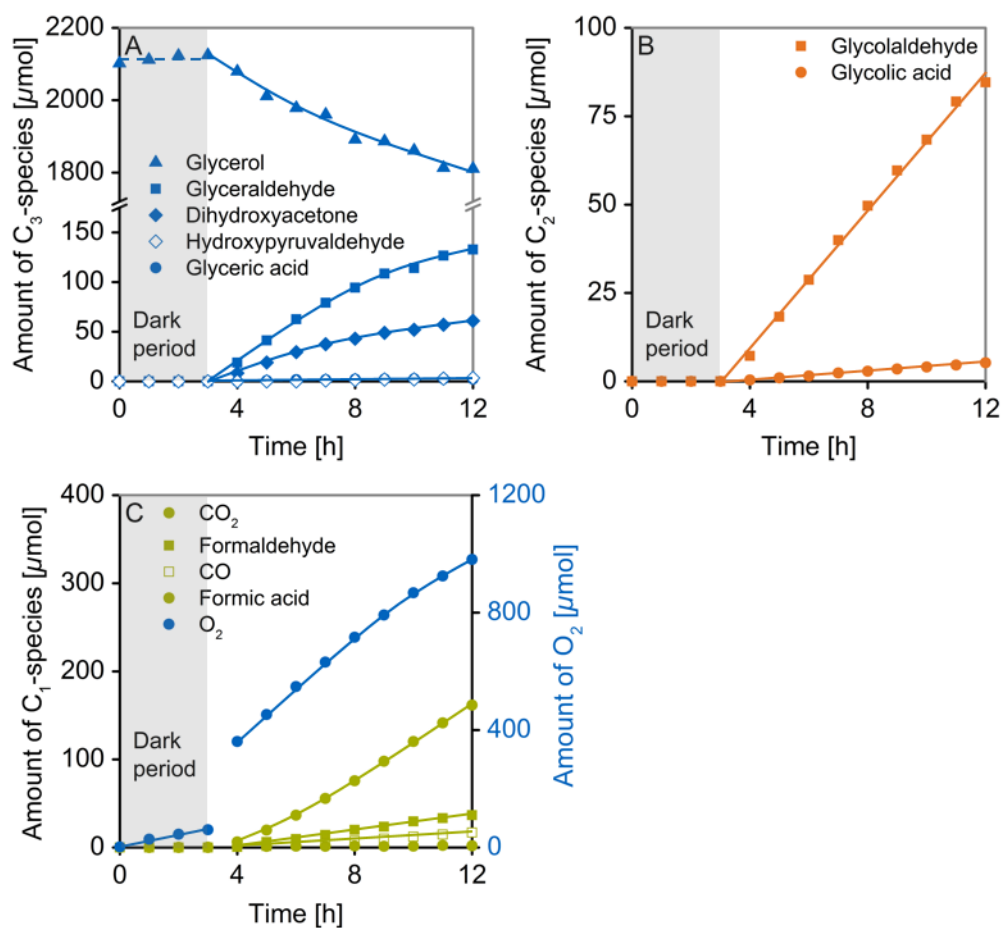


Figure 4.13. Course of glycerol and anodic reaction products during H₂-generation on RhCrO_x/STO-Al. Irradiation was provided after an initial dark period of 3 h. (A) Course of amount of glycerol and C₃-intermediates. (B) Course of C₂-intermediates. (C) Course of C₁-species and O₂. Reaction conditions: 125 mg RhCrO_x/STO-Al, 100 mL liquid, 20 mM glycerol, 4 mM H₂O₂, 288 K, 1 bar Ar, 300 W Xe-lamp (CM1).

4.5 Conclusions

Kinetic coupling of overall water splitting and photoreforming on Rh/STO-Al and RhCrO_x/STO-Al enables efficient H₂-generation combined with the degradation of oxygenates. Glycerol was converted on the STO-Al semiconductor following indirect hole transfer transformations, which predominate as a consequence of the water oxidation activity at the anode. Thus, in the main reaction pathways glycerol oxidized to GAD and DHA, which was followed by further oxidation to glyceric acid and HPA prior to C-C bond cleavage. These routes allow for direct removal of CO₂ and formic acid as C₁-moieties, therefore, avoiding the formation of undesired formaldehyde. Anodic organic oxidation is concluded to be driven by intermediates generated in O₂-evolution catalysis (e.g. ·OH, ·O, and ·OOH). Photogenerated O₂ may be reductively activated on undecorated STO-Al (Rh/STO-Al) to participate in glycerol oxidation without consuming evolved H₂. However, on Rh/STO-Al, H₂ is consumed in the back reaction with O₂ to H₂O, which can be suppressed in the presence of the CrO_x shell (RhCrO_x/STO-Al) or excess of oxygenates. In the absence of the back reaction, overall H₂-evolution rates in presence/absence of oxygenates were independent of oxygenate nature and concentration. Therefore, water and oxygenate oxidation at the anode result in equal quantum efficiencies for the overall process. On the other hand, the selectivity to organic oxidation did depend on oxygenate nature and increased along with concentration. Thus, coupling overall water splitting and photoreforming allows overcoming the drawbacks of both process alone, i.e. H₂ consumption in secondary reactions (overall water splitting) and the dependence of H₂-evolution rates and product selectivity on surface coverage (photoreforming).

4.6 Acknowledgements

K.E.S. gratefully acknowledges financial support by the Fonds der Chemischen Industrie (FCI). The authors would like to thank ESRF in Grenoble, France, for providing beam time at the ID26 station for XAFS experiments. We thank Xaver Hecht for BET measurements, Martin Neukamm for SEM and AAS measurements and Dr. Udishnu Sanyal for TEM imaging. Christine Schwarz is acknowledged for technical assistance in NMR experiments.

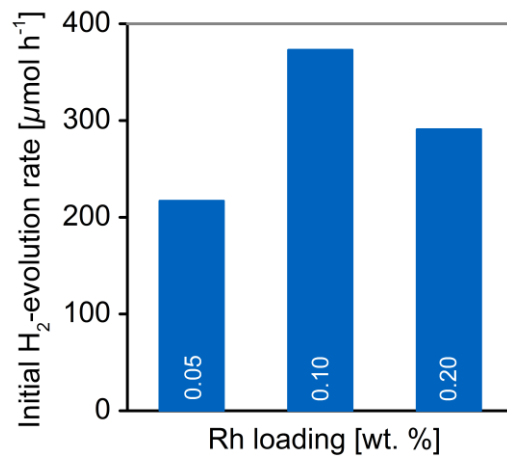
4.7 References

- [1] K. Takanabe, K. Domen, *Green* 1 (2011) 313-322.
- [2] F.E. Osterloh, *Chem. Mater.* 20 (2008) 35-54.
- [3] A. Kudo, Y. Miseki, *Chem. Soc. Rev.* 38 (2009) 253-278.
- [4] K. Maeda, K. Teramura, D. Lu, N. Saito, Y. Inoue, K. Domen, *Angew. Chem. Int. Edit.* 118 (2006) 7970-7973.
- [5] T. Takata, C. Pan, M. Nakabayashi, N. Shibata, K. Domen, *J. Am. Chem. Soc.* 137 (2015) 9627-9634.
- [6] F. Dionigi, P.C.K. Vesborg, T. Pedersen, O. Hansen, S. Dahl, A. Xiong, K. Maeda, K. Domen, I. Chorkendorff, *J. Catal.* 292 (2012) 26-31.
- [7] D. Kondarides, V. Daskalaki, A. Patsoura, X. Verykios, *Catal. Lett.* 122 (2008) 26-32.
- [8] G.L. Chiarello, M.H. Aguirre, E. Selli, *J. Catal.* 273 (2010) 182-190.
- [9] M. Bowker, P.R. Davies, L.S. Al-Mazroai, *Catal. Lett.* 128 (2008) 253-255.
- [10] T.F. Berto, K.E. Sanwald, W. Eisenreich, O.Y. Gutiérrez, J.A. Lercher, *J. Catal.* 338 (2016) 68-81.
- [11] K.E. Sanwald, T.F. Berto, W. Eisenreich, O.Y. Gutiérrez, J.A. Lercher, *J. Catal.* 344 (2016) 806-816.
- [12] G.N. Nomikos, P. Panagiotopoulou, D.I. Kondarides, X.E. Verykios, *Appl. Catal. B* 146 (2014) 249-257.
- [13] X. Fu, J. Long, X. Wang, D.Y.C. Leung, Z. Ding, L. Wu, Z. Zhang, Z. Li, X. Fu, *Int. J. Hydrogen Energ.* 33 (2008) 6484-6491.
- [14] L.S. Al-Mazroai, M. Bowker, P. Davies, A. Dickinson, J. Greaves, D. James, L. Millard, *Catal. Today* 122 (2007) 46-50.
- [15] Y.-J. Cho, G.-h. Moon, T. Kanazawa, K. Maeda, W. Choi, *Chem. Commun.* 52 (2016) 9636-9639.
- [16] Y. Ham, T. Hisatomi, Y. Goto, Y. Moriya, Y. Sakata, A. Yamakata, J. Kubota, K. Domen, *J. Mater. Chem. A* 4 (2016) 3027-3033.
- [17] A. Yamakata, H. Yeilin, M. Kawaguchi, T. Hisatomi, J. Kubota, Y. Sakata, K. Domen, *J. Photoch. Photobio. A* 313 (2015) 168-175.
- [18] H. Kato, M. Kobayashi, M. Hara, M. Kakihana, *Catal. Sci. Technol.* 3 (2013) 1733-1738.

- [19] M. Yoshida, K. Takanabe, K. Maeda, A. Ishikawa, J. Kubota, Y. Sakata, Y. Ikezawa, K. Domen, *J. Phys. Chem. C* 113 (2009) 10151-10157.
- [20] K. Maeda, K. Teramura, D. Lu, N. Saito, Y. Inoue, K. Domen, *J. Phys. Chem. C* 111 (2007) 7554-7560.
- [21] K. Maeda, N. Sakamoto, T. Ikeda, H. Ohtsuka, A. Xiong, D. Lu, M. Kanehara, T. Teranishi, K. Domen, *Chem. Eur. J.* 16 (2010) 7750-7759.
- [22] M. Tromp, J. Moulin, G. Reid, J. Evans, Cr K-edge XANES spectroscopy: ligand and oxidation state dependence-what is oxidation state?, in: *X-Ray Absorption Fine Structure--XAFS* 13, 2007, pp. 699-701.
- [23] H. Kato, Y. Sasaki, N. Shirakura, A. Kudo, *J. Mater. Chem. A* 1 (2013) 12327-12333.
- [24] T. Sano, D.M. Saylor, G.S. Rohrer, *J. Am. Ceram. Soc.* 86 (2003) 1933-1939.
- [25] T.F. Berto, K.E. Sanwald, J.P. Byers, N.D. Browning, O.Y. Gutiérrez, J.A. Lercher, *J. Phys. Chem. Lett.* 7 (2016) 4358-4362.
- [26] R. Dupree, M.H. Lewis, M.E. Smith, *J. Am. Chem. Soc.* 111 (1989) 5125-5132.
- [27] E. Lima, M.-E. Villafuerte-Castrejón, J.M. Saniger, A. Ibarra-Palos, J.E. Sánchez-Sánchez, L.J. Álvarez, *Solid State Ionics* 178 (2008) 1944-1949.
- [28] A.C. Palke, J.F. Stebbins, D.J. Frost, C.A. McCammon, *Am. Mineral.* 97 (2012) 1955-1964.
- [29] F. Stebbins Jonathan, L.-S. Du, K. Kelsey, H. Kojitani, M. Akaogi, S. Ono, *Am. Mineral.* 91 (2006) 337-343.
- [30] F. Stebbins Jonathan, H. Kojitani, M. Akaogi, A. Navrotsky, *Am. Mineral.* 88 (2003) 1161-1164.
- [31] R. Shannon, *Acta Crystallogr. A* 32 (1976) 751-767.
- [32] C. Minero, A. Bedini, V. Maurino, *Appl. Catal. B* 128 (2012) 135-143.
- [33] T. Hisatomi, K. Miyazaki, K. Takanabe, K. Maeda, J. Kubota, Y. Sakata, K. Domen, *Chem. Phys. Lett.* 486 (2010) 144-146.
- [34] T. Hisatomi, K. Maeda, K. Takanabe, J. Kubota, K. Domen, *J. Phys. Chem. C* 113 (2009) 21458-21466.
- [35] J.F. Montoya, M.F. Atitar, D.W. Bahnemann, J. Peral, P. Salvador, *J. Phys. Chem. C* 118 (2014) 14276-14290.
- [36] O. Ken-ichi, Y. Yasunori, T. Hiroki, I. Akira, *Bull. Chem. Soc. Jpn.* 58 (1985) 2023-2028.

- [37] A. Mills, J. Wang, D.F. Ollis, *J. Catal.* 243 (2006) 1-6.
- [38] K.-i. Ishibashi, A. Fujishima, T. Watanabe, K. Hashimoto, *J. Photoch. Photobio. A* 134 (2000) 139-142.
- [39] E.R. Carraway, A.J. Hoffman, M.R. Hoffmann, *Env. Sci. Technol.* 28 (1994) 786-793.
- [40] Y. Mao, C. Schoeneich, K.D. Asmus, *J. Phys. Chem.-US* 95 (1991) 10080-10089.
- [41] G. Waldner, R. Gómez, M. Neumann-Spallart, *Electrochim. Acta* 52 (2007) 2634-2639.
- [42] I. Mora-Seró, T.L. Villarreal, J. Bisquert, Á. Pitarch, R. Gómez, P. Salvador, *J. Phys. Chem. B* 109 (2005) 3371-3380.
- [43] N. Hykaway, W.M. Sears, H. Morisaki, S.R. Morrison, *J. Phys. Chem.-US* 90 (1986) 6663-6667.
- [44] T.L. Villarreal, R. Gómez, M. Neumann-Spallart, N. Alonso-Vante, P. Salvador, *J. Phys. Chem. B* 108 (2004) 15172-15181.
- [45] K.U. Ingold, in: J.K. Kochi (Ed.) *Free radicals*, John Wiley & Sons, New York, 1973, pp. 37-112.
- [46] I.C. Man, H.-Y. Su, F. Calle-Vallejo, H.A. Hansen, J.I. Martínez, N.G. Inoglu, J. Kitchin, T.F. Jaramillo, J.K. Nørskov, J. Rossmeisl, *ChemCatChem* 3 (2011) 1159-1165.
- [47] D.M. Herlihy, M.M. Waegle, X. Chen, C.D. Pemmaraju, D. Prendergast, T. Cuk, *Nat. Chem.* 8 (2016) 549-555.
- [48] X. Chen, S.N. Choing, D.J. Aschaffenburg, C.D. Pemmaraju, D. Prendergast, T. Cuk, *J. Am. Chem. Soc.* 139 (2016) 1830-1841.
- [49] P. Wardman, *J. Phys. Chem. Ref. Data* 18 (1989) 1637-1755.
- [50] Y. Xu, M.A. Schoonen, *Am. Mineral.* 85 (2000) 543-556.
- [51] V.M. Daskalaki, P. Panagiotopoulou, D.I. Kondarides, *Chem. Eng. J.* 170 (2011) 433-439.
- [52] J.O. Bockris, T. Otagawa, *J. Phys. Chem.-US* 87 (1983) 2960-2971.
- [53] P. Salvador, F. Decker, *J. Phys. Chem.-US* 88 (1984) 6116-6120.
- [54] P. Salvador, C. Gutiérrez, *Surf. Sci.* 124 (1983) 398-406.
- [55] S. Goldstein, D. Aschengrau, Y. Diamant, J. Rabani, *Env. Sci. Technol.* 41 (2007) 7486-7490.
- [56] R. Zellner, M. Exner, H. Herrmann, *J. Atmos. Chem.* 10 (1990) 411-425.
- [57] Y. Yamada, M. Yoneda, S. Fukuzumi, *Energ. Environ. Sci.* 8 (2015) 1698-1701.

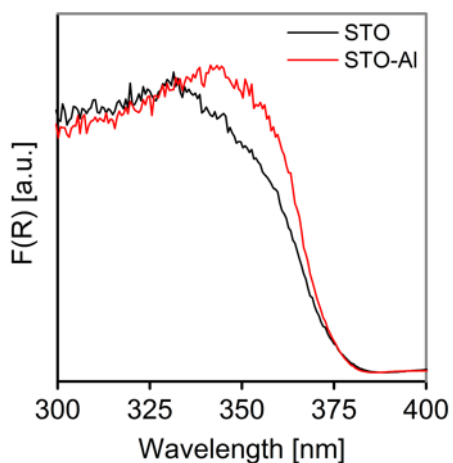
4.8 Supporting information



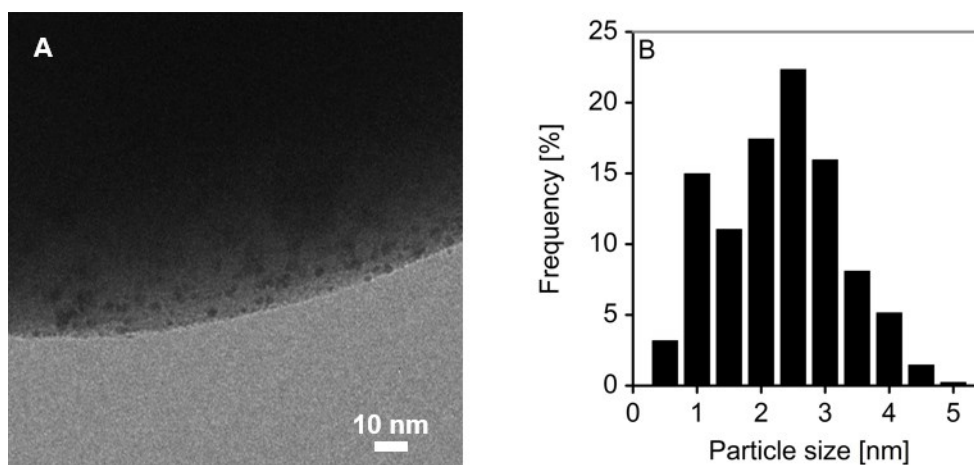
SI-Figure 4.1. Dependence of initial H₂-evolution rates on Rh co-catalyst loading. Reaction conditions: 125 mg Rh/STO-Al, 100 mL aq. methanol (10 Vol.%), 288 K, 1 bar Ar, 300 W Xe-lamp (CM1).

SI-Table 4.1. List of additional ^1H -NMR chemical shifts for signals of C_3 oxygenates not encountered in previous studies on oxygenate photoreforming [10, 11]. Chemical shifts were referenced to an 1,3,5-trihydroxybenzene standard (s, 5.94 ppm, 3 H) used for quantification.

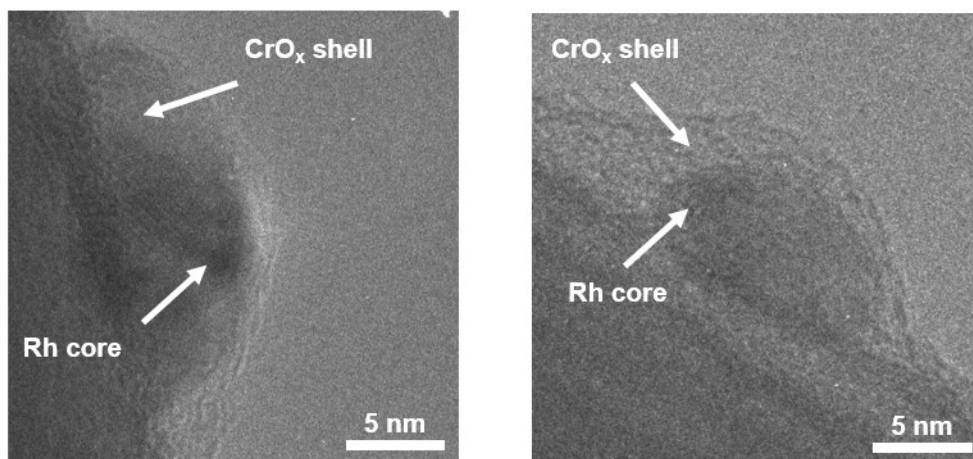
	Compound	Chemical shift [ppm]	Multiplet	J [Hz]	#H
C_3	Hydroxypyruvaldehyde	3.57	s	-	2
		4.90	s	-	1
		5.30	s	-	1
	β -Hydroxypyruvic acid	3.65	s	-	2



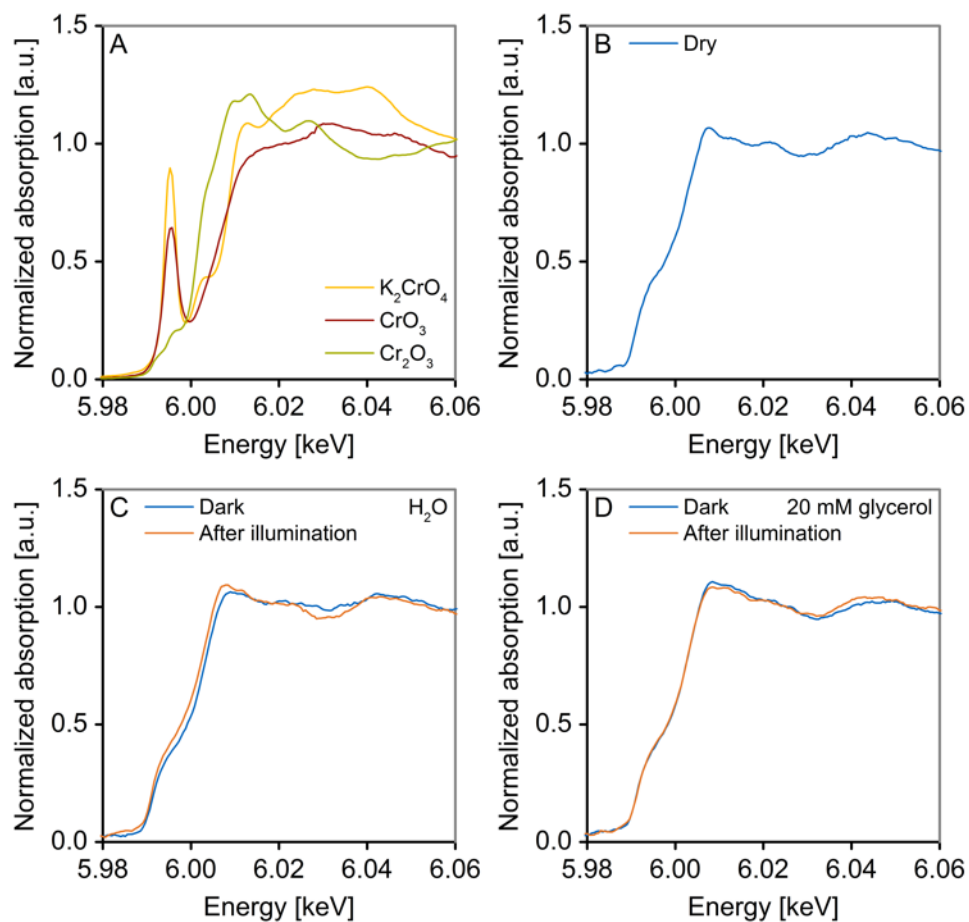
SI-Figure 4.2. DR UV-Vis absorption spectra of SrTiO_3 (STO) and Al-doped (STO-Al). Adapted with permission from ref. 25.



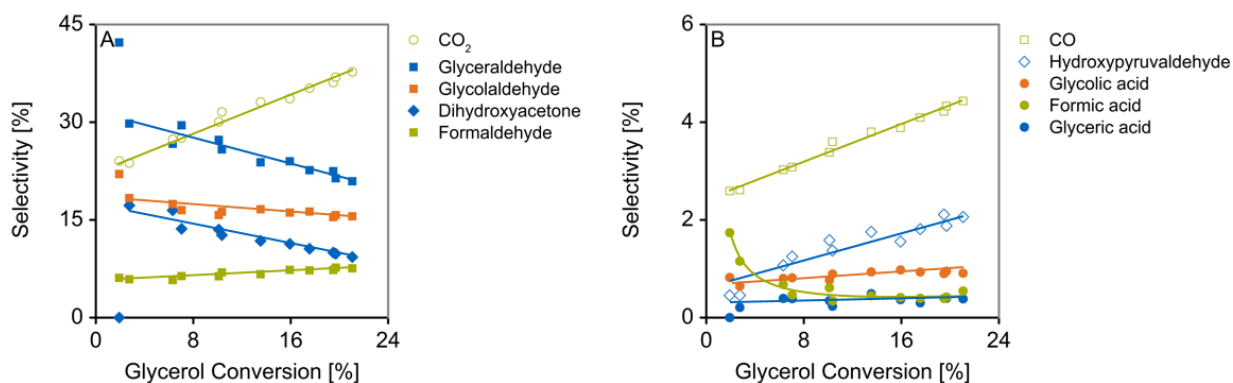
SI-Figure 4.3. (A) TEM micrograph of 0.1 wt.% Rh/STO-Al catalyst after 12 h reaction. (B) Particle size distribution. Reaction conditions: 125 mg photocatalyst, 100 mL aq. glycerol (20 mM), 288 K, 1 bar Ar, 300 W Xe-lamp (CM1).



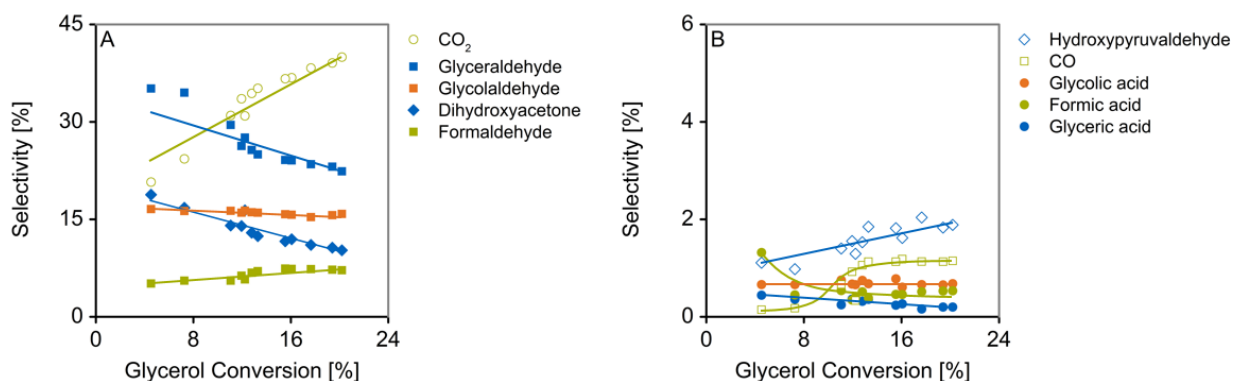
SI-Figure 4.4. TEM micrographs of 0.1 wt.% RhCrO_x/STO-Al catalyst after 12 h reaction and assignment of Rh core and CrO_x shell structures. Reaction conditions: 125 mg photocatalyst, 100 mL aq. glycerol (20 mM), 288 K, 1 bar Ar, 300 W Xe-lamp (CM1).



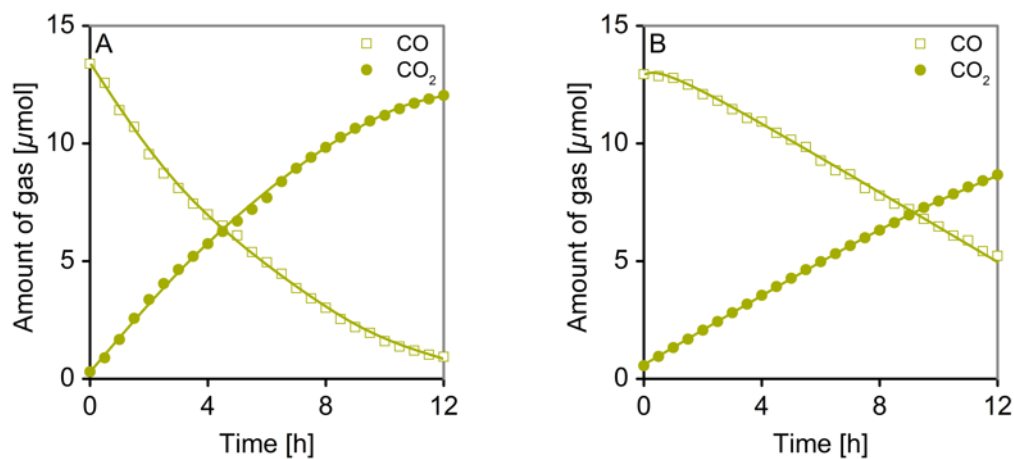
SI-Figure 4.5. Cr K-edge XANES of the $\text{RhCrO}_x/\text{STO-Al}$ (0.1 wt.% Cr) sample recorded in different reaction media prior and after UV-Vis irradiation. (A) Reference spectra. (B) Dry photocatalyst. (C) Spectra recorded in pure H_2O . (D) Spectra recorded in 20 mM glycerol.



SI-Figure 4.6. Selectivities for anodic reaction products – glycerol conversion plot for RhCrO_x/STO-Al. (A) Main products. (B) Minor products. Reaction conditions: 125 mg RhCrO_x/STO-Al, 100 mL aq. glycerol, 288 K (20 mM), 1 bar Ar, 300 W Xe-lamp (CM1).

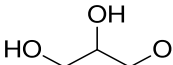
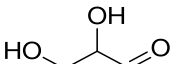
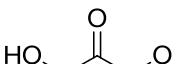
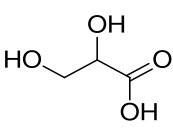
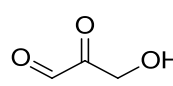
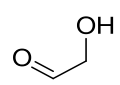
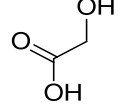
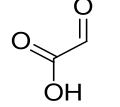
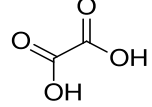
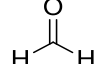
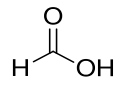


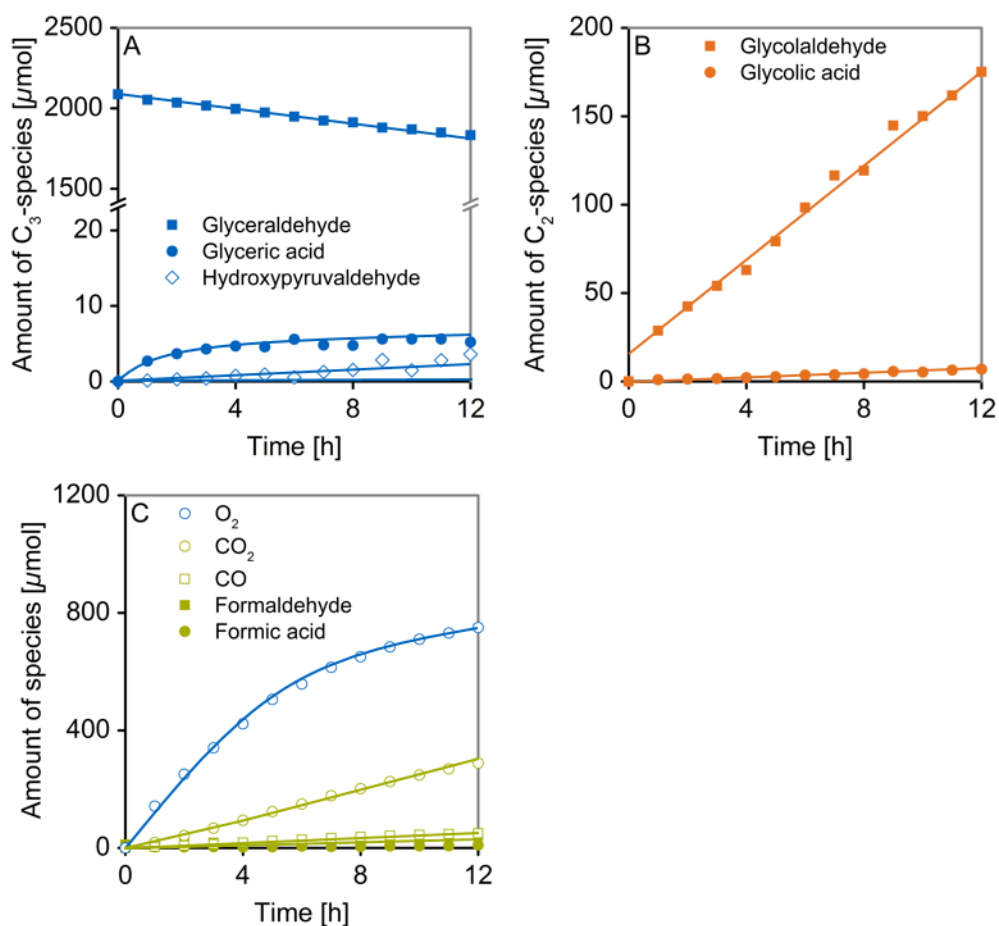
SI-Figure 4.7 Selectivities for anodic reaction products – glycerol conversion plot for Rh/STO-Al. (A) Main products. (B) Minor products. Reaction conditions: 125 mg Rh/STO-Al, 100 mL glycerol (20 mM), 288 K, 1 bar Ar, 300 W Xe-lamp (CM1).



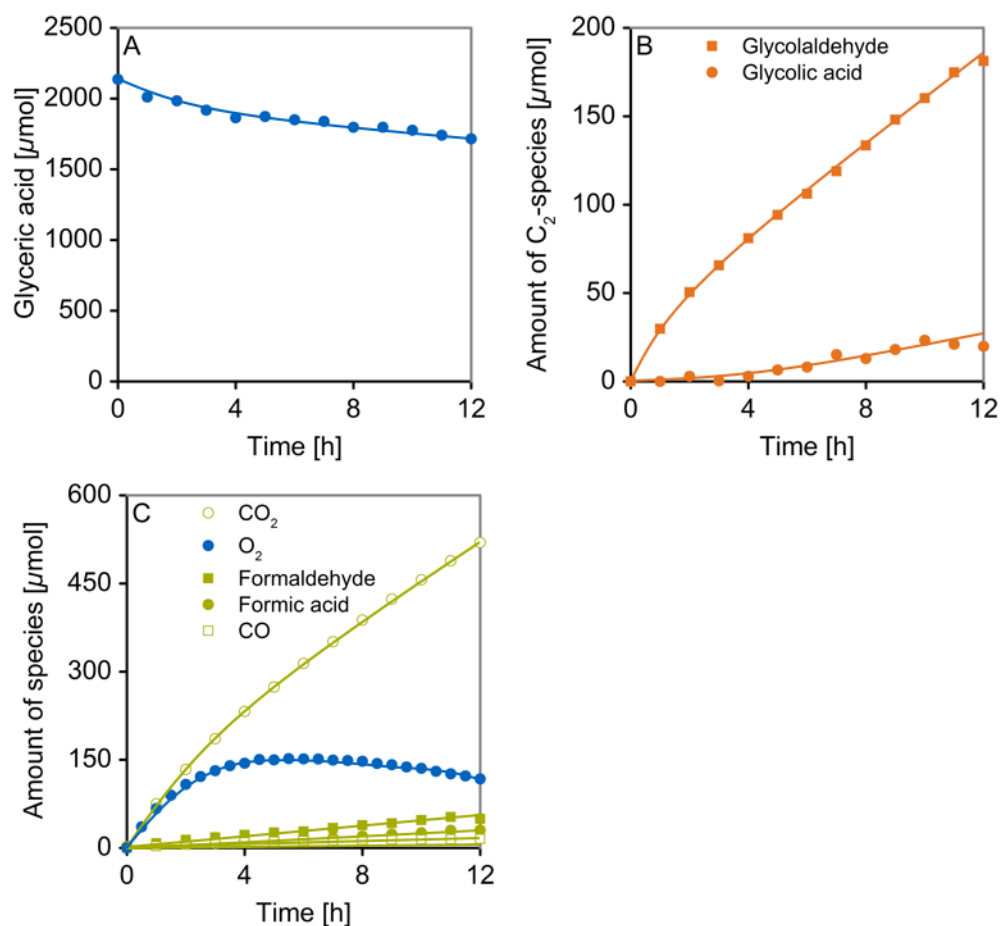
SI-Figure 4.8. Course of CO and CO₂ during oxidative CO removal on (A) Rh/STO-Al and (B) RhCrO_x/STO-Al. The initial CO concentration chosen approximately corresponds to the conditions present after 12 h of glycerol photoreforming on Rh/STO-Al and RhCrO_x/STO-Al. Reaction conditions: 125 mg photocatalyst, 100 mL H₂O (pH unadjusted), 288 K, 1000 ppm (13.5 μmol) CO, 1 bar Ar, 300 W Xe-lamp (CM1).

SI-Table 4.2. Molecular structure of C₁-C₃ oxygenates involved in glycerol photoreforming on STO-Al based photocatalysts and corresponding overall photoreforming reaction equations.

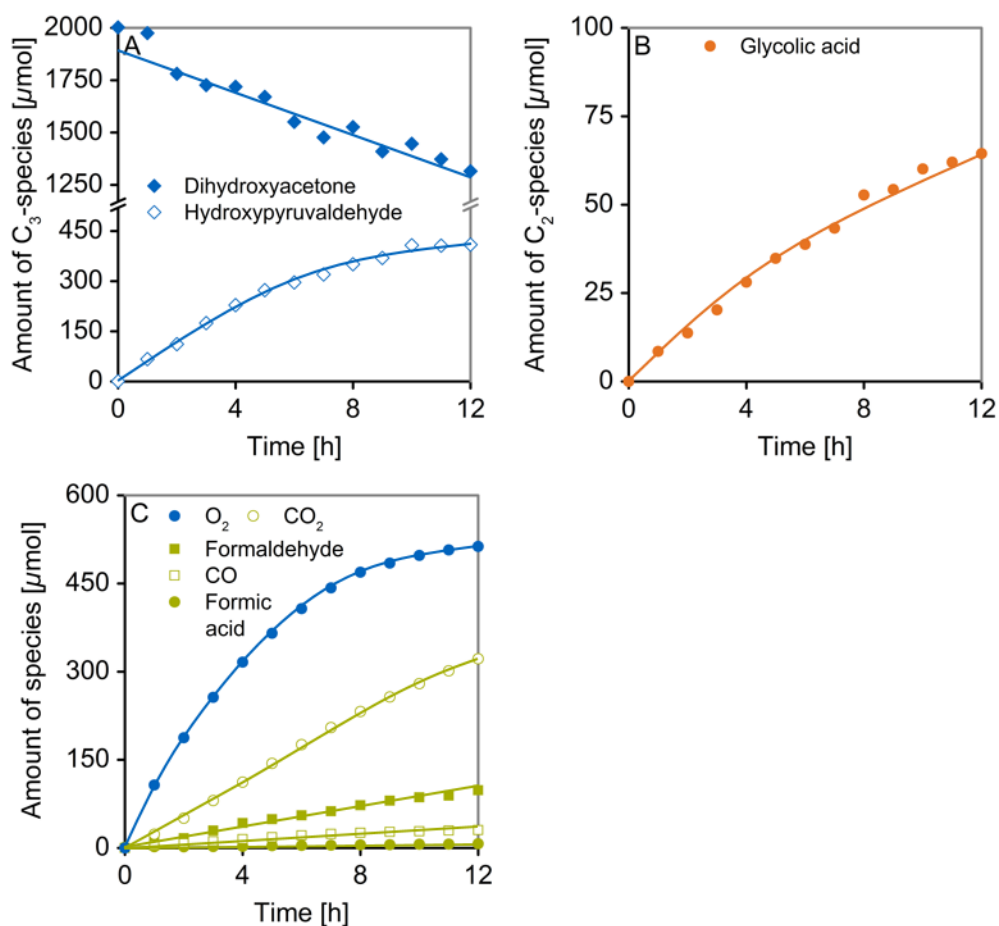
	Compound	Overall reaction equation
C ₃	Glycerol	 + 3 H ₂ O $\xrightarrow{h\nu}$ 3 CO ₂ + 7 H ₂
	Glycer-aldehyde	 + 3 H ₂ O $\xrightarrow{h\nu}$ 3 CO ₂ + 6 H ₂
	Dihydroxy-acetone	 + 3 H ₂ O $\xrightarrow{h\nu}$ 3 CO ₂ + 6 H ₂
	Glyceric acid	 + 2 H ₂ O $\xrightarrow{h\nu}$ 3 CO ₂ + 5 H ₂
	Hydroxy-pyruvalde-hyde	 + 3 H ₂ O $\xrightarrow{h\nu}$ 3 CO ₂ + 5 H ₂
C ₂	Glycolalde-hyde	 + 2 H ₂ O $\xrightarrow{h\nu}$ 2 CO ₂ + 4 H ₂
	Glycolic acid	 + H ₂ O $\xrightarrow{h\nu}$ 2 CO ₂ + 3 H ₂
	Glyoxylic acid	 + H ₂ O $\xrightarrow{h\nu}$ 2 CO ₂ + 2 H ₂
	Oxalic acid	 $\xrightarrow{h\nu}$ 2 CO ₂ + H ₂
C ₁	Form-aldehyde	 + H ₂ O $\xrightarrow{h\nu}$ CO ₂ + 2 H ₂
	Formic acid	 $\xrightarrow{h\nu}$ CO ₂ + H ₂



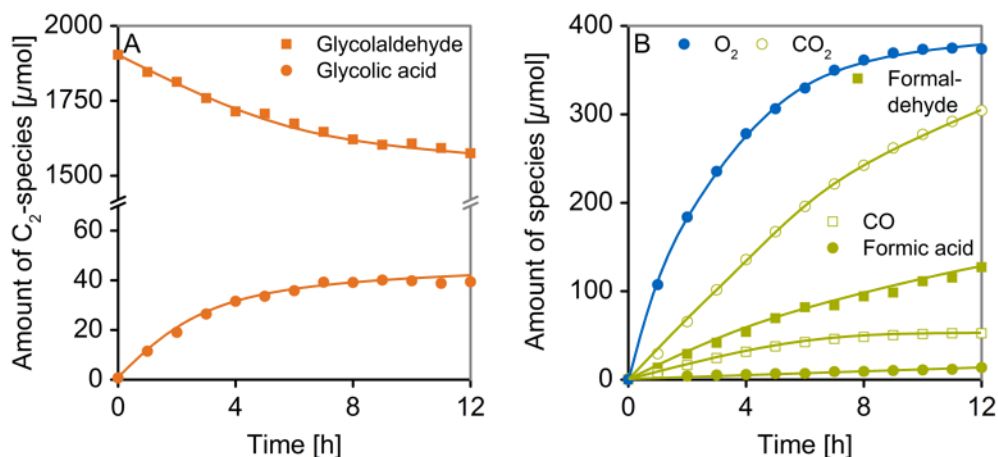
SI-Figure 4.9. Course of glyceraldehyde and anodic reaction products thereof during H_2 -generation on $RhCrO_x/STO-Al$. (A) Course of amount of glyceraldehyde and C_3 -intermediates. (B) Course of C_2 -intermediates. (C) Course of C_1 -species and O_2 . Reaction conditions: 125 mg $RhCrO_x/STO-Al$, 100 mL aq. glyceraldehyde (20 mM), 288 K, 1 bar Ar, 300 W Xe-lamp (CM1).



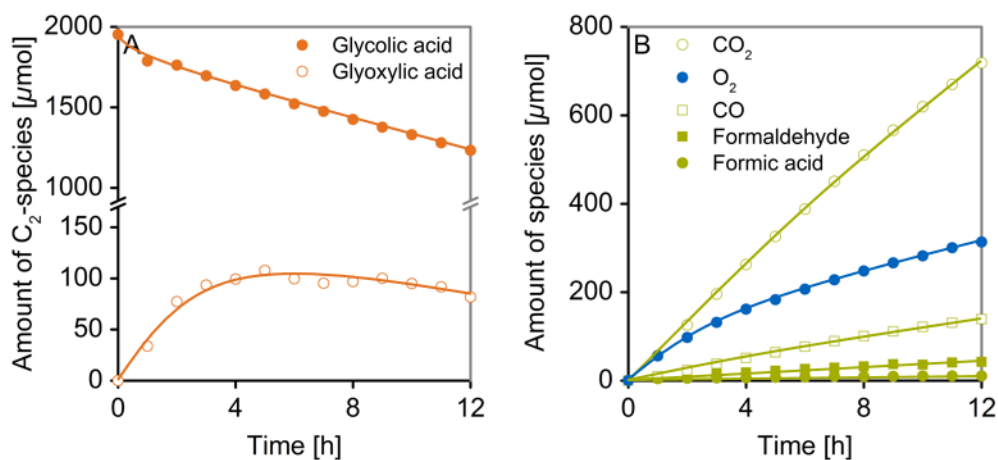
SI-Figure 4.10. Course of glyceric acid and anodic reaction products therefrom during H₂-generation on RhCrO_x/STO-Al. (A) Course of amount of glyceric acid. (B) Course of C₂-intermediates. (C) Course of C₁-species and O₂. Reaction conditions: 125 mg RhCrO_x/STO-Al, 100 mL aq. glyceric acid (20 mM), 288 K, 1 bar Ar, 300 W Xe-lamp (CM1).



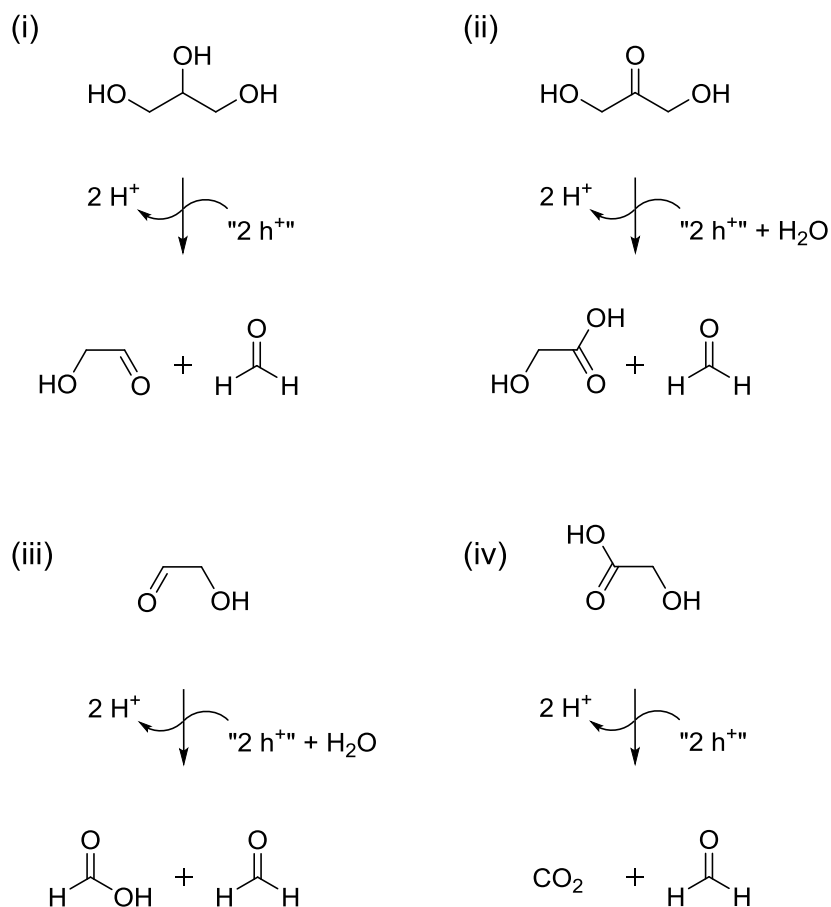
SI-Figure 4.11. Course of dihydroxyacetone and anodic reaction products therefrom during H_2 -generation on $RhCrO_x/STO-Al$. (A) Course of amount of dihydroxyacetone and C_3 -intermediates. (B) Course of C_2 -intermediates. (C) Course of C_1 -species and O_2 . Reaction conditions: 125 mg $RhCrO_x/STO-Al$, 100 mL aq. dihydroxyacetone (20 mM), 288 K, 1 bar Ar, 300 W Xe-lamp (CM1).



SI-Figure 4.12. Course of glycolaldehyde and anodic reaction products therefrom during H_2 -generation on $RhCrO_x/STO-Al$. (A) Course of amount of glycolaldehyde and C_3 -intermediates. (B) Course of C_2 -intermediates. (C) Course of C_1 -species and O_2 . Reaction conditions: 125 mg $RhCrO_x/STO-Al$, 100 mL aq. glycolaldehyde (20 mM), 288 K, 1 bar Ar, 300 W Xe-lamp (CM1).



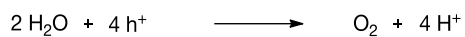
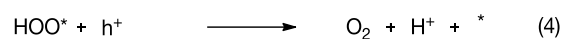
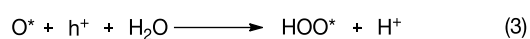
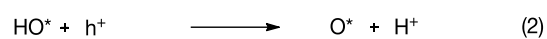
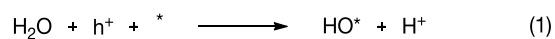
SI-Figure 4.13. Course of glycolic acid and anodic reaction products therefrom during H_2 -generation on $RhCrO_x/STO-Al$. (A) Course of amount of glycolic acid and C_3 -intermediates. (B) Course of C_2 -intermediates. (C) Course of C_1 -species and O_2 . Reaction conditions: 125 mg $RhCrO_x/STO-Al$, 100 mL glycolic acid (20 mM), 288 K, 1 bar Ar, 300 W Xe-lamp (CM1).



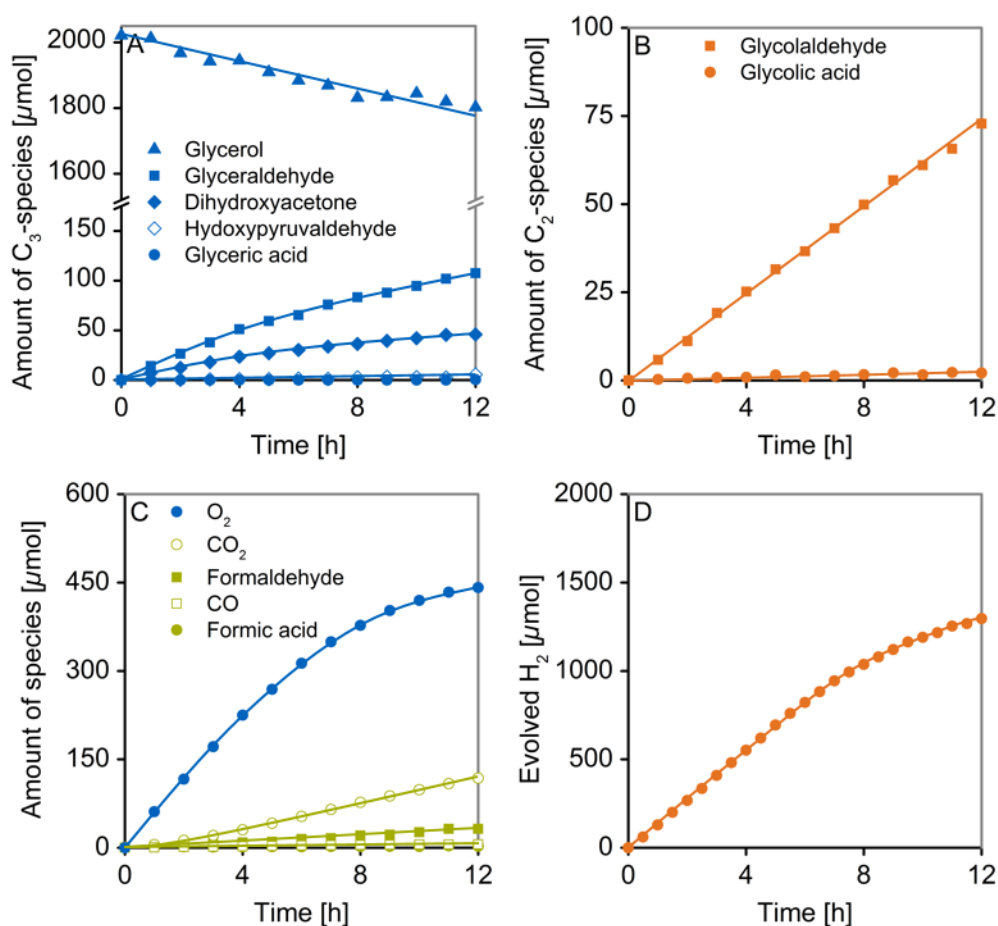
SI-Scheme 4.1. Conceptual reaction pathways for formaldehyde generation during anodic glycerol conversion. Formaldehyde may result from direct hole transfer mediated cleavage of terminal C-C bonds in compounds with hydroxymethyl moieties, i.e (i) glycerol (ii) dihydroxyacetone (iii) glycolaldehyde and (iv) glycolic acid.

Estimation of the number of photons impinging per catalyst particle

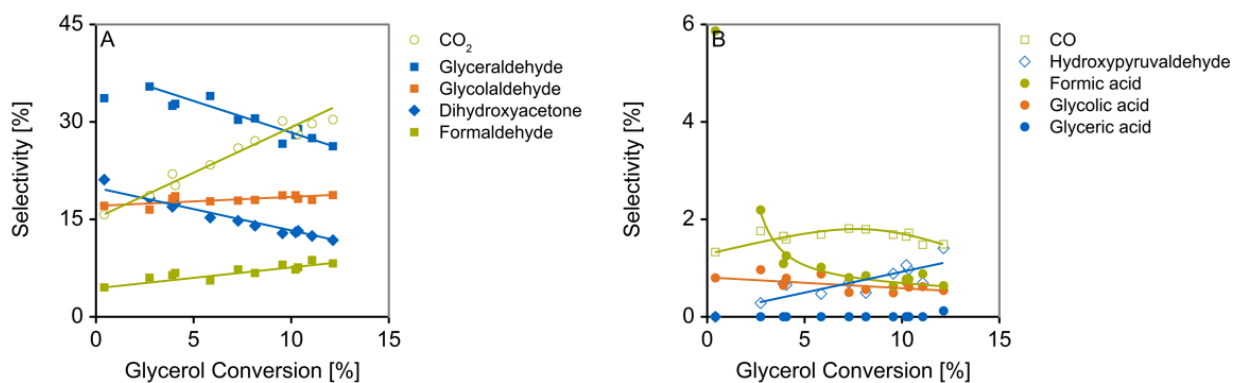
Photon flux (300 W Xe lamp, $\lambda < 390$ nm) :	$8.08 \cdot 10^{17}$ photons s^{-1}
	$1.83 \cdot 10^{16}$ photons $cm^{-2} s^{-1}$
Reactor cross section:	44.2 cm^2
Shape of STO-Al is in the following approximated as ideal cubic ($V = a^3$).	
Edge length cube :	$1.5 \cdot 10^{-4}$ cm
(estimated from SEM)	
Average cross section of a single STO-Al particle:	$2.25 \cdot 10^{-8}$ cm^2
(approximated as a^2)	
Mass catalyst per experiment:	$1.25 \cdot 10^{-1}$ g
Density $SrTiO_3$:	4.81 g cm^{-3}
Total volume of STO-Al particles:	$2.60 \cdot 10^{-2}$ cm^3
Volume of single STO-Al particle:	$3.38 \cdot 10^{-12}$ cm^3
Number of STO-Al particles:	$7.70 \cdot 10^9$, $1.74 \cdot 10^8$ cm^{-2}
Photons impinging per STO-Al particle:	$1.05 \cdot 10^8$ photons s^{-1}



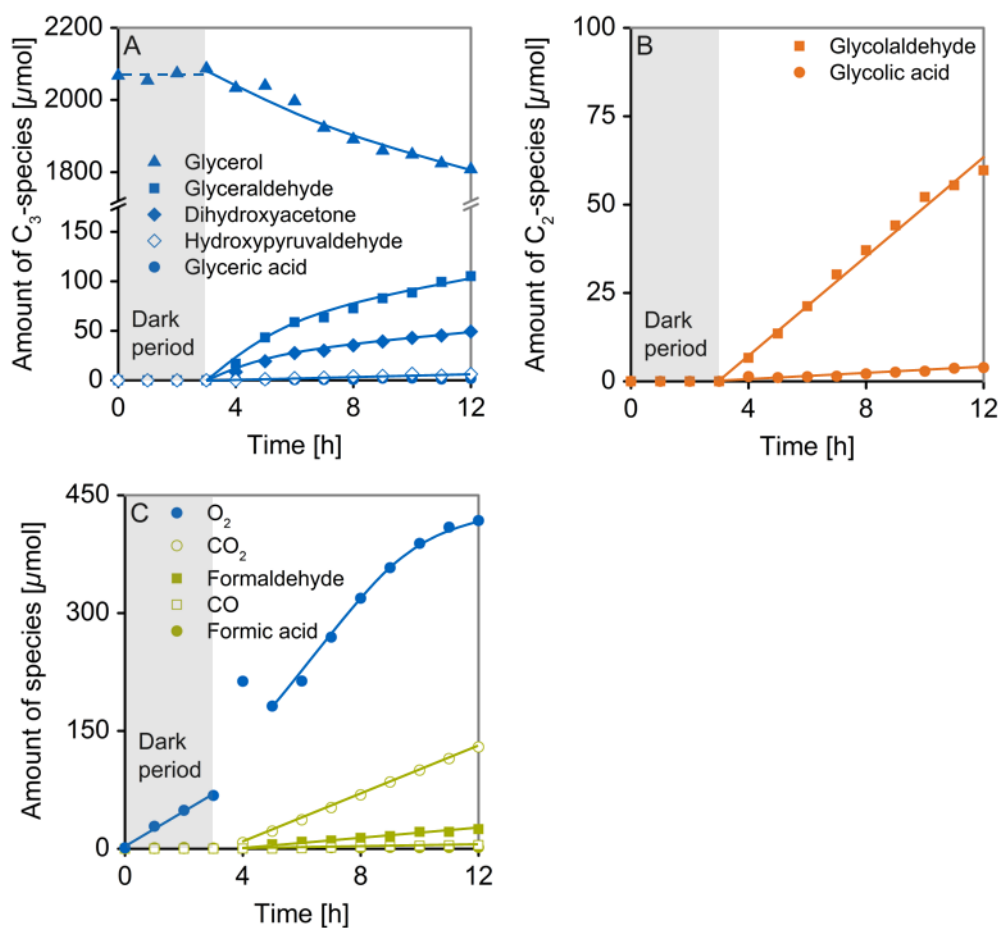
SI-Scheme 4.2. Simplified reaction steps for anodic water oxidation to O₂ over oxide surfaces. The mechanism comprises four sequential proton-coupled hole transfer reactions yielding ·OH, ·O, ·OOH type species as intermediates. The asterisk denotes an empty surface site. Simplified mechanism adopted from ref. 46.



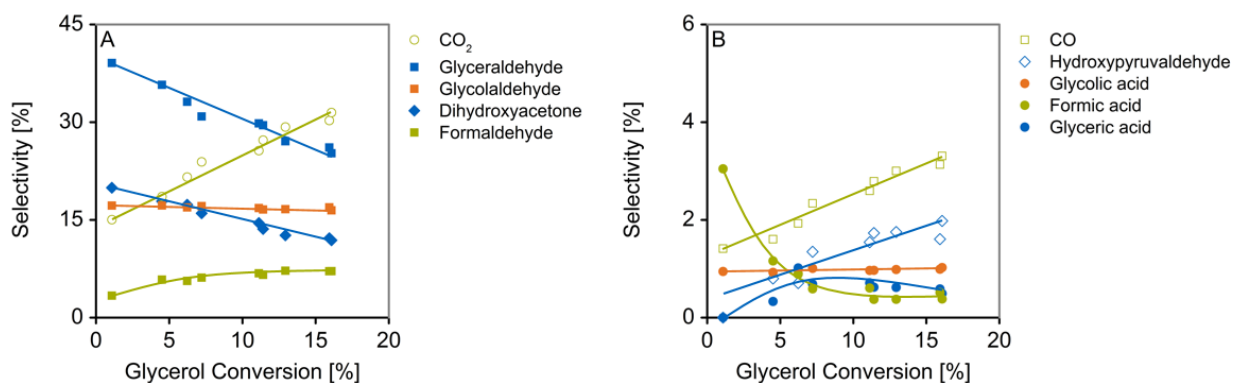
SI-Figure 4.14. Course of glycerol and anodic reaction products during H₂-generation using a physical mixture of RhCrO_x/STO-Al and undecorated STO-Al. (A) Course of amount of glycerol and C₃-intermediates. (B) Course of C₂-intermediates. (C) Course of C₁-species and O₂. (D) Course of evolved H₂. Reaction conditions: 62.5 mg RhCrO_x/STO-Al, 62.5 mg STO-Al, 100 mL aq. glycerol (20 mM), 288 K, 1 bar Ar, 300 W Xe-lamp (CM1).



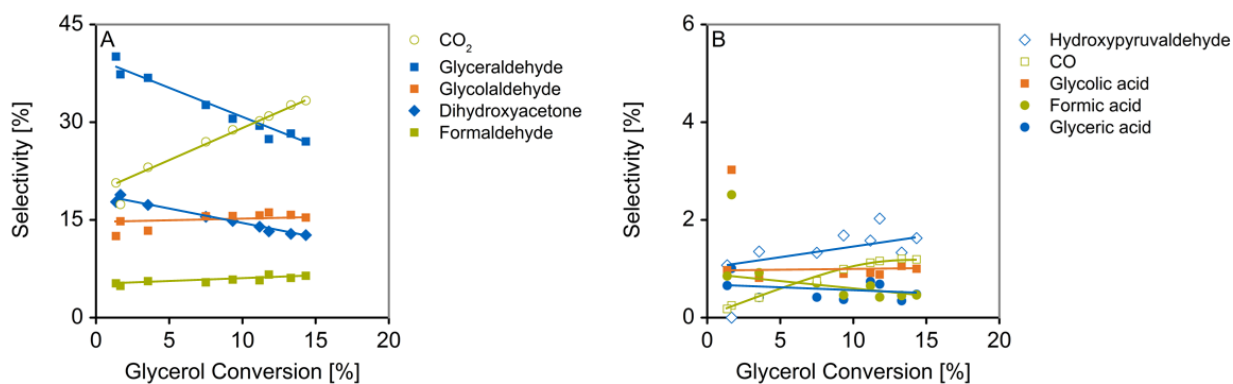
SI-Figure 4.15. Selectivities for anodic reaction products – glycerol conversion plot for physical mixture of RhCrO_x/STO-Al and undecorated STO-Al. (A) Main products. (B) Minor products. Reaction conditions: 62.5 mg RhCrO_x/STO-Al and 62.5 mg STO-Al, 100 mL aq. glycerol (20 mM), 288 K, 1 bar Ar, 300 W Xe-lamp (CM1).



SI-Figure 4.16. Course of glycerol and anodic reaction products during H₂-generation on Rh/STO-Al. Irradiation was provided after an initial dark period of 3 h. (A) Course of amount of glycerol and C₃-intermediates. (B) Course of C₂-intermediates. (C) Course of C₁-species and O₂. Reaction conditions: 125 mg Rh/STO-Al, 100 mL liquid, 20 mM glycerol, 4 mM H₂O₂, 288 K, 1 bar Ar, 300 W Xe-lamp (CM1).



SI-Figure 4.17. Selectivities for anodic reaction products – glycerol conversion plot for RhCrO_x/STO-Al. (A) Main products. (B) Minor products. Reaction conditions: 125 mg RhCrO_x/STO-Al, 100 mL liquid, 20 mM glycerol, 4 mM H₂O₂, 288 K, 1 bar Ar, 300 W Xe-lamp (CM1).



SI-Figure 4.18. Selectivities for anodic reaction products – glycerol conversion plot for Rh/STO-Al. (A) Main products. (B) Minor products. Reaction conditions: 125 mg Rh/STO-Al, 100 mL liquid, 20 mM glycerol, 4 mM H₂O₂, 288 K, 1 bar Ar, 300 W Xe-lamp (CM1).

5. Summary and conclusions

H₂-evolution rates during photoreforming crucially depend on oxygenate nature and concentration, however, the lack of mechanistic understanding of the chemical surface transformations and their role in the kinetics of the overall photocatalytic process has constrained the rational development of photocatalysts.

This thesis addresses this gap by elucidating the reaction pathways, the nature of the organic intermediates, reaction selectivities and oxidation mechanisms involved in the anodic half-reactions towards CO₂ formation on semiconductors (TiO₂ and SrTiO₃) decorated with a noble metal (Rh, Pd, Pt). The kinetic and mechanistic consequences of the anodic chemistry on the net H₂-evolution rates and the mineralization behavior were investigated in dependence of molecular structure of C₁-C₆ (poly)alcohols and aldose sugars as probe molecules. Moreover, investigations in dependence of the nature of the noble metal co-catalyst and the semiconductor's ability for total oxidation of water to O₂ were conducted. Rational strategies to overcome kinetic obstacles were devised on the basis of the mechanistic principles deduced.

Oxidative transformation of C₃-C₆ polyols during photoreforming on a Rh decorated TiO₂-based photocatalyst leads to formation of organic intermediates prior CO₂ formation *via* (i) oxidative scission of C-C bonds (ii) formation of the corresponding α -oxygen functionalized aldoses and ketoses (iii) light-driven dehydration. Direct hole transfer to the chemisorbed oxygenates on Ti(IV) sites with terminal OH-groups is proposed for the C-C cleavage steps. This leads to the formation of alkoxy-radicals that readily undergo β -C-C cleavage to yield two aldose equivalents. Carbonyl groups are formed through an indirect hole transfer mechanism, i.e. local trapping of photogenerated holes at surface lattice oxygen sites [Ti \cdot -O \cdot -Ti] which generates carbon-centered radicals *via* H \cdot abstraction from a C-H bond. In a side reaction, the radicals undergo an acid-catalyzed β -shift to eliminate water. Oxidation of the radicals to stable organic intermediates is completed *via* a current doubling mechanism.

The selectivities between direct and indirect pathways change as a function of polyol chain length. In the dominant pathway, C-C rupture (internal preferred over terminal) is gradually

avored with higher polyol carbon number. This is attributed to an increasing tendency for complexation of coordinatively unsaturated Ti(IV) centers with a higher number of anchoring polyol OH-moieties.

Oxidation rates of C₁-C₃ oxygenates on Rh/TiO₂ follow Langmuir adsorption based rate equations, where the rate constants are independent of substrate nature. Thus, photoreforming rates of these oxygenates primarily depend on the adsorption constants independent of the nature of chemical bond transformation. Along these lines, oxygenate sorption properties primarily control photocatalytic rates and direct the anodic reaction selectivities of polyols on TiO₂.

Photoreforming of sugar aldoses (C₄-C₆) is an essential prospect that would render an abundant class of oxygenates compatible as feedstock for photocatalytic H₂-generation. While total oxidation of linear C₁-C₃ oxygenates to CO₂ (following first-order dependence on concentration) can be achieved on TiO₂ decorated with noble metals (Rh, Pd, Pt), photoreforming of C₄-C₆ aldose sugars (cyclic hemiacetals) proceeds with rapidly declining rates. Using selective isotope labelling, it is shown that cyclic hemiacetals convert *via* a direct hole transfer mechanism to undergo selective oxidative ring opening (α -scission) yielding formate esters. Consecutive formate hydrolysis to the C_{n-1} aldose intermediate is identified as the rate-limiting reaction, which proceeds in a light-driven, redox-neutral reaction under acidic and pH-neutral conditions likely involving both kinds of photogenerated charges. As a consequence, anodic sites on TiO₂ are blocked by formate species, thus enhancing electron-hole recombination. Independent of the nature of the noble metal co-catalyst employed, the cathodic half-reaction does not limit the photocatalytic rates under these conditions. Stable H₂-evolution and glucose conversion over time is attained by alkalinization of the reaction media providing rapid OH⁻-induced hydrolysis of formates. Beyond control of pH, alternative oxidation routes for aldose sugars avoiding the participation of formates and strategies to enhance photocatalytic hydrolysis are mandatory.

The photoreforming studies on TiO₂-based catalysts have revealed further challenges. Formaldehyde, which forms through direct hole transfer-mediated oxidative rupture of terminal C-C bonds in compounds with hydroxymethyl groups, accumulates prior

oxidation to CO_2 due to its weak adsorption. Additionally, quantitative oxygenate oxidation to CO_2 is contingent to decreasing H_2 -evolution rates at high conversions due to the Langmuir-type dependence on oxygenate concentration and coverage.

Coupling overall water splitting and photoreforming on an Al-doped SrTiO_3 semiconductor active in the total oxidation of water to O_2 is demonstrated as a platform capable of overcoming these drawbacks. Under conditions of quantitatively suppressed back-reaction, i.e. using a RhCrO_x (core-shell) co-catalyst, the net H_2 -evolution rates are independent of oxygenate nature, concentration and coverage. Thus, the anodic transformations did not alter the overall photocatalytic rates independent of their nature. In other words, equal quantum efficiencies were obtained irrespective whether photogenerated holes participated in O_2 -evolution or oxygenate oxidations. Ultimately, kinetic coupling of water splitting and photoreforming allows for maintaining high H_2 -evolution rates even at high oxygenate coverages. Conversely, the selectivities to O_2 -evolution and oxygenate oxidation depend on oxygenate nature and concentration. It is shown that as a result of the water oxidation activity, the intermediates in O_2 -evolution catalysis (assumed as $\cdot\text{OH}$, $\cdot\text{O}$ and $\cdot\text{OOH}$) constitute the dominant oxidant in the system. Consequently, glycerol and anodic C_3 -/ C_2 -intermediates were predominantly converted in indirect hole transfer-mediated transformations with low formaldehyde selectivities. Gaseous O_2 concomitantly formed could be activated on an undecorated semiconductor to contribute to glycerol oxidation, thereby, selectively removing it from the gaseous mixture generated.

In summary, the results of this thesis provide clear strategies to minimize accumulation of undesired intermediates achieving quantitative oxidation to CO_2 with stable H_2 -evolution during photoreforming of oxygenated hydrocarbons. These strategies were build up on fundamental insight, i.e. mechanistic understanding of the relations of molecular structure, oxidation mechanism, photoreforming rates and photocatalyst properties. It is expected that these results will lead to optimized photocatalyst synthesis and reaction protocols that advance towards judicious control over oxidation selectivity.

6. Zusammenfassung und Schlussfolgerungen

H₂-Entwicklungsraten während der Photoreformierung sind entscheidend von der Art und Konzentration des eingesetzten Oxygenats abhängig. Jedoch hat der Mangel an mechanistischem Verständnis der chemischen Oberflächenumwandlungen und ihrer Rolle in der Kinetik des photokatalytischen Gesamtprozesses, die rationale Entwicklung von Photokatalysatoren eingeschränkt.

Die vorliegende Dissertation befasst sich mit dieser Diskrepanz, indem die Reaktionspfade, die Identität und Eigenschaften der organischen Intermediate, die Reaktionsselektivitäten und Oxidationsmechanismen, die in den anodischen Halbreaktionen, hin zur Bildung von CO₂, auf Edelmetall (Rh, Pd, Pt) dekorierten Halbleitern (TiO₂ und SrTiO₃) beteiligt sind, aufgeklärt wurden. Die kinetischen und mechanistischen Folgen der anodischen Chemie für die H₂-Entwicklungsraten und das Mineralisierungsverhalten wurden in Abhängigkeit der Molekularstruktur von C₁-C₆ (Poly)alkoholen und Aldose Zuckern als Sondenmoleküle untersucht. Darüber hinaus wurden Untersuchungen in Abhängigkeit der Eigenschaften des Edelmetall Co-Katalysators und der Fähigkeit des Halbleiters zur vollständigen Oxidation von Wasser zu O₂ durchgeführt. Rationale Strategien, um kinetische Hindernisse zu überwinden, wurden auf Basis der abgeleiteten mechanistischen Prinzipien entwickelt.

Oxidative Umsetzung von C₃-C₆ Polyolen während der Photoreformierung auf einem Rh-dekorierten TiO₂-basierten Photokatalysator führt zur Entstehung von organischen Intermediaten, die vor der Produktion von CO₂ über (i) oxidative Spaltung von C-C Bindungen (ii) Ausbildung der korrespondierenden α -Sauerstoff funktionalisierten Aldosen und Ketosen (iii) lichtgetriebene Dehydratisierung, gebildet werden. Direkter Lochtransfer zu den chemisorbierten Oxygenaten auf Ti(IV) Plätzen mit terminalen OH-Gruppen wird für die C-C Spaltungsschritte vorgeschlagen. Dies führt zur Bildung von Alkoxy-Radikalen, welche bereitwillig β -C-C Spaltung erfahren, um zwei Aldosenäquivalente hervor-zubringen. Carbonylgruppen werden durch einen indirekten Lochtransfer Mechanismus gebildet, d.h. durch Lokalisierung von lichterzeugten Löchern an Oberflächen-gittersauerstoffplätzen [Ti \cdot O \cdot Ti], was zur Ausbildung von Kohlenstoff-zentrierten

Radikalen durch H· Abstraktion von einer C-H Bindung führt. In einer Nebenreaktion vollziehen die Radikale einen säurekatalysierten β -Shift, um Wasser abzuspalten. Die Oxidation der Radikale zu stabilen organischen Intermediaten wird durch einen Stromverdopplungsmechanismus abgeschlossen.

Die Selektivitäten zwischen direkten und indirekten Reaktionspfaden verändern sich in Abhängigkeit der Polyol Kettenlänge. Mit zunehmender Polyol Kohlenstoffzahl wird die C-C Spaltung im Hauptreaktionspfad sukzessive begünstigt (interne Bindungen werden bevorzugt vor terminalen Bindungen gespalten). Dieser Umstand wird auf eine zunehmende Tendenz zur Komplexbildung von koordinativ ungesättigten Ti(IV) Zentren mit höherer Zahl an verankernden Polyol OH-Resten zurückgeführt.

Die Oxidationsraten von C₁-C₃ Oxygenaten auf Rh/TiO₂ gehorchen Ratengleichungen, die auf Langmuir Adsorption basieren und in denen die Ratenkonstanten unabhängig von der Art des Reaktanden sind. Folglich sind die Photoreformierungsraten dieser Oxygenate, im Wesentlichen, von den Adsorptionskonstanten, unabhängig von der Art der chemischen Bindungstransformation, bestimmt. In diesem Sinne kontrollieren hauptsächlich die Sorptionseigenschaften der Oxygenate die photokatalytischen Raten und steuern die Reaktionsselektivitäten von Polyolen in den anodischen Halbreaktionen auf TiO₂.

Photoreformierung von Aldose Zuckern (C₄-C₆) stellt eine unverzichtbare Perspektive dar, welche eine ergiebige Klasse von Oxygenaten als Rohstoff für photokatalytische H₂-Erzeugung verfügbar machen würde. Während eine vollständige Oxidation von linearen C₁-C₃ Oxygenaten zu CO₂, (einem Gesetz erster Ordnung in Konzentration folgend) auf TiO₂ dekoriert mit Edelmetallen (Rh, Pd, Pt), erzielt werden kann, so verläuft die Photoreformierung von C₄-C₆ Aldose Zuckern (ringförmige Halbacetale) mit rasant abfallenden Raten. Durch selektive Isotopenmarkierung wird gezeigt, dass ringförmige Halbacetale durch einen direkten Lochtransfer Mechanismus umgewandelt werden, um selektive, oxidative Ringöffnung (α -Spaltung) einzugehen, die zur Bildung von Formiatestern führt. Nachfolgende Formiat Hydrolyse zum C_{n-1} Aldose Intermediat wird als Raten bestimmender Schritt identifiziert, der in einer lichtgetriebenen, redox-neutralen Reaktion in sauren und pH-neutralem Milieu, wahrscheinlich unter Einbeziehung beider Arten von lichterzeugten Ladungsträgerarten, abläuft. Folglich werden Zentren für die

anodischen Halbreaktionen auf TiO_2 durch Formiat Spezies blockiert, wodurch die Elektron-Loch Rekombination gesteigert wird. Unabhängig von der Art des verwendeten Edelmetall Co-Katalysators ist die kathodische Halbreaktion unter diesen Bedingungen nicht limitierend für die photokatalytischen Raten. Zeitlich stabile H_2 -Entwicklung und Umsetzung von Glucose gelingt durch Alkalisierung der Reaktionsmedien, wodurch schnelle OH^- -induzierte Hydrolyse von Formiaten zur Verfügung steht. Über pH-Kontrolle hinaus sind alternative Oxidationswege für Aldose Zucker, welche die Beteiligung von Formiaten vermeiden, und Strategien, um photokatalytische Hydrolyse zu beschleunigen, zwingend notwendig.

Die Photoreformierungsstudien auf TiO_2 -basierten Katalysatoren haben weitere Schwierigkeiten deutlich gemacht. Formaldehyd, welches durch oxidative Spaltung terminaler C-C Bindungen in Verbindungen mit Hydroxymethyl-Gruppen entsteht, akkumuliert vor der Oxidation zu CO_2 aufgrund seiner schwachen Adsorption. Eine quantitative Oxidation von Oxygenaten zu CO_2 bedingt zusätzlich sinkende H_2 -Entwicklungsraten bei hohen Umsätzen, infolge der Langmuir-artigen Abhängigkeit von der Oxygenat Konzentration und dem Bedeckungsgrad.

Die Kopplung von Wasserspaltung und Photoreformierung auf einem Al-dotierten SrTiO_3 Halbleiter, welcher aktiv für die vollständige Oxidation von Wasser zu O_2 ist, wird als Entwicklungsplattform eingeführt, welche imstande ist diese Nachteile zu überwinden. Unter Bedingungen quantitativer Unterdrückung der Rückreaktion, d.h. durch Verwendung eines RhCrO_x (Kern-Hülle) Co-Katalysators, sind die H_2 -Entwicklungsraten unabhängig von der Art, Konzentration und Bedeckung des Oxygenats. Folglich, wurden die photokatalytischen Gesamtraten, unabhängig von der Art der anodischen Umwandlung, nicht verändert. Mit anderen Worten, gleiche Quanteneffizienzen wurden erhalten unabhängig davon, ob lichterzeugte Löcher in der O_2 -Entwicklung oder in der Oxidation der Oxygenate teilnahmen. Letztendlich erlaubt die kinetische Kopplung von Wasserspaltung und Photoreformierung hohe H_2 -Entwicklungsraten, selbst bei hohen Oxygenat Umsätzen, beizubehalten. Umgekehrt, hängen die Selektivitäten für O_2 -Entwicklung und Oxygenat Oxidation von der Art und Konzentration des Oxygenats ab. Es wird gezeigt, dass, als Folge der Wasseroxidationsaktivität, die Intermediate im

Katalysezyklus der O_2 -Entwicklung (als $\cdot OH$, $\cdot O$ und $\cdot OOH$ angenommen), die dominierenden Oxidationsmittel im System darstellen. Somit wurden Glycerin und anodische C_3 -/ C_2 -Intermediate vorwiegend durch indirekten Lochtransfer vermittelte Umwandlungen, mit niedrigen Formaldehyd Selektivitäten, umgesetzt. Gasförmiges O_2 , welches begleitend gebildet wird, kann auf einem undekorierten Halbleiter aktiviert werden, um zur Oxidation von Glycerin beizutragen und es dadurch selektiv von der gebildeten gasförmigen Mischung zu entfernen.

Zusammenfassend legen die Ergebnisse dieser Dissertation wirksame Strategien vor, um die Akkumulation von ungewünschten Intermediaten zu minimieren, während vollständige Oxidation zu CO_2 mit stabiler H_2 -Entwicklung in der Photoreformierung von sauerstoffhaltigen Kohlenwasserstoffen erzielt wird. Diese Strategien wurden, gestützt auf fundamentale Erkenntnisse, d.h. mechanistisches Verständnis der Zusammenhänge von Molekularstruktur, Oxidationsmechanismus, Photoreformierungsraten und den Eigenschaften von Photokatalysatoren, konzipiert. Es wird erwartet, dass diese Ergebnisse zu optimierten Photokatalysatorsynthese- und Reaktionsprotokollen führen werden, welche hin zu einer umsichtigen Kontrolle über die Oxidationsselektivitäten weiterentwickelt werden.

Curriculum vitae

Kai Erik Sanwald

Date/place of birth: April 11, 1988/Aalen

Education

Since 11/2013 **Doctorate as fellow of the Fonds der Chemischen Industrie** Chair of Technical Chemistry 2, Technical University of Munich, Germany, Prof. Dr. J. A. Lercher.

Field of work: *Heterogeneous photocatalysis*

03/13 – 09/13 **Research stay abroad** SUNCAT Center for Interface Science and Catalysis, SLAC National Accelerator Laboratory, Stanford University, USA.

Research supervisors: Prof. Dr. A. Nilsson, Dr. D. Friebel

Field of work: *X-ray absorption spectroscopy of electrocatalysts*

10/11 – 09/13 **Master studies in chemistry** with a focus on physical chemistry, catalysis and reaction engineering, Technical University of Munich, Germany.

Thesis: *In situ X-ray probing of highly active Ni-Fe oxide catalysts for the electrochemical oxygen evolution reaction*

10/08 – 08/11 **Bachelor studies in chemistry** with a focus on energy technology, Ulm University, Germany.

Thesis: *Deactivation of Ru catalysts during selective methanation of CO from feed gas for fuel cells (written in German)*

Institute for Surface Chemistry and Catalysis, Ulm University, Prof. Dr. R. J. Behm.

09/98 – 07/07 **University entrance qualification (Abitur)** Rosenstein-Gymnasium Heubach, Germany.

Internships

- 08/12 – 10/12 **Internship at Clariant Produkte Deutschland GmbH**
BU Catalysts, Bruckmühl-Heufeld, Germany
- 08/10 – 12/10 **Working student at Daimler AG**
Group Research/e-Drive and Future Mobility, Ulm, Germany

Scholarships and awards

- 07/14 – 04/16 Doctoral fellowship of the Fonds der Chemischen Industrie
- 07/14 Jürgen Manchot Studienpreis for excellent study achievements
- 03/13 – 08/13 Fellowship of the Ernest-Solvay-Stiftung
- 05/12 Award by the study commission chemistry of Ulm University for excellent study achievements

List of publications

8. K.E. Sanwald, T. F. Berto, O.Y. Gutiérrez, A. Jentys and J.A. Lercher, Kinetic coupling of water splitting and photoreforming on SrTiO₃-based photocatalysts, *in preparation*.
7. K.E. Sanwald, T. F. Berto, W. Eisenreich, O.Y. Gutiérrez, A. Jentys and J.A. Lercher, Overcoming the rate-limiting reaction during photoreforming of sugar aldoses for H₂-generation, *submitted*.
6. T.F. Berto, K.E. Sanwald, J.P. Byers, N.D. Browning, O.Y. Gutiérrez and J.A. Lercher, Enabling overall water splitting by CO covered noble metal co-catalysts, *J. Phys. Chem. Lett.* 7 (2016) 4358-4362.
5. K.E. Sanwald, T. F. Berto, W. Eisenreich, O.Y. Gutiérrez and J.A. Lercher, Catalytic routes and oxidation mechanisms in photoreforming of polyols, *J. Catal.* 344 (2016) 806-816.
4. T.F. Berto, K.E. Sanwald, W. Eisenreich, O.Y. Gutiérrez and J.A. Lercher, Photoreforming of ethylene glycol over Rh/TiO₂ and Rh/GaN:ZnO, *J. Catal.* 338 (2016) 68-81.
3. D. Friebe, M.W. Louie, M. Bajdich, K.E. Sanwald, Y. Cai, A.M. Wise, M.-J. Cheng, D. Sokaras, T.-C. Weng, R. Alonso-Mori, R.C. Davis, J.R. Bargar, J.K. Nørskov, A. Nilsson and A.T. Bell, Identification of highly active Fe sites in (Ni,Fe)OOH for electrocatalytic water splitting, *J. Am. Chem. Soc.* 137 (2015) 1305-1313.
2. F.F. Schweinberger, M. J. Berr, M. Döblinger, C. Wolff, K.E. Sanwald, A.S. Crampton, C.J. Ridge, F. Jäckel, J. Feldmann, M. Tschurl and U. Heiz, Cluster size effects in the photocatalytic hydrogen evolution reaction, *J. Am. Chem. Soc.* 135 (2013) 13262-13265.
1. M. J. Berr, F.F. Schweinberger, M. Döblinger, K.E. Sanwald, C. Wolff, J. Breimeier, A.S. Crampton, C.J. Ridge, M. Tschurl, U. Heiz, F. Jäckel and J. Feldmann, Size-selected subnanometer cluster catalysts on semiconductor nanocrystal films for atomic scale insights into photocatalysis, *Nano Lett.* 12 (2012) 5903-5906.

Conference contributions

Oral presentations

5. K.E. Sanwald, T. F. Berto, O.Y. Gutiérrez and J.A. Lercher, Photocatalytic transformations of biomass-derived oxygenates for hydrogen generation, 9th European Meeting on Solar Chemistry and Photocatalysis: Environmental Applications (SPEA9), 2016, Strasbourg, France.
4. K.E. Sanwald, T. F. Berto, O.Y. Gutiérrez and J.A. Lercher, Catalytic routes and oxidation mechanisms in photoreforming of oxygenates, TUM Catalysis Research Center Graduate Academy, 2016, Raitenhaslach, Germany.
3. K.E. Sanwald, T. F. Berto, O.Y. Gutiérrez and J.A. Lercher, Photocatalytic pathways for hydrogen production from biomass, 12th European Congress on Catalysis (Europacat XII), 2015, Kazan, Russia.
2. J.A. Lercher, T. F. Berto, K.E. Sanwald and O.Y. Gutiérrez, Reaction pathways of selective photocatalytic oxidation of diols and triols, Irsee VII Symposium: New Insights in Selective Oxidation Catalysis, Electrocatalysis and Catalysis of Biomass, 2015, Kloster Irsee, Germany.
1. K.E. Sanwald, T. F. Berto, O.Y. Gutiérrez and J.A. Lercher, Photochemical hydrogen production from biomass and water over heterogeneous catalysts, SolTech Workshop: Catalysis for Solar Fuels – Fundamental Concepts and Applications, 2015, Garching, Germany.

Poster presentations

4. K.E. Sanwald, T. F. Berto, W. Eisenreich, O.Y. Gutiérrez and J.A. Lercher, Towards H₂-generation through photocatalytic reforming of biomass, 49th Annual Meeting of the German Catalysis Society, 2016, Weimar, Germany.
3. K.E. Sanwald, T. F. Berto, W. Eisenreich, O.Y. Gutiérrez and J.A. Lercher, Kinetic study of reaction pathways in photocatalytic biomass reforming, 48th Annual Meeting of the German Catalysis Society, 2015, Weimar, Germany.

2. K.E. Sanwald, T. F. Berto, O.Y. Gutiérrez and J.A. Lercher, Photocatalytic glycerol reforming with co-catalyst modified GaN:ZnO solid solutions, 562. WE-Heraeus-Seminar: From Sunlight to Fuels – Novel Materials and Processes for Photovoltaic and (Photo)Catalytic Applications, 2014, Bad Honnef, Germany.
1. T. F. Berto, K.E. Sanwald, O.Y. Gutiérrez and J.A. Lercher, Photocatalytic glycerol reforming with co-catalyst modified GaN:ZnO solid solutions, 47th Annual Meeting of the German Catalysis Society, 2014, Weimar, Germany.